

Electrochemical Methods to Study Iron-Sulfur Cluster Proteins

Thesis by
Helen Segal

In Partial Fulfillment of the Requirements for the degree of
Doctor of Philosophy

CALIFORNIA INSTITUTE OF TECHNOLOGY
Pasadena, California

2016
(Defended May 18, 2016)

© 2016

Helen Segal

ACKNOWLEDGEMENTS

I would like to thank all those involved in making this thesis a reality. First, I would like to thank my advisor Doug Rees for his constant help and support. I would also like to thank my thesis committee, Harry Gray, Long Cai, and Judy Campbell, for helpful scientific discussion and advice. I had the privilege of working with a number of very talented scientists in the lab throughout my graduate studies. I am grateful for the support and scientific discussions with: Dr. Jacqueline K. Barton, Dr. Mike Hill, Dr. Andrew Udit, Dr. Keiko Yokoyama, Dr. Anna Arnold, Phil Bartels, Kelsey Boyle, Adam Boynton, Dr. Russ Ernst, Dr. Ariel Furst, Dr. Wendy Geil, Dr. Mike Grodick, Dr. Alexis Komor, Dr. Anna McConnell, Dr. Tim Mui, Dr. Natalie Muren, Liz O'Brien, Dr. Eric Olmon, Dr. Catrina Pheeney, Dr. Christine Romano, Dr. Curtis Schneider, Dr. Katie Schaeffer, Rebekah Silva, Dr. Hang Song, Dr. Pam Sontz, Dr. Alyson Weidman, Andy Zhou, Keisha Dykes, Jenny He, Chengcheng Fan, Nadia Herrera, Julie Hoy, Dr. Chinny Idigo, Dr. Jens Kaiser, Aron Kamajaya, Jeffrey Lai, Allen Lee, Qiwen Li, Phong Nguyen, Pavle, Nikolovski, and Dr. Janet Yang. I would especially like to thank the members of Team Nitro for supporting me through a very challenging transition, and for creating an environment that always made me excited to come to work: Dr. James Howard, Dr. Thomas Spatzal, Dr. Limei Zhang, Dr. Kathryn Perez, Christine Morrison, Belinda Wenke, Andrew Buller, Renee Arias, Keith Beadle, Corinna Probst, and Felix Kolbe. Finally, I would like to thank Phoebe Ray and Maureen Renta for always keeping everything running smoothly in the lab.

I would also like to thank my friends and family for encouraging and supporting me throughout graduate school. I would especially like to thank my roommates, Matt Griffin, Connie Wang, Eric Lubeck, Marvin, and Team Cuddles. Their comradery throughout the last six years has been invaluable. I would like to acknowledge my little brother Zachary. We do not talk very often, but when we do it is magical. I would especially like to thank my parents Andrew Segal and Laurie Segal who taught me the value of hard work and integrity. Their support and trust in me throughout graduate school were essential for the completion of this thesis.

ABSTRACT

Electron transfer between proteins is an important mechanism in multiple biological processes. In this thesis, methods were developed to study electron transfer in two biological contexts: 1) DNA-mediated signaling between DNA binding proteins with 4Fe-4S clusters and 2) nitrogenase.

The first portion of this thesis focuses on the spectroscopic and electrochemical characterization of the iron-sulfur cluster in Dna2. Dna2 is a helicase-nuclease that is involved in Okazaki fragment maturation, double strand break repair, mitochondrial genome maintenance, and telomere maintenance. Dna2 is one of multiple DNA repair and replication proteins that contain a 4Fe-4S cluster, a cofactor that generally participates in electron transfer processes. It has been proposed that these enzymes may use their 4Fe-4S clusters to signal one another over large molecular distances to coordinate their activity on biological time scales through DNA-mediated redox chemistry. A combination of EPR and UV-visible absorption spectroscopy along with electrochemistry studies on DNA-modified gold electrodes was performed to provide insight into the chemical characteristics of the 4Fe-4S cluster in Dna2. These studies also provide a foundation for how DNA charge transport might coordinate the action of eukaryotic DNA repair and replication proteins with 4Fe-4S clusters.

The second portion of this thesis describes the development of electrochemical methods to study nitrogenase, the enzyme that catalyzes the reduction of atmospheric dinitrogen to bioavailable ammonia. First, flavodoxin II, the biological reductant of the Fe-protein of nitrogenase, was characterized using a combination of electrochemical and structural methods to determine the molecular interactions that facilitate reduction of the nitrogenase iron protein. Second, two electrochemical methods, edge-plane pyrolytic graphite electrodes and single crystal gold electrodes modified with ω -functionalized alkane-thiols, were adapted to study the redox chemistry at the iron-sulfur cluster of the Fe-protein. These studies provided insight into both the fundamental characteristics of electron

transfer reactions involving nitrogenase, as well as insight into how to better study this enzyme using electrochemical methods.

PUBLISHED CONTENT AND CONTRIBUTIONS

Grodick, M. A., Segal, H. M., Zwang, T. J., and Barton, J. K. (2014). "DNA-Mediated Signaling by Proteins with 4Fe-4S Clusters is Necessary for Genomic Integrity". In: *Journal of the American Chemical Society* 136.17, pp. 6470–6478. doi: 10.1021/ja501973c.

H. M. S. participated in the design and implementation of the *lac*⁺ reversion assay for MutY activity and participated in the writing of the manuscript.

Sontz, P. A., Muren, N. B., and Barton, J. K. (2012). "DNA Charge Transport for Sensing and Signaling". In: *Accounts of Chemical Research* 45.10, pp. 1792–1800. doi: 10.1021/ar3001298.

Figure 5 reprinted with permission from the copyright holder, American Chemical Society.

Pheeney, C. G., Arnod, A. R., Grodick, M. A., and Barton, J. K. (2013). "Multiplexed Electrochemistry of DNA-Bound Metalloproteins". In: *Journal of the American Chemical Society* 135.32, pp. 11869–11878. doi: 10.1021/ja4041779.

Figure 4 reprinted with permission from the copyright holder, American Chemical Society.

TABLE OF CONTENTS

Acknowledgements.....	iii
Abstract	iv
Published Content and Contributions.....	vi
Table of Contents.....	vii
List of Illustrations and/or Tables.....	ix
Chapter 1: Introduction	1
Iron-Sulfur Clusters in DNA Binding Proteins	1
Nitrogenase	10
References	18
Chapter 2: Purification and Spectroscopic Characterization <i>S. cerevisiae</i> Dna2.....	30
Abstract	30
Introduction.....	31
Methods.....	33
Results	41
Conclusion.....	53
References	54
Chapter 3: Dna2 Electrochemical Characterization on DNA-Modified Gold Electrodes.....	58
Abstract	58
Introduction.....	59
Materials and Methods.....	63
Results	66
Conclusion.....	76
References	78
Chapter 4: Electrochemical Assay to Detect Dna2 Nuclease Activity.....	81
Abstract	81
Introduction.....	81
Materials and Methods.....	84
Results	88
Conclusion.....	93
References	95
Chapter 5: Electrochemical and Structural Characterization of <i>Azotobacter vinelandii</i> Flavodoxin II	97

Abstract	97
Introduction.....	98
Method	101
Results	106
Conclusion.....	116
References	118
 Chapter 6: Electrochemical Studies of the	
<i>Azotobacter vinelandii</i> Nitrogenase Iron Protein	124
Abstract	124
Introduction.....	125
Method	129
Results	135
Conclusion.....	143
References	145
 Appendix 1: Materials for <i>S. cerevisiae</i> Dna2 Expression	
in <i>E. coli</i>	148
Appendix 2: Dna2 Electrochemical Nuclease Assay	
Supporting Figures and Tables	154
Appendix 3: Electrochemical and Structural Characterization	
of <i>Azotobacter vinelandii</i> Flavodoxin II	
Supporting Figures and Tables	170
Appendix 4: A Method for Monitoring DNA Charge Transport	
Signaling Between DNA Repair Proteins	181

LIST OF ILLUSTRATIONS AND/OR TABLES

<i>Number</i>	<i>Page</i>
Figure 1.1 The Structure of DNA.....	2
Figure 1.2 Platforms for Studying DNA Charge Transport.....	3
Figure 1.3 Model for DNA Charge Transport in DNA Repair	7
Table 1.1 DNA Binding Proteins with 4Fe-4S Clusters	8
Figure 1.4 Structure of the Nitrogenase Complex.....	12
Figure 1.5 Electron Transfer in Nitrogenase	13
Table 1.2 Midpoint Potentials of the Nitrogenase Metal Clusters	16
Figure 2.1 <i>S. cerevisiae</i> Dna2	31
Figure 2.2 Crystal Structure of Mouse Dna2 Bound to DNA.....	32
Figure 2.3 Gel Analysis of the Dna2 Purification	37
Figure 2.4 Dna2 Activity Assays.....	41
Figure 2.5 UV-Visible Absorption Spectrum of Dna2	42
Figure 2.6 X-Band EPR Spectrum of Dna2 at 10K	43
Figure 2.7 Dna2 and Dna2 C771A Nuclease Assays	44
Figure 2.8 Dna2 and Dna2 E675A Nuclease Assays	45
Figure 2.9 UV-Visible Absorption Spectra of Dna2 Mutants	46
Figure 2.10 Oxidative Degradation of the 4Fe-4S Cluster in Dna2.....	48
Figure 2.11 UV-Visible Absorption Spectrum of Reduced Dna2	49
Figure 2.12 X-Band EPR Spectrum of Reduced Dna2	51
Table 2.1 EPR Data for DNA Binding Proteins with 4Fe-4S Clusters.....	52
Figure 3.1 DNA Charge Transport on DNA-Modified Gold Electrodes.....	61
Figure 3.2 Protein Electrochemistry on DNA-Modified Gold Electrodes...	63

Table 3.1 Oligonucleotides for Electrochemistry	64
Figure 3.3 Dna2 on DNA-Modified Gold Electrodes	68
Figure 3.4 DNA-Mediated Electrochemistry of DNA Binding Proteins.....	69
Figure 3.5 Signal Intensity Over Time	70
Figure 3.6 Dna2 and Dna2 C771A on DNA-Modified Gold Electrodes	71
Figure 3.7 Dna2 in Nuclease Assay Buffer	72
Figure 3.8 Dna2 in Helicase Assay Buffer.....	74
Figure 3.9 Electronic Coupling Between the Iron-Sulfur Cluster of Dna2 and the DNA on Gold Electrodes.....	75
Figure 4.1 Electrochemical Dna2 Nuclease Assay	83
Figure 4.2 Electrochemical Nuclease Assay on a 5'-Tail DNA Substrate.....	90
Figure 4.3 Dna2 Nuclease Assay on 5'-Tail DNA Substrates with Different Overhang Lengths.....	92
Figure 4.4 Electrochemical Nuclease Assay with the Dna2 E675A Nuclease-Deficient Mutant.....	93
Figure 5.1 Flavodoxin II on Basal plane Graphite Electrodes Modified with DDAB.....	107
Figure 5.2 pH Titration of Flavodoxin II	110
Figure 5.3 Structure of Oxidized Flavodoxin II	111
Figure 5.4 The FMN Binding Site of Flavodoxin II.....	113
Figure 5.5 Model of the Flavodoxin II - Iron Protein Complex.....	115
Figure 6.1 Methods for Studying the Redox Properties of Av2	127
Figure 6.2 Analysis of Purified Nitrogenase Component Proteins	130

Figure 6.3 Acetylene Reduction Assay.....	132
Figure 6.4 Nitrogenase Activity following Preparation for Electrochemistry Experiments	135
Figure 6.5 Av2 Direct Electrochemistry on Edge-Plane Pyrolytic Graphite Electrodes	138
Figure 6.6 Cyclic Voltammograms of Av2 on Single Crystal Gold Electrodes	139
Table 6.1 Midpoint Potential of Av2 on Gold Electrodes.....	140
Figure 6.7 Oxidation of Av2 on Single Crystal Gold Electrodes.....	141
Figure 6.8 Redox Chemistry of Av2 Bound to MgATP on Single Crystal Gold Electrodes.....	142
Table A1.1 Primers for Construction of the Wildtype and Mutant pQTEV-DNA2 Overexpression Plasmids	149
Table A1.2 Primers for Site-Directed Mutagenesis of the Dna2 Overexpression Plasmid.....	150
Table A1.3 Plasmids for Dna2 Overexpression	151
Table A1.4 <i>E. coli</i> Strains for Wildtype and Mutant Dna2 Overexpression.....	152
Table A1.5 <i>E. coli</i> Strains for Storage of the Dna2 Overexpression Plasmids	153
Figure A2.1 Comparison of Wildtype Dna2 and Dna2 E675A Nuclease Activity with Methylene Blue DNA	155
Figure A2.2 Electrochemical Nuclease Assay on the Duplex DNA Substrate.....	156
Figure A2.3 Electrochemical Nuclease Assay on the 5'-Tail with a Two Nucleotide Overhang DNA Substrate ..	157

Figure A2.4	Electrochemical Nuclease Assay on the 5'-Tail with a Twenty Nucleotide Overhang DNA Substrate	158
Figure A2.5	Quantification of DNA on the Working Electrode.....	159
Figure A2.6	Scan Rate Analysis 1	160
Figure A2.7	Scan Rate Analysis 2	161
Figure A2.8	Scan Rate Analysis 3.....	162
Figure A2.9	Scan Rate Analysis 4.....	163
Figure A2.10	Scan Rate Analysis 5.....	164
Figure A2.11	Scan Rate Analysis 6.....	165
Figure A2.12	Scan Rate Analysis 7	166
Figure A2.13	Scan Rate Analysis 8.....	167
Table A2.1	Oligonucleotides for the Electrochemical Nuclease Assay	168
Table A2.2	DNA Substrates for the Electrochemical Nuclease Assay	169
Figure A3.1	Cyclic Voltammogram of Flavodoxin II on Unmodified Basal Plane Graphite Electrodes	171
Figure A3.2	Cyclic Voltammogram of Flavodoxin II Purified from <i>E. coli</i>	172
Figure A3.3	Cyclic Voltammogram of FMN	173
Figure A3.4	Cyclic Voltammogram of Flavodoxin II with the High and Low Potential Species.....	174
Figure A3.5	Flavodoxin II Scan Rate Analysis	175
Figure A3.6	FMN Scan Rate Analysis.....	176
Figure A3.7	Potential Reduction Mechanisms of FMN Bound by Flavodoxin II.....	177

Table A3.1	Midpoint Potentials of <i>Azotobacter vinelandii</i> Flavodoxin II	178
Table A3.2	Data Collection and Refinement Statistics for <i>A. vinelandii</i> Flavodoxin II (<i>nifF</i>).....	179
Table A3.3	Predicted Amino Acid Residue Interactions Between Flavodoxin II and the Iron Protein.....	180
Figure A4.1	Helper Function Assay.....	183
Figure A4.2	In-frame Inactivation of <i>dinG</i> via the Wanner Method	186
Table A4.1	Primers for Construction of the DinG Helper Function Assay Plasmids and <i>E. coli</i> Strains	190
Figure A4.3	Results of the Helper Function Assay for MutY Activity	191
Figure A4.4	Growth Curves for the CC104 <i>E. coli</i> Strain	193

INTRODUCTION

Proteins have evolved to bind a range of metal centers that are required for enzymatic activity. These metal centers have many functions, including but not limited to stabilizing protein structure, acting as a Lewis Acid-Base, or participating in redox reactions (1-3). This latter role involves electron transfer between redox-active transition metal centers, and constitutes an important step in reactions catalyzed by enzymes, like ribonucleotide reductase and the respiratory chain complex, that sustain the growth and proliferation of organisms. Additionally, this type of reaction occurs in enzymes, like hydrogenase and nitrogenase, that are models for the development of environmentally friendly catalysts for industrial processes (1). Thus, studies of electron transfer in metal-binding proteins can advance the general understanding of both human health and industrial catalyst development. In this thesis, methods were developed to study inter- and intra-protein electron transfer in two different systems: (1) DNA binding proteins that contain 4Fe-4S clusters and (2) nitrogenase.

Iron-Sulfur Clusters in DNA Binding Proteins

DNA is composed of a series of heterocyclic, aromatic base pairs surrounded by a sugar phosphate backbone (4). The π -orbitals of the planar nucleobases stack in a manner that is reminiscent of the orbital overlap in conductive π -stacked solids, like graphite (**Figure 1**). Consistent with this observation, shortly after the double helix structure of B-form DNA was discovered, it was proposed that the base pairs could be a medium for charge transport (5,6). Using multiple experimental strategies for studying both ground state and excited state electron transfer through DNA (**Figure 2**), the Barton lab has confirmed this prediction, and has established that DNA acts as a molecular wire to facilitate rapid charge transport over large molecular distances of up to 100 nanometers. This

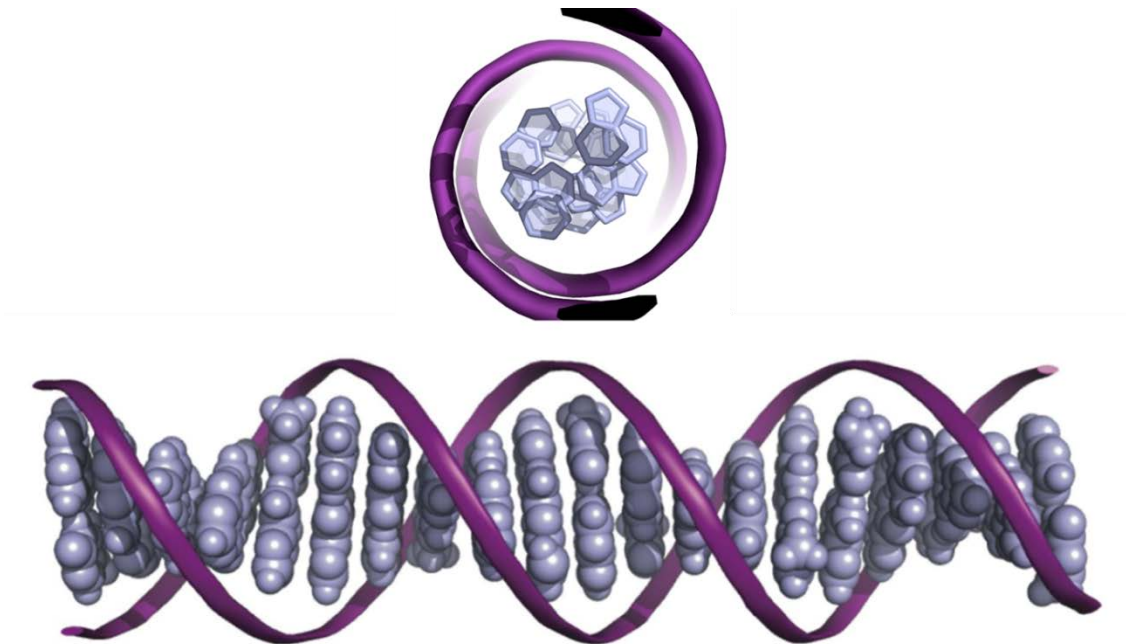


Figure 1.1. The Structure of DNA. (Top) A top-down view of DNA. (Bottom) A side view of DNA. The sugar phosphate backbone is shown in dark purple while the nucleobases are shown in light purple. The π -orbitals of the nucleobases overlap such that they create a conduit for electron transfer.

finding, along with the discovery that small perturbations in DNA structure attenuate charge transport, has provided a basis for studying this chemistry within a cell (7-9).

DNA charge transport (CT) has been studied in multiple biological contexts, including long-range activation of redox-active transcription factors, protection of DNA from oxidative damage, and detection of damaged or mismatched base pairs by DNA repair proteins (10-17). In order for proteins to participate in this type of signaling, they must bind DNA and have a redox active cofactor that can participate in electron transfer reactions. Common cofactors of this type include: NAD^+ / NADH , $\text{FADH}_2/\text{FAD}^+$, copper-containing cofactors, and iron-containing cofactor, such as hemes and iron-sulfur clusters (1). Traditionally, redox-active cofactors were not common in DNA binding proteins; however, in the last decade a number of proteins involved in DNA and RNA metabolism have been identified as

4Fe-4S cluster binding proteins (**Tables 1**). The role of the 4Fe-4S clusters in these proteins remains enigmatic (18, 19).

DNA Glycosylases with 4Fe-4S Clusters. The first DNA repair protein in which a 4Fe-4S cluster was observed was Endonuclease III (EndoIII), a DNA glycosylase (20). Since this original discovery, DNA glycosylases have served as a model system for preliminary characterization of DNA-mediated charge transport signaling between DNA repair proteins.

DNA glycosylases are the enzymes responsible for the first step in the base excision repair pathway in which damaged nucleobases are excised to initiate repair of DNA lesions prior to replication. Thus, DNA glycosylases are able to search an entire genome to find and repair DNA lesions that often have only minor chemical and structural differences from the canonical Watson-Crick base pairs (21-23). A subset of DNA glycosylases contain a 4Fe-4S cluster, which is positioned within 15Å of the DNA binding site of these enzymes (24, 25).

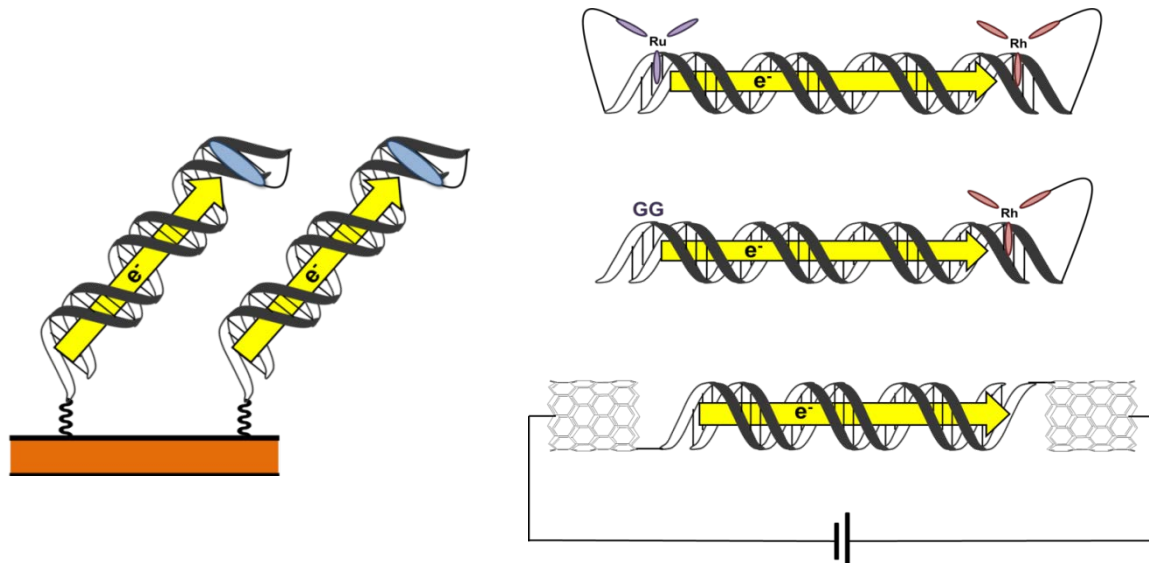


Figure 1.2. Platforms for Studying DNA Charge Transport. (Left) DNA-modified electrodes with a redox probe. (Top Right) DNA-mediated quenching of the luminescence of a donor metallointercalator by an acceptor metallointercalator. (Middle Right) DNA-mediated oxidation of guanine by a metallointercalator that is a photo-oxidant. (Bottom Right) A single molecule device for studying DNA conductivity that consists of a piece of DNA covalently attached across a gap in a carbon nanotube.

Therefore, the 4Fe-4S cluster is close enough to the DNA nucleobases to theoretically allow for electron transfer between this metal center and the DNA.

Although the distance between the 4Fe-4S cluster in EndoIII is sufficient for electron transfer to occur between the protein and the DNA, experimental evidence suggested that this cofactor was not redox-active. Specifically, the 4Fe-4S cluster in EndoIII could not be reduced at a biologically relevant potential, and it could not be oxidized without degradation (20). These observations suggested that this cofactor had a purely structural role. However, work from the David lab showed that although the 4Fe-4S cluster in MutY, a structurally related DNA glycosylase, was required for DNA binding, it was not required for protein folding or thermal stability (26). Consistent with these findings, the Barton lab has proposed that this iron cofactor is in fact redox-active, and participates in DNA-mediated electron transfer rather than having a purely structural role (10, 15-17).

The first insight into the redox activity of the 4Fe-4S cluster in DNA glycosylases was the observation that DNA binding shifts the midpoint potential of this iron cofactor. The DNA bound potential of the 2+/3+ couple of the 4Fe-4S cluster in three DNA glycosylases, Endonuclease III, MutY, and UDG, was measured on DNA-modified gold electrodes to be 80 mV v. NHE (27, 28). Using cyclic voltammetry, it was observed that the redox process being monitored was reversible, which suggested that DNA binding prevented the oxidative degradation of the protein that was observed in the absence of DNA. Furthermore, experiments done to directly compare the midpoint potential of EndoIII with or without DNA on highly oriented pyrolytic graphite (HOPG) electrodes revealed that there was a negative 200 mV shift in midpoint potential upon DNA binding (29). Since there is no significant change in protein conformation when bound to DNA, this shift in potential corresponds to a three orders of magnitude higher EndoIII DNA binding affinity when the 4Fe-4S cluster is in the 3+ oxidation state relative to the 2+ oxidation state. What is responsible for this large change in redox potential upon DNA binding?

To answer this question, a family of EndoIII mutants was created to alter the electrostatic interactions around the 4Fe-4S cluster while maintaining wild type DNA binding affinity (30). The midpoint potentials of these mutant proteins were compared on DNA-modified gold electrodes to determine how changing electrostatics around the 4Fe-4S cluster affects the midpoint potential of the protein. The EndoIII mutants did not have a significantly different DNA-bound midpoint potential from that of wild type EndoIII. This result is consistent with the observation that the electrostatic environment created by the polyanionic DNA is responsible for the dramatic shift in the DNA-bound midpoint potential of the 4Fe-4S cluster in EndoIII.

Two key principles were determined from the experiments described above. First, DNA binding by DNA repair and replication proteins that contain 4Fe-4S clusters shifts the midpoint potential of the iron cofactor and prevents the oxidative degradation of these metal centers. The Nernst equation predicts that this shift in potential corresponds to a three orders of magnitude higher affinity for DNA when the protein is in its oxidized form relative to its reduced form. Second, the polyanionic nature of DNA is responsible for the negative shift in midpoint potential observed upon protein binding to DNA.

DNA Helicases with 4Fe-4S Clusters. SFII family DNA helicases contain a 4Fe-4S cluster, which has been well conserved throughout evolution. The 4Fe-4S cluster in these helicases seems to act as a wedge that separates double helical DNA in a process that is driven by ATP hydrolysis (31-34). Notably, upon ATP hydrolysis, it is thought that the 4Fe-4S cluster is brought closer to the DNA nucleobases, which in turn could facilitate electron transfer from the 4Fe-4S cluster of the helicase to the DNA (16, 17). This phenomenon has been observed for XPD from *Sulfolobus Acidocaldarius*, which has a midpoint potential of 80mV v. NHE as measured on DNA-modified gold electrodes. An increase in signal intensity as measured by cyclic voltammetry upon ATP addition suggests better electronic

coupling between the 4Fe-4S cluster of XPD and the electrode upon ATP hydrolysis.

The *E. coli* DNA helicase DinG, another SFII family helicase, has also been studied extensively to determine the redox properties of its 4Fe-4S cluster. These studies have provided conflicting information about the redox properties of the 4Fe-4S cluster in DinG. Specifically, one study out of the Ding lab indicated that, in contrast to DNA glycosylases, the 4Fe-4S cluster in DinG was not susceptible to oxidative degradation. Additionally, using chemical redox titrations, it was determined that the 4Fe-4S cluster of DinG could be reversibly cycled between the 1+ and 2+ oxidation states with a midpoint potential of -390 ± 23 mV v. NHE at pH 8.0 (35). Notably, none of these studies tested the redox behavior of DinG when bound to DNA. In contrast, a second study suggested that the 4Fe-4S cluster in DinG could be oxidized to the 3+ oxidation state. Furthermore, when bound to DNA, the midpoint potential of the 2+/3+ couple of the 4Fe-4S cluster in DinG was 80 mV v. NHE. The 1+/2+ couple of the 4Fe-4S cluster could not be determined from these experiments (17). Like XPD, addition of ATP led to an increase in the signal intensity of the $[4\text{Fe-4S}]^{2+/3+}$ couple as measured by cyclic voltammetry on DNA-modified gold electrodes. Thus, this study showed that the similarity in midpoint potential between DNA glycosylases and DNA helicases when bound to DNA suggests electrons can be transferred between their metal centers in a DNA-mediated self-exchange reaction (16, 17).

A Model for DNA Charge Transport in DNA Repair. The chemical characteristics of the 4Fe-4S clusters in DNA repair proteins described above are the basis for a model for how these proteins signal each other with DNA-mediated redox chemistry as a first step in DNA damage detection (**Figure 3**) (10, 15-17). This model provides a mechanism by which DNA repair proteins can use DNA CT to scan the genome for sites of damage. In this model, the 4Fe-4S cluster of a DNA repair protein becomes oxidized by an oxidant endogenous to the cell, like a

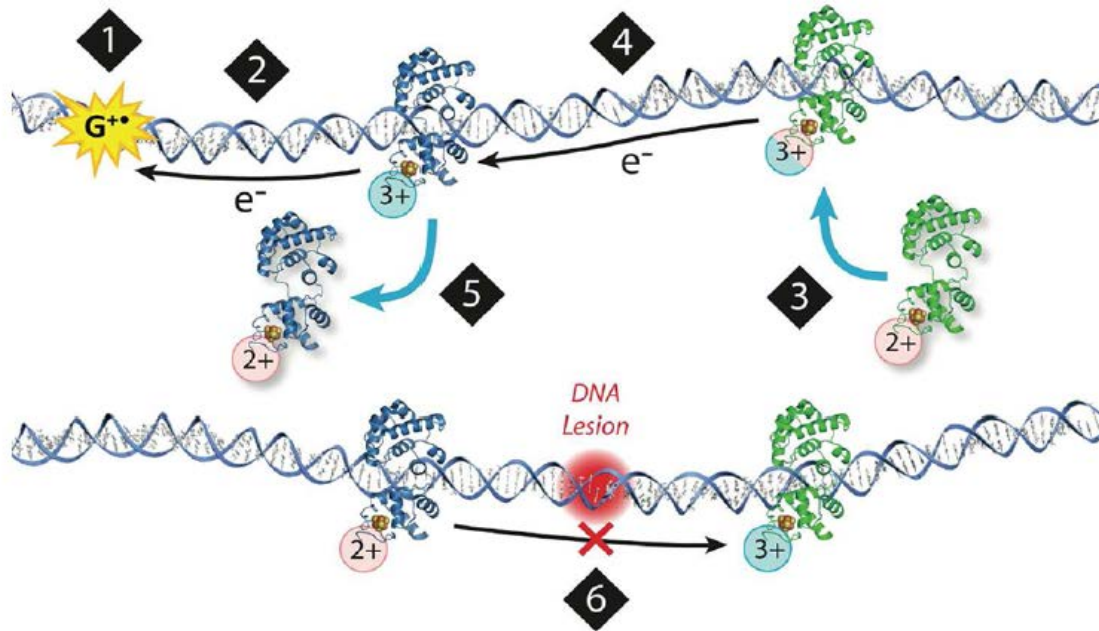


Figure 1.3. Model for DNA Charge Transport in DNA Repair. In the cytoplasm of *E. coli*, the 4Fe-4S cluster in the DNA binding protein is in the 2+ oxidation state. This protein can then bind DNA, shifting the midpoint potential of the 4Fe-4S cluster in the protein such that it is more susceptible to oxidation. The presence of a common oxidant, like a guanine radical (1) oxidizes the 4Fe-4S cluster to the 3+ oxidation state (2). A protein with a 4Fe-4S cluster in the 2+ oxidation state becomes oxidized to the 3+ oxidation state upon binding to DNA, and releases an electron into the DNA π -stack. If there is no intervening DNA lesion, this electron can reduce the 4Fe-4S cluster of a distal enzyme. Since the protein has a lower affinity for DNA when its 4Fe-4S cluster is in the 2+ oxidation state, the protein is more likely to dissociate from the DNA and bind in a new region of the genome. If there is a mismatch between the two enzymes, charge transport will be attenuated, and both enzymes will remain bound to DNA in their oxidized form. These proteins can then undergo 1D diffusion along DNA to find and repair the DNA lesion. Figure 5 from Reference 88.

guanine radical (14, 47). If a second DNA repair protein binds downstream of the first protein, and there is no intervening lesion, the second protein injects an electron into the DNA π -stack. This electron can travel through the DNA to reduce the distally bound protein. Once in the 2+ oxidation state, this protein has a low affinity for DNA, and dissociates to undergo 3D diffusion to a new area of the genome. However, if there is a site of DNA damage between these two

Table 1.1. DNA Binding Proteins with 4Fe-4S Clusters

Enzyme	Pathway/Function	Enzymatic Activity	Reference
MutY	Base excision repair (BER)	DNA Glycosylase	14, 15, 17, 25-27, 41-49
Endonuclease III	BER	DNA Glycosylase	15-17, 20, 24, 27-30, 50-60
Family 4 UDG	BER	DNA Glycosylase	27, 61-63
Demeter		DNA Glycosylase	64, 65
SP Photolyase		Direct Repair	66-69
AddB	Recombination repair	Helicase-nuclease	70, 71
Dna2	Replication, Recombination repair	Helicase-nuclease	72
Exonuclease V	Mitochondrial replication and recombination	5'-exonuclease	73
Cas4	CRISPR antiviral defense	Nuclease	74-76
Rad3/XPD	Transcription-coupled repair, Nucleotide excision repair	Helicase	16, 31-34, 77
FancJ	Recombination repair	Helicase	31
ChlR1	Chromosome segregation	Helicase	18, 19
DOG-1	Anti-recombinase, Telomere maintenance	Helicase	18, 19
RTEL1	Telomere maintenance, Replication	Helicase	18, 19, 78, 79
Replicative Helicase Mitochondria	Mitochondrial Replication	Helicase	80
DinG	Recombination repair	Helicase	17, 35
Primase (p58)	Replication, Recombination repair	RNA primer polymerase	81-83
RNA polymerase	Transcription	RNA polymerase	84-85
DNA Polymerase α	Replication	DNA polymerase	86
DNA Polymerase δ	Replication, Recombination Repair	DNA polymerase	86
DNA Polymerase ϵ	Replication	DNA polymerase	86, 87
DNA Polymerase ζ	Translesion DNA Synthesis	DNA polymerase	86

proteins, DNA CT cannot occur and the 4Fe-4S cluster of the distal protein will remain in the 3+ oxidation state. This DNA repair protein remains bound to DNA, and processes along the double helix via 1D diffusion to find and repair the site of damage as described by established mechanisms (36-39). This model provides an explanation for how redox-active DNA repair proteins, like MutY, which are found at a low copy number of about 30 per cell (40), can scan the genome for damaged nucleobases within the doubling time of *E. coli*.

A mathematical model was developed to prove that DNA CT could increase the efficiency of the DNA glycosylase search process (15). This model compared the search time of MutY as a function of DNA CT distance and percentage of protein with an oxidized 4Fe-4S cluster. This model showed that without DNA CT, a protein that was maintained at a copy number of 30 per cell would take 46 minutes to search the entire *E. coli* genome using 1D diffusion along the DNA helix. However, if DNA CT could occur over just 200 base pairs, then with only 20% of total protein in the 3+ oxidation state, the search time could be reduced to 8 minutes. When considering the feasibility of these search times it is important to remember that the doubling time of *E. coli* is about 30 minutes. Additionally, under normal growth conditions, in which low mutagenesis is observed, there must be a mechanism to repair DNA damage prior to replication and cell division. Thus, a search process that relies on purely 1D diffusion cannot provide an explanation for how proteins present on the order of tens of copies per cell could search, let alone repair, DNA damage in the entire *E. coli* genome prior to replication. This model for DNA-mediated signaling in DNA repair could provide an additional mechanism by which these proteins localize to sites of DNA damage within the cell.

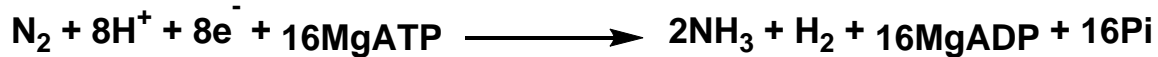
Conclusion. In this thesis, methods were developed to study the model for DNA CT in DNA repair. Specifically, to understand the applicability of the model described above to eukaryotic systems, the chemical characteristics of the 4Fe-4S cluster in Dna2, a eukaryotic helicase-nuclease involved in DNA repair and replication, were determined with a variety of spectroscopic and electrochemical

techniques. Electrochemical studies of the metal center in Dna2 provided insight into the role of this cofactor within eukaryotic DNA repair and replication. In addition to the Dna2 studies, a biological assay was developed to study DNA-mediated signaling between MutY, EndoIII, and DinG as a first step in DNA damage detection. The combination of these studies provided insight into how DNA-mediated redox signaling could be used within the cell.

Nitrogenase

Nitrogenase is the only enzyme found in nature that catalyzes the reduction of atmospheric dinitrogen to bioavailable ammonia in a process known as nitrogen fixation (89). The only other mechanism by which significant amounts of ammonia are produced from dinitrogen is by an industrial method called the Haber-Bosch process, which employs extremely high temperatures (350-550 °C) and pressures (250-350 atm) along with a heterogeneous metal catalyst to drive this reaction (90-92). The Haber-Bosch process is employed as the industrial method to fix dinitrogen for use in the production of artificial fertilizers, which helps to sustain food production. This process currently consumes up to 2% of global energy production, and this energy demand will continue to expand as the food requirement increases with the population (93, 94). A better understanding of the mechanism of nitrogenase, which uses energy derived from ATP hydrolysis at ambient pressure and temperature to reduce dinitrogen, could help guide development of alternate, less energy intensive, nitrogen fixation methods.

Nitrogenase is composed of two different proteins, the Fe-protein and the MoFe-protein (**Figure 4**), and together this protein complex catalyzes the following reaction:



The Fe-protein is a 63 kDa γ_2 homodimer that contains a single 4Fe-4S cluster that bridges the two monomers. This protein is the physiological reductant of the MoFe-protein, and uses ATP hydrolysis at two ATP binding sites to gate electron transfer to the metal centers in the MoFe-protein (95-98). The Fe-protein can only function as an ATPase when in complex with the MoFe-protein. The MoFe-protein is a 230 kDa $\alpha_2\beta_2$ heterotetramer, which contains two different metal cofactors, the P-cluster and the FeMo-cofactor. The P-cluster is an 8Fe-7S cluster, which serves as a gateway for electrons into the FeMo-cofactor. The FeMo-cofactor is the site of substrate reduction, and consists of a 7Fe:9S:1C:1Mo-R-homocitrate cluster (96-100). Although the MoFe-protein is composed of 2 α - and 2 β -subunits, and thus contains two FeMo-cofactor active sites, each $\alpha\beta$ pair acts independently to catalyze nitrogen reduction. Substrates can only bind to the FeMo-cofactor when it has been reduced by 2-4 electrons relative to the state of the cofactor as isolated in the presence of the reductant sodium dithionite (89, 97). Thus, prior to substrate reduction, multiple rounds of electron transfer from the 4Fe-4S cluster of the Fe-protein to the P-cluster, and from the P-cluster to the FeMo-cofactor must occur in a mechanism that is gated by ATP hydrolysis.

Electron Transfer in Nitrogenase. The mechanism of electron transfer between the different metal centers in nitrogenase has been studied using a combination of X-ray crystallography and electrochemistry (96, 97, 101). Electrochemical methods provided information about the midpoint potentials of the nitrogenase metal clusters. Thus, these experiments yielded thermodynamic information to assess the feasibility of different electron transfer mechanisms (**Table 2**) (107-114). X-ray crystallography has provided data on the distances between the metal cofactors in different conformational states of the enzyme complex. In general, single-step electron transfer between two metal centers is extremely sensitive to the distance between the metal clusters with facile electron transfer occurring only between

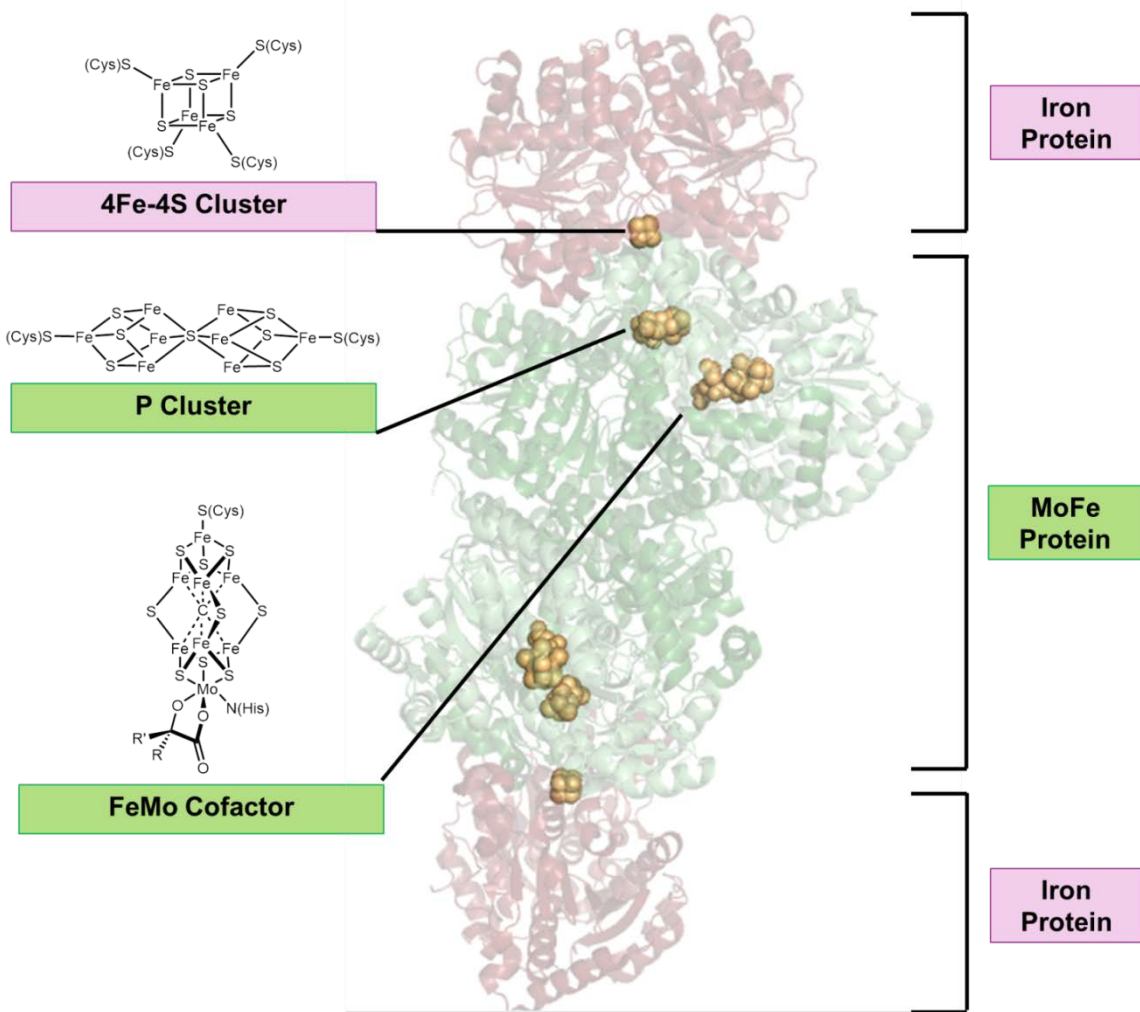


Figure 1.4. Structure of the Nitrogenase Complex. The structure of the *Azotobacter vinelandii* nitrogenase complex with AMP-PCP bound to the Fe-protein (PDB Entry = 4WZB). The nucleotide binding sites are not shown in this structure. The Fe-protein is shown in pink and the MoFe-protein is shown in green. The metal centers are highlighted in yellow. The chemical structures of the three nitrogenase metal clusters are shown in black.

cofactors separated by distances less than about 15 Å (102-104). Therefore, these studies have provided insight into possible electron transfer mechanisms by considering the distances between the metal clusters in different protein conformational states.

Structural Studies of Electron Transfer in Nitrogenase. The Fe-protein is a member of a family of P-type NTPases that undergo structural changes upon ATP binding and hydrolysis (96-98). Consistent with this categorization, the Fe-protein has been shown to undergo a conformational rearrangement upon ATP binding and hydrolysis that allows for complex formation with the MoFe-protein in an arrangement that positions the 4Fe-4S cluster of the Fe-protein within electron transfer distance of the P-cluster (Figure 5) (101). In all states of the nitrogenase complex, the distance between the P-cluster and the FeMo-cofactor is about 19 Å. However, the distance between the 4Fe-4S cluster of the Fe-protein and the P-cluster of the MoFe-protein varies depending on what nucleotides are bound by the Fe-protein. Specifically, when either no nucleotide or ADP was bound by the Fe-protein the distance between the two cofactors was about 23 Å. In contrast, when AMP-PCP, an ATP mimic, was bound by the Fe-protein the distance between the cofactors decreased to about 18 Å. These different conformations suggest that in the AMP-PCP bound state of the nitrogenase complex, the electron transfer rate could be two to three orders of magnitude faster relative to that for the

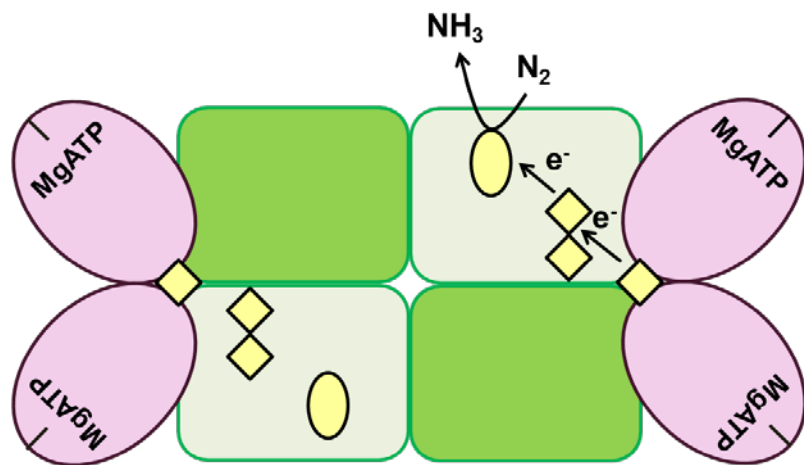


Figure 1.5. Electron Transfer in Nitrogenase. Prior to substrate reduction electrons must transfer from the 4Fe-4S cluster of the Fe-protein to the P-cluster of the MoFe-protein. Then, the electrons are transferred from the P-cluster of the MoFe-protein to the FeMo-cofactor of the MoFe-protein. Electron transfer is gated by conformational changes induced by ATP binding and hydrolysis at the Fe-protein.

nucleotide free form of nitrogenase (101). Thus, it was proposed that nucleotide binding, and potentially also hydrolysis, could gate electron transfer between the 4Fe-4S cluster of the Fe-protein and the P-cluster of the MoFe-protein. In addition to distances between the cofactors in nitrogenase, another important value for determining the feasibility of different electron transfer mechanisms is the midpoint potential of the metal cofactors.

Thermodynamic Properties of the Fe-Protein. Despite its relatively modest midpoint potential, the Fe-protein is the only known biological reductant capable of reducing the FeMo-cofactor to a state that is competent for substrate reduction. The 4Fe-4S cluster in the Fe-protein is unusual in that it can exist in three different oxidation states (105, 106). The three different oxidation states of the 4Fe-4S cluster in the Fe-protein are 0 ($S = 0, 4$), 1+ ($S = 1/2, 3/2$), and 2+ ($S = 0$) (89, 97).

The midpoint potential of the 1+/2+ couple of the 4Fe-4S cluster in the Fe-protein is -300 mV v. NHE (107). Upon MgATP binding or MgADP binding, the midpoint potential of the Fe-protein shifts about -120 mV or -160 mV, respectively (108). The midpoint potential of the Fe-protein also undergoes a negative potential shift upon binding the MoFe-protein in the presence of aluminum fluoride-MgADP, an ATP hydrolysis mimic. The potential of the Fe-protein in this complex could not be determined; however, it was concluded that it must be significantly less than -550 mV v. NHE (109). Thus, the midpoint potential of the $[4\text{Fe}-4\text{S}]^{1+/2+}$ couple shifts such that there is a larger driving force for electron transfer from the 4Fe-4S cluster of the Fe-protein to the metal centers in the MoFe-protein in the nucleotide-bound state of the nitrogenase complex.

There is less known about the midpoint potential of the 1+/0 couple of the Fe-protein, and there are discrepancies in the literature about the midpoint potential of this transition. In one report, the potential was found to be -460 mV v. NHE, while in a second report the potential was reported to be -790 mV v. NHE (110, 111). If the true potential of this reaction is closer to the latter value it would most likely not be a biologically relevant redox couple. However, if the true

midpoint potential was about -460 mV v. NHE, this transition would be important in the nitrogenase mechanism. Initial results have suggested that in *Azotobacter vinelandii* one of the biological reductants of nitrogenase, flavodoxin II, can reduce the Fe-protein to its all ferrous form; however, these results remain controversial (106). Thus, the biological relevance of the all-ferrous form of the Fe-protein depends on the true value of the midpoint potential of the 4Fe-4S^{1+/0} couple.

Thermodynamic Properties of the MoFe-Protein. Electrochemical methods were also used to study the midpoint potential of the two metal centers in the MoFe-protein. Chemical redox titrations have indicated that the P-cluster reversibly cycles through four different oxidation states; however, the net charge on the P-cluster in any of the oxidation states is not known (97). The four different oxidation states that the P-cluster cycles through are the P^N (S = 0), P^{Semiox} (S = 1/2, 5/2) , P^{Ox1} (S = 3,4), and P^{Ox2} (S = 1/2, 7/2) states. As isolated in the presence of sodium dithionite, the P-cluster is in the P^N oxidation state. The midpoint potential of both the P^{N/Semiox} and P^{Semiox/Ox1} couple is -307 mV v. NHE. The midpoint potential of the P^{Ox1}/P^{Ox2} couple is +90 mV v. NHE (97, 112, 113). Upon binding to the Fe-protein in the presence of an ATP hydrolysis mimic, the midpoint potentials of both the P^{N/Semiox} and P^{Semiox/Ox1} couples of the P-cluster shift such that they are significantly more negative. Thus, in the two-protein nitrogenase complex, the midpoint potential of the P-cluster shifts such that there is a larger driving force to reduce the MoFe protein (109).

The other metal cluster in the MoFe-protein is the FeMo-cofactor, and it has been hypothesized that this cofactor cycles through three different oxidation states: M^{Ox}, M^N, and M^R. Like the P-cluster, the net charge on the FeMo-cofactor has not been determined for any oxidation state of the metal center (97,115). When the MoFe-protein is isolated in the presence of sodium dithionite, the FeMo-cofactor is in the M^N oxidation state with a spin state of S=3/2. The M^R oxidation state is the fully reduced form of the FeMo-cofactor, which is the only state of the cofactor to which substrates and inhibitors can bind (89, 97). The only measured midpoint

Table 1.2. Midpoint Potentials of the Nitrogenase Metal Centers.

Protein	Metal Cofactor	Redox Couple	Midpoint Potential (mV v. NHE)	Other Notes	Reference
Fe-Protein	4Fe-4S Cluster	1+/2+	-300	---	107
Fe-Protein	4Fe-4S Cluster	1+/2+	-460	MgADP Bound	108
Fe-Protein	4Fe-4S Cluster	1+/2+	-420	MgATP Bound	108
Fe-Protein	4Fe-4S Cluster	1+/2+	< -550	ADP-AlF ₄ Bound in Complex with the MoFe-Protein	109
Fe-Protein	4Fe-4S Cluster	1+/0	-460	---	110
Fe-Protein	4Fe-4S Cluster	1+/0	-790	---	111
MoFe-Protein	P-Cluster	P ^{N/Semiox}	-307	---	112
MoFe-Protein	P-Cluster	P ^{Semiox/Ox1}	-307	---	112
MoFe-Protein	P-Cluster	P ^{Ox1/Ox2}	90	---	112
MoFe-Protein	P-Cluster	P ^{N/Semiox}	< -550	ADP-AlF ₄ Bound in Complex with the Fe-Protein	109
MoFe-Protein	P-Cluster	P ^{Semiox/Ox1}	-430	ADP-AlF ₄ Bound in Complex with the Fe-Protein	109
MoFe-Protein	FeMo-Cofactor	M ^{N/Ox}	-42	---	114

*All potentials are reported for the nitrogenase component protein isolated from *Azotobacter vinelandii*.

potential for the FeMo-cofactor is for the reversible one-electron transition between the M^{Ox} and M^N oxidation states. This potential was measured to be -42 mV v.NHE (89, 114). Unlike the P-cluster, the midpoint potential of the FeMo-cofactor does not change upon formation of the nitrogenase complex. The midpoint potential of

the M^N/M^R couple is unknown (109). Thus, it is not clear what potential is required for substrate binding to the FeMo-cofactor.

Conclusion. The electrochemical and structural studies of nitrogenase are consistent with a mechanism of electron transfer from the 4Fe-4S of the Fe-protein to the P-cluster followed by electron transfer from the P-cluster to the FeMo-cofactor, the site of substrate reduction. This electron transfer process is gated by ATP binding and hydrolysis at the Fe-protein, which initiates a series of conformational changes in the nitrogenase complex. Despite progress made in the understanding of electron transfer in nitrogenase, there are still a number of questions that remain regarding how eight electrons can be delivered to dinitrogen to produce ammonia during nitrogen reduction. In this thesis, electrochemical methods were developed as tools to investigate these questions. Direct electrochemistry on single crystal gold electrodes and edge-plane pyrolytic graphite electrodes provided insight into the redox properties of the 4Fe-4S cluster of the Fe-protein isolated from *Azotobacter vinelandii*. Surfactant-modified basal plane graphite electrodes were also developed as a method for studying the redox properties of flavodoxin II, a biological reductant of nitrogenase. This method was complemented with structural studies to better characterize the interaction between flavodoxin II and the Fe-protein of nitrogenase with a focus on determining the molecular interactions that facilitate reduction of the 4Fe-4S cluster of the Fe-protein to its all ferrous state. In combination, this research has provided insight into the biological mechanism of electron transfer to and through nitrogenase.

References

1. Bertini, I., Harry B. Gray, Edward I. Stiefel, and Joan Silverstone Valentine. Biological Inorganic Chemistry: Structure and Reactivity. Sausalito: University Science Books, 2007. Print.
2. Liu, J., Chakraborty, S., Hosseinzadeh, P., Yu, Y., Tian, S., Petrik, I., Bhagi, A., and Lu, Y. (2014) Metalloproteins Containing Cytochrome, Iron-Sulfur, or Copper Redox Centers. *Chem Rev.* 114, 4366-4469.
3. Winkler, J. R. and Gray, H. B. (2014) Electron Flow through Metalloproteins. *Chem Rev.* 114, 3369-3380.
4. Watson, J. D. and Crick, F. H. C. (1953) A Structure for Deoxyribose Nucleic Acid. *Nature.* 171, 737-738.
5. Eley, D. D. and Spivey, D. I. (1962) Semiconductivity of Organic Substances. Part 9 – Nucleic Acid in the Dry State. *Trans. Faraday Soc.* 58, 411-415.
6. O'Neill, M. A. and Barton, J.K. (2005) Sequence-Dependent DNA Dynamics: The Regulator of DNA-mediated Charge Transport. *Chapter 2*, 27-75 from Wagenknecht, H.-A. Charge Transfer in DNA: From Mechanism to Application. *WILEY-VCH Verlag GmbH & Co.*
7. Genereux, J. C. and Barton, J. K. (2010) Mechanisms for DNA Charge Transport. *Chem Rev.* 110, 1642-1662.
8. Delaney, S. and Barton, J. K. (2003) Long-Range DNA Charge Transport. *J Org Chem.* 68, 6475-6483.
9. Muren, N. B., Olmon, E. D., and Barton, J. K. (2012) Solution, Surface, and Single Molecule Platforms for the Study of DNA-Mediated Charge Transport. *Phys Chem Chem Phys.* 14, 13754-13771.
10. Genereux, J. C., Boal, A. K., and Barton, J. K. (2010) DNA-Mediated Charge Transport in Redox Sensing and Signaling. *J Am Chem Soc.* 132, 891-905.

11. Gorodetsky, A. A., Dietrich, L. E. P., Lee, P. E., Demple, B., Newman, D. K., and Barton, J. K. (2008) DNA Binding Shifts the Redox Potential of the Transcription Factor SoxR. *Proc. Natl. Acad. Sci. USA*. 105, 3684-3689.
12. Lee, P. E., Demple, B., and Barton, J. K. (2009) DNA-Mediated Redox Signaling for Transcriptional Activation of SoxR. *Proc. Natl. Acad. Sci. USA* 106, 13164-13168.
13. Arnold, A. R. and Barton, J. K. (2013) DNA Protection by the Bacterial Ferritin Dps via DNA Charge Transport. *J. Am. Chem. Soc.* 135, 15726-15729.
14. Yavin, E., Boal, A. K., Stemp, E. D. A., Boon, E. M., Livingston, A. L., O'Shea, V. L., David, S. S., and Barton, J. K. (2005) Protein-DNA Charge Transport: Redox Activation of a DNA Repair Protein by Guanine Radical. *Proc. Natl. Acad. Sci. USA*. 102, 3546-3551.
15. Boal, A. K., *et al.* (2009) Redox Signaling Between DNA Repair Proteins for Efficient Lesion Detection. *Proc. Natl. Acad. Sci. U.S.A.* 106, 15237-15242.
16. **a)** Mui, T. P., Fuss, J. O., Ishida, J. P., Tainer, J. A., and Barton, J. K. (2011) ATP-Stimulated, DNA-Mediated Redox Signaling by XPD, a DNA Repair and Transcription Helicase. *J. Am. Chem. Soc.* 133, 16378-16381.
b) Sontz, P. A., Mui, T. P., Fuss, J. O., Tainer, J. A., and Barton, J. K. (2012) DNA Charge Transport as a First Step in Coordinating the Detection of Lesions by Repair Proteins. *Proc. Natl. Acad. Sci. USA*. 109, 1856-1861.
17. Grodick, M. A., Segal, H. M., Zwang, T. J., and Barton, J. K. (2014) DNA-Mediated Signaling by Proteins with 4Fe-4S Clusters Is Necessary for Genomic Integrity. *J. Am. Chem. Soc.* 136, 6470-6478.
18. White, M. F. and Dillingham, M. S. (2012) Iron-Sulphur Clusters in Nucleic Acid Processing Enzymes. *Curr. Op. Struct. Biol.* 22, 94-100.
19. Wu, Y. and Brosch, R. M. Jr. (2012) DNA Helicase and Helicase-Nuclease Enzymes with a Conserved Iron-Sulfur Cluster. *Nucleic Acids Res.* 40, 4247-4260.
20. Cunningham, R. P., *et al.* (1989) Endonuclease III is an Iron-Sulfur Protein. *Biochem.* 28, 4450-4455.

21. Friedman, J. I. and Stivers, J. T. (2010) Detection of Damaged DNA Bases by DNA Glycosylase Enzymes. *Biochem.* 49, 4957.
22. Breimer, L. H. and Lindahl T. (1984) DNA Glycosylase Activities for Thymine Residues Damaged by Ring Saturation, Fragmentation, or Ring Contraction are Functions of Endonuclease III in *Escherichia coli*. *J. Biol. Chem.* 259, 5543–5548.
23. Au, K. G., Clark, S., Miller, J. H., and Modrich, D. (1989) *Escherichia coli* *mutY* Gene Encodes an Adenine Glycosylase Active on G-A Mispairs. *Proc. Natl. Acad. Sci. USA.* 86, 8877-8881.
24. Fromme, J. C. and Verdine, G. L. (2003) Structure of a Trapped Endonuclease III-DNA Covalent Intermediate. *EMBO J.* 22, 3461-3471.
25. Fromme, J. C., Banerjee, A., Huang, S. J., and Verdine, G. L. (2004) Structural Basis for Removal of Adenine Mispaired with 8-Oxoguanine by MutY Adenine DNA Glycosylase. *Nature.* 427, 652-656.
26. Poreelo, S. L., Cannon, M. J., and David, S. S. (1998) A Substrate Recognition Role for the [4Fe-4S]²⁺ Cluster of the DNA Repair Glycosylase MutY. *Biochem.* 37, 6465-6475.
27. Boal, A. K., Yavin, E., Lukianova, O. A., O'Shea, V. L., David, S. S., and Barton, J. K. (2005) DNA-Bound Redox Activity of DNA Repair Glycosylases Containing [4Fe-4S] Clusters. *Biochem.* 44, 8397-8407.
28. Romano, C. A.* Sontz, P. A.* and Barton, J. K. (2011) Mutants of the Base Excision Repair Glycosylase, Endonuclease III: DNA Charge Transport as a First Step in Lesion Detection. *Biochem.* 50, 6133-6145.
29. Gorodetsky, A. A., Boal, A. K., and Barton, J. K. (2006) Direct Electrochemistry of Endonuclease III in the Presence and Absence of DNA. *J Am Chem Soc.* 128, 12082-12083.
30. Pheeney, C. G., Arnod, A. R., Grodick, M. A., and Barton, J. K. (2013) Multiplexed Electrochemistry of DNA-Bound Metalloproteins. *J Am Chem Soc.* 135, 11869-11878.

31. Rudolf, J., Makrantoni, V., Ingledew, W. J., Stark, M. J., and White, M. F. (2006) The DNA Repair Helicases XPD and FancJ have Essential Iron-Sulfur Domains. *Mol Cell.* 23, 801-808.
32. Fan, L., *et al.* (2008) XPD Helicase Structures and Activities: Insights into the Cancer and Aging Phenotypes from XPD Mutations. *Cell.* 133, 789-800.
33. Liu, H., *et al.* (2008) Structure of the DNA Repair Helicase XPD. *Cell.* 133, 801-812.
34. Wolski, S. C., *et al.* (2008) Crystal Structure of the FeS Cluster-Containing Nucleotide Excision Repair Helicase XPD. *PLoS Biology.* 24, e149.
35. Ren, B., Duan, X., and Ding, H. (2009) Redox Control of the DNA Damage-Inducible Protein DinG Helicase Activity via its Iron-Sulfur Cluster. *J Biol Chem.* 284, 7746-7755.
36. Blainey, P. C., van Oijen, A. M., Banerjee, A., Verdine, G. L., and Xie, X. S. (2006) A Base-Excision DNA-Repair Protein finds Intrahelical Lesion Bases by Fast Sliding in Contact with DNA. *Proc Natl Acad Sci.* 103, 5752-5757.
37. Nelson, S. R., Dunn, A. R. Kathe, S. D., Warshaw, D. M., and Wallace, S. S. (2014) Two Glycosylase Families Diffusively Scan DNA using a Wedge Residue to Probe for and Identify Oxidatively Damaged Bases. *Proc Natl Acad Sci.* 111, E2091-E2099.
38. Nelson, S. R., Dunn, A. R. Kathe, S. D., Warshaw, D. M., and Wallace, S. S. (2014) Two Glycosylase Families Diffusively Scan DNA Using a Wedge Residue to Probe for and Identify Oxidatively Damaged Bases. *Proc Natl Acad Sci. USA.* 111, E2091-E2099.
39. Dunn, A. R., Kad, N. M., Nelson, S. R., Warshaw, D. M., and Wallace, S. S. (2011) Single Qdot-Labeled Glycosylase Molecules Use a Wedge Amino Acid to Probe for Lesions while Scanning Along DNA. *Nucleic Acids Res.* 39, 7487-7498.
40. Demple, B. and Harrison, L. (1994) Repair of Oxidative Damage to DNA: Enzymology and Biology. *Ann Rev Biochem.* 63, 915-948.

41. Golinelli, M. P., Chmiel, N. H., and David, S. S. (1999) Site-Directed Mutagenesis of the Cysteine Ligands to the [4Fe-4S] Cluster of *Escherichia coli* MutY. *Biochem.* 38, 6997-7007.
42. Chepanoske, C. L., Golinelli, M. P., Williams, S. D., and David, S. S. (2000) Positively Charged Residues within the Iron-Sulfur Cluster Loop of *E. coli* MutY Participate in Damage Recognition and Removal. *Arch Biochem Biophys.* 380, 11-9.
43. Boon, E. M., Pope, M. A., Williams, S. D., David, S. S., and Barton, J. K. (2002) DNA-Mediated Charge Transport as a Probe of MutY/DNA Interaction. *Biochem.* 41, 8464-8470.
44. Lu, A. L. and Wright, P. M. (2003) Characterization of an *Escherichia coli* Mutant MutY with a Cysteine to Alanine Mutation at the Iron-Sulfur Domain. *Biochem.* 42, 3742-3750.
45. Boon, E. M., Livingston, A. L., Chmiel, N. H., David, S. S., and Barton, J. K. (2004) DNA-Mediated Charge Transport for DNA Repair. *Proc Natl Acad Sci USA.* 100, 12543-12547.
46. Lee, C. Y., Bai, H., Houle, R., Wilson, G. M., and Lu, A. L. (2004) An *Escherichia coli* MutY Mutant without the Six-Helix Barrel Domain is a Dimer in Solution and Assembles Cooperatively into Multisubunit Complexes with DNA. *J Biol Chem.* 279, 52653-52663.
47. Yavin, E., Stemp, E. D., O'Shea, V. L., David, S. S., and Barton, J. K. (2006) Electron Trap for DNA-Bound Repair Enzymes: A Strategy for DNA-Mediated Signaling. *Proc Natl Acad Sci USA.* 103, 3610-3614.
48. Bai, H. and Lu, A. L. (2007) Physical and Functional Interactions Between *Escherichia coli* MutY Glycosylase and Mismatch Repair Protein MutS. *J Bacteriol.* 189, 902-910.
49. Engstrom, L. M., Brinkmeyer, M. K., Ha, Y., Raetz, A. G., Hedman, B., Hodgson, K. O., Solomon, E. I., and David, S. S. (2014) A Zinc Linchpin Motif in the MUTYH Glycosylase Interdomain Connector is Required for Efficient Repair of DNA Damage. *J Am Chem Soc.* 136, 7829-7832.
50. Fu, W., O'Handley, S., Cunningham, R. P., and Johnson, M. K. (1992) The Role of the Iron-Sulfur Cluster in *Escherichia coli* Endonuclease III. A Resonance Raman Study. *J Biol Chem.* 267, 16135-16137.
51. Kuo, C. F., McRee, D. E., Cunningham, R. P., and Tainer, J. A. (1992) Crystallization and Crystallographic Characterization of the Iron-Sulfur

Containing DNA-repair Enzyme Endonuclease III from *Escherichia coli*. *J Mol Biol.* 227, 347-351.

52. Duo, C. F., McRee, D. E., Fisher, C. L., O'Handley, S. F., Cunningham, R. P., and Tainer, J. A. (1992) Atomic Structure of the DNA Repair [4Fe-4S] Enzyme Endonuclease III. *Science.* 258, 434-440.

53. Thayer, M. M., Aheran, H., Xing, D., Cunningham, R. P., and Tainer, J. A. (1995) Novel DNA Binding Motifs in the DNA Repair Enzyme Endonuclease III Crystal Structure. *EMBO J.* 14, 4108-4120.

54. Aspinwall, R., et al. (1997) Cloning and Characterization of a Functional Human Homolog of *Escherichia coli* Endonuclease III. *Proc Natl Acad Sci USA.* 94, 109-114.

55. You, H. J., Swanson, R. L., and Doetsch, P. W. (1998) *Saccharomyces cerevisiae* Posseses Two Functional Homologues of *Escherichia coli* Endonuclease III. *Biochem.* 37, 6033-6040.

56. Alseth, I., Eide, L., Pirovano, M., Rognes, T., Seeberg, E., and Bjørås, M. (1999) The *Saccharomyces cerevisiae* Homologues of Endonuclease III from *Escherichia coli*, Ntg1 and Ntg2, are Both Required for Efficient Repair of Spontaneous and Induced Oxidative DNA Damage in Yeast. *Mol Cell Biol.* 19, 3779-3787.

57. Shekhtman, A., McNaughton, L., Cunningham, R. P., and Baxter, S. M. (1999) Identification of the *Archaeoglobus fulgidus* Endonuclease III DNA Interaction Surface using Heteronuclear NMR Methods. *Structure.* 7, 919-930.

58. Roldán-Arjona, T., García-Ortiz, M. V., Ruiz-Rubio, M., and Ariza, R. R. (2000) cDNA Cloning, Expression and Functional Characterization of an *Arabidopsis thaliana* Homologue of the *Escherichia coli* DNA Repair Enzyme Endonuclease III. *Plant Mol Biol.* 44, 43-52.

59. Rogers, P. A., Eide, L., Klungland, A., and Ding, H. (2003) Reversible Inactivation of *E. coli* Endonuclease III via Modification of Its [4Fe-4S] Cluster by Nitric Oxide. *DNA Repair.* 2, 809-817.

60. Moe, E., Sezer, M., Hildebrandt, P., and Todorovic, S. (2015) Surface Enhanced Vibrational Spectroscopic Evidence for an Alternative DNA-Independent Redox Activation of Endonuclease III. *Chem. Commun.* 51, 3255-3257.

61. Hinks, J. A., Evans, M. C., DeMiguel, Y., Sartori, A. A., Jiricny, J., and Pearl, L. H. (2002) An Iron-Sulfur Cluster in the Family 4 Uracil-DNA Glycosylases. *J Biol Chem.* 277, 16936-16940.
62. Hoseki, J., Okamoto, A., Masui, R., Shibata, T., Inoue, Y., Yokoyama, S., and Kuramitsu, S. (2003) Crystal Structure of a Family 4 Uracil-DNA Glycosylase from *Thermus thermophiles* HB8. *J Mol Biol.* 333, 515-526.
63. Engstrom, L. M., Partington, O. A., and David, S. S. (2012) An Iron-Sulfur Cluster Loop Motif in the *Archaeoglobus fulgidus* Uracil-DNA Glycosylase Mediates Efficient Uracil Recognition and Removal. *Biochem.* 51, 5187-5197.
64. Mok, Y. G., Uzawa, R., Lee, J., Weiner, G. M., Eichman, B. F., Fischer, R. L., and Huh, J. H. (2010) Domain Structure of the DEMETER 5-Methylcytosine DNA Glycosylase. *Proc Natl Acad Sci USA.* 107, 19225-19230.
65. Brooks, S. C., Fischer, R. L., Huh, J. H., and Eichman, B. F. (2014) 5-Methylcytosine Recognition by *Arabidopsis thaliana* DNA Glycosylases DEMETER and DML3. *Biochem.* 53, 2525-2532.
66. Cheek, J. and Broderick, J. B. (2002) Direct H Atom Abstraction from Spore Photoproduct C-6 Initiates DNA Repair in the Reaction Catalyzed by Spore Photoproduct Lyase: Evidence for a Reversibly Generated Adenosyl Radical Intermediate. *J Am Chem Soc.* 124, 2860-2861.
67. Buis, J. M., Cheek, J., Kaliri E., and Broderick, J. B. (2006) Characterization of an Active Spore Photoproduct Lyase, a DNA Repair Enzyme in the Radical S-adenosylmethionine Superfamily. *J Biol Chem.* 281, 25994-26003.
68. Oberpichler, I., et al. (2011) A Photolyase-Like Protein from *Agrobacterium tumefaciens* with an Iron-Sulfur Cluster. *PLoS One.* 6, e26775.
69. Zhang, F., Scheerer, P., Oberpichler, I., Lamparter, T., and Kraub, N. (2013) Crystal Structure of a Prokaryotic (6-4) Photolyase with an Fe-S Cluster and a 6,7-Dimethyl-8-ribityllumazine Antenna Chromophore. *Proc Natl Acad Sci USA.* 110, 7217-7222.
70. Yeeles, J. T., Cammack, R., and Dillingham, M. S. (2009) An Iron-Sulfur Cluster is Essential for the Binding of Broken DNA by AddAB-Type Helicase-Nucleases. *J Biol Chem.* 284, 7746-7755.

71. Cromie, G.A. (2009) Phylogenetic Ubiquity and Shuffling of the Bacterial RecBCD and AddAB Recombination Complexes. *J Bacteriol.* 191, 5076-5084.

72. **a)** Pokharel, S. and Campbell, J. L. (2012) Cross Talk Between the Nuclease and Helicase Activities Dna2: Role of an Essential Iron-Sulfur Cluster Domain. *Nucleic Acids Res.* 40, 7821-7830. **b)** Zhou, C. Pourmal, S., and Pavletich, N. P. (2015) Dna2 Nuclease-Helicase Structure, Mechanism and Regulation by Rpa. *eLIFE.* 4, e09832.

73. Sparks, J. L, Kumar, R., Singh, M., Wold, M. S., Pandita, T. K., and Burgers, P. M. (2012) Human Exonuclease 5 is a Novel Sliding Exonuclease Required for Genomic Stability. *J Biol Chem.* 287, 42773-42783.

74. Zhang, J., Kasciukovic, T., and White, M. F. (2012) The CRISPR Associated Protein Cas4 is a 5' to 3' DNA Exonuclease with an Iron-Sulfur Cluster. *PLoS One.* 7, e47232.

75. Lemak, S., *et al.* (2013) Toroidal Structure and DNA Cleavage by the CRISPR-Associated [4Fe-4S] Cluster Containing Cas4 Nuclease SS0001 from *Sulfolobus solfataricus*. *J Am Chem Soc.* 135, 17476-17487.

76. Lemak, S., *et al.* (2014) The CRISPR-Associated Cas4 Protein Pcal_0546 from *Pyrobaculum calidifontis* Contains a [2Fe-2S] Cluster: Crystal Structure and Nuclease Activity. *Nucleic Acids Res.* 42, 11144-11155.

77. Pugh, R. A., *et al.* (2008) The Iron-Containing Domain is Essential in Rad3 Helicases for Coupling of ATP Hydrolysis to DNA Translocation and for Targeting the Helicase to the Single-Stranded DNA-Double Stranded DNA Junction. *J Biol Chem.* 283, 1732-1743.

78. Uringa, E. J., Youds, J. L., Lisingo, K., Lansdorp, P. M., and Boulton, S. J. (2011) RTEL1: An Essential Helicase for Telomere Maintenance and the Regulation of Homologous Recombination. *Nucleic Acids Res.* 39, 1647-1655.

79. Landry, A. P. and Ding, H. (2014) The N-terminus Domain of Human DNA Helicase Rtel1 Contains a Redox Active Iron-Sulfur Cluster. *Biome Res Int.* Article ID 285791.

80. Stiban, J., Farnum, G. A., Hovde, S. L., and Kaguni, L. S. (2014) The N-Terminal Domain of the Drosophila Mitochondrial Replicative DNA

Helicase Contains an Iron-Sulfur Cluster and Binds DNA. *J Biol Chem.* 289, 24032-24042.

81. Klinge, S., Hirst, J., Maman, J. D., Krude, T., and Pellegrini, L. (2007) An Iron-Sulfur Domain of the Eukaryotic Primase is Essential for RNA Primer Synthesis. *Nature Struct Mol Biol.* 14, 875-877.

82. Weiner, B. E., et al. (2007) An Iron-Sulfur Cluster in the C-Terminal Domain of the p58 Subunit of Human DNA Primase. *J Biol Chem.* 282, 33444-33451.

83. Vaithiyalingam, S., Warren, E. M., Eichman, B. F., and Chazin, W. J. (2010) Insights into Eukaryotic DNA Priming from the Structure and Functional Interactions of the 4Fe-4S Cluster Domain of Human DNA Primase. *Proc Natl Acad Sci USA.* 107, 13684-13689.

84. Hirata, A., Klein, B. J., and Mrakami, K. S. (2008) The X-Ray Crystal Structure of RNA Polymerase from Archaea. *Nature.* 451, 851-854.

85. Lessner, F. H., Jennings, M. E., Hirata, A., Duin, E. C., and Lessner, D. J. (2012) Subunit D of RNA Polymerase from *Methanosarcina acetivorans* Contains Two Oxygen-Labile [4Fe-4S] Clusters: Implications for Oxidant-Dependent Regulation of Transcription. *J Biol Chem.* 287, 18510-18523.

86. Netz, D. J., et al. (2011) Eukaryotic DNA Polymerases Require an Iron-Sulfur Cluster for the Formation of Active Complexes. *Nature Chem Biol.* 8, 125-132.

87. Jain, R., et al. (2014) An Iron-Sulfur Cluster in the Polymerase Domain of Yeast DNA Polymerase ϵ . *J Mol Biol.* 426, 301-308.

88. Sontz, P. A., Muren, N. B., and Barton, J. K. (2012) DNA Charge Transport for Sensing and Signaling. *Acc Chem Res.* 45, 1792-1800.

89. Spatzal, T. (2015) The Center of Biological Nitrogen Fixation: FeMo Cofactor. *Z Anorg Allg Chem.* 1, 10-17.

90. Topham, Susan, A. "The History of the Catalytic Synthesis of Ammonia." *Catalysis Science and Technology.* Vol. 7. Berlin-Heidelberg: Springer-Verlag, 1985. 1-50. Print.

91. Yiokari, C. G., Pitselis, G. E., Polydoros, D. G., Katsaounis, A. D., and Vayenas, C. G. (2000) High-Pressure Electrochemical Promotion of

Ammonia Synthesis over an Industrial Iron Catalyst. *J Phys Chem A*. 104, 10600-10602.

92. Alberty, R. A. (1994) Thermodynamics of the Nitrogenase Reactions. *J Biol Chem*. 269, 7099-7102.

93. Galloway, J. N., et al. (2008) Transformation of the Nitrogen Cycle: Recent Trends, Questions, and Potential Solutions. *Science*. 320, 889-892.

94. Erisman, J. W., Sutton, M. A., Galloway, J., Klimont, Z., and Winiwarter, W. (2008) How a Century of Ammonia Synthesis Changed the World. *Nature Geosci*. 1, 636-639.

95. Georgiadis, M. M., Komiya, H., Chakrabarti, P., Woo, D., Kornuc, J. J., and Rees, D. C. (2002) Crystallographic Structure of the Nitrogenase Iron Protein from *Azotobacter vinelandii*. *Science*. 257, 1653-1659.

96. Howard, J. B. and Rees, D. C. (2006) How Many Metals Does it Take to Fix N₂? A Mechanistic Overview of Biological Nitrogen Fixation. *Proc Natl Acad Sci USA*. 103, 17088-17093.

97. Burgess, B. K. and Lowe, D. J. (1996) Mechanism of Molybdenum Nitrogenase. *Chem Rev*. 96, 2983-3011.

98. Seefeldt, L. C., Hoffman, B. M., and Dean, D. R. (2009) Mechanism of Mo-Dependent Nitrogenase. *Ann Rev Biochem*. 78, 701-722.

99. Einsle, O., Tezcan, A. F., Andrade, S. L., Schmid, B., Yoshida, M., Howard, J. B., and Rees, D. C. (2002) Nitrogenase MoFe Protein at 1.16 Å Resolution: A Central Ligand in the FeMo Cofactor. *Science*. 297, 1696-1700.

100. Spatzal, T., Aksoyoglu, M., Zhang, L., Andrade, S. L. A., Schleicher, E., Weber, S., Rees, D. D., and Einsle, O. (2011) Evidence for Interstitial Carbon in Nitrogenase FeMo Cofactor. *Science*. 334, 940.

101. Tezcan, F. A., Kaiser, J. T., Mustafi, D., Walton, M. Y., Howard, J. B., and Rees, D. C. (2005) Nitrogenase Complexes: Multiple Docking Sites for a Nucleotide Switch Protein. *Science*. 309, 1377-1380.

102. Winkler, J. R. and Gray, H. B. (2014) Long-Range Electron Tunneling. *J Am Chem Soc*. 136, 2930-2939.

103.Langen, R., Chang, I.-J., Germanas, J. P., Richards, J. H., and Gray, H. B. (1995) Electron Tunneling in Proteins: Coupling Through a Beta Strand. *Science*. 268, 1733-1735.

104.Regan, J. J., Di Bilio, A. J., Langen, R., Skov, L. K., Winkler, J. R., Gray, H. B., and Onuchic, J. N. (1995) Electron Tunneling in Azurin: The Coupling Across a Beta-Sheet. *Chem Biol*. 2, 489-496.

105.Angrove, H. C., Yoo, S. J., Münck, E., and Burgess, B. K. (1998) An All-Ferrous State of the Fe Protein of Nitrogenase. Interaction with Nucleotides and Electron Transfer to the MoFe Protein. *J Biol Chem*. 273, 26330-26337.

106.Lowery, T. J., Wilson, P. E., Zhang, B., Bunker, J., Harrison, R. G., Nyborg, A. C., Thiriot, D., and G. D. (2006) Flavodoxin Hydroquinone Reduces *Azotobacter vinelandii* Fe Protein to the All-Ferrous Redox State with a S=0 Spin State. *Proc Natl Ac Sci USA*. 103, 1131-17136.

107.Ryle, M. J. and Seefeldt, L. C. (1996) Elucidation of a MgATP Signal Transduction Pathway in the Nitrogenase Iron Protein: Formation of a Conformation Resembling the MgATP-Bound State by Protein Engineering. *Biochem*. 35, 4766-4775.

108.Ryle, M. J. and Seefeldt, L. C. (1996) The [4Fe-4S] Cluster Domain of the Nitrogenase Iron Protein Facilitates Conformational Changes Required for the Cooperative Binding of Two Nucleotides. *Biochem*. 35, 15654-15662.

109.Spee, J. H., Arendsen, A. F., Wassink, H., Marritt, S. J., Hagen, W. R., and Haaker, H. (1998) Redox Properties and Electron Paramagnetic Resonance Spectroscopy of the Transition State Complex of *Azotobacter vinelandii* Nitrogenase. *FEBS Lett*. 432, 55-58.

110.Watt, G. D. and Reddy, K. R. N. (1994) Formation of an All Ferrous Fe₄S₄ Cluster in the Iron Protein Component of *Azotobacter vinelandii* Nitrogenase. *J Inorg Biochem*. 53, 281-294.

111.Guo, M., Sulc, F., Ribbe, M. W., Farmer, P. J., and Burgess, B. K. (2002) Direct Assessment of the Reduction Potential of the [4Fe-4S]^{1+/0} Couple of the Fe Protein from *Azotobacter vinelandii*. *J Am Chem Soc*. 124, 12100-12101.

112. Pierik, A. J., Wassink, H., Haaker, H., and Hagen, W. R. (1993) Redox Properties and EPR Spectroscopy of the P Clusters of *Azotobacter vinelandii* MoFe Protein. *Eur J Biochem.* 212, 51-61.

113. Margan, T. V., Mortenson, L. E., McDonald, J. W., Watt, G. D. (1988) Comparison of Redox and EPR Properties of the Molybdenum Iron Proteins of *Clostridium pasteurianum* and *Azotobacter vinelandii* Nitrogenases. *J Inorg Biochem.* 33, 111-120.

114. O'Donnell, M. J. and Smith, B. E. (1978) Electron-Paramagnetic-Resonance Studies on the Redox Properties of the Molybdenum-Iron Protein of Nitrogenase Between +50 and -450 mV. *Biochem J.* 173, 831-838.

115. Bjornsson, R., Neese, F., Schrock, R. R., Einsle, O., and DeBeer, S. (2015) The Discovery of Mo(III) in FeMoco: Reuniting Enzyme and Model Chemistry. *J Biol Inorg Chem.* 20, 447-460.

Chapter 2

PURIFICATION AND SPECTROSCOPIC CHARACTERIZATION OF *S. CEREVIAE* DNA2

Abstract

Dna2 is a eukaryotic helicase-nuclease that has multiple roles in genome maintenance. This protein binds a 4Fe-4S cluster in its nuclease domain that is required for maximum nuclease and ATPase activity. In this chapter, a new overexpression and purification procedure is described to isolate *S. cerevisiae* Dna2 from *E. coli*. The purified protein was active as both a nuclease and a DNA-dependent ATPase. Purification of Dna2 mutants suggested that there were no contaminating metal binding proteins, nucleases, or DNA-independent ATPases. Additionally, UV-visible absorption spectroscopy and EPR spectroscopy revealed that purified Dna2 could bind a 4Fe-4S cluster. This metal center was susceptible to oxidation to the 3Fe-4S cluster by potassium ferricyanide. Additionally, these studies suggested that the $[4\text{Fe-4S}]^{3+}$ cluster could be generated upon oxidation of Dna2. The 3Fe-4S cluster could be reduced by one electron to the 0 oxidation state. Although the EPR and UV-visible absorption spectrum of Dna2 changed upon reduction with sodium dithionite, the absence of certain features on the EPR spectrum prevented assignment of the reduced protein as the $[4\text{Fe-4S}]^{1+}$ cluster. These results provide a basic characterization of the iron-sulfur cluster in Dna2, which can serve as a foundation for future studies of how chemical changes to the iron-sulfur cluster could regulate Dna2 enzymatic activity.

Introduction

Dna2 is a helicase-nuclease that is involved in Okazaki fragment maturation, recombinational repair, mitochondrial genome maintenance, and telomere maintenance (1-4). This protein is composed of a RecB-like nuclease domain and a SF1B helicase domain. The C-terminal SF1B helicase domain of Dna2 is a 5' to 3' helicase, which binds and hydrolyzes adenosine triphosphate to separate double stranded DNA (**Figure 2.1**) (5). The RecB-like nuclease domain at the N-terminus of the protein is responsible for its dual nuclease activity (5' to 3' and 3' to 5') (5,6). This domain also contains an evolutionarily conserved 4Fe-4S cluster, which is essential for coordinating the helicase and nuclease activity of Dna2 (7).

There is no structure of *S. cerevisiae* Dna2; however, a 2.3 Å structure of the mouse homolog bound to DNA revealed that it is a cylindrical protein (**Figure 2.2**) (8). The nuclease domain forms its base, and consists of a doughnut-like structure through which DNA can pass. This nuclease domain also contains a 4Fe-4S cluster, which is located about 13 Å from the protein-bound ssDNA. The helicase domain packs on top of the nuclease domain, continuing the cylindrical hole that binds the DNA substrate. A β-barrel stock and an oligonucleotide binding domain also interact with the DNA. Notably, the nuclease domain seems to act as a base to stabilize the overall structure of the protein. The portion of the nuclease domain that binds the 4Fe-4S cluster interacts with the β-barrel domain, which

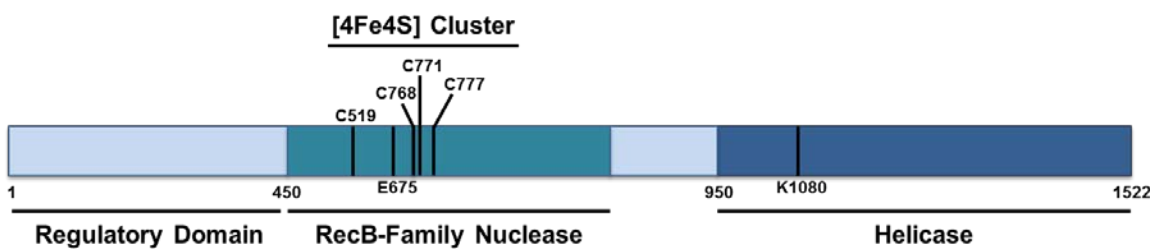


Figure 2.1. *S. cerevisiae* Dna2. Four cysteines, C519, C768, C771, and C777, in the RecB-family nuclease domain ligate the 4Fe-4S cluster in Dna22. Glutamate 675 (E675) is important for Dna2 nuclease activity. Lysine 1080 (K1080) is important for Dna2 helicase activity.

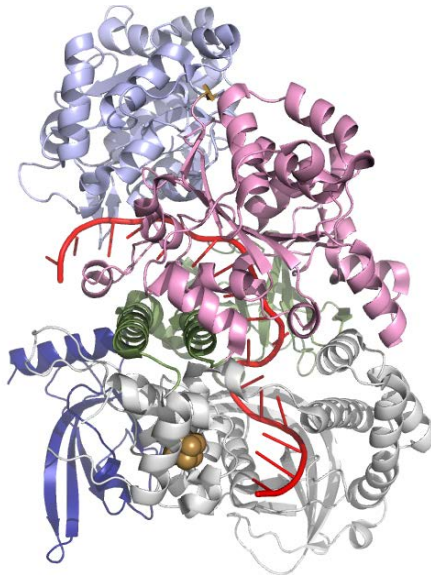


Figure 2.2. Crystal Structure of Mouse Dna2 Bound to DNA. The different domains of Dna2 are colored as follows: dark blue = oligonucleotide binding domain, white = nuclease domain, green = β -barrel domain, pink = helicase 1A domain, and light blue = helicase 2A domain. The 4Fe-4S cluster is shown in gold. ssDNA is shown in red. The α -domain and ADP are not shown. (PDB Code: 5EAX)

also stabilizes the helicase domain of Dna2. Thus, the 4Fe-4S cluster domain is positioned such that any distortions caused by chemical modification of the iron-sulfur cluster could have a profound effect on the nuclease activity, helicase activity, and/or DNA binding affinity of the protein.

The iron-sulfur cluster in Dna2 is conserved throughout eukaryotes from yeast to humans, and this motif is one of the prototypical members of a new structural family called the iron-staple nucleases (9). Nucleases of this structural family contain a 4Fe-4S cluster that is ligated by four cysteine residues, three of which are found as the motif $\text{CX}_2\text{CX}_5\text{C}$. The fourth ligating cysteine is located about 250 amino acids away from the other three cysteines (7). Mutagenesis studies have suggested that the iron-sulfur cluster in *S. cerevisiae* Dna2 is important for enzymatic activity, but not essential for DNA binding (7). Despite this important role in enzymatic activity, little is known about the chemical characteristics of the iron-sulfur cluster.

A purification strategy for *S. cerevisiae* Dna2 was developed to isolate this protein. This procedure allowed for the purification of Dna2 at high concentrations appropriate for spectroscopic analysis. The isolated protein contained an intact 4Fe-4S cluster, and had both nuclease and ATPase activity similar to that observed for Dna2 purified with other protocols. Since defects in 4Fe-4S cluster loading cause a severe decrease in the nuclease and ATPase activity of Dna2, this result provided additional support to the observation that purified Dna2 contained an intact 4Fe-4S cluster. A series of Dna2 mutants were purified using the new strategy to confirm that there were no contaminating metal binding proteins, nucleases, or DNA-independent ATPases. Finally, spectroscopic methods were used to determine the accessible oxidation states of the iron-sulfur cluster. These experiments lay a foundation for studies of how the oxidation state of the iron-sulfur cluster bound by Dna2 could regulate the enzymatic activity of this protein.

Methods

Materials. Glycerol and sodium chloride were purchased from Macron fine chemicals. Tryptone, yeast extract, and agar were purchased from BD. Isopropyl β -D-1-thiogalactopyranoside (IPTG) and dithiothreitol (DTT) was purchased from Research Products International (RPI). PBS buffer was purchased from Cellgro. All other chemicals were purchased from Sigma-Aldrich. The buffers were adjusted to the indicated pH at room temperature with 6M NaOH. All columns for Dna2 purification were purchased from GE Healthcare. The γ -³²P adenosine triphosphate was ordered from MP Biomedicals. All of the solutions used for making denaturing polyacrylamide gels were purchased from National Diagnostics. The pGal18-DNA2 construct was a gift from the Campbell lab (Caltech). All oligonucleotide primers were purchased from IDT DNA.

Full Length Dna2 Overexpression Plasmid. The full *DNA2* gene was cloned into the BamHI and NotI sites of the pQTEV vector (Addgene, ID: 31291) such that there was an N-terminal hepta-histidine tag and a TEV cleavage site when Dna2 was expressed from this construct (10). The Gibson assembly method was used to make the full length Dna2 overexpression construct (11). The pQTEV overexpression vector (~5 µg) was double restriction enzyme digested with 50 units of BamHI-HF (NEB) and 50 units of NotI-HF (NEB) for twenty hours at 37 °C. The *DNA2* gene was PCR amplified from the pGal18-*DNA2* (7) vector in two separate fragments with the first four primers outlined in **Table A1.1**, dNTP mix (Roche), and Hi Fi Taq Polymerase (Roche). The PCR products were purified by gel extraction (Qiagen). The Gibson assembly reaction was set-up such that 50 fmol of each of the digested pQTEV plasmid and PCR products were added to water to a final volume of 10 µL. 10 µL of 2x Gibson Assembly Master Mix (NEB) was added to the DNA substrates. The reaction was incubated at 50 °C for one hour. The reaction mixture was transformed into TOP10 electrocompetent cells (Invitrogen) via electroporation. Any colonies that were selected on LB ampicillin (100 µg/mL) agar plates were screened for the desired plasmid by sequencing the plasmids with the eight check primers outlined at the bottom of **Table A1.1** (Laragen).

The codon that encoded the N-terminal methionine of Dna2 was removed to avoid undesired initiation of translation at the beginning of the Dna2 gene rather than at the start of the N-terminal hepta-histidine tag. The methionine codon deletion was made by site-directed mutagenesis of pQTEV-*DNA2* using the oligonucleotide primers that are shown in **Table A1.1** and a QuikChange Lightning Site-Directed Mutagenesis Kit (Agilent). The primers used in the mutagenesis reaction were pQTEV-yDna2 N-Met Del. Forward and pQTEV-yDna2 N-Met Del. Reverse. Following mutagenesis, the plasmids were sent for sequencing with the eight check primers presented at the bottom of **Table A1.1** (Laragen). The isolated plasmid was transformed into Rosetta2 (DE3) pLysS cells (Novagen) to make the strain for Dna2 overexpression.

Full Length Dna2 Mutant Overexpression Plasmids and E. coli Strains. The indicated point mutations were constructed by site-directed mutagenesis of the pQTEV-DNA2 plasmid using the oligonucleotide primers that are shown in **Table A1.2** and a QuikChange Lightning Site-Directed Mutagenesis Kit (Agilent). Following mutagenesis, the plasmids were sent for sequencing with the eight check primers outlined in **Table A1.1** (Laragen). The plasmids encoding mutant Dna2 (**Table A1.3**) were transformed into Rosetta2 (DE3) pLysS cells (Novagen) to make the strains for mutant Dna2 overexpression (**Table A1.4**).

Wildtype Dna2 and Mutant Dna2 Overexpression and Purification. The protocol for purification of *S. cerevisiae* Dna2 was adapted from the procedure developed by Dr. Julien Lafrance-Vanassee (Tainer lab). The following buffers were prepared, were adjusted to the correct pH at room temperature, and were filtered with a 0.2 micron filter: histrap buffer A (20 mM trizma-HCl, pH 8, 0.5 M NaCl, 0.5 mM DTT); histrap buffer B (20 mM trizma-HCl, pH 8, 0.5 M NaCl, 0.5 M Imidazole, 0.5 mM DTT); anion exchange buffer A (20 mM trizma-HCl, pH 8, 0.1 mM EDTA, 2 mM DTT), anion exchange buffer B (20 mM trizma-HCl, pH 8, 1 M NaCl, 0.1 mM EDTA, 2 mM DTT), and gel filtration buffer (20 mM trizma-HCl, pH 8, 200 mM NaCl, 0.1 mM EDTA, 2 mM DTT). Dithiothreitol (DTT) was added to all buffers the day of Dna2 purification.

A single colony from an LB chloramphenicol (25 µg/mL) ampicillin (100 µg/mL) agar plate streaked with the Rosetta2 (DE3) pLysS cells that contained the Dna2 overexpression plasmid was used to inoculate a 10 mL overnight starter culture supplemented with 100 µg/mL ampicillin and 25 µg/mL chloramphenicol. The starter culture was diluted 1:100 into 1L of terrific broth medium containing 50 µg/mL ampicillin and 25 µg/mL chloramphenicol. The Rosetta2 (DE3) pLysS strains containing the wild type Dna2 and mutant Dna2 overexpression plasmids were grown to late exponential phase ($OD_{600} \sim 1.0$) at 37 °C with shaking (150 RPM) in an Innova43 incubator shaker. Then, the temperature of the incubator

was dropped to 16 °C, and overexpression of Dna2 was induced by addition of IPTG to a final concentration of 200 µM in each culture. The cultures were incubated for 20 hours at 16 °C with shaking (150 RPM). The cells were pelleted via centrifugation at 6238 x g for 10 minutes. The cell pellets were transferred to 50 mL polypropylene tubes, and were re-pelleted via centrifugation at 6238 x g for 10 minutes. All centrifugation steps were performed at 4 °C. The supernatant was decanted, and the cell pellets were washed with PBS buffer (Cellgro). About 10g of cell paste per liter of media was isolated with this procedure. The cell pellets were stored in the -80 °C freezer until Dna2 purification.

All lysis steps were carried out on ice at room temperature. The Rosetta2 (DE3) pLysS cell pellets were thawed on ice. The cell pellets were re-suspended in lysis buffer (20 mM Trizma-HCl, 500 mM NaCl, 10 mM Imidazole, 0.5 mM DTT, pH 8.0) with a homogenizer. The lysis buffer also contained complete protease inhibitor tablets (Roche) at a concentration of one tablet per 50 mL of buffer. The cells were lysed with a microfluidizer (Microfluidics Corp.). The cell debris was pelleted by centrifugation in a floor centrifuge (Sorvall RC6+) at 21,580 x g in the F14-6x250y rotor at 4 °C (FiberLite). The supernatant was filtered with a 0.45 micron filter.

All subsequent purification steps were performed at 10 °C in a deli case (VWR). The filtered cell lysate was loaded with a Pump P960 (GE Healthcare) to two 5 mL HisTrap HP columns connected in tandem with a Pump P960. The column was attached to an Akta FPLC (GE Healthcare), and the column was washed with 8 column volumes 99% HisTrap Buffer A/1% HisTrap Buffer B. Then, the following wash steps were performed: a gradient from 1 to 10% HisTrap Buffer B over 4 column volumes, a gradient from 10-11% HisTrap Buffer B over 8 column volumes, a gradient from 11-100% HisTrap Buffer B over 4 column volumes, and 5 column volumes of 100% HisTrap Buffer B. Dna2 eluted from the HisTrap column between 30% and 70% HisTrap Buffer B.

Following the HisTrap column, Dna2 was exchanged into 20% Anion Exchange Buffer B /80% Anion Exchange Buffer A on a HiPrep 26/10 desalting

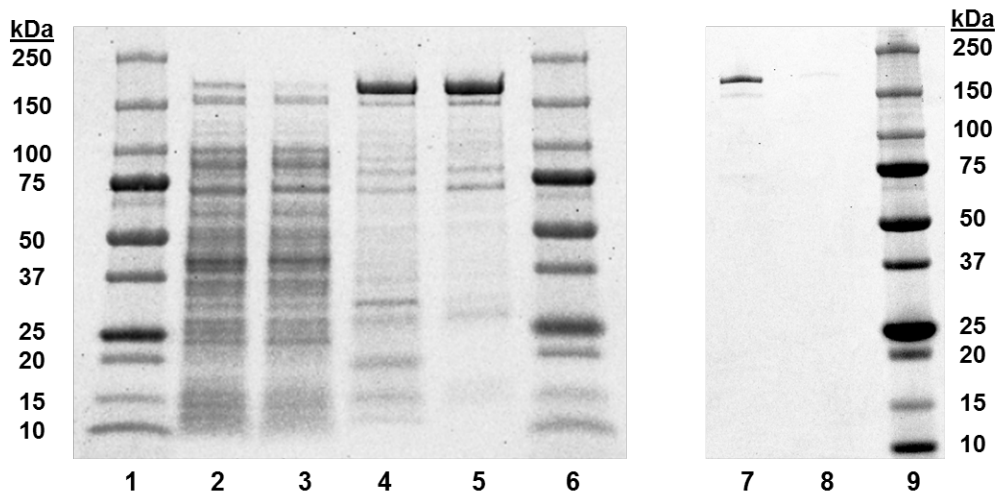


Figure 2.3. Gel Analysis of the Dna2 Purification. Coomassie-stained denaturing polyacrylamide gel showing the purity of Dna2 throughout the purification procedure. Lane 1 = Precision Plus Dual Color Protein Marker (BioRad), Lane 2 = Cell Lysate, Lane 3 = HisTrap Flow Through, Lane 4 = Post-HiTrap Column, Lane 5 = Post-HiTrapQ Column, Lane 6 = Precision Plus Dual Color Protein Marker (BioRad), Lane 7 = Post-Size Exclusion Column, Lane 8 = Post-Size Exclusion Column (1/10 Dilution), Lane 9 = Precision Plus Dual Color Protein Marker (BioRad).

column. The protein was loaded to a 5mL HiTrapQ anion exchange column with a Pump P960. The HiTrapQ column was first washed with 20% Anion Exchange Buffer B/80% Anion Exchange Buffer A. Then, Dna2 was eluted from the column with a gradient from 20-100% Anion Exchange Buffer B over 8 column volumes. The protein eluted between 30% and 50% Anion Exchange Buffer B. There was a second peak on the 280nm absorption trace, which corresponded to DNA. The protein was concentrated in an Amicon centrifuge tube (100,000 MWCO) to a final volume of about 2mL.

The protein purified through the HiTrapQ column was loaded to the Superdex200 GL10/300 column. The maximum volume of protein loaded to the column was 500 μ L. Dna2 eluted from this column in two peaks. The first protein fraction eluted in the void volume, which corresponded to the eluent fractions between 7.5-9 mL post-injection of the protein to the column. This protein was

aggregated Dna2, and had lower ATPase and nuclease activity than the protein that eluted from the column in the second peak of the chromatogram. The second batch of Dna2 that eluted from the column corresponded to the eluent fractions that Dna2 was expected to elute from the column based on its size (protein was found in eluent fractions 10-12.5 mL post-injection of protein to the column) (**Figure 2.7**). The protein collected in the second peak was concentrated in an Amicon centrifuge tube (100,000 MWCO) to a final concentration of 25-100 μ M. This protein was aliquoted to cryotubes, and was flash frozen in liquid nitrogen. The protein was stored in the -80 °C freezer.

The concentration of protein was estimated based off of the absorption of the sample at 280nm. The extinction coefficient of the protein at 280nm is 97,530 $M^{-1} cm^{-1}$ (12). The concentration of protein that contained a 4Fe-4S cluster was estimated based off of the absorption of the sample at 410nm. The extinction coefficient at 410nm was estimated as 17,000 $M^{-1} cm^{-1}$ based on literature precedence (13). The purity of the isolated protein was analyzed on a denaturing polyacrylamide gel (**Figure 2.3**). The size of Dna2 was approximately 175 kDa.

Dna2 Nuclease Activity Assay. A 5'-tail DNA substrate (5'-TTCACGAGATTACTTACTGCGGCTACATGATGCATCGTTAGGCGATTCCGCCTAACGATGCATCATGT -3') (IDT DNA) was 5'-radiolabeled with a previously published procedure (7). The nuclease reaction mixture consisted of varying concentrations of Dna2 with 20 fmol radiolabeled 5'-tail DNA substrate in 25 mM Trizma-HCl, pH 8, 0.05 mg/mL BSA, 1 mM DTT, and 1 mM MgCl₂. The reactions were incubated at 37 °C for thirty minutes. Then, the reactions were inactivated by incubation at 95 °C for five minutes. The reaction mixtures were loaded to a 12 % sequencing gel, and a 90W potential was applied to the gel. The gel was exposed to a phosphor screen (GE Healthcare). The phosphor screen was imaged on the Typhoon imager (GE Healthcare). All gel images were processed with ImageQuant software (GE Healthcare).

Dna2 ATPase Activity Assay. A 5'-tail DNA substrate (5'-TTCACGAGATTACTTACTGCGGCTACATGATGCATCGTTAGGCGATTCCGCCTAACGATGCATCATGT -3') (IDT DNA) was used as the DNA substrate in this experiment (7). The ATPase reaction mixture consisted of 1200 fmoles of Dna2 incubated with 8.8 μ moles of the 5'-tail DNA substrate in the ATPase assay reaction buffer (40 mM trizma-HCl, pH 7.5, 0.1 mg/mL BSA, 8 mM ATP, 5 mM MgCl₂, 2.5 mM DTT, 25 mM NaCl, 5 % glycerol) to a final volume of 50 μ L. The reactions were incubated at 37 °C for thirty minutes. Then, the reactions were stopped by adding BioMol green reagent (Enzo Life Sciences). The plates were incubated at room temperature for one hour. Then, the absorption at 650 nm of the ATPase assay reaction mixture was determined with a plate reader. A phosphate standard curve was used to calculate the amount of phosphate present in each ATPase activity reaction.

UV-Visible Absorption Spectroscopy of wildtype Dna2. The Cary UV-visible spectrometer was zeroed with gel filtration buffer without DTT (20 mM trizma-HCl, 200 mM NaCl, 0.1 mM EDTA, pH 8.0). All absorption spectra were background corrected with the absorption spectrum of gel filtration buffer. All absorption spectra were acquired in 50 μ L quartz cuvettes (Starna Cells, Inc.). This procedure was used for the acquisition of all subsequent UV-visible absorption spectra. Potassium ferricyanide was dissolved in gel filtration buffer, and this solution was added to the protein such that the oxidant was in three-fold molar excess over the protein.

For experiments that monitored the reduction of Dna2 by sodium dithionite, 15 μ M Dna2 was combined with sodium dithionite to a final concentration of 2 mM. All sample preparation was performed in a McCoy chamber that had a 95% H₂ / 5% N₂ atmosphere with less than 1ppm O₂. The dithionite solution was also prepared anaerobically with gel filtration buffer that had been degassed with argon. The quartz cuvette that contained the protein solution was sealed with a rubber septum, and was removed from the McCoy chamber for measurements.

Electron Paramagnetic Resonance Spectroscopy of Dna2. On the day that EPR spectra were acquired, Dna2 that had been purified through the HiTrapQ column was thawed on ice, and was purified on the Superdex200 GL10/300 size exclusion column. X-band EPR spectra were acquired on a Bruker EMX spectrometer. All spectra were acquired at 10K, a temperature that was maintained with an Oxford continuous-flow helium cryostat. All samples were assembled, except for the protein. The protein was added to the solution immediately before the sample was frozen in liquid nitrogen. EPR parameters were as follows: receiver gain = 5.02e+003, modulation amplitude = 4G, microwave power = 12.847 mW. This procedure was used for the acquisition of all subsequent EPR spectra unless indicated otherwise. All reported spectra were obtained by subtracting the spectrum of gel filtration buffer from the spectrum of the sample. The EPR spectra presented are all the first derivative of the acquired spectra.

All EPR samples were prepared aerobically unless indicated. $K_3Fe(CN)_6$ solutions were prepared aerobically. 100 μ M Dna2 was combined with 2 mM potassium ferricyanide, and this solution as incubated on ice for 15 minutes prior to transfer to an EPR tube (Wilmad Lab Glass). The sample was flash frozen in liquid nitrogen.

100 μ M as purified Dna2 was combined with sodium dithionite to a final concentration of 2 mM sodium dithionite in a McCoy chamber that had an atmosphere of 95% N_2 / 5% H_2 with less than 1ppm O_2 . The dithionite solution was also prepared in the chamber with gel filtration buffer that had been degassed with argon. The Dna2 and sodium dithionite solution was added to the quartz EPR tube. The sample was flash frozen in liquid nitrogen immediately after removal from the anaerobic chamber.

To prepare Dna2 samples for EPR without any oxygen in the original protein sample, the protein was degassed on a Schlenk line for one hour. The Dna2 solution was quickly cycled between vacuum and argon ten times every fifteen minutes. The solution was left under argon between cycles. The solution

was stirred during the course of the procedure, and was kept on ice. The protein solution was sealed, and was brought into the McCoy chamber. 150 μ L of 85 μ M Dna2 E675A was added to an EPR tube. Sodium dithionite was added to the protein solution to a final concentration of 4 mM. This solution was added to a quartz EPR tube. Samples were removed from the McCoy chamber, and were immediately frozen with liquid nitrogen.

Results

Purification of wildtype Dna2. The *S. cerevisiae* Dna2 gene was cloned into a pQTEV plasmid such that the protein was expressed with an N-terminal hepta-histidine tag. This protein was overexpressed in the Rosetta2 (DE3) pLysS *E. coli* strain. Dna2 was purified over a series of three columns: a Ni-NTA column, a

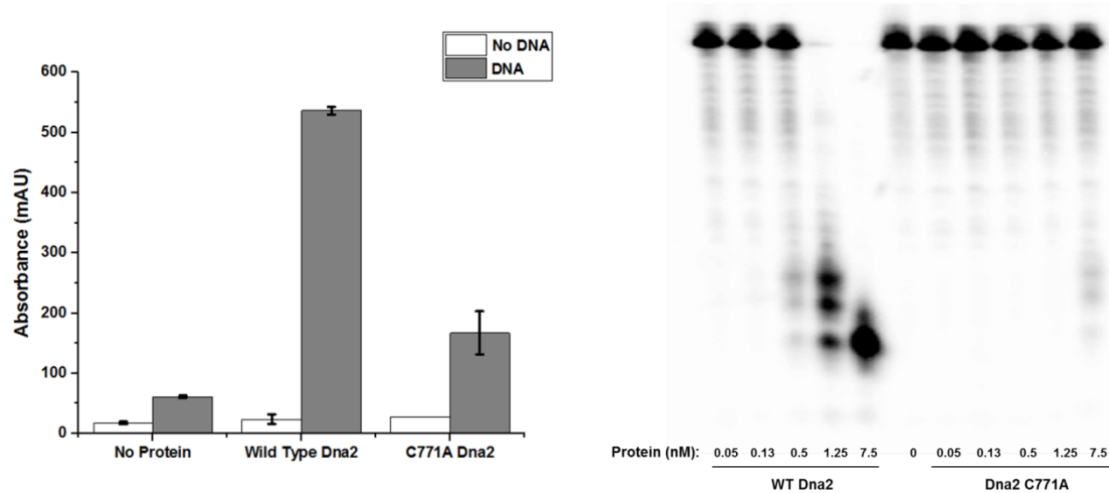


Figure 2.4. Dna2 Activity Assays. Dna2 purified from *E. coli* is active as a nuclease and as a DNA-dependent ATPase. (Left) Dna2 ATPase activity measured using a colorimetric phosphate detection assay. An increase in absorption at 650nm indicates an increase in the total amount of free phosphate in the assay mixture. The ATPase reaction mixture consisted of 1200 fmoles of Dna2 incubated with 8.8 μ moles of the 5'-tail DNA substrate in 40 mM Trizma-HCl, pH 7.5, 0.1mg/mL BSA, 8 mM ATP, 5 mM MgCl₂, 2.5 mM DTT, 25 mM NaCl, 5 % glycerol. Each bar represents the average of two experiments. Error is reported as standard error. (Right) Phosphorimage of the sequencing gel with the nuclease reactions performed with wild type Dna2 and Dna2 C771A.

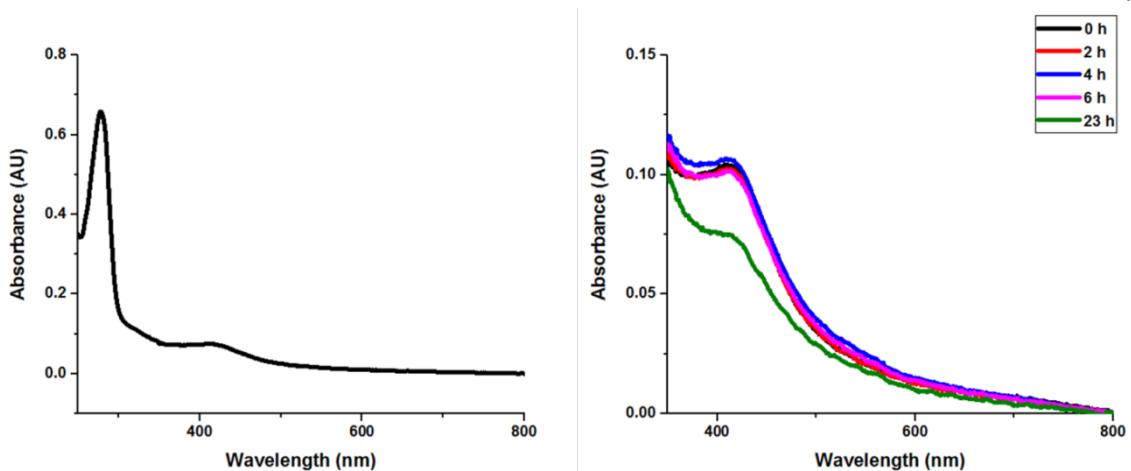


Figure 2.5. UV-Visible Absorption Spectrum of Dna2. (Left) The UV-visible absorption spectrum of Dna2 in 20 mM trizma-HCl, 200 mM NaCl, 0.1 mM EDTA, pH 8. (Right) The absorption spectrum of Dna2 over the course of 23 hours. The top right of the spectrum indicates the length of time the protein was at room temperature prior to spectrum acquisition.

HiTrapQ anion exchange column, and a Superdex200 size exclusion column. Trypsin digest followed by liquid chromatography tandem mass spectrometry (LC-MS-MS) analysis of the purified protein indicated that Dna2 was isolated during this purification. This method also allowed for the identification of DnaK as the major contaminating protein in the purification. Other chaperone proteins like GroEL, DnaJ, and GrpE also contaminated purified Dna2.

Dna2 as isolated using this method contained a 4Fe-4S cluster. The percentage of Dna2 that contained an intact 4Fe-4S cluster was defined as the cluster loading. This value was estimated by comparing the absorption at 280nm to the absorption at 410nm. The average cluster loading for Dna2 isolated with this purification protocol ranged from 65-80%.

The nuclease and ATPase activity of Dna2 isolated with the new purification scheme was analyzed and compared to results recorded in the literature. This assay revealed that the protein was active, and that the activity of the protein was the same as Dna2 purified from *S. cerevisiae* (Figure 1) (7,14). Specifically, in the

literature, Dna2 has been observed to completely degrade DNA substrates at concentrations above 7 nM. The DNA substrate was partially degraded at concentrations of 2 nM. Similar to these observations, in the work describe in this study, the DNA substrate was completely degraded at Dna2 concentrations above 7 nM. Partial degradation of the substrate was observed at Dna2 concentrations of 1.5 nM.

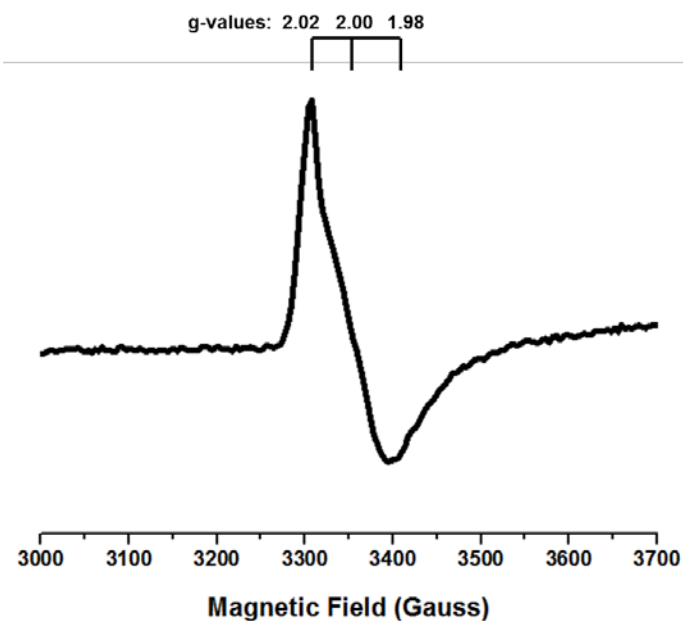


Figure 2.6. X-Band EPR Spectrum of Dna2 at 10K. EPR Spectrum of Dna2 as isolated in 20mM trizma-HCl, 200mM NaCl, 0.1 mM EDTA, pH 8.

Wild type Dna2 was also active as an ATPase when bound to DNA. As observed previously, Dna2 was not active as an ATPase when DNA was not present. Thus, there were no DNA-independent ATPases that co-purified with wildtype Dna2.

Spectroscopic Characterization of the Iron-Sulfur Cluster in Dna2. The UV-visible absorption spectrum of Dna2 had a broad peak, with a maximum at 415nm in addition to the peak at 280nm that indicated the presence of aromatic amino acid residues in the protein. This spectrum suggests that the isolated protein binds a 4Fe-4S cluster. The 4Fe-4S cluster in Dna2 was not stable over time as evidenced by a large decrease in absorption at 415nm after 23 hours (**Figure 2.5**).

The iron-sulfur cluster in Dna2 was also characterized with electron paramagnetic resonance (EPR) spectroscopy. As isolated, the majority of the 4Fe-4S cluster in Dna2 was most likely in the EPR silent 2+ oxidation state. However,

there was a signal centered at $g = 2.00$ on the X-band EPR spectrum of the isolated protein (**Figure 2.6**). Thus, a fraction of the isolated protein bound a 3Fe-4S cluster (15,16). There was a second signal observed with $g = 4.3$. In biological samples, this signal is often attributed to high-spin mononuclear Fe^{3+} ions that are in sites of low symmetry (17,18). Thus, this signal was assigned to ferric iron that was present due to degradation of the iron-sulfur cluster. Consistent with this assignment, the signal with an average g -value of 4.3 decreased in intensity when the EPR samples were prepared anaerobically, suggesting that this signal was largely generated by iron-sulfur cluster degradation during aerobic sample preparation.

Purification of Dna2 Mutants. Three Dna2 mutants were isolated to confirm that there were no contaminants in the purified protein that could interfere with experiments. The Dna2 C771A mutant contains alanine in place of one cysteine residue that ligates the 4Fe-4S cluster in Dna2. This mutant was isolated to confirm that there were no co-purifying metal binding proteins (7). The nuclease-deficient Dna2 E675A mutant was purified to confirm that there were no contaminating nucleases (5). A third Dna2 mutant, Dna2 P504S, was also purified

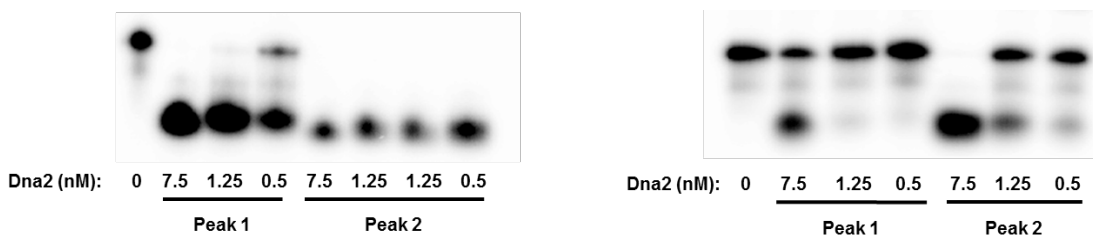


Figure 2.7. Dna2 and Dna2 C771A Nuclease Assays. Dna2 nuclease assay immediately following purification by size exclusion chromatography. (*Left*) Phosphoradiogram of the 12% denaturing polyacrylamide gel with the products of the nuclease reaction assays performed with Dna2 immediately after elution from the Superdex200 size exclusion column in the column void volume (Peak 1) and the expected Dna2 eluent fraction (Peak 2). (*Right*) Phosphoradiogram of the 12% denaturing polyacrylamide gel with the products of the nuclease reaction assays performed with the Dna2 C771A mutant directly following elution from the Superdex200 size exclusion column in the column void volume (Peak 1) and the predicted Dna2 eluent fraction (Peak 2).

to determine whether this protein bound a 4Fe-4S cluster. Notably, proline 504 is an evolutionarily conserved residue in Dna2, and mutation of this residue to serine has resulted in both deficiencies in protein activity as well as phenotypic changes similar to those Dna2 mutants designed to disrupt iron-sulfur cluster binding (7).

Dna2 C771A. The Dna2 C771A mutant was purified with the same protocol that was used to isolate wildtype Dna2. As determined by UV-visible absorption spectroscopy, iron-sulfur cluster incorporation into the Dna2 C771A mutant was less than that observed for wildtype Dna2, which was consistent with previous results (7). The total 4Fe-4S cluster loading for the purified protein was estimated to be 9%. The UV-visible absorption spectrum of Dna2 C771A was distinct from that observed for the wildtype protein. There were two major peaks in this spectrum, but the size of these peaks was significantly smaller than those observed for wild type Dna2. The first peak had a maximum at 425 nm while the second peak was centered at ~330 nm (Figure 2.9). This second peak was consistent with the typical absorption spectrum of a 3Fe-4S cluster. Thus, there may have been a small amount of the Dna2 C771A mutant isolated that bound a 3Fe-4S cluster. This result agrees with observations made in the literature that DNA binding proteins with a single mutation at a ligating cysteine residue still bind a 3Fe-4S cluster (19,20).

The nuclease and ATPase activity of Dna2 C771A isolated with the new purification procedure was analyzed and compared to values recorded in the literature (7). Consistent with previous reports, the ATPase and nuclease activity of Dna2 C771A was less than that of the wildtype protein (Figure 2.4). However, if

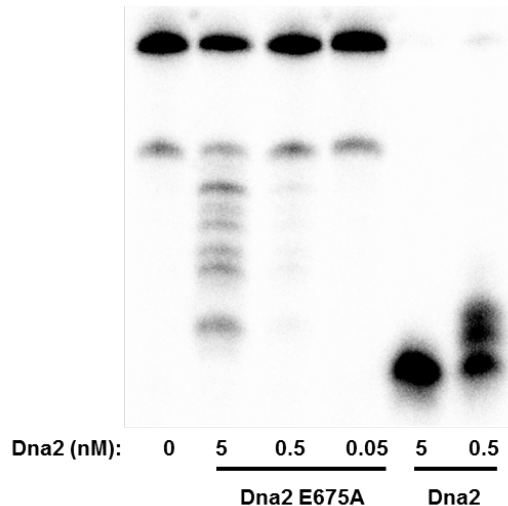


Figure 2.8. Dna2 and Dna2 E675A Nuclease Assay. Comparison of Dna2 E675A and wildtype Dna2 nuclease activity. Phosphoradiogram of the 12% sequencing gel that contained the nuclease assay reactions.

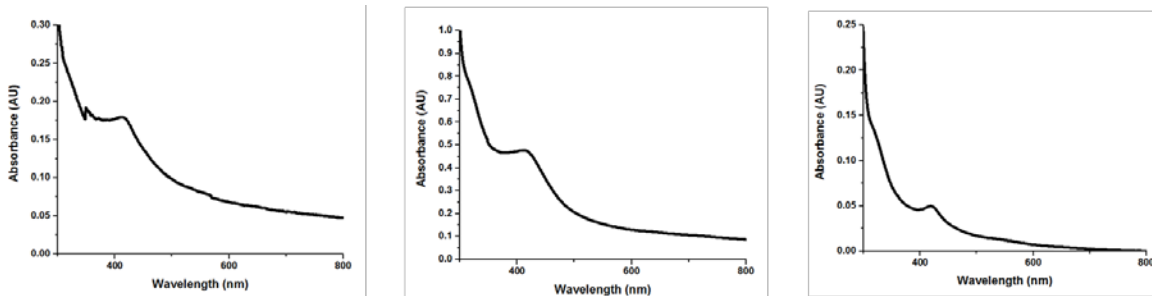


Figure 2.9. UV-Visible Absorption Spectra of Dna2 Mutants. (Left) 23 μ M Dna2 C771A (Middle) 30 μ M Dna2 E675A (Right) 9 μ M Dna2 P504S. All mutant proteins were suspended in 20mM trizma-HCl, 200 mM NaCl, 0.1 mM EDTA, pH 8.

the nuclease activity of this mutant was measured directly after the size exclusion column prior to freezing the sample, it was greater than that observed previously for the C771A mutant protein isolated from *S. cerevisiae* (Figure 2.7). Specifically, nearly complete degradation of the DNA substrate was observed for Dna2 C771A purified with this procedure at concentrations above 7.5 nM whereas in the literature complete degradation of a DNA substrate was not observed even at Dna2 concentrations up to 100 nM. At concentrations of Dna2 less than 1.25nM there was still a large amount of the starting substrate observed, suggesting that this mutant protein is less active than the isolated wildtype protein. The ATPase activity of the Dna2 C771A mutant as isolated with this procedure was similar to that observed in previous purifications. However, additional studies could provide insight into how the new purification method affects both the helicase and ATPase activity of the Dna2 C771A mutant.

Dna2 E675A. The Dna2 E675A mutant was purified using the same protocol as was used to isolate wildtype Dna2. This protein did not have any defects in iron-sulfur cluster stability as determined by UV-Visible absorption spectroscopy (Figure 2.9). The total 4Fe-4S cluster loading of the purified protein was estimated to be 80%. Additionally, the X-band EPR spectrum of Dna2 E675A was the same as that observed for wildtype Dna2 (data not shown).

The nuclease and ATPase activity of Dna2 E675A isolated with the new purification procedure were analyzed and compared to those observed for

purification performed in the literature (**Figure 2.8**) (5). Consistent with previous reports, the mutant protein was active as a DNA-dependent ATPase. The Dna2 E675A mutant had a significant decrease in nuclease activity with only a small amount of nuclease activity observed at protein concentrations up to 7.5 nM.

Dna2 P504S. Dna2 P504S was purified using the same protocol as was used to isolate wildtype Dna2. This protein did not have any defects in iron-sulfur cluster stability as determined with UV-visible absorption spectroscopy. The total 4Fe-4S cluster loading was estimated to be about 80%. Dna2 P504S has phenotypic similarities to the Dna2 cysteine mutants that have impaired iron-sulfur cluster binding. Thus, future studies with this mutant, which retains an iron-sulfur cluster but has deficiencies in both nuclease and helicase activity, could provide insight into potential roles for the iron-sulfur cluster in Dna2.

The 4Fe-4S Cluster in Dna2 is Susceptible to Oxidation by Potassium Ferricyanide. Dna2 was combined with a three-fold molar excess of potassium ferricyanide to investigate whether the iron-sulfur cluster could be oxidized to form $[4\text{Fe-4S}]^{3+}$. Upon oxidation with potassium ferricyanide, there was a significant decrease in the absorption at 410 nm. These absorption changes suggested that the 4Fe-4S cluster in Dna2 was susceptible to oxidative degradation with the 3Fe-4S cluster as a transient product of iron-sulfur cluster oxidation (**Figure 2.10**). There was no evidence for formation of the $[4\text{Fe-4S}]^{3+}$ cluster with this technique.

EPR spectroscopy also suggested that the 4Fe-4S cluster in Dna2 was susceptible to oxidative degradation. The X-band EPR spectrum of purified Dna2 oxidized with an excess of potassium ferricyanide contained three major signals at $g = 2.00$, $g = 4.3$, and $g = 9.6$ (**Figure 2.10**). The first signal was assigned to the 3Fe-4S cluster. This signal had primary g -values of 1.98, 2.00, 2.02 with a feature at a g -value of 2.10. The latter value suggests that a small amount of the $[4\text{Fe-4S}]^{3+}$ cluster was formed upon oxidation with potassium ferricyanide (21). The signal at a g -value of 9.6 also increased in intensity following oxidation. This signal was most likely due to a 3Fe-4S cluster in a tetrahedral configuration ($S=5/2$). This

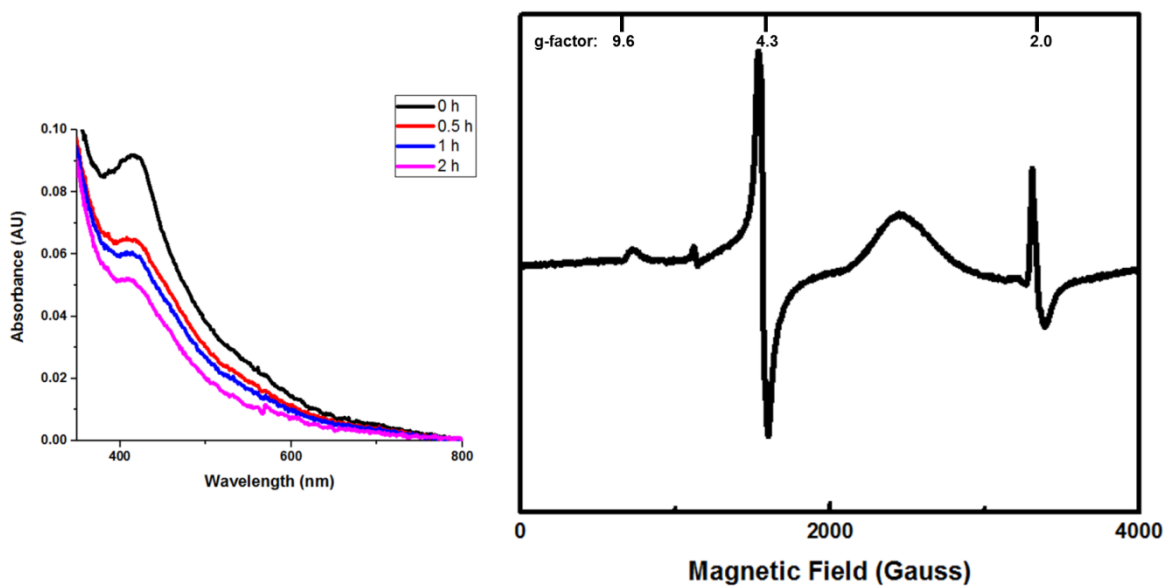


Figure 2.10. Oxidative Degradation of the 4Fe-4S Cluster in Dna2. (Left) The UV-Visible absorption spectrum of Dna2 with a three-fold molar excess of potassium ferricyanide at different times following oxidant addition. (Right) X-band EPR spectrum of 100 μ M Dna2 with 2mM potassium ferricyanide at 10K. The peaks were assigned as follows from right to left: $g = 2$ – $[3\text{Fe-4S}]^{1+}$ ($S=1/2$), $g = 2.10$ – $[4\text{Fe-4S}]^{3+}$, $g = 4.3$ – free ferric iron or $[3\text{Fe-4S}]^{1+}$ ($S=3/2$), $g = 9.6$ – $[3\text{Fe-4S}]^{1+}$. The broad peak at about 1800 gauss is due to excess potassium ferricyanide.

signal has been previously observed for purple aconitase (22). Thus, these spectroscopic studies suggest that Dna2 contains a 4Fe-4S cluster that is susceptible to oxidation with the 3Fe-4S cluster and $[4\text{Fe-4S}]^{3+}$ cluster as products of iron-sulfur cluster oxidation.

Reaction of the Iron-Sulfur Cluster in Dna2 with Sodium Dithionite. To further understand the redox properties of the 4Fe-4S cluster in Dna2, the reduction of this metal center was investigated using spectroscopic methods. The UV-visible absorption spectrum of Dna2 in the presence of sodium dithionite suggested that the iron cofactor in the protein was being reduced to the 1+ oxidation state. The absorption maximum of the 4Fe-4S cluster shifted to slightly higher wavelengths of 425 nm upon reduction (**Figure 2.11**). When the protein was exposed to air the original absorption band with a maximum at 415 nm was restored; however, there

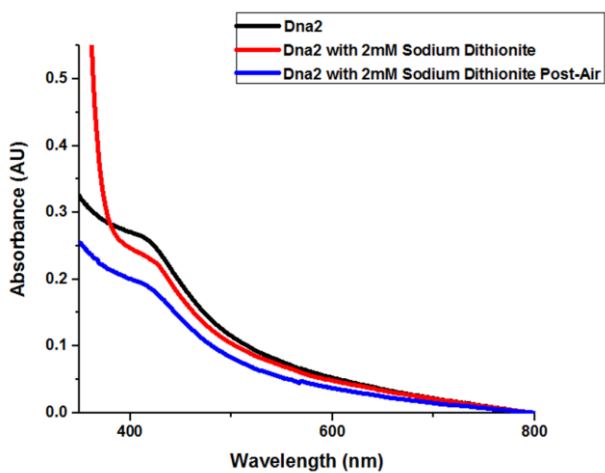


Figure 2.11 UV-Visible Absorption Spectrum of Reduced Dna2. The black trace is 15 μ M Dna2, the red trace is 15 μ M Dna2 reduced with 2 mM sodium dithionite. The blue trace corresponds to the reduced protein after it was exposed to air for 1.5 hours. All protein was suspended in 20 mM trizma-HCl, 200 mM NaCl, 0.1 mM EDTA, pH 8.

was significant protein precipitation, so the absorption at 415nm decreased relative to the protein prior to reduction with sodium dithionite.

EPR spectroscopy also suggested that the 4Fe-4S cluster in Dna2 could be reduced by sodium dithionite. Specifically, a primary signal at a g-value of 1.88 was observed for Dna2 reduced with 2 mM sodium dithionite. This signal was consistent with the formation of the 4Fe-4S cluster in the 1+ oxidation state, and was not present in samples containing 2 mM sodium

dithionite without protein. However, this spectrum was missing primary signals at $g = 1.94$ and $g = 2.06$, which are typical of a $[4\text{Fe-4S}]^{1+}$ cluster (21,24,33,39). The signal centered at $g = 2.00$ decreased in intensity upon reduction of the sample with sodium dithionite, suggesting that the 3Fe-4S cluster had been reduced from the 1+ oxidation state to the EPR silent all ferrous state. Thus, both the 4Fe-4S cluster and the 3Fe-4S cluster could be reduced by excess sodium dithionite. Furthermore, when all oxygen was removed from protein samples prior to addition of sodium dithionite, complete reduction of the 3Fe-4S cluster could be observed along with disappearance of the $g = 4.3$ signal. Only the broad signal at $g = 1.88$ could still be observed under these conditions (Figure 2.12).

Comparison of the Redox Properties of DNA Binding Proteins with 4Fe-4S Clusters. A number of DNA binding proteins with 4Fe-4S clusters discovered to date have been studied with UV-Visible absorption spectroscopy and EPR

spectroscopy. All of these analyses provide evidence that these proteins bind 4Fe-4S clusters; however, these experiments also show that the 4Fe-4S clusters do not all share the same redox properties (**Table 2.1**). In general, consistent with observations from UV-Visible absorption spectroscopy, the DNA binding proteins are purified aerobically with a $[4\text{Fe-4S}]^{2+}$ cluster. This cofactor is EPR silent. Depending on the conditions under which the protein was isolated, there is a variable amount of protein purified with a $[3\text{Fe-4S}]^{1+}$ cluster. This cluster can generally be reduced to $[3\text{Fe-4S}]^0$ with sodium dithionite, which is consistent with the results observed for the iron-sulfur cluster in Dna2.

Reduction of the $[4\text{Fe-4S}]^{2+}$ cluster to the $[4\text{Fe-4S}]^{1+}$ cluster has not been observed by EPR spectroscopy for all DNA binding proteins with 4Fe-4S clusters. Specifically, it was observed that the iron-sulfur cluster in the following DNA binding proteins could be reduced to the 1+ oxidation state: Endonuclease III, Uracil DNA glycosylase, the 4Fe-4S cluster in the polymerase domain of Polymerase epsilon, RNA polymerase, DinG, and Rtel1 (13,27,30,31,35). The metal center in these proteins was reduced to $[4\text{Fe-4S}]^{1+}$. The DNA binding proteins that are not reduced to the 1+ oxidation state include: MutY, the deoxyribodipyrimidine photolyase PhrB, eukaryotic primase, Rad3/XPD, AddAB, and polymerase delta (9,15,26,28,29,34). Notably, the recombinant C-terminal domains of the eukaryotic replicative DNA polymerases as purified from *E. coli* can be reduced to the 1+ oxidation state by sodium dithionite even though the iron-sulfur cluster in the complete DNA polymerase δ protein complex cannot be reduced (34). Although the EPR spectrum of Dna2 changed upon reduction by sodium dithionite, it did not have the characteristic spectrum of a $[4\text{Fe-4S}]^{1+}$ cluster. The 3Fe-4S cluster bound by this protein was reduced to the all ferrous state by sodium dithionite, but future studies will need to confirm the reduction of the 4Fe-4S cluster in Dna2 to the 1+ oxidation state.

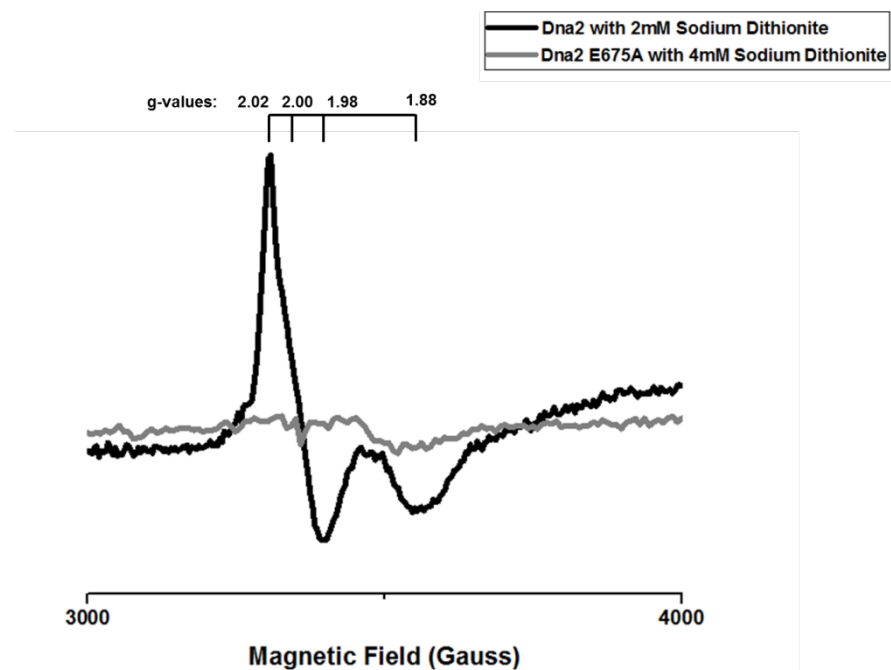


Figure 2.12. X-band EPR Spectrum of Reduced Dna2. Comparison of the X-band EPR spectrum of 100 μ M wild type Dna2 reduced with 2mM sodium dithionite and 86 μ M Dna2 E675A reduce with 4mM sodium dithionite. Dioxygen was not removed from the wild type Dna2 sample prior to reduction whereas dioxygen was removed from the Dna2 E675A sample prior to reduction.

MutY, UDG, and eukaryotic DNA primase are the only DNA binding proteins with spectroscopic evidence for oxidation of the 4Fe-4S cluster to the 3+ oxidation state (15,33). The experiments herein reported provide evidence for the oxidation of the 4Fe-4S cluster in Dna2 to the 3+ oxidation state. However, in these experiments there was also a significant amount of oxidative degradation of the 4Fe-4S cluster to the 3Fe-4S cluster and free ferrous iron observed upon oxidation of the protein. Oxidative degradation of the 4Fe-4S cluster in DNA binding proteins has been observed for the majority of DNA binding proteins with 4Fe-4S clusters with the exception of the DNA helicase DinG and the recombinant C-terminal domains of the eukaryotic replicative DNA polymerases (27,34).

Table 2.1. EPR Data for DNA Binding Proteins with 4Fe-4S Clusters

Protein	Cluster	g-value	References
MutY	$[3\text{Fe-4S}]^{1+}$ $[4\text{Fe-4S}]^{3+}$	2.02, 1.99 2.06, 2.08	23, 15
Endonuclease III	$[3\text{Fe-4S}]^{1+}$ $[4\text{Fe-4S}]^{1+}$	2.03, 2.01, 1.99 2.04, 1.92, 1.88	15, 24
<i>Archaeoglobus fulgidus</i> UDG	$[3\text{Fe-4S}]^{1+}$ $[4\text{Fe-4S}]^{3+}$	2.02 2.04, 2.13	15
<i>Pyrobaculum aerophilum</i> UDG	$[3\text{Fe-4S}]^{1+}$ $[4\text{Fe-4S}]^{1+}$ $[4\text{Fe-4S}]^{3+}$	2.02 2.06, 1.95, 1.85 2.12, 2.04	24
SP Lyase	$[3\text{Fe-4S}]^{1+}$ $[4\text{Fe-4S}]^{1+}$	2.02 2.03, 1.93, 1.89	25
PhrB	$[3\text{Fe-4S}]^{1+}$ $[4\text{Fe-4S}]^{3+}$	2.004, 1.981, 2.057	26
DinG	$[4\text{Fe-4S}]^{1+}$	2.005, 1.944, 1.918	27
<i>S. acidocaldarius</i> XPD	$[3\text{Fe-4S}]^{1+}$	2.02, 1.99	28
<i>Ferroplasma acidarmanus</i> Rad3	$[3\text{Fe-4S}]^{1+}$	2.022, 2.01, 1.98	29
RtelN	$[4\text{Fe-4S}]^{1+}$	2.050, 1.994, 1.918	30
RNA polymerase	$[4\text{Fe-4S}]^{1+}$	2.075, 1.974, 1.938, 1.897	31
<i>S. cerevisiae</i> primase	$[3\text{Fe-4S}]^{1+}$ $[4\text{Fe-4S}]^{3+}$	2.02, 2.01 2.11, 2.09, 2.0, 1.95	32
Human DNA primase	$[4\text{Fe-4S}]^{3+}$	2.087, 2.040, 2.013	33
<i>S. cerevisiae</i> Polymerase ϵ C-terminal Domain	$[4\text{Fe-4S}]^{1+}$	2.04, 1.93	34
<i>S. cerevisiae</i> Polymerase ϵ Δ C-terminal Domain	$[4\text{Fe-4S}]^{1+}$	2.090, 2.023, 1.98, 1.90	35
<i>S. cerevisiae</i> Polymerase δ C-terminal Domain	$[4\text{Fe-4S}]^{1+}$	2.04, 1.93	34
<i>S. cerevisiae</i> Polymerase ζ C-terminal Domain	$[4\text{Fe-4S}]^{1+}$	2.04, 1.93	34
<i>S. cerevisiae</i> Polymerase δ Complex	$[3\text{Fe-4S}]^{1+}$	2.02	34
<i>B. subtilis</i> AddAB	$[3\text{Fe-4S}]^{1+}$	2.019, 1.997, 1.962	9
<i>S. cerevisiae</i> Dna2	$[3\text{Fe-4S}]^{1+}$ $[4\text{Fe-4S}]^{1+}$ $[4\text{Fe-4S}]^{3+}$	2.02, 2.00, 1.98 1.88 2.10	This Work

Conclusion

A purification strategy was developed for the expression and purification of *S.cerevisiae* Dna2. The isolated protein had full enzymatic activity, and nearly complete 4Fe-4S cluster incorporation. Purification of Dna2 mutants using this protocol revealed that there were no contaminating metal binding proteins, DNA-independent ATPases, or nucleases in the purified protein. This purification strategy allowed for isolation of protein for characterization of the 4Fe-4S cluster in Dna2 by UV-visible absorption spectroscopy and EPR spectroscopy. These studies showed that as purified Dna2 was isolated with the majority of the protein in the EPR silent 2+ oxidation state, and with a fraction of the protein binding a $[3\text{Fe-4S}]^{1+}$ cluster. The 4Fe-4S cluster in Dna2 was susceptible to oxidation by potassium ferricyanide to generate the $[3\text{Fe-4S}]^{1+}$, Fe^{3+} , and $[4\text{Fe-4S}]^{3+}$. The 3Fe-4S cluster in Dna2 could be reduced by sodium dithionite, but studies aimed at determining whether Dna2 could be reduced to $[4\text{Fe-4S}]^{1+}$ were inconclusive. The observations made in this chapter along with recent biochemical and structural studies suggest that different oxidation states of the iron-sulfur cluster in Dna2 exist, and reversible redox chemistry that cycles between these different states could regulate Dna2 enzymatic activity.

References

1. Bae, S.-H., Bae, K.-H., Kim, J.-A., and Seo, Y.-S. (2001) RPA Governs Endonuclease Switching During Processing of Okazaki Fragments in Eukaryotes. *Nature*. 412, 456-461.
2. Zhu, Z., Chung, W.-H., Shim, E. Y., Lee, S. E., and Ira, G. (2008) Sgs1 Helicase and Two Nucleases Dna2 and Exo1 Resect DNA Double-Strand Break Ends. *Cell*. 134, 981-994.
3. Choe, W., Budd, M., Imamura, O., Hoopes, L., and Campbell, J. L. (2002) Dynamic Localization of an Okazaki Fragment Processing Protein Suggests a Novel Role in Telomere Replication. *Mol Cell Biol*. 22, 4202-4217.
4. Duxin, J. P., Dao, B., Martinsson, P., Rajala, N., Guittat, L., Campbell, J. L., Spelbrink, J. N., and Stewart, S. A. (2009) Human Dna2 is a Nuclear and Mitochondrial DNA Maintenance Protein. *Mol Cell Biol*. 29, 4274-4282.
5. Budd, M. E., Choe, W. C., Campbell, J. L. (2000) The Nuclease Activity of the Yeast DNA2 Protein, which is Related to the RecB-Like Nucleases, is Essential *In Vivo*. *J Biol Chem*. 275, 16518-16529.
6. Stewart, J. A., Campbell, J. L., and Bambara, R. A. (2010) Dna2 is a Structure-Specific Nuclease, with Affinity for 5'-Flap Intermediates. *Nucleic Acids Res*. 38, 920-930.
7. Pokharel, S. and Campbell, J. L. (2012) Cross Talk Between the Nuclease and Helicase Activities of Dna2: Role of an Essential Iron-Sulfur Cluster Domain. *Nucleic Acids Res*. 40, 7821-7830.
8. Zhou, C., Pourmal, S., and Pavletich, N. P. (2015) Dna2 Nuclease-Helicase Structure, Mechanism and Regulation by Rpa. *eLIFE*. 4, e09832.
9. Yeeles, J. T., Cammack, R., and Dillingham, M. S. (2009) An Iron-Sulfur Cluster is Essential for the Binding of Broken DNA by AddAB-Type Helicase-Nucleases. *J Biol Chem*. 284, 7746-7755.
10. Scheich, C., Niesen, F. H., Seckler, R., and Büssow, K. (2004) An Automated *In Vitro* Protein Folding Screen Applied to a Human Dynactin Subunit. *Protein Sci*. 13, 370-380.

11. Gibson, D. G., *et al.* (2009) Enzymatic Assembly of DNA Molecules up to Several Hundred Kilobases. *Nature Methods*. 6, 343-345.
12. Gasteiger, E., Hoogland, C., Gattiker, A., Duvaud, S., Wilkins, M. R., Appel, R. D., and Bairoch, A. *Protein Identification and Analysis Tools on the ExPASy Server*; (In) John M. Walker (ed): The Proteomics Protocols Handbook, Humana Press (2005). Pp. 571-607.
13. Cunningham, R. P., *et al.* (1989) Endonuclease III is an Iron-Sulfur Protein. *Biochem*. 28, 4450-4455.
14. Levikova, M., Klaue, D., Seidel, R., and Cejka, P. (2013) Nuclease Activity of *Saccharomyces cerevisiae* Dna2 Inhibits Its Potent DNA Helicase Activity. *Proc Natl Ac Sci USA*. 110, E1992-E2001.
15. Boal, A. K., Yavin, E., Lukianova, O. A., O'Shea, V. L., David, S. S., Barton, J. K. (2005) DNA-bound Redox Activity of DNA Repair Glycosylases Containing [4Fe-4S] Clusters. *Biochem*. 44, 8397-8407.
16. Kennedy, M. C., Mende-Mueller, L., Blondint, G. A., and Beinert, H. (1992) Purification and Characterization of Cytosolic Aconitase from Beef Liver and Its Relationship to the Iron-Responsive Element Binding Protein. *Proc Natl Acad Sci. USA*. 89, 11730-11734.
17. Taboy, C. H., Vaughan, K. G., Mietzner, T. A., Aisen, P., and Crubliss, A. L. (2001) Fe³⁺ Coordination and Redox Properties of a Bacterial Transferrin. *J Biol Chem*. 276, 2719-2724.
18. Bou-Abdallah, F. and Chasteen, N. D. (2008) Spin Concentration Measurements of High-Spin ($g' = 4.3$) Rhombic Iron(III) Ions in Biological Samples: Theory and Application. *J Biol Inorg Chem*. 13, 15-24.
19. Engstrom, L. M., Partington, O. A., and David, S. S. (2012) An Iron-Sulfur Cluster Loop Motif in the *Archaeoglobus fulgidus* Uracil-DNA Glycosylase Mediates Efficient Uracil Recognition and Removal. *Biochem*. 51, 5187-5197.
20. Lu, A. L. and Wright, P. M. (2003) Characterization of an *Escherichia coli* Mutant MutY with a Cysteine to Alanine Mutation at the Iron-Sulfur Domain. *Biochem*. 42, 3742-3750.

21. Lippard, S. J. and Berg, J. M. *Principles of Bioinorganic Chemistry*. University Science Books, 1994. Print.
22. Kennedy, M. C., et al. (1984) Evidence for the Formation of a Linear [3Fe-4S] Cluster in Partially Unfolded Aconitase. *J Biol Chem.* 259, 14463-14471.
23. Yavin, E., Boal, A. K., Stemp, E. D. A., Boon, E. M., Livingston, A. L., O'Shea, V. L., David, S. S., and Barton, J. K. (2005) Protein-DNA Charge Transport: Redox Activation of a DNA Repair Protein by Guanine Radical. *Proc Nat Acad Sci USA.* 102, 3546-3551.
24. Hinks, J. A., Evans, M. C., DeMiguel, Y., Sartori, A. A., Jiricny, J., and Pearl, L. H. (2002) An Iron-Sulfur Cluster in the Family 4 Uracil-DNA Glycosylases. *J Biol Chem.* 277, 16936-16940.
25. Buis, J. M., Cheek, J., Kaliri E., and Broderick, J. B. (2006) Characterization of an Active Spore Photoproduct Lyase, a DNA Repair Enzyme in the Radical S-adenosylmethionine Superfamily. *J Biol Chem.* 281, 25994-26003.
26. Oberpichler, I., et al. (2011) A Photolyase-Like Protein from *Agrobacterium tumefaciens* with an Iron-Sulfur Cluster. *PLoS One.* 6, e26775.
27. Ren, B., Duan, X., and Ding, H. (2009) Redox Control of the DNA Damage Inducible Protein DinG Helicase Activity via Its Iron-Sulfur Cluster. *J Biol Chem.* 284, 7746-7755.
28. Rudolf, J., Makrantoni, V., Ingledew, W. J., Stark, M. J., and White, M. F. (2006) The DNA Repair Helicases XPD and FancJ Have Essential Iron-Sulfur Domains. *Mol Cell.* 23, 801-808.
29. Pugh, R. A., et al. (2008) The Iron-Containing Domain is Essential in Rad3 Helicases for Coupling of ATP Hydrolysis to DNA Translocation and for Targeting the Helicase to the Single-Stranded DNA-Double Stranded DNA Junction. *J Biol Chem.* 283, 1732-1743.
30. Landry, A. P. and Ding, H. (2014) The N-Terminus Domain of Human DNA Helicase Rtel1 Contains a Redox Active Iron-Sulfur Cluster. *Biome Res Int.* Article ID 285791.
31. Lessner, F. H., Jennings, M. E., Hirata, A., Duin, E. C., and Lessner, D. J. (2012) Subunit D of RNA Polymerase from *Methanoscincina acetivorans* Contains Two Oxygen-Labile [4Fe-4S] Clusters: Implications for Oxidant-Dependent Regulation of Transcription. *J Biol Chem.* 287, 18510-18523.

32. Klinge, S., Hirst, J., Maman, J. D., Krude, T., and Pellegrini, L. (2007) An Iron-Sulfur Domain of the Eukaryotic Primase is Essential for RNA Primer Synthesis. *Nature Struct Mol Biol.* 14, 875-877.
33. Weiner, B. E., et al. (2007) An Iron-Sulfur Cluster in the C-Terminal Domain of the p58 Subunit of Human DNA Primase. *J Biol Chem.* 282, 33444-33451.
34. Netz, D. J., et al. (2011) Eukaryotic DNA Polymerases Require an Iron-Sulfur Cluster for the Formation of Active Complexes. *Nature Chem Biol.* 8, 125-132.
35. Jain, R., et al. (2014) An Iron-Sulfur Cluster in the Polymerase Domain of Yeast DNA Polymerase ϵ . *J Mol Biol.* 426, 301-308.
36. Genereux, J. C., Boal, A. K., and Barton, J. K. (2010) DNA-Mediated Charge Transport in Redox Sensing and Signaling. *J Am Chem Soc.* 132, 891-905.
37. White, M. F. and Dillingham, M. S. (2012) Iron-Sulphur Clusters in Nucleic Acid Processing Enzymes. *Curr Opin Struct Biol.* 22, 94-100.
38. Wu, Y. and Brosh, R. M. Jr. (2012) DNA Helicase and Helicase-Nuclease Enzymes with a Conserved Iron-Sulfur Cluster. *Nucleic Acids Res.* 40, 4247-4260.
39. Lindahl, P. A., Gorelick, N. J., Münck, E., and Orme-Johnson, W. H. (1987) EPR and Mössbauer Studies of Nucleotide-bound Nitrogenase Iron Protein from *Azotobacter vinelandii*. *J Biol Chem.* 31, 14945-14953.

DNA2 ELECTROCHEMICAL CHARACTERIZATION ON DNA-MODIFIED GOLD ELECTRODES

Abstract

The redox activity of the 4Fe-4S cluster in Dna2 was monitored on DNA-modified gold electrodes. The midpoint potential of this iron cofactor was 60 ± 20 mV v. NHE, which was assigned as the 2+/3+ couple of the 4Fe-4S cluster by comparison to other DNA binding proteins. A mutant of Dna2, Dna2 C771A, which binds an unstable 4Fe-4S cluster was not redox active on DNA-modified gold electrodes, suggesting that the observed signal was due to redox chemistry at the iron-sulfur cluster. Similar to other DNA binding proteins with 4Fe-4S clusters, there was no signal observed for Dna2 on gold electrodes modified with ssDNA. Additionally, the signal intensity as measured by cyclic voltammetry was less on working electrodes modified with double stranded DNA with an abasic site relative to undamaged double stranded DNA. These results are consistent with the observed redox process occurring via a DNA-mediated electron transfer mechanism. In addition to preliminary characterization of the DNA-bound midpoint potential of Dna2, the electronic coupling between the iron-sulfur cluster and the DNA was assessed under conditions that favored either the helicase or nuclease activity of Dna2. Addition of adenosine triphosphate (ATP) to the bulk protein solution on the electrode surface, activating the helicase activity of Dna2, led to an increase in the signal intensity as measured by cyclic voltammetry. In contrast, addition of $MgCl_2$ to activate the nuclease activity of Dna2, led to a broadening of the cathodic and anodic peak intensity with a decrease in signal intensity. These results suggested that the electronic coupling between the iron cofactor in Dna2 and the DNA changed depending on the enzymatic activity of the protein. Specifically, ATP hydrolysis that occurs while Dna2 is active as a helicase

enhances electronic coupling between the DNA and iron-sulfur cluster, whereas the iron-sulfur cluster does not efficiently participate in DNA-mediated charge transfer when Dna2 is active as a nuclease.

Introduction

DNA-modified gold electrodes are a platform for studying DNA-mediated electron transfer between an electrode and reactants in the ground state (1,2). These electrodes are prepared by depositing DNA modified with an alkane-thiol linker onto a gold working electrode such that a covalent bond forms between the sulfur on the DNA and the gold surface of the electrode. During this process, the DNA self assembles into monolayers in which the DNA is positioned at a 45° angle relative to the gold surface (3). The DNA can either be modified with a redox active probe prior to deposition to the surface or a DNA binding redox active probe can be added to the electrode surface following DNA monolayer formation. Then, the characteristics of electron transfer through DNA can be monitored by analyzing the flow of electrons from the working electrode, through the DNA base pair π -system, to the probe (1,2). Although the exact mechanism of charge transport on DNA-modified electrodes is distinct from that observed in excited state studies with metal complexes, the general principles of DNA CT are conserved between both types of experiments: 1) small perturbations in DNA structure attenuate charge transport and 2) charge transport occurs over large molecular distances with shallow distance dependence.

The observation that small perturbations to DNA structure attenuate charge transport on DNA-modified gold electrodes was made early in the development of this technique. Initial cyclic voltammetry experiments with self-assembled monolayers of DNA covalently modified with daunomycin showed that a cytosine-adenine mismatch base pair in the center of a DNA duplex decreased the flow of electrons through the DNA relative to a DNA duplex without a mismatched base

pair (1). This observation was later replicated with a variety of intercalating redox-active probes and DNA sequences (2,4-6). These early experiments were performed on a single working electrode. In recent years, the Barton lab has developed a multiplexed electrode platform that is well suited for the high-throughput study of DNA CT in larger DNA substrates of up to 100 base pairs in length (**Figure 3.1**) (7,8). Using this platform, it was observed that, regardless of whether electron transfer occurred in a twenty nucleotide DNA duplex or a one hundred nucleotide DNA duplex, the electron transfer rate was limited by tunneling through the alkane-thiol linker. These results provided a lower bound on the rate of electron transfer through the DNA of $>10^8 \text{ s}^{-1}$, a result that was consistent with the observation that the length of the alkane-thiol linker was inversely proportional to the rate of electron transfer (9). Furthermore, the DNA substrates that were used in these experiments had nicks in the sugar phosphate backbone. Thus, it was concluded that the electrons were transported through the DNA base pair π -system, regardless of the integrity of the sugar phosphate backbone (8,10). All of these observations suggest that, consistent with DNA acting as a molecular wire, ground state electron transfer through the π -system of the nucleobases occurs at a fast rate with shallow distance dependence. This multiplex chip platform was used for all experiments described in this chapter.

DNA-modified gold electrodes can also be used to study redox-active DNA binding proteins, providing insight into the redox chemistry of the 4Fe-4S cluster in DNA glycosylases and DNA helicases (14-17). These studies have allowed for the determination of both the thermodynamic properties of the redox process occurring at the iron-sulfur cluster, as well as the mechanism of charge transport from the metal center of the protein to the electrode. These experiments revealed that DNA binding shifts the midpoint potential of the iron-sulfur cluster in DNA binding proteins by 200 mV such that the DNA bound potential of the 2+/3+ couple of the 4Fe-4S cluster is 80 mV v. NHE (11-16). Additionally, this technique allowed for the measurement of the electronic coupling between the iron-sulfur cluster of a protein and the DNA to which it is bound (**Figure 3.2**). Using this strategy, proteins

with altered electron transport properties have been found in disease-relevant mutants of both the DNA glycosylase Endonuclease III and the DNA helicase XPD (18,19). Since these mutant proteins had no difference in enzymatic activity or stability, it was concluded that they have a mutation that attenuates the flow of electrons from the DNA attached to the electrode to the 4Fe-4S cluster of the protein. The identification of charge transport deficient mutants has provided insight into potential electron transport mechanisms within these proteins, as well as tools for studying the role of DNA CT in disease.

The final type of experiment that can be done to characterize redox-active proteins on DNA-modified gold electrodes is assaying enzymatic activity at the DNA that modifies the electrode. The prototypical example of this type of experiment was the characterization of the ATPase activity of the DNA helicases

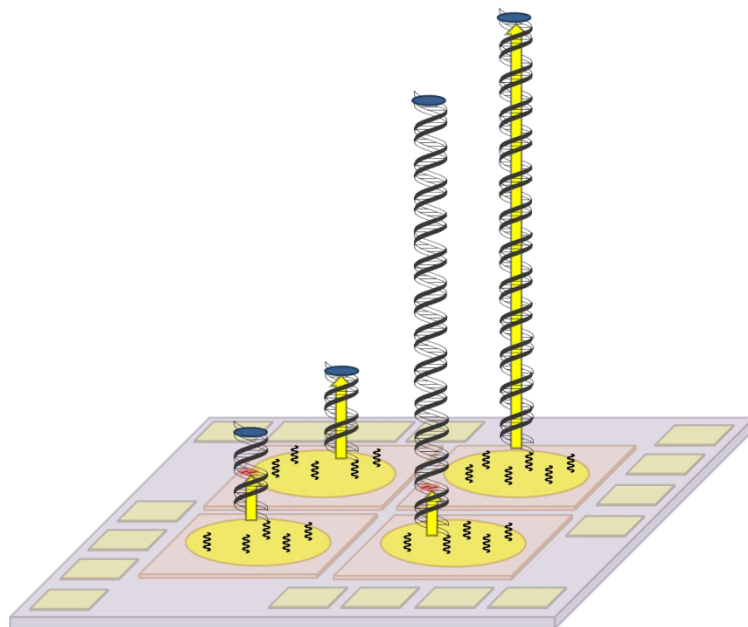


Figure 3.1. DNA Charge Transport on DNA-Modified Gold Electrodes. Schematic of a multiplex chip with four different types of DNA deposited to the four different quadrants of the chip: one hundred nucleotide duplex DNA, one hundred nucleotide duplex DNA with a mismatched DNA base pair, seventeen nucleotide duplex DNA, and seventeen nucleotide duplex DNA with a mismatched DNA base pair. A single mismatched base pair (red) in either DNA duplex attenuates electron transfer (yellow arrow) from the electrode surface to the redox probe that was covalently attached to the DNA.

DinG and XPD (13,16). Specifically, it was observed that the electronic coupling between the DNA and the iron-sulfur cluster in these DNA helicases increases upon ATP hydrolysis. Thus, ATP hydrolysis was proposed to cause a structural change that facilitated electron transfer through the DNA to the 4Fe-4S cluster of the protein. This change in electronic coupling could be directly visualized as a change in signal intensity as measured with cyclic voltammetry, which allowed for the monitoring of DNA helicase ATPase activity at the electrode surface.

In this chapter, the midpoint potential of Dna2 was determined to be 60 ± 20 mV v. NHE on gold electrodes modified with different DNA substrates. Consistent with the observed redox chemistry occurring at the iron-sulfur cluster of Dna2, there was no signal at this potential for the Dna2 C771A mutant. This mutant has defects in 4Fe-4S cluster binding (20). Variation in the amount of charge transported between the iron-sulfur cluster in Dna2 and the electrode on different DNA substrates suggested that the signal at 60 ± 20 mV v. NHE was the midpoint potential of Dna2 bound to DNA. Specifically, the amount of charge that flowed from the electrode to the iron-sulfur cluster bound by Dna2 was significantly less when single stranded DNA (ssDNA) and double stranded DNA (dsDNA) with an abasic site modified the electrode relative to an undamaged dsDNA substrate (2,11).

The redox activity of the iron-sulfur cluster in Dna2 was also assayed under conditions that favored either helicase or nuclease activity. The signal intensity of the cathodic and anodic peak on the cyclic voltammogram of Dna2 increased upon addition of ATP, which activates Dna2 as a helicase. Thus, consistent with observations made on other DNA helicases, electronic coupling between the iron-sulfur cluster in Dna2 and the electrode is enhanced when the protein is acting as a helicase. The addition of magnesium chloride, which activates the nuclease activity of the protein, led to broadening of both the anodic and cathodic peak on the cyclic voltammogram along with a decrease in signal intensity. Therefore, electronic coupling between the iron-sulfur cluster of Dna2 and the electrode is decreased when this protein is active as a nuclease. These experiments suggest

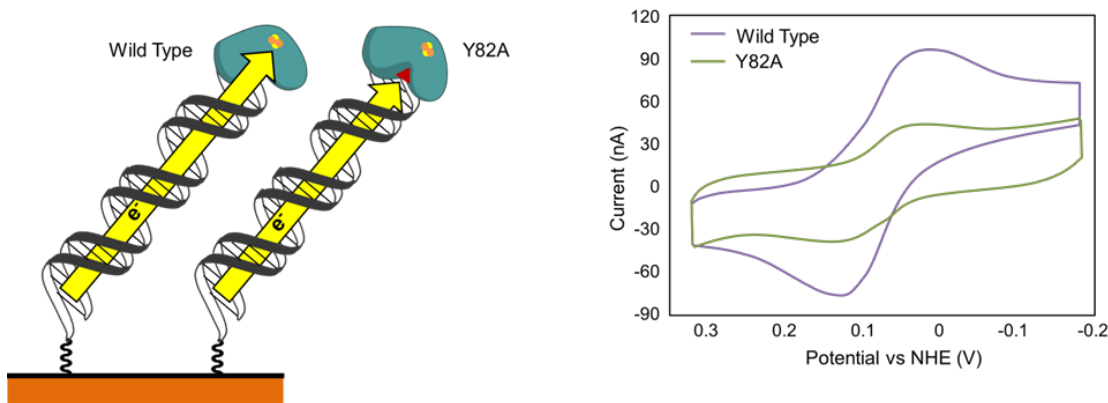


Figure 3.2. Protein Electrochemistry on DNA-Modified Gold Electrodes. DNA-modified gold electrodes are an experimental platform for determining both the midpoint potential of the 4Fe-4S cluster and the efficiency of electron transfer from the DNA to the 4Fe-4S cluster in DNA glycosylases. (Left) On the left is a schematic of electron transfer from the electrode through the DNA to the iron-sulfur cluster in the DNA glycosylase Endonuclease III (EndoIII). On the right, is a schematic of electron transfer through the DNA to the iron-sulfur cluster of EndoIII Y82A, a charge transport deficient mutant of EndoIII. The tyrosine to alanine mutation (red) disrupts electron transfer pathway through the protein without affecting its structure or enzymatic activity. (Right) This decrease in charge transport efficiency can be monitored by standard electrochemical techniques, like cyclic voltammetry.

that Dna2 has a 4Fe-4S cluster that is redox-active when bound to DNA, and that the electronic coupling between the iron-sulfur cluster and the DNA vary with the enzymatic activity of the protein.

Materials and Methods

Wildtype Dna2 and Dna2 C771A Overexpression and Purification. The protein used in the experiments described in this chapter was isolated as described in 'Wildtype Dna2 and Mutant Dna2 Overexpression and Purification' in the methods section of chapter 2 of this thesis.

Oligonucleotide Preparation. All DNA substrates were purchased from IDT DNA (**Table 3.1**). All single stranded DNA was purified with a reverse phase PLRP-S column (Agilent) on an 1100 series HPLC (Agilent). A 50 mM ammonium acetate/acetonitrile gradient was used to purify the DNA. The disulfide DNA was incubated in 80% acetic acid/20% water for 25 minutes at room temperature. Then, the disulfide modified DNA was reduced with 4M DTT in tris buffer (10 mM tris-HCl, pH8.5) at room temperature for 45 minutes. Both the thiol DNA and the unmodified DNA was purified by reverse phase chromatography. All single-stranded DNA was precipitated with ethanol, and suspended in phosphate buffer (5 mM sodium phosphate, 50 mM sodium chloride, pH 7).

The oligonucleotides were characterized with matrix assisted laser desorption ionization time of flight mass spectrometry (Applied Biosystems Voyager DE-PRO MALDI TOF-MS). The absorption spectrum of the purified single stranded DNA was obtained on a Cary UV-visible absorption spectrometer. All spectra were zeroed and baseline corrected with the absorption spectrum of phosphate buffer. The molar concentration of DNA was estimated with the absorption of the DNA at 260 nm and the extinction coefficient of the DNA as predicted by the IDT DNA oligoanalyzer tool. The complementary single-stranded DNA stocks were diluted in phosphate buffer such that the final concentration of each strand was 50 μ M. The DNA solutions were degassed with argon, and annealed by heating to 90 °C followed by cooling to ambient temperature over

Table 3.1. Oligonucleotides for Electrochemistry

Oligonucleotide Name	Oligonucleotide Sequence
HMS2 disulfide	5'- disulfide*-GTGCTGCAACGTGTCTGCGC -3'
HMS2 thiol	5'- thiol-GTGCTGCAACGTGTCTGCGC -3'
HMS2 complement	5'- CAGACGAGAGCGCAGACACGTTGCAGCAC -3'
HMS2 abasic	5'-CAGACGAGAGCGCAGACACGTTGCA(Abasic)CAC -3'

*5ThioMC6-D/ modification from IDT DNA.

ninety minutes. All DNA was annealed immediately prior to use in each electrochemistry experiment.

Multiplex Chip Preparation, Assembly of DNA Self-Assembled Monolayers (SAMs), and Electrochemical Measurements. The multiplex chips were made as described previously by Dr. Catrina Pheeney and Phil Bartels (15). DNA SAMs were assembled on the gold working electrodes of the multiplex chips using previously described procedures (15). Only high density DNA self-assembled monolayers were used for the studies described in this chapter. High density DNA SAMs were formed by addition of 100 mM MgCl₂ to the DNA that was deposited to the gold working electrode. A platinum wire served as the auxiliary electrode. The reference electrode was a solid state Ag/AgCl electrode (Warner Instruments). All measurements were made with a BAS CV50W model electrochemical analyzer. All data was analyzed with Ch Instruments software.

Direct Electrochemistry of Dna2 on DNA-Modified Gold Electrodes. 20 μ M Dna2 was added to gold working electrodes that were modified with either HMS2 ssDNA (HMS2 thiol) or HMS2 dsDNA (HMS2 thiol with HMS2 complement). All DNA strands shown in parenthesis were annealed as described above to form the indicated DNA substrates. The protein was in storage buffer (20 mM sodium phosphate, pH 7.5, 0.5 mM EDTA, 100 mM NaCl, 20 % glycerol). Cyclic voltammograms were acquired between -0.4V to 0.1V v. Ag/AgCl.

Direct Electrochemistry of Dna2 C771A on DNA-Modified Gold Electrodes. 8 μ M Dna2 C771A was added to gold working electrodes that were modified with HMS2 ssDNA (HMS2 thiol), HMS2 dsDNA (HMS2 thiol with HMS2 complement), or HMS2 abasic dsDNA (HMS2 thiol with HMS2 abasic). All DNA strands shown in parenthesis were annealed as described above to form the indicated DNA substrate. The protein assayed was stored in gel filtration buffer (20 mM trizma-HCl, pH 8, 0.1 mM EDTA, 200 mM NaCl, 2 mM DTT). This Dna2 mutant was

prone to aggregation during purification on the Superdex200 size exclusion column. The major peak, which corresponded to the first Dna2 fraction that eluted from the column, was assayed in this experiment. Cyclic voltammograms were acquired between -0.4V to 0.1V v. Ag/AgCl at the following time points following Dna2 addition to the electrode surface: 0 hours, 1 hour, 3 hours, 7 hours, and 19 hours.

Direct Electrochemistry of Dna2 in Nuclease Assay Buffer on DNA-Modified Gold Electrodes. In this experiment, 8 μ M Dna2 was added to two identical gold working electrodes that were modified with HMS2 well-matched duplex (HMS2 thiol with HMS2 duplex. The protein was stored in gel filtration buffer (20 mM trizma-HCl, pH 8, 0.1 mM EDTA, 200 mM NaCl, 2 mM DTT). 2 mM MgCl₂ in gel filtration buffer was added to one of the multiplex chips to stimulate nuclease activity. Cyclic voltammograms were acquired between -0.4V to 0.1V v. Ag/AgCl at the following time points following Dna2 addition to the electrode surface: 0 hours, 3 hours, 18.5 hours, and 24 hours.

Direct Electrochemistry of Dna2 in ATPase Assay Buffer on DNA-Modified Gold Electrodes. In this experiment, 20 μ M Dna2 was added to two identical gold working electrodes that were modified with HMS2 well-matched duplex (HMS2 thiol with HMS2 duplex). The protein was stored in gel filtration buffer (20 mM trizma-HCl, pH 8, 0.1 mM EDTA, 200 mM NaCl, 2 mM DTT). 4 mM ATP and 2 mM MgCl₂ was added to one of the multiplex chips. Cyclic voltammograms were acquired between -0.4V to 0.1V v. Ag/AgCl at the following time points after Dna2 addition to the electrode surface: 0 hours, 1 hour, 2 hours, 3 hours, and 6 hours.

Results

Cyclic voltammetry of Dna2 on DNA-modified Gold Electrodes. The redox activity of Dna2 was monitored by cyclic voltammetry on gold working electrodes modified with a variety of DNA substrates. Using this technique, the midpoint potential of the

protein was determined to be 60 ± 20 mV v. NHE (**Figure 3.3**). The signal intensity was proportional to the square root of the scan rate, which suggested that the observed redox process was diffusion-limited (21). Since this redox process was diffusion-limited under all conditions assayed, the electron transfer rate could not be estimated using the Laviron method (22).

The mechanism of electron transfer for the observed redox process was investigated by studying electron transfer to the iron-sulfur cluster of Dna2 on gold electrodes modified with different DNA substrates. These experiments were performed to determine whether the redox process observed was due to electron transfer from the gold working electrode through the DNA to the iron-sulfur cluster of the protein. The DNA substrates that were used in these experiments included a 5'-tail DNA substrate that contained a nine nucleotide overhang and a twenty nucleotide duplex region (HMS2 dsDNA), a twenty nucleotide single stranded DNA substrate (HMS2 ssDNA), and a 5'-tail DNA substrate that contained a nine nucleotide overhang and a twenty nucleotide duplex region with an abasic site three base pairs from the site of DNA attachment to the gold electrode (HMS2 abasic dsDNA).

DNA-mediated charge transport cannot occur in single stranded DNA, so the signal intensity on this substrate should be much less than the signal intensity on dsDNA. DNA Charge transport to the iron-sulfur cluster of Dna2 should also be attenuated by structural perturbation in the DNA that results from the presence of a DNA lesion such as an abasic site (11,15). Thus, if the process observed by cyclic voltammetry is a DNA-mediated process, the amount of charge that transfers from the electrode through the DNA to the protein should be attenuated in the electrodes modified with ssDNA or dsDNA abasic. This result would manifest itself as a decrease in the signal intensity of the cathodic and anodic peaks on the cyclic voltammogram (**Figure 3.4**).

In addition to variation in DNA substrates, different types of self-assembled DNA monolayers can also be assembled by changing the conditions under which the DNA monolayers are formed by the addition of magnesium chloride. Previous

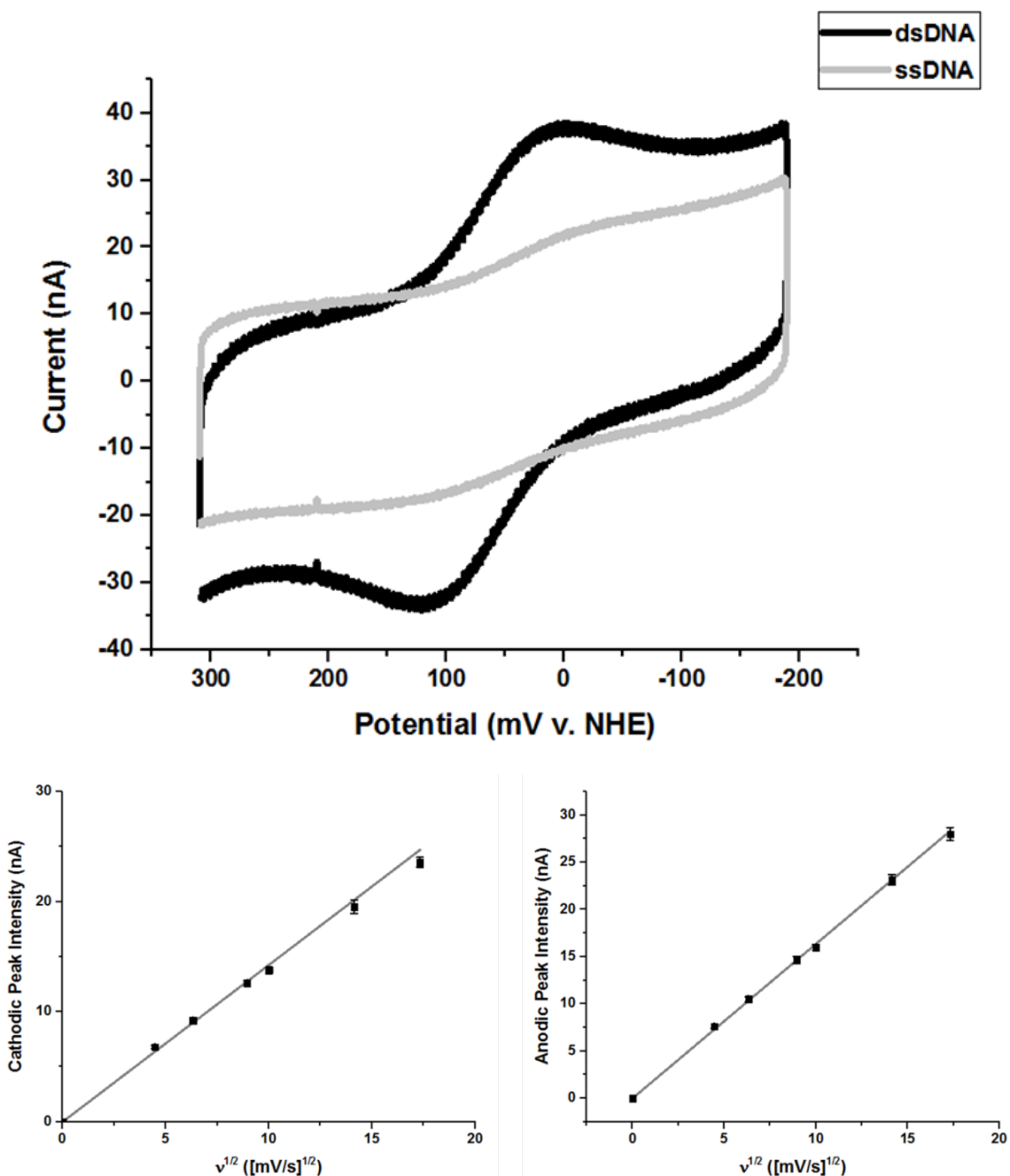


Figure 3.3. Dna2 on DNA-Modified Gold Electrodes. (Top) Cyclic voltammograms of Dna2 on DNA-modified gold electrodes acquired at a scan rate of 100 mV/s after seven hours of incubation of Dna2 on the electrode surface. The black trace is a cyclic voltammogram of Dna2 on HMS2 dsDNA. The gray trace is a cyclic voltammogram of Dna2 on HMS2 ssDNA. (Bottom) Scan Rate dependence of the signal intensity of Dna2 on gold electrode modified with HMS2 dsDNA for the cathodic (Left) and anodic (Right) peaks.

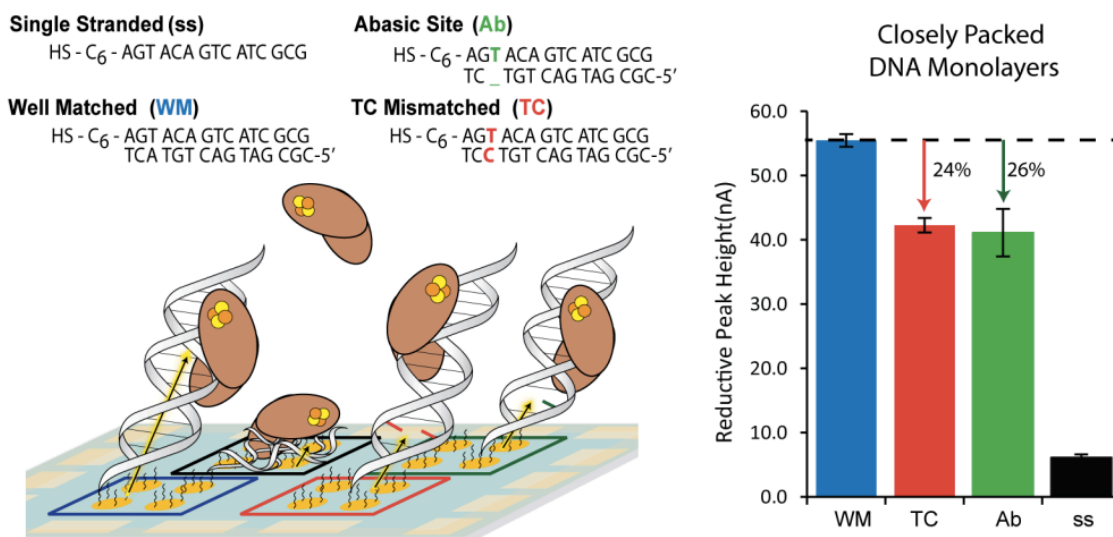


Figure 3.4. DNA-Mediated Electrochemistry of DNA Binding Proteins. The amount of current that flows from the working electrode to the 4Fe-4S cluster of the protein can be quantified on electrodes modified with a variety of DNA substrates. The maximum amount of current is observed with well-matched duplex DNA substrates (blue). When a mismatch (red) or abasic site (green) is placed at the base of the DNA duplex, the amount of current is less than for the well-matched DNA substrate. On single stranded DNA (black), which is not capable of mediating DNA charge transport, the smallest amount of current is observed. Figure 4 from Reference 15.

experiments suggested that the use of high density DNA monolayers can decrease the amount of direct surface electron transfer to the 4Fe-4S cluster of proteins, and thus increase the amount of protein oxidized by a DNA-mediated mechanism (15). Since direct electron transfer from the electrode through the DNA to the iron-sulfur cluster of DNA binding proteins is predominantly observed on high density self-assembled DNA monolayers, all experiments herein described were performed on DNA-modified gold electrodes prepared under conditions that formed this type of DNA film.

The midpoint potential of Dna2 on all of the DNA substrate was 60 ± 20 mV v. NHE. As predicted, the absolute magnitude of the signal intensity observed by cyclic voltammetry varied depending on the DNA substrate or type of DNA monolayer on the electrode surface. The signal intensity was consistently larger for the protein on the gold electrode with dsDNA rather than ssDNA (Figure 3.3). The

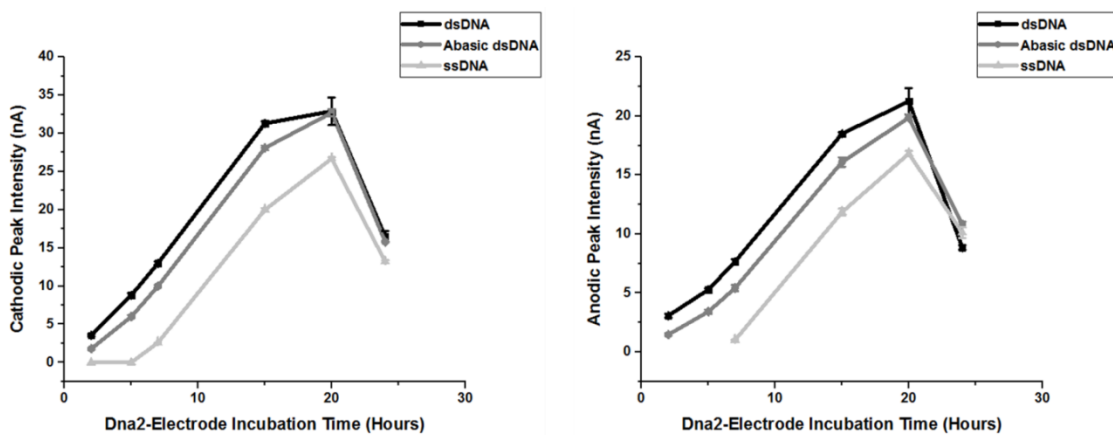


Figure 3.5. Signal Intensity Over Time. Signal intensity over time of Dna2 on DNA-Modified gold electrodes. Each value is an average of the data from four separate electrodes. The error was reported as standard error. (Left) Cathodic peak intensity over time. (Right) Anodic peak intensity over time. The DNA substrate that modified the gold electrode is indicated in the legend (dsDNA = HMS2 dsDNA, Abasic dsDNA = HMS2 abasic dsDNA, ssDNA = HMS2 ssDNA).

signal intensity of HMS2 abasic dsDNA was smaller than the signal intensity of HMS2 dsDNA up to fifteen hours following addition of Dna2 to the surface of the electrode (**Figure 3.5**). Notably, on all DNA substrates, the signal intensity increased over the course of twenty-four hours. After about twenty-four hours, the signal intensity started to decrease (**Figure 3.5**). The time dependence of the signal intensity is consistent with previous observations of the redox chemistry of DNA binding proteins on DNA-modified gold electrodes (15).

Cyclic Voltammetry of Dna2 C771A on DNA-Modified Gold Electrodes. The Dna2 C771A mutant, which contained a cysteine to alanine mutation at one of the cysteine residues that ligates the 4Fe-4S cluster in Dna2, was added to a DNA-modified gold electrode modified with HMS2 dsDNA (20). This experiment was done to determine whether the 4Fe-4S cluster in Dna2 was associated with the signal at 60 ± 20 mV v. NHE. A small signal with a midpoint potential of 80 mV v. NHE could be observed for the protein at nineteen hours following addition of Dna2 C771A to the working electrode; however, this signal was less than 2 nA.

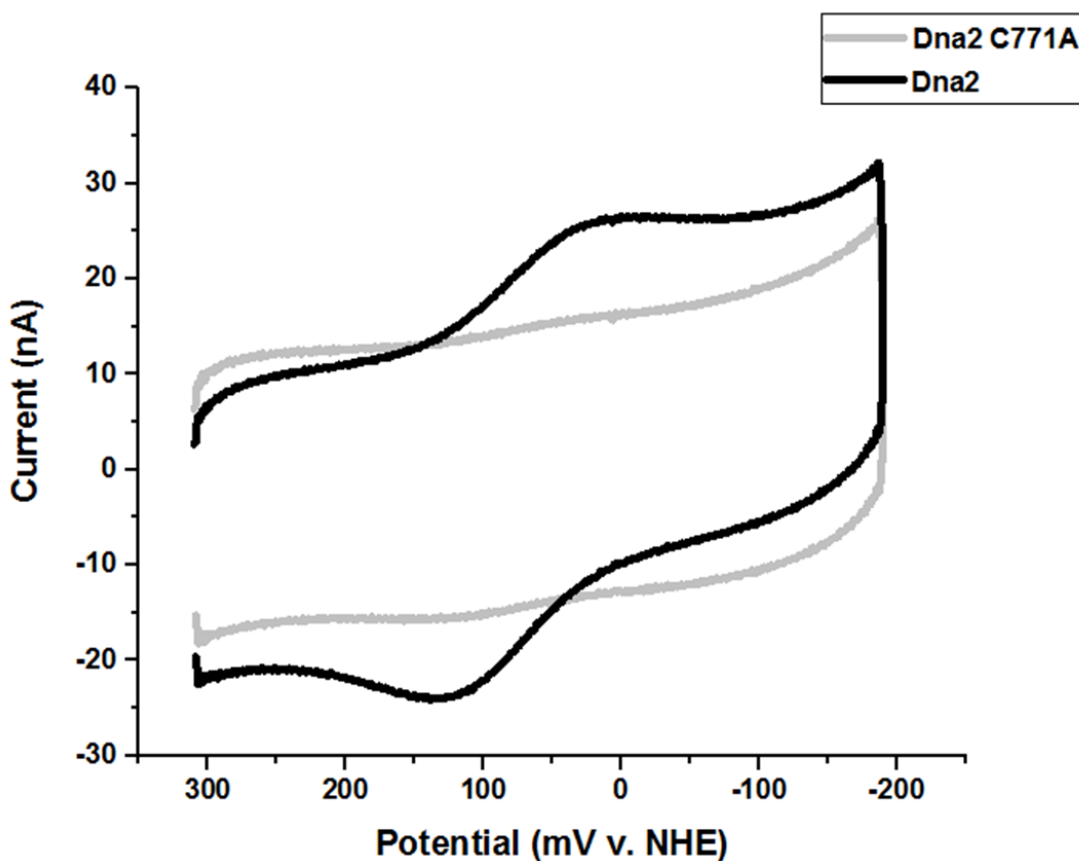


Figure 3.6. Dna2 and Dna2 C771A on DNA-Modified Gold Electrodes. Cyclic voltammogram acquired at a scan rate of 100 mV/s after seven hour incubation of the protein on the electrode surface.

To confirm that the electrode surface was intact, wild type Dna2 protein was added to the chip at the same concentration as the mutant protein. The signal intensity that was observed for wild type Dna2 was significantly larger than that observed for the Dna2 C771A mutant as measured by cyclic voltammetry (**Figure 3.6**). This experiment suggested that redox activity at the iron cofactor in Dna2 was being monitored on the DNA-modified gold electrodes.

Cyclic voltammetry of Dna2 in Nuclease Assay Buffer on DNA-Modified Gold Electrodes. The electronic coupling between the iron-sulfur cluster of Dna2 and the DNA that modified the gold electrode was investigated under conditions that

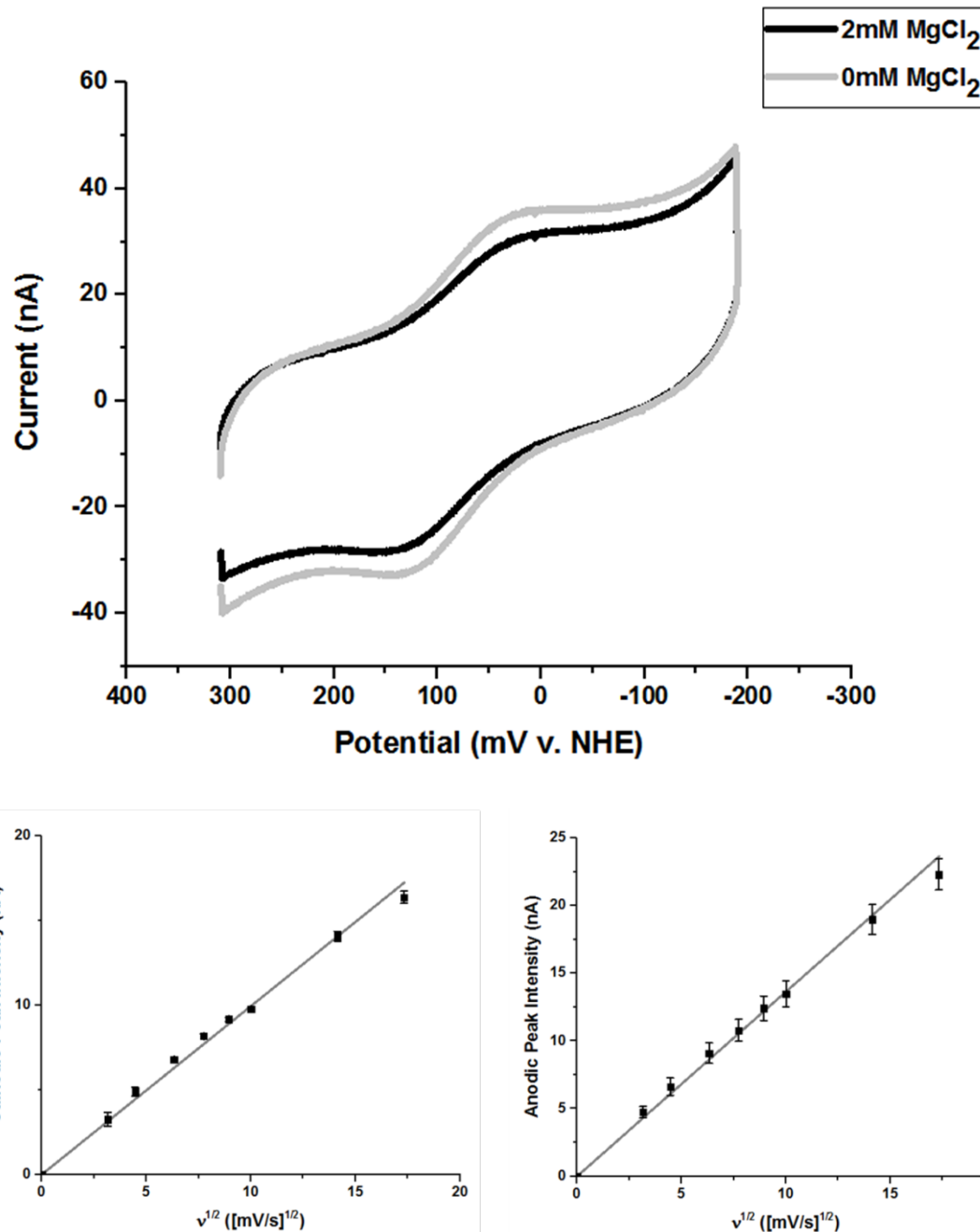


Figure 3.7. Dna2 in Nuclease Assay Buffer. (Top) All cyclic voltammograms are the average of data acquired at 100 mV/s from eight different electrodes. The black trace is the average of cyclic voltammograms acquired in nuclease assay buffer that contains 2 mM MgCl₂. The gray trace is the average of cyclic voltammograms acquired in gel filtration buffer with 0 mM MgCl₂. (Bottom) Scan Rate dependence of the signal intensity of the cathodic (Left) and anodic (Right) peaks of Dna2 on gold electrode modified with HMS2 dsDNA in nuclease assay buffer.

favored Dna2 nuclease activity. The signal intensity as measured with cyclic voltammetry reports on the current that passes from the electrode to a redox-active species. Therefore, a larger signal is synonymous with better electronic coupling between the iron-sulfur cluster and the electrode via the DNA. Conversely, a smaller signal indicates poor electronic coupling between the iron-sulfur cluster and the electrode. Since the observed redox process is DNA-mediated, and thus the current that passes from the electrode to the redox active species occurs via the DNA, the signal intensity as measured by cyclic voltammetry also reports on the electronic coupling between the iron cofactor and the DNA.

Dna2 is active as a nuclease only when magnesium chloride is present in the assay buffer. Additionally, Dna2 is active as a nuclease on DNA substrates that contain a 5'-ssDNA overhang, like the 5'-tail DNA substrate used in the previous experiments (HMS2 dsDNA) (23). Thus, two multiplex chips were modified with the HMS dsDNA substrate, and Dna2 was added to both chips. 2 mM magnesium chloride was added to one chip to activate Dna2 nuclease activity, and the cyclic voltammograms of Dna2 on the two chips were compared to evaluate the redox chemistry of Dna2 when active as a nuclease. This experiment provided two insights into the redox process occurring under these conditions (**Figure 3.7**). First, the magnitude of the signal intensity of Dna2 in the presence of 2 mM MgCl₂ on the gold working electrode was smaller than that of the protein without MgCl₂ in the buffer. Second, the kinetics of the redox process observed under both conditions was diffusion limited. These results suggest that although the kinetics of the redox process are the same under both conditions assayed, activation of the nuclease activity leads to a decrease in electronic coupling between Dna2 and the electrode.

Cyclic voltammetry of Dna2 in ATPase Assay Buffer on DNA-Modified Gold Electrodes. To determine the extent of electronic coupling between the iron-sulfur cluster in Dna2 and the DNA when Dna2 was active as a helicase, two multiplex chips were modified with the HMS2 dsDNA substrate and side-by-side comparison was made of the redox process occurring on the two chips upon

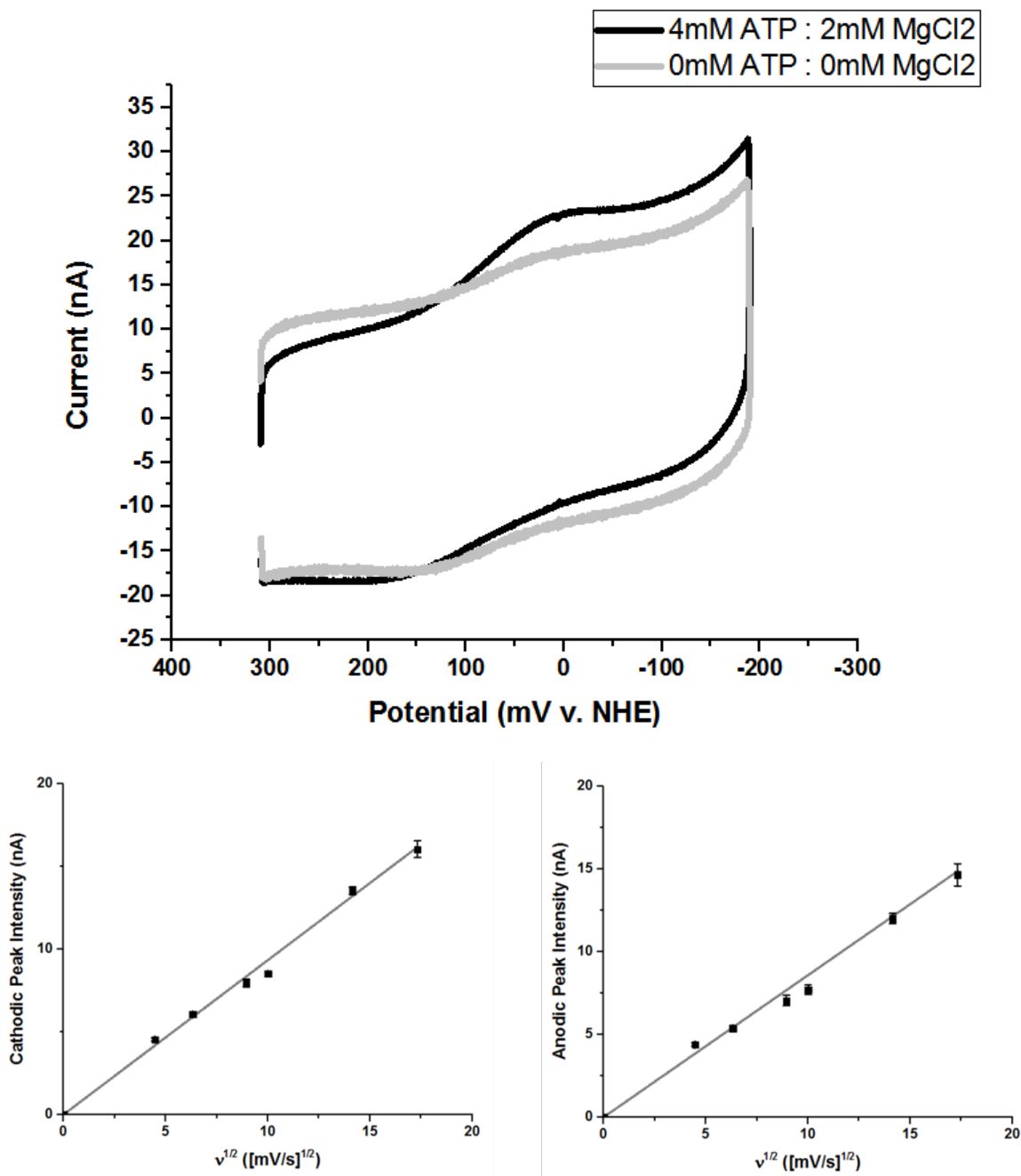


Figure 3.8. Dna2 in Helicase Assay Buffer. (Top) All cyclic voltammograms are the average of data acquired at 100 mV/s from eight different electrodes. The black trace is the cyclic voltammogram acquired in helicase assay buffer that contains 4mM ATP : 2mM MgCl₂. The gray trace is the cyclic voltammogram acquired in gel filtration buffer. (Bottom) Scan Rate dependence of the signal intensity of the cathodic (Left) and anodic (Right) peaks of Dna2 on gold electrode modified with HMS2 dsDNA in helicase assay buffer.

addition of Dna2 and ATP. 4 mM ATP and 2 mM magnesium chloride were added to one of the multiplex chips to activate Dna2 helicase activity while inhibiting nuclease activity (23). Notably, the DNA-dependent ATPase activity was assayed under these buffer conditions with the HMS2 dsDNA substrate in solution to confirm that Dna2 did bind DNA under these assay conditions (data not shown).

The addition of ATP led to an increase in signal intensity and broadening of the cathodic peak on the cyclic voltammogram of Dna2 (**Figure 3.8**). ATP addition also increased the peak splitting on the cyclic voltammogram. The anodic peak intensity did not immediately increase as rapidly as the cathodic peak intensity; however, over time the anodic peak intensity increased such that it was about equal in size to the cathodic peak intensity. Thus, although the signal intensity increased upon activation of the helicase activity of the protein, the redox process occurring at the electrode was less reversible than the same redox process in the absence of ATP. Consistent with the other experiments performed in this study, the redox process observed in the presence of ATP was diffusion limited. These

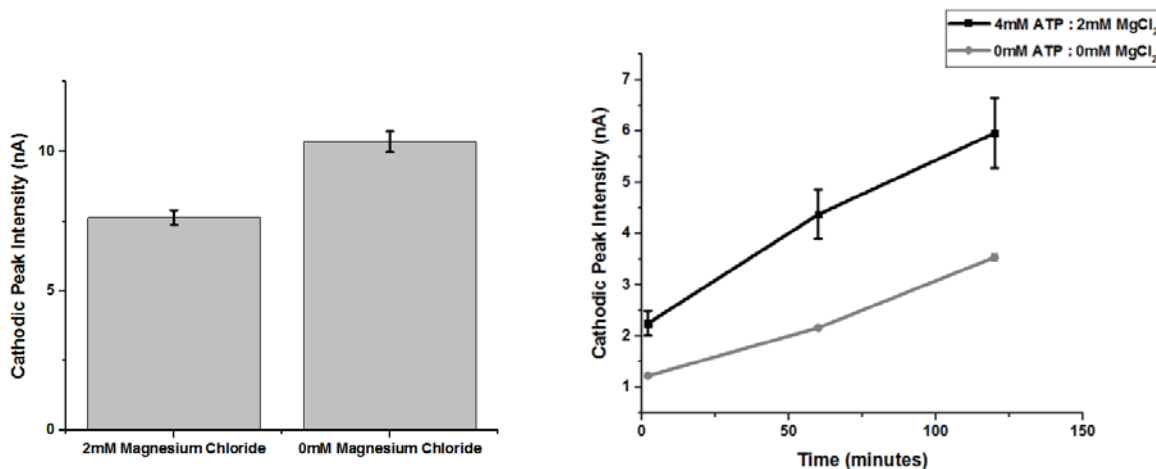


Figure 3.9. Electronic Coupling Between the Iron-Sulfur Cluster of Dna2 and the DNA on Gold Electrodes. (Left) The cathodic peak intensity of Dna2 under nuclease conditions after 18.5 hours of incubation on the electrode surface. Each bar represents the average data from seven electrodes. (Right) The cathodic peak intensity of Dna2 under Dna2 helicase assay conditions. Each point represents the average of data from eight different electrodes. All cyclic voltammograms were acquired at a scan rate of 100 mV/s.

observations are consistent with the results obtained with the helicases DinG and XPD, that ATP hydrolysis facilitates electronic coupling with the DNA (13,16).

Conclusion

Dna2, a eukaryotic helicase-nuclease that binds an iron-sulfur cluster, was studied on DNA-modified gold electrodes to better characterize the redox properties of the metal center in this enzyme. Cyclic voltammetry of Dna2 on DNA-modified gold electrodes revealed that the iron-sulfur cluster in this protein has a midpoint potential of 60 ± 20 mV v. NHE. Analysis of the Dna2 C771A mutant on the DNA-modified electrodes showed that the redox couple observed by cyclic voltammetry for wild type Dna2 was occurring at the iron cofactor. Furthermore, the redox activity of the iron-sulfur cluster in Dna2 was assayed under conditions that should activate either the helicase or the nuclease activity of this protein (**Figure 3.9**). The nuclease activity of Dna2 was activated by addition of $MgCl_2$ to the reaction, which led to an overall decrease in electronic coupling between the DNA and the iron-sulfur cluster. Conversely, addition of ATP to the reaction, which stimulates helicase activity and inhibits nuclease activity, led to an increase in electronic coupling between the DNA and the iron-sulfur cluster.

The electrochemical results presented in this chapter are consistent with recent structural studies of mouse Dna2, a homolog of *S. cerevisiae* Dna2. These studies revealed that the iron-sulfur cluster in Dna2 is positioned near the site of DNA binding in the nuclease domain (24). Thus, the stabilization of the 3+ oxidation state through electrostatic interaction with the DNA could lead to a large shift in midpoint potential of the 2+/3+ couple of the 4Fe-4S cluster. Additionally, the structure revealed that the β -barrel domain in Dna2 could serve as a hinge that mediates the interaction between the helicase and the nuclease domains where the iron-sulfur cluster is located (**Figure 2.2**). This observation provides insight into how ATP hydrolysis, which occurs at a different domain of Dna2, could regulate electronic coupling between the iron-sulfur cluster and the DNA. In combination,

the electrochemical and structural studies of Dna2 provide support for a mechanism in which Dna2 can participate in DNA-mediated redox chemistry while active as a DNA helicase.

References

1. Kelley, S. O., Barton, J. K., Jackson, N., and Hill, M. G. (1997) Electrochemistry of Methylene Blue Bound to a DNA-Modified Electrode. *Bioconjugate Chemistry*. 8, 31-37.
2. Kelley, S. O., Jackson, N. M., Hill, M. G., and Barton, J. K. (1999) Long Range Electron Transfer Through DNA Films. *Agnew Chem Int Ed Eng*. 38, 941-945.
3. Kelley, S. O., Barton, J. K., Jackson, N. M., McPherson, L. D., Potter, A. B., Spain, E. M., Allen, M. J., and Hill, M. G. (1998) Orienting DNA Helices on Gold Using Applied Electric Fields. *Langmuir*.14, 6781-6784.
4. Kelley, S. O., Boon, E. M., Barton, J. K., Jackson, N. M., and Hill, M. G. (1999) Single-Base Mismatch Detection Based on Charge Transduction Through DNA. *Nucleic Acids Res*. 27, 4830-4837.
5. Pheeney, C. G. and Barton, J. K. (2013) Intraduplex DNA-Mediated Electrochemistry of Covalently Tethered Redox-Active Reporters. *J Am Chem Soc*. 135, 14944-14947.
6. Pheeney, C. G. and Barton, J. K. (2012) DNA Electrochemistry with Tethered Methylene Blue. *Langmuir*. 28, 7063-7070.
7. Slinker, J. D., Muren, N. B., Gorodetsky, A. A., and Barton, J. K. (2010) Multiplexed DNA-Modified Electrodes. *J Am Chem Soc*. 132, 2769-2774.
8. Slinker, J. D., Muren, N. B., Renfrew, S. E., and Barton, J. K. (2011) DNA Charge Transport Over 34 nm. *Nat Chem*. 3, 230-235.
9. Drummond, T. G., Hill, M. G., and Barton, J. K. (2004) Electron Transfer Rates in DNA Films as a Function of Tether Length. *J Am Chem Soc*. 126, 15010-15011.
- .
10. Liu, T. and Barton, J. K. (2005) DNA Electrochemistry Through the Base Pairs Not the Sugar-Phosphate Backbone. *J Am Chem Soc*. 127, 10160-10161.

11. Boal, A. K., Yavin, E., Lukianova, O. A., O'Shea, V. L., David, S. S., and Barton, J. K. (2005) DNA-Bound Redox Activity of DNA Repair Glycosylases Containing [4Fe-4S] Clusters. *Biochem.* 44, 8397-8407.
12. Romano, C. A.*, Sontz, P. A.* and Barton, J. K. (2011) Mutants of the Base Excision Repair Glycosylase, Endonuclease III: DNA Charge Transport as a First Step in Lesion Detection. *Biochem.* 50, 6133-6145.
13. Mui, T. P., Fuss, J. O., Ishida, J. P., Tainer, J. A., and Barton, J. K. (2011) ATP-Stimulated, DNA-Mediated Redox Signaling by XPD, a DNA Repair and Transcription Helicase. *J Am Chem Soc.* 133, 16378-16381.
14. Gorodetsky, A. A., Boal, A. K., and Barton, J. K. (2006) Direct Electrochemistry of Endonuclease III in the Presence and Absence of DNA. *J Am Chem Soc.* 128, 12082-12083.
15. Pheeney, C. G., Arnod, A. R., Grodick, M. A., and Barton, J. K. (2013) Multiplexed Electrochemistry of DNA-Bound Metalloproteins. *J Am Chem Soc.* 135, 11869-11878.
16. Grodick, M. A., Segal, H. M., Zwang, T. J., and Barton, J. K. (2014) DNA-Mediated Signaling by Proteins with 4Fe-4S Clusters Is Necessary for Genomic Integrity. *J Am Chem Soc.* 136, 6470-6478.
17. Genereux, J. C., Boal, A. K., and Barton, J. K. (2010) DNA-Mediated Charge Transport in Redox Sensing and Signaling. *J Am Chem Soc.* 132, 891-905.
18. Boal, A. K., *et al.* (2009) Redox Signaling Between DNA Repair Proteins for Efficient Lesion Detection. *Proc Natl Acad Sci USA.* 106, 15237-15242.
19. Sontz, P. A., Mui, T. P., Fuss, J. O., Tainer, J. A., and Barton, J. K. (2012) DNA Charge Transport as a First Step in Coordinating the Detection of Lesions by Repair Proteins. *Proc Natl Acad Sci USA.* 109, 1856-1861.
20. Pokharel, S. and Campbell, J. L. (2012) Cross Talk Between the Nuclease and Helicase Activities of Dna2: Role of an Essential Iron-Sulfur Cluster Domain. *Nucleic Acids Res.* 40, 7821-7830.
21. Bard, A. J. and Faulkner, L. R. *Electrochemical Methods – Fundamental and Application*, 2nd ed.; Joh Wiley & Sons: New York, 2000; pp.580-631.

22. Laviron, E. (1979) General Expression of the Linear Potential Sweep Voltammogram in the Case of Diffusionless Electrochemical Systems. *J Electroanal Chem and Interfacial Electrochem.* 101, 19-28.
23. Budd, M. E. and Campbell, J. L. (1995) A Yeast Gene Required for DNA Replication Encodes a Protein with Homology to DNA Helicases. *Proc Natl Acad Sci USA.* 92, 7642-7646.
24. Zhou, C. Pourmal, S., and Pavletich, N. P. (2015) Dna2 Nuclease-Helicase Structure, Mechanism and Regulation by Rpa. *eLIFE.* 4, e09832.

ELECTROCHEMICAL ASSAY TO DETECT DNA2 NUCLEASE ACTIVITY

Abstract

Dna2 is a helicase-nuclease that prevents genomic instability through its multifunctional roles in DNA replication and recombinational repair. Either aberrant Dna2 expression or inactivating mutations in the gene that encodes Dna2 can lead to the development of human diseases, such as cancer. Thus, an assay to effectively detect the activity of this protein could prove to be an important diagnostic tool. Herein a novel electrochemical assay is described for the detection of Dna2 nuclease activity on a gold electrode modified with different DNA substrates. This assay could reliably detect nanomolar differences in Dna2 concentrations. Additionally, nuclease activity could be detected for wild type Dna2, but not for the nuclease-deficient E675A mutant, highlighting the specificity of this assay. The system was further validated by testing Dna2 nuclease activity on a variety of 5'-tail DNA substrates with different 5'-tail overhang lengths. This assay provides a faster alternative to more traditional radioactivity-based Dna2 nuclease activity assays, and constitutes the first Dna2 nuclease activity assay that does not rely on radioactivity. The simplicity, efficiency, and low cost of this assay will make it an appropriate alternative for both research and diagnostic applications aimed at monitoring Dna2 nuclease activity.

Introduction

Dna2 is a helicase-nuclease that is evolutionarily conserved in eukaryotes. This protein has multiple roles in the cell, including Okazaki fragment maturation,

recombinational repair, mitochondrial genome maintenance, and telomere maintenance (1-4). This protein is composed of a RecB-like nuclease domain that has dual DNA nuclease activity (5' to 3' and 3' to 5') and a SF1B helicase domain that has 5' to 3' DNA helicase activity (5,6).

In human cells, aberrant Dna2 activity has been implicated in the development of disease since its nuclease activity helps repair double strand breaks that result from either oncogenic or chemical stress, thereby alleviating cellular stresses that would otherwise cause senescence (7). Therefore, overexpression of Dna2 in cells that contain activated oncogenes could increase cell proliferation, resulting in the neoplastic progression of tumors. Consistent with this hypothesis, Dna2 expression is significantly increased in some human cancers, such as breast and pancreatic cancer. In these contexts, Dna2 expression levels were inversely correlated with patient survival. Conversely, Dna2 deficiency resulted in cellular senescence (7). Together these findings suggest that Dna2 enzymatic activity could be an important biomarker of cancer. In addition to its role in cancer progression, mutations in Dna2 that inactivate nuclease activity contribute to the development of genetic disorders that lead to progressive myopathies and Seckel syndrome (8,9).

The role of Dna2 in disease development and progression make this protein a potential biomarker of disease, so strategies for detecting Dna2 nuclease activity out of complex patient samples could serve as a useful diagnostic tool. Additionally, the role of Dna2 nuclease activity in cancer progression makes it a potential chemotherapeutic target, requiring a high throughput way to screen potential nuclease inhibitors. Despite the need for methodologies that can be easily multiplexed to develop the aforementioned technologies, there is currently only one known method for monitoring Dna2 nuclease activity *in vitro*. This approach requires radioactive isotope labeling of DNA along with sequencing gel analysis of DNA fragments, which makes the full assay both time consuming and expensive. An electrochemical nuclease activity assay for Dna2 would provide a more economical and higher throughput alternative to the radioactivity-based

method. Herein, we develop the first example of an alternative Dna2 nuclease activity assay, and demonstrate its ability to rapidly detect Dna2 nuclease activity on a multiplexed gold electrode platform.

In this assay, Dna2 nuclease activity was detected on DNA-modified gold electrodes (**Figure 4.1**). Dna2 DNA substrates were modified with methylene blue at the 5'-ssDNA overhang of a 5'-tail DNA substrate. Methylene blue is a redox active dye, so the total concentration of methylene blue modified DNA attached to the electrode surface can be monitored by cyclic voltammetry. Dna2 can cleave DNA at the ssDNA-dsDNA junction of a 5'-tail DNA substrate to liberate methylene

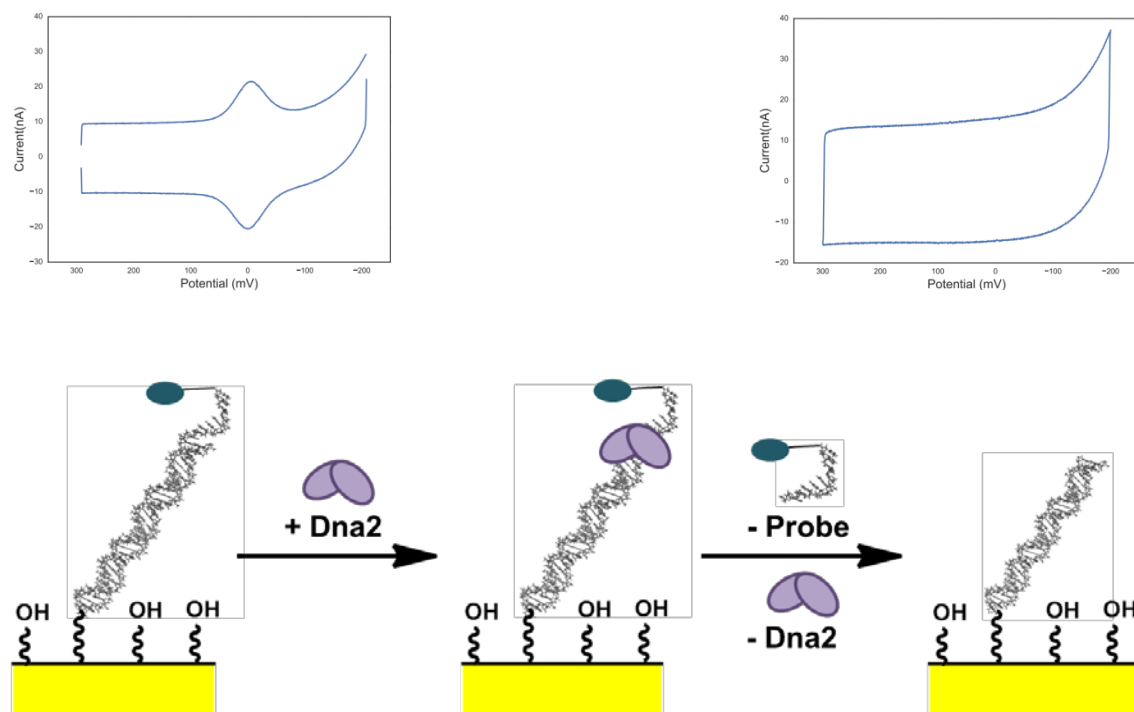


Figure 4.1. Electrochemical Dna2 Nuclease Assay. Prior to Dna2 addition to the electrode surface, methylene blue-modified DNA is covalently attached to the working electrode surface, and the presence of methylene blue can be detected by cyclic voltammetry (left). Dna2 is then added to the surface of the electrode at which point it will bind and cleave the DNA at the ssDNA-dsDNA junction. This reaction should liberate the portion of the DNA substrate that contains methylene blue such that it can be washed away from the surface of the electrode. If Dna2 is active as a nuclease on the DNA that is covalently attached to the electrode surface, then all of the methylene blue should be removed from the DNA bound to the electrode. Thus, methylene blue should no longer be detected by cyclic voltammetry (right).

blue from the electrode such that it could be washed away. Thus, active Dna2 causes a decrease in the redox signal for methylene blue on the electrode surface following strand cleavage. This assay was validated using a nuclease deficient form of Dna2, Dna2 E675A. The sensitivity of the electrochemical nuclease assay was further assessed by comparing Dna2 activity on different DNA substrates. Consistent with results obtained with established radioactivity-based nuclease activity assays, Dna2 had maximum activity on DNA substrates with 5'-overhangs (10). Together, these studies demonstrate that a robust and fast Dna2 nuclease activity assay was developed, which could be used in place of the traditional radioactivity-based assay for the detection of Dna2 nuclease activity.

Materials and Methods

DNA Synthesis and Purification. All oligonucleotides were purchased from IDT DNA. The sequences for these oligonucleotides are shown in **Table A2.1**. Prior to use, all DNA substrates were purified by reverse phase chromatography. A PLRP-S column (Agilent) was used as the hydrophobic stationary phase. The DNA was loaded to the column in 50 mM ammonium acetate, and DNA was eluted from the column with a gradient of acetonitrile that increased to 15 % acetonitrile / 85 % 50 mM ammonium acetate over forty minutes. The DNA samples were desalted by ethanol precipitation. The purified DNA substrates were either stored in phosphate buffer (5 mM sodium phosphate, pH 7, 50 mM NaCl) or were further modified by reaction of the amine-modified DNA with methylene blue or by reduction of disulfide DNA with dithiothreitol (RPI Corp). Carboxylic acid-modified methylene blue was covalently attached to the 5'-amino-modified DNA substrate and purified according to previously described procedures (11,12). The DNA was desalted by ethanol precipitation, and was stored in phosphate buffer.

The 5'-tail disulfide DNA was reduced with dithiothreitol dissolved in buffer EB (Qiagen). Following reduction, the DNA was purified on a Nap5 size exclusion column; the DNA was eluted from the column with phosphate buffer. The reduced

5'-tail disulfide DNA (referred to as 5'-tail thiol DNA) was purified by reverse phase chromatography. A PLRP-S column (Agilent) was used as the hydrophobic stationary phase. The DNA was loaded to the column in 50 mM ammonium acetate, and DNA was eluted from the column with a gradient of acetonitrile that increased to 15 % acetonitrile / 85% 50 mM ammonium acetate over the course of forty minutes. The DNA samples were desalted by ethanol precipitation. The DNA substrates were dissolved in phosphate buffer. The 5'-tail thiol DNA substrate was degassed with argon prior to storage at -20 °C. All 5'-tail thiol DNA was used within three weeks of disulfide bond reduction.

The DNA substrates were all analyzed with matrix-assisted laser desorption/ionization time of flight (MALDI-TOF) mass spectrometry to confirm that all DNA substrates had the correct mass. The final concentration of each DNA substrate was determined by UV-visible absorption spectroscopy. The extinction coefficients used to calculate the final DNA concentration were calculated with the IDT DNA Oligoanalyzer tool. These extinction coefficients are outlined in **Table A2.1**. The extinction coefficient for the 5'-tail overhang DNA with methylene blue was calculated by adding the extinction coefficient of the DNA substrate at 260 nm to the extinction coefficient of the methylene blue derivative at 260 nm (10, 300 M⁻¹cm⁻¹; 11).

The annealed DNA substrates were made by combining equimolar (50 µM) amounts of each DNA substrate as indicated in **Table A2.2**. The volume of the DNA solution was 100 µL, and this solution was degassed with argon prior to annealing the DNA on the thermal cycler. The DNA was annealed by heating the solution to 95 °C followed by cooling of the solution to 4 °C over the course of 1.5 hours. The annealed DNA was immediately deposited on the working electrode for each experiment.

Wildtype Dna2 and Dna2 E675A Overexpression and Purification. The protein used in the experiments described in this chapter was isolated as described in

'Wildtype Dna2 and Mutant Dna2 Overexpression and Purification' in the methods section of chapter 2 of this thesis.

Solution Dna2 Nuclease Assay with Methylene Blue Modified DNA. The DNA substrate for radiolabeling was annealed by combining equimolar amounts of the following DNA substrates: 50 μ M 5'-tail overhang with methylene blue and 50 μ M 5'-tail complement for TT labeling. The volume of the DNA solution was 100 μ L. This solution was degassed with argon prior to annealing by heating to 95 °C followed by cooling to 4 °C over the course of 1.5 hours.

The DNA substrate was radiolabeled at the 3'-end of both strands with terminal transferase as follows: 10 μ L of 50 μ M 5'-tail methylene blue DNA, 5 μ L of 10x terminal transferase buffer (NEB), 5 μ L of 2.5 mM CoCl₂, 5 μ L of dATP (α -³²P) (Perkin Elmer), 2 μ L of terminal transferase (20,000 U/mL – NEB), and 23 μ L deionized water. The reaction was incubated at 37 °C for three hours. Then, the DNA was purified with a Micro Bio-Spin Chromatography Column (BioRad). The DNA was stored at -20 °C.

Dna2 (50 μ M) was diluted to the following concentrations in nuclease assay buffer (25 mM trizma-HCl, pH 8, 0.05 mg/mL BSA, 1 mM DTT, 1 mM MgCl₂): 1000 fmol/ μ L, 100 fmol/ μ L, 10 fmol/ μ L, and 1 fmol/ μ L. Dna2 E675A (55 μ M) was diluted to the following concentrations in nuclease assay buffer: 1000 fmol/ μ L, 100 fmol/ μ L, 10 fmol/ μ L, and 1 fmol/ μ L. 1 μ L of each of the Dna2 and Dna2 E675A dilutions was added to separate reaction mixtures to start the reaction. The reactions were incubated at 37 °C for 30 minutes. The reactions were stopped by incubation at 95 °C for five minutes. The reactions were dried in a vacuum centrifuge, then were re-suspended in 5 μ L of formamide loading buffer. The samples were run on a 12% sequencing gel. The sequencing gel was exposed to a phosphorimaging screen (GE Healthcare), and was imaged on a Typhoon FLA 9000 (GE Healthcare).

Chip Preparation and DNA Self Assembled Monolayer (SAM) Formation.

Integrated multiplex chips with an internal platinum reference electrode and an internal platinum auxiliary electrode were prepared as described previously (13). Multiplex chips were washed and assembled using previously described methods (13). The chips were ozone cleaned for 15 minutes. DNA SAMs were assembled on the gold working electrodes of the multiplex chips by incubating 25 μ M of the 5'-tail with methylene blue DNA duplex on the working electrode overnight at room temperature in a humid environment.

Electrochemical Nuclease Assay. Following DNA SAM formation, the chip was washed with phosphate buffer (5 mM sodium phosphate, pH 7, 50 mM NaCl). The electrode was backfilled with 1 mM 6-mercaptophexanol in phosphate buffer that contained 5 % glycerol for 45 minutes at room temperature. Then, the working electrode was rinsed with phosphate buffer. A cyclic voltammogram was acquired at a scan rate of 100 mV/s over a potential window of 0 to -0.5 mV v. platinum. Experiments were performed only if there were no major redox peaks on the cyclic voltammogram except for that characteristic of methylene blue. A second background cyclic voltammogram was acquired after the chips were washed with TBP buffer (5 mM sodium phosphate, pH 7, 50 mM NaCl, 4 mM MgCl₂, 4 mM spermidine, 50 μ M EDTA, 10 % glycerol). The chips were washed with nuclease assay buffer (20 mM trizma-HCl, pH 8, 0.05 mg/mL BSA, 2 mM MgCl₂). All buffer was removed from the chip prior to addition of the nuclease assay reactions on the working electrode.

Dna2 was diluted in nuclease assay buffer. 1 μ L of each protein stock solution was added to 19 μ L nuclease assay buffer such that the final protein concentrations in the reactions were: 5 μ M, 1 μ M, 500 nM, 250 nM, 120 nM, 60 nM, and 30 nM. 20 μ L nuclease assay buffer was added to one quadrant of the integrated chip as a negative control. The reactions were started by addition of Dna2, and the integrated chips were incubated at 30 °C for 30 minutes. The reactions were removed from the multiplex chips, and the chips were washed five

times with TBP buffer. A cyclic voltammogram was acquired at a scan rate of 100 mV/s over a potential window of 0 to -0.5 mV v. platinum.

The percent of DNA cleaved by Dna2 was calculated by measuring the area of the methylene blue cathodic and anodic peaks before and after the nuclease assay. All data was analyzed with Ch Instruments software. All measurements were made with a BAS CV50W model electrochemical analyzer.

Results

Nuclease Activity Assay with 5'-Tail Methylene Blue DNA in Solution. Dna2 binds DNA via a threading mechanism in which the 5'-tail of a DNA substrate is passed through the enzyme prior to being cleaved (14). If there is a block on the 5'-tail of the DNA substrate, such as a hybridized oligonucleotide or streptavidin, the DNA substrate cannot be bound in this way. However, Dna2 can process DNA substrates that are modified at the 5'-tail with a small molecule such as biotin. Therefore, an assay was performed to confirm that DNA modified on the 5'-end with methylene blue was a substrate for the nuclease domain of Dna2. As expected, Dna2 was active as a nuclease on the methylene blue labeled DNA substrate. Dna2 cleaved the DNA substrate at the ssDNA-dsDNA junction of the 5'-tail substrate with a ten nucleotide overhang to leave duplex DNA (**Figure A2.1**). Additionally, consistent with results from the literature, a Dna2 E675A mutant was much less active as a nuclease than wild type Dna2 on this DNA substrate (5).

Self-Assembled Monolayer Formation of 5'-Tail DNA Substrates. In the established radioactivity-based nuclease activity assay, the level of Dna2 activity is dependent on the DNA substrate (10). Specifically, Dna2 displays maximal nuclease activity on DNA substrates that have a 5'-tail ssDNA overhang greater than fifteen nucleotides in length. Dna2 is progressively less active on 5'-tail substrates with shorter overhangs, with essentially no Dna2 nuclease activity observed on duplex DNA. The activity of Dna2 on 5'-tail DNA substrates with

different overhang lengths was assessed in the present assay to determine whether the same trends were observed in the electrochemical nuclease assay.

To validate the electrochemical nuclease assay, four different DNA substrates were synthesized to contain covalent methylene blue at the 5'-end of the DNA distal from the gold electrode. The substrates used in this experiment consisted of duplex DNA, 5'-tail DNA with a two nucleotide overhang, 5'-tail DNA with a ten nucleotide overhang, and 5'-tail DNA with a twenty nucleotide overhang (**Table A2.2**). These DNA substrates were all deposited onto a gold electrode to form a self-assembled monolayer to determine whether monolayer formation was affected with any of these substrates. The total amount of DNA adsorbed to the working electrode surface was about the same regardless of the DNA substrate that was being used to form monolayers. Furthermore, the amount of DNA attached to the electrode was on the same order of magnitude as that used in the ^{32}P nuclease activity assay (**Figure A2.5**). Therefore, direct comparison could be made between Dna2 activity on gold electrodes modified with the different DNA substrates, since the same amount of DNA was attached to the electrodes.

The self-assembled monolayers of the different methylene blue-modified DNA substrates had slightly different characteristics as assessed by monitoring the redox activity of methylene blue by cyclic voltammetry (**Figure 1 and Figures A2.2-A2.4**). Consistent with previous observations, the cathodic peak was more diffuse for both the duplex DNA and 5'-tail DNA with a two nucleotide overhang. This observation suggested that there may be multiple pathways for reduction of methylene blue in these monolayers. Previously, it was suggested that in these types of DNA assemblies, there are two routes for electron transfer, one through the DNA and one directly from the electrode surface (12). The shape of the cathodic peak for the 5'-tail DNA with a ten nucleotide overhang and the 5'-tail DNA with a twenty nucleotide overhang suggested that direct electron transfer from the working electrode to methylene blue was the major electron transfer mechanism. Notably, reduction of methylene blue is thought to facilitate methylene blue unbinding from the DNA, so the oxidation of this probe is always via the

surface of the electrode (12,15). Consistent with this observation, there was no difference in the anodic peak shape for the different types of DNA monolayers.

It was confirmed that the methylene blue DNA substrates were covalently bound to the electrode surface by monitoring changes in both the cathodic and anodic current intensity with respect to the scan rate. Both the cathodic and anodic current intensity increased linearly in response to increasing scan rate (**Figures A2.6-A2.14**). Thus, the DNA substrates were covalently linked to the gold electrode rather than diffusing in solution (16).

Dna2 Nuclease Activity on Gold Electrodes Modified with 5'-Tail DNA Substrates. In the assay described in this report, the amount of Dna2 nuclease activity was quantified by measuring the percentage of DNA cleaved on the electrode surface. This measurement was made by first evaluating the total amount of DNA present on the electrode surfaces prior to addition of Dna2 based on the signal intensity of the anodic peak for methylene blue. The amount of residual DNA on the electrode was calculated based on the signal intensity of the anodic peak for methylene blue after the nuclease assay reaction had been removed from the electrode. The

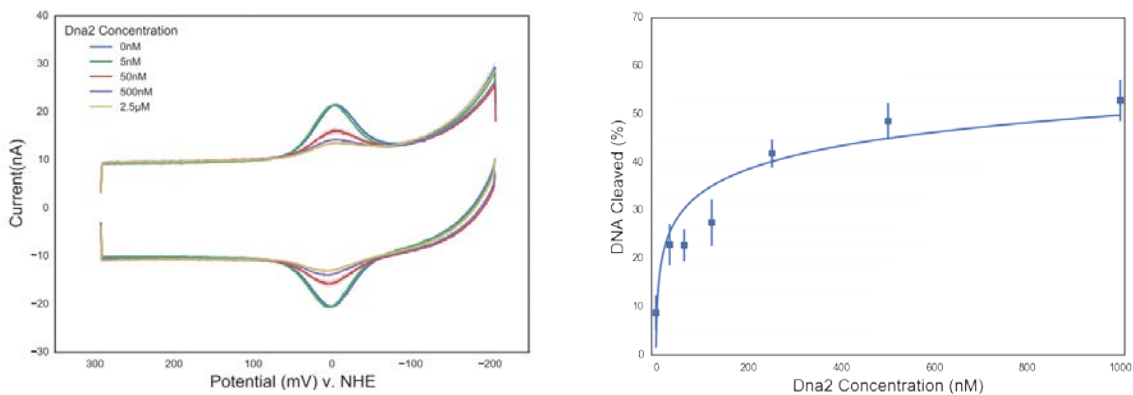


Figure 4.2. Electrochemical Nuclease Assay on a 5'-Tail DNA Substrate. (Left) Cyclic voltammograms of electrodes modified with 5'-tail DNA substrate with a ten nucleotide overhang following nuclease activity assay. The concentration of Dna2 used in each activity assay is shown in the top left corner of the voltammogram. **(Right)** Quantification of Dna2 nuclease activity on a 5'-tail DNA substrate with a ten nucleotide overhang. Error was calculated as standard error.

cathodic peak intensity could not be used to accurately determine the amount of Dna2 activity due to both the broadening of this peak upon protein addition, as well as interference from an oxygen-dependent signal at negative potentials.

As expected, Dna2 was active as a nuclease on DNA substrates covalently attached to the working electrode surface. There was an increase in the amount of DNA cleaved as Dna2 was titrated into the nuclease assay (**Figure 4.2**). These results suggested that this assay could effectively distinguish differences in Dna2 concentrations. Notably, the maximum amount of DNA that was cleaved on the surface was about 50% of the total methylene blue present on the electrode surface. This observation is consistent with previous studies, and suggests that the residual DNA was in a conformation that could not be processed by DNA binding proteins (17).

In general, as was observed for the radioactivity-based nuclease assay, Dna2 was more active on the 5'-tail DNA substrates that had longer overhangs (**Figure 4.3**). However, there were two differences in DNA substrate preference between the results obtained in the established radioactivity-based nuclease assay versus the results obtained in the electrochemical nuclease assay that are important to consider when developing this platform for diagnostic applications. First, Dna2 had about the same activity on the 5'-tail with a ten nucleotide overhang DNA substrate and the 5'-tail with a twenty nucleotide overhang DNA substrate. In the radioactivity-based assay, Dna2 was significantly more active on 5'-tail DNA substrates with a twenty nucleotide overhang relative to an eight nucleotide overhang.

The second unexpected result was that there was a significant amount of Dna2 nuclease activity observed on the 5'-tail DNA substrate with a two nucleotide overhang. This may have occurred because the presence of the covalently linked methylene blue destabilized DNA duplex formation. If this destabilization manifested itself at the top of the DNA duplex nearest the overhang, then the DNA duplex may de-hybridize, forming a larger overhang than designed for this

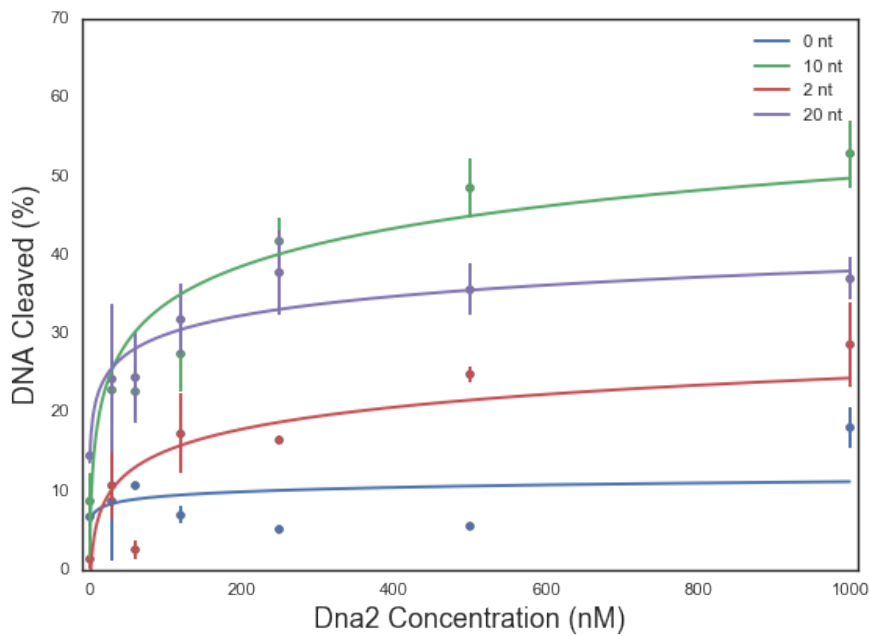


Figure 4.3. Dna2 Nuclease Activity on 5'-Tail DNA Substrates with Different Overhang Lengths. Comparison of Dna2 nuclease activity on different DNA-modified gold electrodes. The 5'-tail overhang length for each substrate assay is shown on the top right of the graph. Error was calculated as standard error.

substrate. These observations suggest that the maximum Dna2 nuclease activity, which was unbiased by interaction of the DNA with the electrode or by chemical modification, was observed on the 5'-tail DNA substrate with a ten nucleotide overhang. Therefore, this DNA substrate should be used in the development of this method for any diagnostic applications.

Dna2 E675A Nuclease Activity on DNA-Modified Gold Electrodes. To determine the specificity of Dna2 nuclease activity, the electrochemical nuclease assay was performed with a nuclease-deficient form of Dna2, Dna2 E675A. As expected, the nuclease deficient Dna2 E675A mutant exhibited a decrease in nuclease activity relative to the wildtype enzyme (Figure 4.4). This sensitivity is essential for detection of mutant forms of human Dna2, such as the Arg284His, Lys313Glu, and Val723Ile mutants. These mutant proteins have deficient nuclease

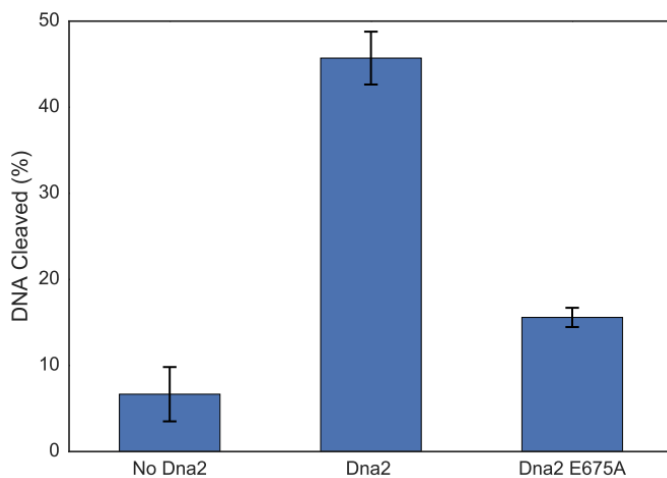


Figure 4.4. Electrochemical Nuclease Assay with the Dna2 E675A Nuclease-Deficient Mutant. The total protein concentration for each assay was 500 nM. The DNA substrate was the 5'-tail with a ten nucleotide overhang. Error was calculated as standard error.

activity, and are linked to the development of progressive myopathy (8). Thus, the detection of the Dna2 E675A mutant suggests this assay can be used to detect the types of defects in Dna2 nuclease activity that could serve as a biomarker of disease

Conclusion

A fast and robust nuclease activity assay for Dna2 was developed. This constitutes the first Dna2 nuclease activity assay that does not require radioactivity. With this assay, Dna2 nuclease activity could be detected at nanomolar concentrations, with a wide dynamic range of detection. Therefore, this assay could be used to measure differences in Dna2 concentration across samples, which would be necessary to monitor Dna2 nuclease activity in cancer. The specificity of this assay was confirmed with a nuclease deficient mutant, Dna2 E675A, suggesting that this assay could be used for the effective detection of nuclease deficient mutants of Dna2. These types of mutants are often indicative of

disease progression. Finally, the assay was further validated by comparison of the relative amounts of nuclease activity on DNA substrates that were known to have a distinct pattern of degradation based on established radioactivity assays. The speed, simplicity, and reliability of this assay makes it a useful alternative for the development of more high throughput methods for the screening of small molecule inhibitors or the diagnosis of diseases associated with aberrant Dna2 nuclease activity.

References

1. Bae, S.-H., Bae, K.-H., Kim, J.-A., and Seo, Y.-S. (2001) RPA Governs Endonuclease Switching During Processing of Okazaki Fragments in Eukaryotes. *Nature*. 412, 456-461.
2. Zhu, Z., Chung, W.-H., Shim, E. Y., Lee, S. E., and Ira, G. (2008) Sgs1 Helicase and Two Nucleases Dna2 and Exo1 Resect DNA Double-Strand Break Ends. *Cell*. 134, 981-994.
3. Choe, W., Budd, M., Imamura, O., Hoopes, L., and Campbell, J. L. (2002) Dynamic Localization of an Okazaki Fragment Processing Protein Suggests a Novel Role in Telomere Replication. *Mol Cell Biol*. 22, 4202-4217.
4. Duxin, J. P., Dao, B., Martinsson, P., Rajala, N., Guittat, L., Campbell, J. L., Spelbrink, J. N., and Stewart, S. A. (2009) Human Dna2 is a Nuclear and Mitochondrial DNA Maintenance Protein. *Mol Cell Biol*. 29, 4274-4282.
5. Budd, M. E., Choe, W. C., Campbell, J. L. (2000) The Nuclease Activity of the Yeast DNA2 Protein, which is Related to the RecB-Like Nucleases, is Essential *In Vivo*. *J Biol Chem*. 275, 16518-16529.
6. Stewart, J. A., Campbell, J. L., and Bambara, R. A. (2010) Dna2 is a Structure-Specific Nuclease, with Affinity for 5'-Flap Intermediates. *Nucleic Acids Res*. 38, 920-930.
7. Peng, G., et al. (2012) Human Nuclease/Helicase DNA2 Alleviates Replication Stress by Promoting DNA End Resection. *Cancer Res*. 72, 2802-2813.
8. Ronchi, D., et al. (2013) Mutations in DNA2 Link Progressive Myopathy to Mitochondrial DNA Instability. *Am J Hum Genet*. 92, 293-300.
9. Shaheen, R., et al. (2014) Genomics Analysis of Primordial Dwarfism Reveals Novel Disease Genes. *Genome Res*. 24, 291-299.
10. Levikova, M., Klaue, D., Seidel, R., and Cejka, P. (2013) Nuclease Activity of *Saccharomyces cerevisiae* Dna2 Inhibits its Potent DNA Helicase Activity. *Proc Natl Ac Sci USA*. 110, E1992-E2001.

11. Pheeney, C. G. and Barton, J. K. (2012) DNA Electrochemistry with Tethered Methylene Blue. *Langmuir*. 28, 7063-7070.
12. Pheeney, C. G. and Barton, J. K. (2013) Intraduplex DNA-Mediated Electrochemistry of Covalently Tethered Redox-Active Reporters. *J Am Chem Soc*. 135, 14944-14947.
13. Pheeney, C. G., Arnold, A. R., Grodick, M. A., and Barton, J. K. (2013) Multiplexed Electrochemistry of DNA-Bound Metalloproteins. *J Am Chem Soc*. 135, 11869-11878.
14. Balakrishnan, L., Polaczek, P., Pokharel, S., Campbell, J. L., and Bambara, R. A. (2010) Dna2 Exhibits a Unique Strand End-Dependent Helicase Function. *J Biol Chem*. 285, 38661-38868.
15. Boon, E. M., Barton, J. K., Bhaghat, V., Nerissian, M., Wang, W., and Hill, M. G. (2003) Reduction of Ferricyanide by Methylene Blue at a DNA-Modified Rotating-Disk Electrode. *Langmuir*. 19, 9255-9259.
16. Bard, A. J. and Faulkner, L. R. *Electrochemical Methods – Fundamental and Application*, 2nd ed.; Joh Wiley & Sons: New York, 2000; pp.580-631.
17. Muren, N. B. and Barton, J. K. (2013) Electrochemical Assay for the Signal-On Detection of Human DNA Methyltransferase Activity. *J Am Chem Soc*. 135, 16632-16640.

ELECTROCHEMICAL AND STRUCTURAL CHARACTERIZATION OF *AZOTOBACTER VINELANDII* FLAVODOXIN II

Abstract

In *Azotobacter vinelandii*, flavodoxin II is a biological reductant of the nitrogenase Fe-protein. It has been proposed that this flavodoxin can donate two low potential electrons to reduce the iron-sulfur cluster of the Fe-protein to its all ferrous state. To better understand this process, the redox properties of flavodoxin II were monitored on surfactant-modified basal plane graphite electrodes. These studies revealed that flavodoxin II has two distinct redox couples as measured by cyclic voltammetry at about -483 ± 1 mV v. NHE (at pH 7.5) and at about -187 ± 9 mV v. NHE (at pH 7.5). The first, low potential redox couple was assigned as the hydroquinone/semiquinone couple while the second, high potential redox couple was assigned as the semiquinone/quinone couple. However, this high potential redox process was most likely due to a combination of electron transfer to the flavodoxin and to free FMN. This study constitutes the first example of a direct electrochemical method that could measure the midpoint potential of the semiquinone/quinone redox couple. The kinetics of the flavodoxin II redox processes were diffusion-limited, suggesting that the protein could diffuse in the films with an approximate rate of $6.4 \times 10^{-8} \pm 5.1 \times 10^{-8}$ cm²/s. Unexpectedly, the pH dependence of the midpoint potential of the hydroquinone/semiquinone couple was best fit as a proton-coupled two electron process with pK_a of about 6.1, suggesting that flavodoxin II may be capable of the concerted transfer of two low potential electrons. X-ray crystallography was used to characterize the structure of the flavodoxin in the oxidized quinone and two-electron reduced hydroquinone

oxidation states observed in the electrochemical experiments. These studies revealed no major structural rearrangements upon reduction of the cofactor except for an amide flip at Gly58 that facilitated hydrogen binding between the carbonyl of the amide backbone of this residue and N5 of FMN. The structure of flavodoxin II was used to build a model for how this protein might interact with and reduce the Fe-protein in a biological context.

Introduction

The formation of bioavailable ammonia from the reduction of atmospheric dinitrogen is an important reaction in the nitrogen cycle. Nitrogenase is the enzyme that catalyzes this process using energy derived from ATP hydrolysis to form two molecules of ammonia and one molecule of H₂ from N₂. This enzyme consists of a complex of two proteins: the Fe-protein and the MoFe-protein. The MoFe-protein is the site of dinitrogen reduction while the Fe-protein serves as the reductant of the MoFe-protein (1,2). Nitrogenase substrates can only bind to the FeMo-cofactor when it has been reduced. Thus, prior to substrate reduction, multiple rounds of electron transfer from the 4Fe-4S cluster of the Fe-protein to the P-cluster, and from the P-cluster to the FeMo-cofactor must occur in a mechanism that is gated by ATP hydrolysis. Although it is clear that reduction of dinitrogen to ammonia requires that eight electrons be delivered from the reduced iron-sulfur cluster of the Fe-protein to the MoFe-protein, the biological source of these electrons remains less characterized. It has been proposed that two of the biological reductants of the Fe-protein are a ferredoxin (3-5) and a flavodoxin, the latter is encoded in the *nif* operon (6-9). In *Azotobacter vinelandii*, these reductants are ferredoxin I and flavodoxin II (8).

Although there is redundancy in biological reductants of nitrogenase in *Azotobacter vinelandii*, four observations suggest that flavodoxin II is one of the predominant reductant of the Fe-protein in a variety of organisms. First, it was observed that deletion of *K. pneumoniae* *nifF* resulted in a complete loss of nitrogen reduction in that organism, suggesting that in some bacteria, flavodoxin II

is solely responsible for donating electrons to nitrogenase (11). Second, the expression level of flavodoxin II in the cell is upregulated under nitrogen fixing conditions (12). Third, the Fe-protein and nitrogenase-associated flavodoxin from different organisms form a stable complex *in vitro* (5,7,10). Stopped-flow spectrophotometry experiments suggested that *R. capsulatus* and *K. pneumoniae* flavodoxin forms a complex with the *K. pneumoniae* Fe-protein with a K_D of 0.44 μM and >730 μM , respectively. Notably, when the *K. pneumoniae* Fe-protein bound nucleotides, such as MgATP, the K_D of this complex dropped to 13 μM . For both of these systems, electron transfer from the reduced flavodoxin to the Fe-protein was rapid with electron transfer rates of greater than $10^6 \text{ M}^{-1}\text{s}^{-1}$. Finally, *in vitro* nitrogenase activity assays using flavodoxin II as a source of electrons have also suggested that this flavodoxin can act as an electron donor to nitrogenase since there was an increase in nitrogenase activity when this protein was included in *in vitro* nitrogenase activity assays (7,13). Furthermore, energy utilization by the Fe-protein was enhanced when flavodoxin II was employed as a reductant in *in vitro* assays rather than the chemical reductant sodium dithionite. Specifically, with flavodoxin as the biological reductant the ATP/2e⁻ ratio decreased from four to two suggesting that flavodoxin II could reduce the Fe-protein to its unique all ferrous state, allowing for two electrons to be transferred per ATP hydrolyzed by the Fe-protein (13). The reduction of the *Azotobacter vinelandii* Fe-protein to the all ferrous form by flavodoxin II has been shown with a variety of spectroscopic experiments (14).

Despite the unique chemistry that has been proposed for *Azotobacter vinelandii* flavodoxin II in which it is capable of reducing the Fe-protein to an all ferrous state, this protein is a prototypical long chain flavodoxin, which non-covalently binds a flavin mononucleotide (FMN) cofactor (15,17). This cofactor can exist in three different oxidation states: oxidized quinone, one-electron reduced semiquinone, and two-electron reduced hydroquinone. In solution, free FMN cycles between the oxidized quinone and two-electron reduced hydroquinone due to rapid disproportionation of the semiquinone state in aqueous solutions (16).

When bound by flavodoxin, the semiquinone form of FMN is stabilized, which allows for the sequential transfer of one electron at low redox potentials. Thus, in general, flavodoxin bound FMN cycles between the semiquinone and the hydroquinone state in most low-potential redox reactions (15).

Although the general α/β fold of flavodoxin II is similar to other flavodoxins, there are a couple of distinguishing structural features cited that could explain the low midpoint potential observed for the semiquinone/hydroquinone couple between -458 mV v. NHE and -515 mV v. NHE, as well as the relatively high midpoint potential observed for the quinone/semiquinone couple (12, 18, 25-28). These observations were initially made through studies of a mutant form (Cys69Ala) of *Azotobacter* flavodoxin II purified from *E. coli* (19). Unlike most known long-chain flavodoxins, there is no hydrogen bonding to N5 of FMN when the protein is in its oxidized form. This would increase the midpoint potential of the quinone/semiquinone couple through destabilization of the quinone form of FMN. Additionally, negatively charged, acidic residues near N1 of FMN could decrease the hydroquinone/semiquinone redox couple by destabilizing the fully reduced hydroquinone FMN. A polar leucine on the *re* face of FMN rather than the tryptophan present in other long-chain flavodoxins could further lower the midpoint potential of the semiquinone/hydroquinone couple. Finally, the presence of glycine at position 58 rather than an amino acid with a bulkier side chain is thought to stabilize the semiquinone oxidation state by decreasing the energy of an amide bond flip at that position. This rearrangement allows for hydrogen bonding to N5 of FMN, which becomes protonated upon either one or two electron reduction of the cofactor. This would lead to an overall decrease in the midpoint potential of the semiquinone/hydroquinone couple of flavodoxin II relative to other long-chain flavodoxins.

In this paper, a series of X-ray crystallography and electrochemistry experiments were performed to better characterize the interaction of flavodoxin II and the Fe-protein of nitrogenase with a focus on determining the molecular interactions that facilitate reduction of the 4Fe-4S cluster of the Fe-protein to its all

ferrous state. First, a new method was developed to determine the redox properties of *Azotobacter vinelandii* flavodoxin II on surfactant-modified basal plane graphite electrodes. This method was designed to mimic the environment of FMN upon binding to the Fe-protein. These studies were complemented with studies to determine the structural changes occurring for the redox processes observed using electrochemical methods. Finally, a structural model was built to describe how flavodoxin II and the Fe-protein could interact to facilitate reduction of the Fe-protein.

Methods

Azotobacter Cell Growth and Flavodoxin II Purification. Cell growths and protein purifications were carried out as previously described for isolation of *Azotobacter vinelandii* nitrogenase (20,21). Cell lysis was performed under argon atmosphere with an Avestin Emulsiflex C5 homogenizer. The cell lysate was cleared by centrifugation, and was loaded to a 70mL HiTrapQ anion exchange column (GE Healthcare). The nitrogenase component proteins were eluted from the ion exchange column with a gradient from 150 mM NaCl to 1M NaCl over thirty column volumes. The flavodoxin eluted from the column at conductivity values between 39 to 40 mS/cm. The protein was further purified on a size exclusion column (Superdex200, 26/60, GE Healthcare) to separate flavodoxin II from any contaminating Fe-protein. The protein was quantified by Bradford assay using a BSA standard curve.

Strain Construction for Overexpression of Flavodoxin II in E. coli. The flavodoxin II overexpression plasmid was prepared by Genescript USA, Inc. In this plasmid, the *Azotobacter vinelandii nifF* gene was cloned into the pET21b(+) vector between the NdeI-BamHI restriction enzyme cut sites. A stop codon was included at the C-terminus of the gene so that the protein was expressed without affinity tags. The

nifF gene was optimized for *E. coli* codon usage. The plasmid was transformed into *E. coli* BL21 (DE3) cells for overexpression of flavodoxin II.

E. coli Cell Growth and Purification of Flavodoxin II. The protocol for purification of *Azotobacter vinelandii* flavodoxin II was adapted from previously published protocols (19,22). The following buffers were prepared, were adjusted to the correct pH at room temperature, and were filtered with a glass fiber filter: anion exchange buffer A (50 mM tris-HCl, pH 7.5, 150 mM NaCl, 2 mM DTT), anion exchange buffer B (50 mM tris-HCl, pH 7.5, 1 M NaCl, 2 mM DTT), and size exclusion buffer (50 mM tris-HCl, pH 7.5, 200 mM NaCl). Dithiothreitol (DTT) was added to all buffers the day of each protein purification. Dioxygen was removed from the size exclusion column buffer prior to use in the purification by iterative cycles of vacuum followed by argon filling.

An overnight starter culture of the flavodoxin II overexpression strain supplemented with 100 μ g/mL ampicillin was incubated at room temperature with shaking overnight. The starter culture was diluted 1:100 into 1 L of Luria Broth medium containing 50 μ g/mL ampicillin. The cultures were grown to late exponential phase ($OD_{600} \sim 0.6-0.8$) at 37 °C with shaking. Overexpression of flavodoxin II was induced by addition of IPTG to a final concentration of 0.5 mM in each culture. The cultures were incubated for 16 hours at 37 °C with shaking. The cells were pelleted via centrifugation at 6238 x g for ten minutes. The cell pellets were stored at -80 °C until purification.

All lysis steps were carried out on ice at room temperature. The BL21 (DE3) cell pellets were thawed on ice. The cell pellets were re-suspended in anion exchange buffer A with a homogenizer. The lysis buffer also contained complete protease inhibitor tablets (Roche) at a concentration of one tablet per 50 mL of buffer. The cells were lysed with an Avestin Emulsiflex C5 homogenizer. The cell debris was pelleted by centrifugation in a floor centrifuge at 13,000 x g at 4 °C for 35 minutes.

The cleared cell lysate was loaded to two 5 mL HiTrapQ HP anion exchange columns connected in tandem using an Akta FPLC (GE Healthcare). The protein was purified by anion exchange column as described previously (19,22) Following the anion exchange column, the protein was loaded to a Superdex200 size exclusion column. The protein that eluted from the column was collected, and was concentrated in an Amicon filter centrifuge tube (10,000 MWCO) to a final concentration of about 10 μ M. This protein was flash frozen in liquid nitrogen. The protein was stored under liquid nitrogen.

The concentration of protein was estimated based on the absorption of the sample at 452 nm. The extinction coefficient of the protein at 452 nm is 11,300 M⁻¹ cm⁻¹ (22). The concentration of protein that bound a flavin mononucleotide cofactor was estimated from the ratio of the absorption of the sample at 274 nm to the absorption of the sample at 452 nm. The ratio of Abs₂₇₄/Abs₄₅₂ was about 7, which was higher than that cited previously for the purification of the oxidized form of this protein (22). The protein concentration was also quantified by Bradford assay with a BSA standard curve. The total protein yield was about 0.2 mg of protein per gram of cell paste. The purity of the isolated protein was analyzed on a denaturing polyacrylamide gel.

Preparation of Flavodoxin II for Electrochemistry Experiments. Prior to electrochemistry experiments, sodium dithionite was removed from all protein samples using a PD10 column (GE Healthcare). This procedure was performed in a McCoy anaerobic chamber with a 95 % / 5 % Ar / H₂ atmosphere with less than 0 ppm dioxygen. The column was first equilibrated in five column volumes of electrochemistry buffer (50 mM potassium phosphate, pH 7.5, 150 mM NaCl) with 10 mM sodium dithionite. Then, the column was equilibrated in five column volumes of electrochemistry buffer. All buffers were filtered with a 0.2 micron filter, and all oxygen was removed from the buffer by iterative cycles of vacuum followed by filling with argon. The protein was exchanged into electrochemistry buffer using the PD10 column. UV-visible absorption spectroscopy was used to quantify protein

concentration, and to determine the extent of protein oxidation during the course of sample preparation. Following this procedure, the protein was flash frozen in liquid nitrogen, and was transported to Occidental College under liquid nitrogen for experiments.

Preparation of DDAB Films on Basal Plane Graphite Electrodes. The basal plane graphite electrodes were cut into cylinders with an area of 0.2 cm². Prior to experiments, the basal plane graphite electrodes were polished with 0.3 micron and 0.05 micron alumina resin. The electrodes were cleaned by sonication for 10 minutes, then the electrodes were dried with a heat gun. 5 μ L of 10 mM DDAB in deionized water was deposited to the electrode. The 10 mM DDAB solution was sonicated for 45 minutes prior to being deposited to the electrode. The films dried slowly overnight on the electrode in a closed environment.

Electrochemistry with DDAB-Modified Basal Plane Graphite Electrodes. All experiments were performed in a glovebox that had a nitrogen atmosphere. Dioxygen was removed from buffers used in electrochemistry experiments by iterative cycles of vacuum followed by filling with argon. The protein solution was put in the central compartment of a two-compartment electrochemical cell. The DDAB-modified basal plane graphite electrode was placed in the protein solution along with the platinum auxiliary electrode. The solid state Ag/AgCl reference electrode (Warner Instruments) was connected to the cell with the working electrode via a luggin capillary.

Alternatively, the basal plane graphite electrode was soaked in a 200 μ M flavodoxin II solution for twenty minutes. Then, the electrode was transferred to phosphate buffer (10 mM potassium phosphate, pH 7) along with a platinum auxiliary electrode. All measurements were made with a Ch instruments potentiostat. All data was analyzed with Ch instruments software.

pH Titration. The electrochemical cell was assembled, and the electrochemical measurements were acquired as described above. The DDAB-modified basal plane graphite electrode was soaked in a 200 μ M flavodoxin II solution for twenty minutes. The electrode was assayed in the following buffers: 10 mM potassium phosphate (pH 7.9), 10 mM potassium phosphate (pH 7.6), 10 mM potassium phosphate (pH 7), 10 mM potassium phosphate (pH 6.6), 10 mM potassium phosphate (pH 6), 10 mM sodium phosphate (pH 5.6), 10 mM sodium phosphate (pH 5.4), 10 mM sodium acetate (pH 4.3), and 10 mM sodium acetate (pH 3.9). The electrodes were incubated for ten minutes in the buffer solution prior to square wave voltammogram acquisition. The pH of all buffers was confirmed following the experiment.

Crystallization and Data Collection. Flavodoxin II was crystallized using the sitting drop vapor diffusion method in an anaerobic chamber containing a 90 % Ar / 10 % H₂ atmosphere. The reservoir solution contained 23-28 % PEG 3350 (v/v), 0.15-0.3 M MgCl₂·6H₂O, and 100 mM tris-HCl, pH 8.5. Crystals were obtained between 3-6 months after setting up the crystallization experiment, and were bright yellow in color indicating that the flavodoxin was in the oxidized quinone state. The flavodoxin crystals were reduced by addition of 0.5 μ L of a 50 mM sodium dithionite solution to the 2 μ L drop that contained the crystals. The chamber that contained the crystals was sealed, and was incubated at room temperature for 1.5 hours. The oxidized flavodoxin crystals were cryo-protected by transferring the crystals into a 5 μ L drop of 7 % 2-methyl-2,4-pentanediol in the reservoir solution (v/v). The reduced flavodoxin crystals were cryo-protected by transferring the crystals into a 5 μ L drop of 7 % 2-methyl-2,4-pentanediol in the reservoir solution (v/v) that contained 5 mM sodium dithionite. Diffraction data were collected at 12,400 eV at the Stanford Synchrotron Radiation Lightsource (SSRL) beamline 12-2 with a Dectris Pilatus 6M detector.

Structure Solution and Refinement. The data were indexed, integrated, and scaled using XDS and Scala (23,24). Structural refinement and rebuilding was done in REFMAC5 and Coot (24). All protein structures were rendered in PyMol.

Results

Electrochemistry on DDAB-Modified Basal Plane Graphite Electrodes. The redox properties of *Azotobacter vinelandii* flavodoxin II have been studied using both a direct electrochemical method and by EPR-monitored redox titrations (**Table A3.1**) (12,18,25-28). With these methods, it was observed that the measured potentials for the semiquinone/hydroquinone couple (E_1) are the lowest observed for any long chain flavodoxin, and range from -458 mV v. NHE to -524 mV v. NHE at pH 8, depending on experiment type and purification method. The measured potential of the quinone/semiquinone couple is -183 mV v. NHE, which has never been observed using direct electrochemical methods. To better characterize the redox behavior of *Azotobacter vinelandii* flavodoxin II, a new method for monitoring the redox properties of this protein was developed on surfactant-modified basal plane graphite electrodes.

Surfactant-modified electrodes have been extensively used to study the redox chemistry of many proteins, like myoglobin and cytochrome P450 (29-31). In this technique, synthetic or natural surfactants can be used to form ordered films of stacked bilayers on an electrode, which mimic biological membranes found in nature. Although these films were originally developed to study the redox behavior of membrane proteins in a biologically relevant environment, the observation that direct electron transfer for myoglobin was observed on electrodes modified with these films, suggested that they could be used as a general tool for monitoring the redox chemistry of proteins. Since that time, a number of studies have been

performed that examine the redox properties, the spectroscopic characteristics, and the electrocatalytic activity of proteins in these films (32-34).

In this study, the redox behavior of *Azotobacter vinelandii* flavodoxin II was characterized on basal plane graphite electrodes coated with a film of the surfactant dioctyldimethylammonium bromide (DDAB). This film was chosen because the positive charge on the headgroup of the DDAB, as well as the decrease in solvent accessibility of FMN in these films could mimic the environment of FMN upon binding of flavodoxin II to the Fe-protein. Additionally, this study constitutes one of the first examples of a protein that contains a flavin cofactor with this technique, and thus provides insight into the redox behavior of flavoproteins with this method (35). Cyclic voltammetry on DDAB-modified basal plane graphite electrodes revealed that there were two redox active species present when cyclic voltammograms were acquired with the working and auxiliary electrodes in a 200 μ M flavodoxin II solution: a low potential redox species with a midpoint potential of -483 ± 1 mV v. NHE (at pH 7.5) and a high potential redox

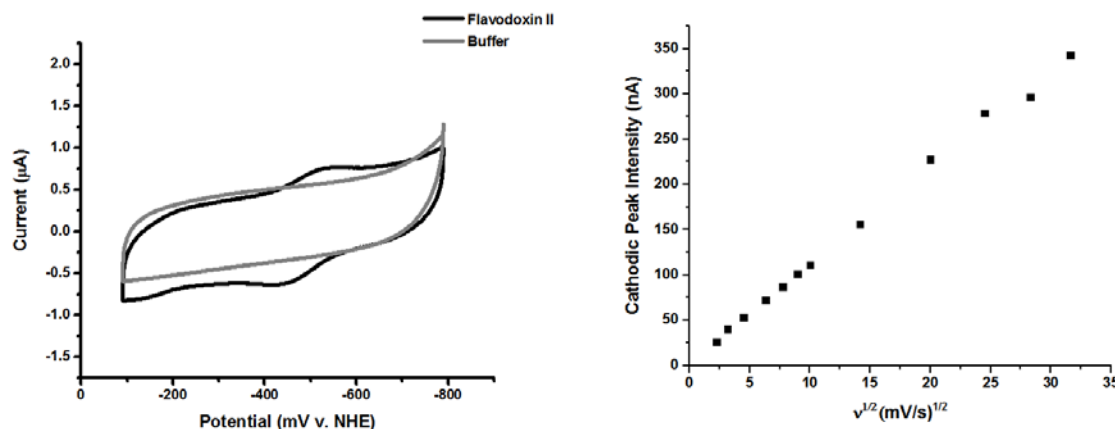


Figure 5.1. Flavodoxin II on Basal Plane Graphite Electrodes Modified with DDAB. (Left) The electrodes were placed in 50 mM potassium phosphate, pH 7.5, 150 mM NaCl. A cyclic voltammogram was acquired at a scan rate of 10 mV/s (gray). The electrode was placed in a 200 μ M solution of flavodoxin II in 50 mM potassium phosphate, pH 7.5, 150 mM NaCl. A cyclic voltammogram was acquired at a scan rate of 10 mV/s (Black). (Right) Dependence of the cathodic peak signal intensity on the scan rate for the low potential peak of the cyclic voltammogram of flavodoxin II on DDAB-modified basal plane graphite electrodes. The electrode was initially soaked in 200 μ M flavodoxin II in 50 mM potassium phosphate, pH 7.5, 200 mM NaCl.

species with a midpoint potential of -187 ± 9 mV v. NHE (at pH 7.5) (**Figure 1**).

The low potential species underwent a reversible redox process whereas the high potential redox species appeared to be quasi-reversible with oxidation occurring more readily than reduction. These redox processes were observed immediately upon submersion of the DDAB-modified electrode in protein solution. There was no signal associated with either redox process on unmodified basal plane graphite electrodes or on DDAB-modified electrodes placed in buffer (**Figures 1 and A3.1**). Recombinant flavodoxin II purified from *E. coli* rather than from the native organism had the same redox-active species observed by cyclic voltammetry, suggesting that the redox activity of flavodoxin II was being observed rather than that of a contaminating protein (**Figure A3.2**).

The low potential species was assigned to the hydroquinone/semiquinone redox couple based on similarity to previously measured midpoint potentials. Identification of the high potential redox-active species was challenging since the magnitude and reversibility of this peak was more variable. The amount of this species present in solution was inversely proportional to the amount of the low-potential redox active species as monitored by cyclic voltammetry. This observation was especially evident during the pH titrations when there was an increase in the high potential redox active species at low pH where the protein is less stable (28). Notably, the increase in this high potential peak was irreversible when the electrode was re-submerged in a neutral buffer. This observation in combination with the cyclic voltammogram of free FMN on DDAB-modified basal plane graphite electrodes provided for the initial assignment of the high potential peak as the two-electron hydroquinone/quinone couple of FMN in solution (**Figure A3.3**). However, given the similarity of the midpoint potential of the hydroquinone/quinone couple of FMN and the semiquinone/quinone couple of flavodoxin II, as well as results from the pH titration described later in this paper it is possible that both redox-active species are present in solution. Notably, the rapid disproportionation and slow electrode kinetics of the one-electron reduced

flavodoxin II semiquinone could explain why the high potential and low potential redox peaks are not present at a 1:1 ratio on the cyclic voltammogram (36).

In addition to analyzing the redox activity of flavodoxin II directly in a solution of this protein, the DDAB-modified basal plane graphite electrodes could be loaded with the protein, and the electrode moved to a phosphate buffer solution. The protein remained stable in the surfactant film during the course of the experiment on the order of hours. However, slow diffusion of the protein out of the films was responsible for a decrease in signal intensity over time at the electrode surface. This method was used for all subsequent scan rate and pH experiments. Under these conditions, the midpoint potentials of the two redox active species were shifted to -454 ± 7 mV v. NHE for the low potential redox species and -164 ± 12 for the high potential redox species. This result is consistent with previous observations that differences in ion concentration between the positively-charged surfactant film and the solution result in a shift in the midpoint potential of flavodoxin II (37,38).

The kinetics of the redox process were studied to determine if flavodoxin II diffused in the DDAB films on the time scale of voltammogram acquisition. Only the robust, low potential species was monitored with this method. The signal intensity of the low potential redox process observed in these films was proportional to the square root of the scan rate (**Figure 1 and S6**). Thus, the redox process occurring at the electrode was diffusion-limited, suggesting that flavodoxin II was diffusing in the surfactant film. This result was consistent with the kinetics observed for other proteins, like myoglobin and cytochrome c (39,40). However, there are also examples of proteins that are immobile in surfactant films, like hemoglobin and cytochrome P450 (41,42). The Randles-Sevcik equation could be used to estimate the diffusion constant of flavodoxin II in surfactant films as $6.4 \times 10^{-8} \pm 5.1 \times 10^{-8} \text{ cm}^2/\text{s}$ (43). This estimate assumes that the protein concentration is about the same in solution as in the surfactant film, and that it is a one electron redox process. This diffusion rate is less than $1.3 \times 10^{-6} \text{ cm}^2/\text{s}$, which would be the

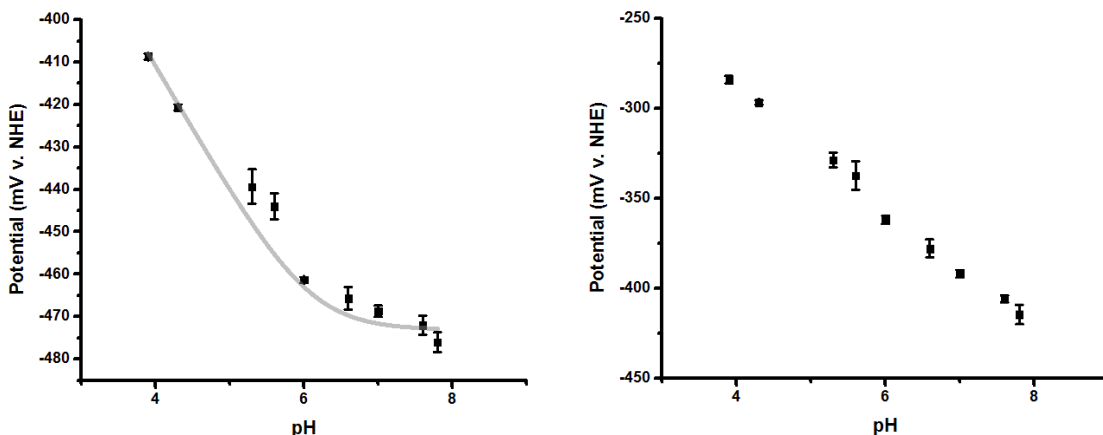


Figure 5.2. pH Titration of Flavodoxin II. (Top) Dependence of the midpoint potential of the low potential redox species on the solution pH. Each data point is the average of three separate experiments. Error is reported as standard error. The gray line is a simulation of the observed redox process using the Nernst equation with $n=2$. **(Bottom)** Dependence of the midpoint potential of the high potential redox species on the solution pH. Each data point is the average of three separate experiments. Error is reported as standard error.

diffusion constant of a perfectly spherical protein the size of flavodoxin II undergoing Brownian motion in solution.

The pH dependence of the midpoint potential of flavodoxin II was also assessed on DDAB-modified basal plane graphite electrodes to further characterize this system. The pH range evaluated in these studies was from pH 3.9 to 7.8. Consistent with previous studies using carbon electrodes modified with neomycin, the pH dependence of the low potential redox species was largely invariant up to pH 6 at which point there was a linear increase in potential with decreasing pH that was best modeled as a one proton-coupled two electron transfer process. When fit with the Nernst equation, this data was consistent with a single one proton coupled two electron transfer reaction, with the pK_a of this proton estimated to be 6.1 (**Figure 2**). This was in contrast to a previous study, which found two pK_a values for the reduced (hydroquinone) flavodoxin ($pK_{\text{Red},1} = 5.39 \pm 0.08$ and $pK_{\text{Red},2} = 7.84 \pm 0.14$) and one pK_a value for the oxidized flavodoxin (semiquinone) of 7.84 ± 0.14 . Analysis of the low potential peak suggested that

this peak varied linearly with the pH at all pH values tested with a slope of 45 mV/pH unit (**Figure 2**). FMN has a pK_a of about 6.4-6.7 for the protonation of reduced molecules (44). Thus, the observed pH titration of the low potential redox process is not consistent with the behavior of FMN, and instead is consistent with the observed redox process being the quinone/semiquinone couple (45). The pH titrations indicate that the potential of both the hydroquinone/semiquinone and the semiquinone/quinone couples can be measured with the electrochemical method developed in this paper. However, these studies in combination with previous results suggest that at low pH less than 6, a proton coupled two electron transfer reaction could occur at the flavodoxin, suggesting that flavodoxin II may be capable of donating two low potential electrons at the electrode.

X-Ray Crystallography. The crystal structure of *A. vinelandii* flavodoxin II was

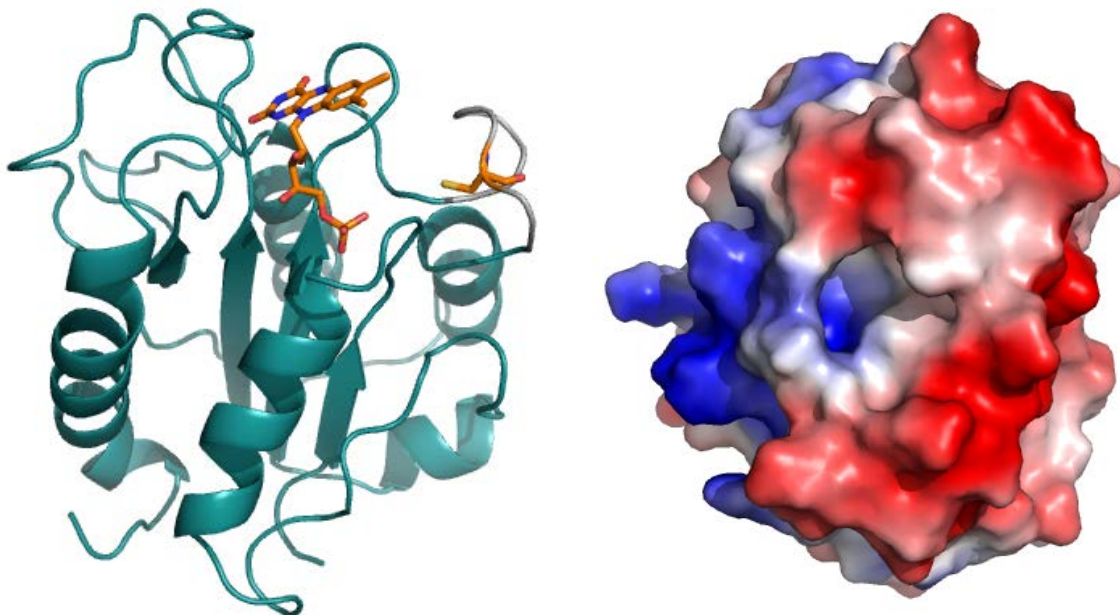


Figure 5.3. Structure of Oxidized Flavodoxin II. (Left) Ribbon structure of oxidized flavodoxin II. The FMN cofactor is shown in orange. The eight amino acid stretch proposed to be involved in mediating the flavodoxin Fe-protein interaction is shown in gray. The position of Cys69 is shown in orange. (Right) Electrostatic surface potential diagram of flavodoxin II showing the two charged surfaces proposed to interact with the Fe-protein.

solved with the protein in different oxidation states. The structure of the protein with a FMN cofactor in the quinone oxidation state was solved at 1.17 Å resolution. Molecular replacement was performed with a model of the Cys69Ala mutant of *Azotobacter vinelandii* flavodoxin II (19). The two-electron reduced protein, with an FMN cofactor in the hydroquinone form, was solved using molecular replacement with the model of oxidized flavodoxin II solved in this paper. The refinement statistics for the two models are given in **Table A3.2**.

The overall three-dimensional fold of flavodoxin II in both oxidation states was consistent with the prototypical α/β -fold of long chain flavodoxins. The N-terminus of the protein is the location of the first β -strand of four parallel β -strands that form the core of the protein. This β -sheet core is highly conserved in the flavodoxin protein family (46). The structure of the wild type flavodoxin differs from the structure of the Cys69Ala mutant in that the β 2 and β 5a strands from the mutant structure are disordered in the wildtype structure of flavodoxin II. Like the structure of the Cys69Ala mutant, the wildtype structure also consists of five α -helices that pack against the β -sheet core. There are multiple disordered loop regions within the structure, with the most important being the 50s loop and the 100s loop that connect the structured areas of the protein, and are involved in hydrogen bonding interactions with FMN. There are two other structural features that distinguish flavodoxin II from other flavodoxins. First, this protein has an insertion of 22-amino acids that precedes the fourth β -strand, which is characteristic of long chain flavodoxins, and provides the basis to classify this protein in that family (47). Second, this protein has an insertion of eight amino acid residues (amino acids 64-71) near the FMN cofactor preceding the third alpha helix of this protein that is generally found in nitrogenase-associated flavodoxins. These amino acids have been proposed to be involved in complex formation with the Fe-protein of nitrogenase.

The FMN molecule is bound non-covalently by flavodoxin II in a flat conformation that places the dimethyl benzene edge of the molecule at the edge of the protein. The other half of FMN is buried in the interior of the protein where an

extensive network of hydrogen bonds to the pyrimidine and phosphate portions of FMN bind this cofactor to the protein. Specifically, the hydroxyl groups in the loop located from Ser9 to Thr14 are within hydrogen bonding distance of the phosphate at the base of the ribosyl chain. Additionally, amino acid residues 56-60 in the 50s loop of flavodoxin II have been shown to form important hydrogen bonding interactions with the allooxazine ring of FMN. Although the identity of the specific amino acid residues in this region vary, the interaction of these residues with FMN not only hold the cofactor in place, but also help set the midpoint potential of the redox couples of this cofactor. Furthermore, residues 58-59 in this region are involved in a peptide flip during reduction of the cofactor, and will be the topic of later discussion. Interactions between the 100s loop of flavodoxin II and FMN between amino acid residues 98-107 also facilitate binding of FMN to the apoprotein. These interactions are similar to those previously observed in the structure of the Cys69Ala mutant of flavodoxin II (19).

The overall structures of both the wild type and Cys69Ala mutants of flavodoxin II are similar. The major difference between the crystal structure of the Cys69Ala flavodoxin II mutant and wildtype flavodoxin II is the identity of the side chain position at residue 69 (**Figure 3**). In the wildtype flavodoxin II, the sulfur of

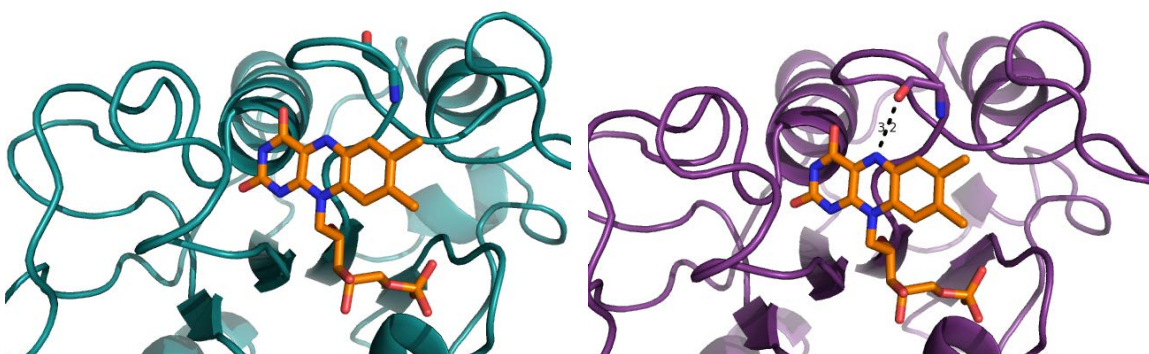


Figure 5.4. The FMN Binding Site of Flavodoxin II. (Left) The FMN binding site in oxidized flavodoxin II. The carbonyl of Gly58 is highlighted in stick form, and is pointing away from N5 of FMN. (Right) The FMN binding site in reduced flavodoxin II. The carbonyl of Gly58 is highlighted in stick form, and is within hydrogen bonding distance of N5 of FMN. FMN is shown in orange.

this amino acid residue is pointing toward the interior of the protein in a solvent-exposed region of the protein near the FMN cofactor. This cysteine residue is within the loop of flavodoxin II at which interaction of the flavodoxin and the Fe-protein are proposed, and thus the identity of the position of this residue will be important in determining the interactions that facilitate formation of this protein complex.

The structural changes in flavodoxin II upon reduction of the FMN cofactor with sodium dithionite were also studied by X-ray crystallography (**Figure 4**). The reduction of the protein to the hydroquinone state was determined based on bleaching of the yellow color in the crystal. Previously, it was observed that structural changes in flavodoxins occur at positions 58-59 upon reduction (49-51). In general, the residue at position 58, which in the case of flavodoxin II is glycine, is in the “O-down” conformation with the carbonyl of the amide backbone pointing away from FMN (49). Since the oxidized form does not contain a proton at the N5 of the isoalloxazine ring, H-bonding from other amino acid residues in the protein stabilize this form of the cofactor. Upon reduction to the hydroquinone state, the amide bond flips such that the carbonyl is placed in an “O-up” conformation that is able to hydrogen bond with the protonated N5 position of FMN. Consistent with the observations made of other flavodoxins, the structure of *Azotobacter vinelandii* flavodoxin II revealed that there were no other major conformational changes the peptide flip of the Gly58 carbonyl within 3.2 Å of the protonated N5 of FMN. This conformational change allowed for hydrogen bonding between the protein and FMN to stabilize the hydroquinone form of the cofactor. This structure provides insight into the structure of flavodoxin II that can form a complex with the Fe-protein capable of electron transfer.

Model of the Flavodoxin - Fe-Protein Complex. The ClusPro2.0 algorithm was used to construct a model of the complex that the Fe-protein and the flavodoxin form during Fe-protein reduction (52-55). This model suggested that the Fe-protein and the flavodoxin come together such that the FMN cofactor and the Fe-

S cluster are positioned within 6-8 Å of one another. The two proteins bind via electrostatic interactions with two strongly charged regions on the flavodoxin facilitating this binding mode. Specifically, in the model of complex formation, the overall negative charge of the flavodoxin surrounding FMN interacts with the overall positive charge of the amino acids surrounding the iron-sulfur cluster of the Fe-protein. Notably, the change in electrostatic environment around FMN could shift the potential of this cofactor from that observed in the electrochemistry experiments, lowering the midpoint potential of the semiquinone/quinone couple. This shift in potential could decrease the gap between the two redox couples of FMN, potentially making transfer of two low potential electrons feasible (56). There is also a region of the flavodoxin that has a net positive charge, which can interact

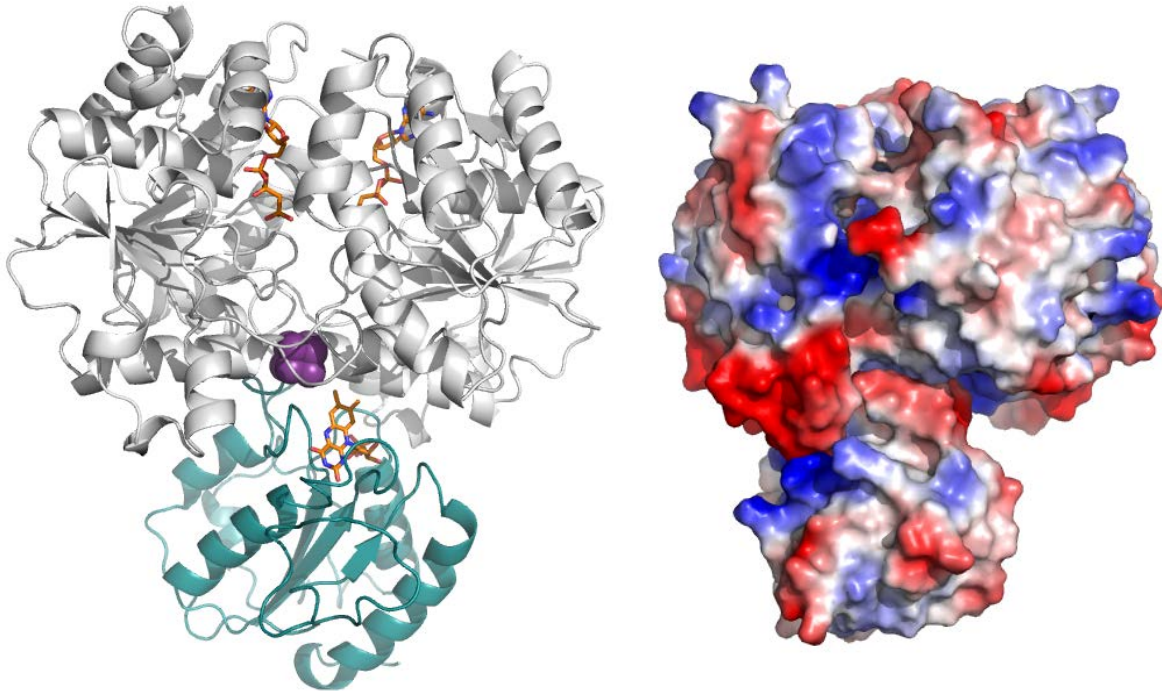


Figure 5.5. Model of the Flavodoxin II-Iron Protein Complex. (Top) Ribbon diagram of the model of flavodoxin II (teal) binding to the Fe-protein (gray) bond to MgAMP-PCP. The FMN cofactor and the AMP-PCP molecules are shown in orange. The iron-sulfur cluster is shown in purple. **(Bottom)** Electrostatic surface potential diagram of the Fe-protein flavodoxin II complex.

with a negatively charged region at the base of Av2 during complex formation (**Figure 5.5**).

The binding mode in this model also brings the eight amino acid insertion found in nitrogenase-associated flavodoxins to the interface of the two proteins, facilitating their interaction. Of particular interest in the context of this model is Asp68, which is positioned near the Fe-protein iron-sulfur cluster; however, the exact position of the side chain of this residue could not be determined due to disorder of this side chain. Cys69 and Glu70 although pointing away from the Fe-S cluster is also located near this cofactor, and upon possible rearrangement of the flexible loop during binding could be important in the mechanism of Fe-protein reduction. In addition to these residues, there are a number of other amino acid residues that could be involved in interactions that facilitate binding of the Fe-protein and flavodoxin II (**Table A3.3**).

The ClusPro algorithm was also used to build models of the flavodoxin II interaction with nucleotide-bound forms of the Fe-protein that had originally been solved in complex with the MoFe-protein. The models built with both the Fe-protein bound to MgAMP-PCP, an ATP mimic, and the Fe-protein in a mixed nucleotide form, binding one molecule of MgAMP-PCP and one molecule of MgADP, placed the iron-sulfur cluster of the Fe-protein within 3-5Å of FMN. Furthermore, electrostatic interactions in these models suggest that interaction of these forms of the Fe-protein would bind the flavodoxin with higher affinity than the Fe-protein with no nucleotide bound. These models provide insight into the mechanism by which flavodoxin II could reduce the Fe-protein to drive nitrogen reduction in a biological context.

Conclusion

Flavodoxin II is a biological reductant of the Fe-protein of nitrogenase, which donates electrons to the MoFe-protein during dinitrogen reduction. This protein can cycle through three different oxidation states; however, it has been

proposed that only the hydroquinone/semiquinone couple of the FMN cofactor has a sufficiently low midpoint potential to reduce the Fe-protein. A new technique was developed for studying the redox properties of flavodoxin II on surfactant-modified basal plane graphite electrodes. The results of these experiments suggested that flavodoxin II is capable of donating two low potential electron to the iron-sulfur cluster of the Fe-protein. Thus, depending on the true midpoint potential of the Fe-protein, flavodoxin II could reduce the Fe-protein to its all ferrous state (57,58). The structure of both the oxidized and reduced forms of flavodoxin II revealed the structural changes that occur in this protein upon two electron reduction to the hydroquinone form. As was observed for other long chain flavodoxins, an amide bond flip occurs at Gly58 that leads to stabilization of the N5 position of FMN via hydrogen bonding in the reduced structure. The structural studies provided a basis for a model describing complex formation between the Fe-protein and flavodoxin II, which suggested that these proteins bind such that the 4Fe-4S cluster in the Fe-protein is positioned within 6-8Å of the FMN of flavodoxin II in the absence of nucleotide binding. Thus, electron transfer could occur between these cofactors. Furthermore, this model suggested that residues 68-70 within the flexible eight amino acid insertion of flavodoxin II could be important in this redox process given their proximity to the iron-sulfur cluster of the Fe-protein. The electrochemical and structural studies presented in this chapter provide insight into the mechanism by which flavodoxin II could reduce the Fe-protein to an all ferrous state in a biological context.

References

1. Howard, J. B. and Rees, D. C. (2006) How Many Metals Does it Take to Fix N₂? A Mechanistic Overview of Biological Nitrogen Fixation. *Proc Natl Acad Sci USA*. 103, 17088-17093.
2. Burgess, B. K. and Lowe, D. J. (1996) Mechanism of Molybdenum Nitrogenase. *Chem Rev.* 96, 2983-3011.
3. Benemann, J. R., Yoch, D. C., Valentine, R. C., and Arnon, D. I. (1971) The Electron Transport System in Nitrogen Fixation by Azotobacter. IV. Requirements for NADPH-Supported Nitrogenase Activity. *Biochim Biophys Acta*. 226, 206-212.
4. Yoch, D. C. and Arnon, D. I. (1972) Two Biologically Active Ferredoxins from the Aerobic Nitrogen-Fixing Bacterium *Azotobacter vinelandii*. *J Biol Chem.* 247, 4514-4520.
5. Hallenbeck, P. C. and Gennaro, G. (1998) Stopped-Flow Kinetic Studies of Low Potential Electron Carriers of the Photosynthetic Bacterium, *Rhodobacter capsulatus*: Ferredoxin I and NiF. *Biochim Biophys Acta*. 1365, 435-442.
6. Yates, M. G. (1972) Electron Transport to Nitrogenase in *Azotobacter chroococcum*: Azotobacter Flavodoxin Hydroquinone as an Electron Donor. *FEBS Lett.* 27, 63-67.
7. Thorneley, R. N. F. and Deistung, J. (1998) Electron-Transfer Studies Involving Flavodoxin and a Natural Redox Partner, the Iron Protein of Nitrogenase. *Biochem J.* 253, 587-595.
8. Martin, A. E., Burgess, B. K., Iismaa, S. E., Smartt, C. T., Jacobson, M. R., and Dean, D. R. (1989) Characterization of an *Azotobacter vinelandii* Strain with Mutations in the Genes Encoding Flavodoxin and Ferredoxin I. *J Bacteriol.* 171, 3162-3167.
9. Duyvis, M. G., Wassink, H., and Haaker, H. (1998) Nitrogenase of *Azotobacter vinelandii*: Kinetic Analysis of the Fe Protein Redox Cycle. *Biochem.* 37, 17345-17354.
10. Peelen, S., Wijmenga, S., Erbel, P. J., Robson, R. L., Eady, R. R., and Vervoort, J. (1996) Possible Role of a Short Extra Loop of the Long-Chain Flavodoxin from *Azotobacter chroococcum* in Electron Transfer to

Nitrogenase: Complete ¹H, ¹⁵N, and ¹³C Backbone Assignments and Secondary Solution Structure of the Flavodoxin. *J Biomol NMR*. 7, 315-330.

11. Shah, V. K., Stacey, G., and Brill, W. J. (1983) Electron Transport to Nitrogenase: Characterization of Pyruvate:Flavodoxin Oxidoreductase, the *nifJ* Gene Product. *J Biol Chem*. 258, 12064-12068.
12. Klugkist, J., Voorberg, J., Haaker, H., and Veeger, C. (1986) Characterization of Three Different Flavodoxins from *Azotobacter vinelandii*. *Eur J Biochem*. 155, 33-40.
13. Erickson, J. A., Nyborg, A. C., Johnson, J. L., Truscott, S. M., Gunn, A., Nordmeyer, F. R., and Watt, G. D. (1999) Enhanced efficiency of ATP hydrolysis during nitrogenase catalysis utilizing reductants that form the all-ferrous redox state of the Fe protein. *Biochem*. 38, 14279-14285.
14. Lowery, T. J., Wilson, P. E., Zhang, B., Bunker, J., Harrison, P. G., Nyborg, A. C., Thiriot, D., and Watt, G. D. (2006) Flavodoxin Hydroquinone Reduces *Azotobacter vinelandii* Fe Protein to the All-Ferrous Redox State with a S=0 Spin State. *Proc Natl Ac Sci USA*. 103, 17131-17136.
15. Mayhew, S. G. and Ludwig, M. L. (1975) *Flavodoxins and electron-transferring flavoproteins*. Academic Press, New York, NY.
16. Anderson, R. F. (1983) Energetics of the One-Electron Reduction Steps of Riboflavin, FMN and FAD to Their Fully Reduced Forms. *Biochim Biophys Acta*. 722, 158-162.
17. Mayhew, S. G. and Tollin, G. (1992) General properties of flavodoxins, in *Chemistry and biochemistry of flavoenzymes* (Müller, F., ed.) vol. 3, pp. 389-426, CRC press, Boca Raton, FL.
18. Watt, G. D. (1979) An Electrochemical Method for Measuring Redox Potentials of Low Potential Proteins by Microcoulometry at Controlled Potentials. *Anal Biochem*. 99, 399-407.
19. Alagaratnam, S., van Pouderoyen, G., Pijning, T., Dijkstra, B. W., Cavazzini, D., Rossi, G. L., van Dongen, W. M. A. M., van Mierlo, C. P. M., Berkel, W. J. H., and Canters, G. W. (2005) A Crystallographic Study of Cys69Ala Flavodoxin II from *Azotobacter vinelandii*. Structural Determinants of Redox Potential. *Protein Sci*. 14, 284-2295.

20. Spatzal, T., Aksoyoglu, M., Zhang, L., Andrade, S. L. A., Schleicher, E., Weber, S., Rees, D. D., and Einsle, O. (2011) Evidence for Interstitial Carbon in Nitrogenase FeMo Cofactor. *Science*. 334, 940.
21. Spatzal, T., Perez, K. A., Einsle, O., Howard, J. B., and Rees, D. C. (2014) Ligand Binding to the FeMo-Cofactor: Structure of CO-Bound and Reactivated Nitrogenase. *Science*. 345, 1620-1623.
22. van Mierlo, C. P. M., van Dongen, W. M. A. M., Vergeldt, F., van Berkel, W. J. H., and Steensma, E. (1998) The Equilibrium Unfolding of *Azotobacter vinelandii* Apoflavodoxin II Occurs via a Relatively Stable Folding Intermediate. *Protein Sci.* 7, 2331-2344.
23. Kabsch, W. (2010) XDS. *Acta Crystallographica Section D Biological Crystallography*. 66, 125-132.
24. Winn, M. D., Ballard, C. C., Cowtan, K. D., Dodson, E. J., Emsley, P., Evans, P. R., Keegan, R. M., Krissinel, E. B., Leslie, A. G., McCoy, A., McNicholas, S. J., Murshudov, G. N., Pannu, N. S., Potterton, E. A., Powell, H. R., Read, R. J., Vagin, A., and Wilson, K. S. (2011) Overview of the CCP4 Suite and Current Developments. *Acta Crystallography*. D67, 235-242.
25. Taylor, M. F., Boylan, M. H., and Edmondson, D. E. (1990) *Azotobacter vinelandii* Flavodoxin: Purification and Properties of the Recombinant, Dephospho Form Expressed in *Escherichia coli*. *Biochem.* 29, 6911-6918.
26. Yoch, D. C. (1972) The Electron Transport System in Nitrogen Fixation by Azotobacter. IV. Some Oxidation-Reduction Properties of Azotoflavin. *Biochem Biophys Res Commun.* 49, 335-342.
27. Barman, B. G. and Tollin, G. (1972) Flavine-Protein Interactions in Flavoenzymes. Thermodynamics and Kinetics of Reduction of *Azotobacter* Flavodoxin. *Biochem.* 11, 4755-4759.
28. Steensma, E., Heering, H. A., Hagen, W. R., and Van Mierlo, C. P. M. (1996) Redox Properties of Wild-type, Cys69Ala, and Cys69Ser *Azotobacter vinelandii* Flavodoxin II as Measured by Cyclic Voltammetry and EPR Spectroscopy. *Eur J Biochem.* 235, 167-172.
29. Rusling, J. F. (1998) Enzyme Bioelectrochemistry in Cast Biomembrane-Like Films. *Acc Chem Res.* 31, 363-369.

30. Nassar, A.-E. F., Rusling, J. F., Tominaga, M., Yanagimoto, J., and Nakashima, N. (1996) Electrochemistry of Cast Films of Ferredoxin and Lipid Bilayers on Electrodes. *J Electroanal Chem.* 416, 183-185.
31. Fleming, B. D., Tian, Y., Bell, S. G., Wong, L.-L., Urlacher, V., and Hill, H. A. O. (2003) Redox Properties of Cytochrome P450_{BM3} Measured by Direct Methods. *Eur J Biochem.* 270, 4082-4088.
32. Nassar, A.-E. F., Rusling, J. F., and Kumosinski, T. F. (1997) Salt and pH Effects on Electrochemistry of Myoglobin in Thick Films of a Bilayer-Forming Surfactant. *Biophys Chem.* 67, 107-116.
33. Udit, A. K., Hagen, K. D., Goldman, P. J., Star, A., Gillan, J. M., Gray, H. B., and Hill, M. G. (2006) Spectroscopy and Electrochemistry of Cytochrome P450 BM3-Surfactant Film Assemblies. *J Am Chem Soc.* 128, 10320-10325.
34. Blair, E., Greaves, J., and Farmer, P. J. (2004) High-Temperature Electrocatalysis Using Thermophilic P450 CYP119: Dehalogenation of CCl₄ to CH₄. *J Am Chem Soc.* 126, 8632-8633.
35. Fleming, B. D., Tian, Y., Bell, S. G., Wong, L.-L., Urlacher, V., and Hill, H. A. O. (2003) Redox Properties of Cytochrome P450_{BM3} Measured by Direct Methods. *Eur J Biochem.* 270, 4082-4088.
36. Heering, H. A. and Hagen, W. R. (1996) Complex Electrochemistry of Flavodoxin at Carbon-Based Electrodes Results from a Combination of Direct Electron Transfer, Flavin-Mediated Electron Transfer and Comproportionation. *J Electroanal Chem.* 404, 249-260.
37. Redepenning, J. and Anson, F. C. (1987) Permselectivities of Polyelectrolyte Electrode Coatings as Inferred from Measurements with Incorporated Redox Probes or Concentration Cells. *J Phys Chem.* 91, 4549-4553.
38. Ceres, D. M., Udit, A. K., Hill, H. D., Hill, M. G., and Barton, J. K. (2007) Differential Ionic Permeation of DNA-Modified Electrodes. *J Phys Chem.* 111, 663-668.
39. Tominaga, M., Yanagimoto, J., Nassar, A.-E. F., Rusling, J. F., and Nakashima, N. (1996) Incorporation and Direct Electron Transfer of

Chlorella Ferredoxin in the Bilayer Films of Cationic Lipids on Electrodes. *Chem Lett.* 7, 523-524.

40. Rusling, J. F. and Nassar, A.-E. F. (1993) Enhanced Electron Transfer for Myoglobin in Surfactant Films on Electrodes. *J Am Chem Soc.* 115, 11891-11897.

41. Udit, A. K., Hindoyan, N., Hill, M. G., Arnold, F. H., and Gray, H. B. (2005) Protein-Surfactant Film Voltammetry of Wild-Type and Mutant Cytochrome P450 BM3. *Inorg Chem.* 44, 4109-4111.

42. Lu, Z., Huang, Q., and Rusling, J. F. (1997) Films of Hemoglobin and Didodecyldimethylammonium Bromide with Enhanced Electron Transfer Rates. *J Electroanal Chem.* 423, 59-66.

43. Bard, A. J. and Faulkner, L. R. *Electrochemical Methods – Fundamental and Application*, 2nd ed.; Joh Wiley & Sons: New York, 2000; pp.580-631.

44. Draper, R. D. and Ingraham, L. L. (1968) A Potentiometric Study of the Flavin Semiquinone Equilibrium. *Arch Biochem Biophys.* 125, 802-808.

45. Astuti, Y., Topoglidis, E., Briscoe, P. B., Fantuzzi, A., Gilardi, G., and Durrant, J. R. (2004) Proton-Coupled Electron Transfer of Flavodoxin Immobilized on Nanostructured Tin Dioxide Electrodes: Thermodynamics versus Kinetics Control of Protein Redox Function. *J Am Chem Soc.* 126, 8001-8009.

46. Ludwig, M. L. and Luschinsky, C. L. (1992) Structure and Redox Properties of Clostridial Flavodoxin. In *Chemistry and biochemistry of flavoenzymes* (ed. F. Müller), Vol. 3, p. 427-466. CRC Press, Boca Raton, FL.

47. Hoover, D. M. and Ludwig, M. L. (1997) A Flavodoxin that is Required for Enzyme Activation: The Structure of Oxidized Flavodoxin from *Escherichia coli* at 1.8 Å Resolution. *Protein Sci.* 6, 2525-2537.

48. Ludwig, M. L., Patridge, K. A., Metzger, A. L., Dixon, M. M., Eren, M., Feng, Y., and Swenson, R. P. (1997) Control of Oxidation-Reduction Potentials in Flavodoxin from *Clostridium beijerinckii*: The Role of Conformation Changes. *Biochem.* 36, 1259-1280.

49. Hoover, D. M., Drennan, C. L., Metzger, A. L., Osborne, C., Weber, C. H., Patridge, K. A., and Ludwig, M. L. (1999) Comparison of Wild-type and

Mutant Flavodoxins from *Anacystis nidulans*. Structural Determinants of the Redox Potential. *J Mol Biol.* 294, 725-743.

50. Watt, W., Tulinsky, A., Swenson, R. P., and Watenpaugh, K. D. (1991) Comparison of the Crystal Structures of a Flavodoxin in Its Three Oxidation States at Cryogenic Temperatures. *J Mol Biol.* 218, 195-208.

51. Boal, A. K., Cotruvo Jr., J. A., Stubbe, J., and Rosenzweig, A. C. (2010) Structural Basis for Activation of Class Ib Ribonucleotide Reductase. *Science.* 329, 1526-1530.

52. Kozakov, D., Beglov, D., Bohnuud, T., Mottarella, S. E., Xia, B., Hall, D. R., and Vajda, S. (2013) How Good is Automated Protein Docking? *Proteins: Structure, Function, and Bioinformatics.* 81, 2159-2166.

53. Kozakov, D., Brenke, R., Comeau, S. R., and Vajda, S. (2006) PIPER: An FFT-Based Protein Docking Program with Pairwise Potentials. *Proteins: Structure, Function, and Bioinformatics.* 65, 392-406.

54. Comeau, S. R., Gatchell, D. W., Vajda, S., and Camacho, C. J. (2004) ClusPro: An Automated Docking and Discrimination Method for the Prediction of Protein Complexes. *Bioinformatics.* 20, 45-50.

55. Comeau, S. R., Gatchell, D. W., Vajda, S., and Camacho, C. J. (2004) ClusPro: A Fully Automated Algorithm for Protein-Protein Docking. *Nucleic Acids Res.* 32, W96-W99.

56. Rivas, L., Soares, C. M., Baptista, A. M., Simaan, J., Di Paolo, R. E., Margida, D. H., and Hildebrandt, P. (2005) Electric-Field-Induced Redox Potential Shifts of Tetraheme Cytochromes c_3 Immobilized on Self-Assembled Monolayers: Surface-Enhanced Resonance Raman Spectroscopy and Simulation Studies. *Biophys J.* 88, 4188-4199.

57. Watt, G. D. and Reddy, K. R. N. (1994) Formation of an All Ferrous Fe_4S_4 Cluster in the Iron Protein Component of *Azotobacter vinelandii* Nitrogenase. *J Inorg Biochem.* 53, 281-294.

58. Guo, M., Sulc, F., Ribbe, M. W., Farmer, P. J., and Burgess, B. K. (2002) Direct Assessment of the Reduction Potential of the $[4Fe-4S]^{1+/0}$ Couple of the Fe Protein from *Azotobacter vinelandii*. *J Am Chem Soc.* 124, 12100-12101.

ELECTROCHEMICAL STUDIES OF THE *AZOTOBACTER VINELANDII* NITROGENASE IRON PROTEIN

Abstract

The Fe-protein is the biological reductant of the MoFe-protein. In this chapter, two electrochemical methods were developed to study the redox chemistry occurring at the iron-sulfur cluster of the Fe-protein. These methods were developed to answer two different questions regarding the nitrogenase mechanism: 1) to determine the true midpoint potential of the 1+/0 couple of the 4Fe-4S cluster in the Fe-protein, and 2) to determine the midpoint potential of a mixed-nucleotide form of the Fe-protein.

The first electrochemical method adapted to study the Fe-protein was edge-plane pyrolytic graphite electrodes. This system was used to determine the midpoint potential of the 1+/0 couple of the 4Fe-4S cluster. Although the $[4\text{Fe}-4\text{S}]^{1+/2+}$ couple could be studied with this method, the large charging current at low potentials precluded measurement of the midpoint potential of the $[4\text{Fe}-4\text{S}]^{0/1+}$ couple. Additionally, this method was used to study the $[4\text{Fe}-4\text{S}]^{1+/2+}$ couple of the Fe-protein bound to either MgATP or MgADP. However, unlike literature precedence in which the midpoint potential of the Fe-protein shifted upon nucleotide binding, nucleotide binding did not lead to a shift in the midpoint potential of the 4Fe-4S cluster on edge-plane pyrolytic graphite electrodes. Thus, this method was not used to study the Fe-protein in the mixed nucleotide state.

Single crystal gold electrodes modified with eight different types of self-assembled monolayers (SAMs) were also used to study the redox chemistry of the Fe-protein. These studies revealed a single reversible redox active species on the gold electrodes with slow oxidation kinetics, and a midpoint potential ranging from -36 to -119 mV v. NHE. The variation in midpoint potential between the different

electrodes was attributed to differences in protein binding affinity for the electrodes. Although reproducible, the high potential of the observed redox process suggested that it was not relevant to nitrogenase catalysis, and was instead most likely a degradation product of the iron cofactor in the Fe-protein. Thus, this method was not used to further study the Fe-protein. The series of experiments presented in this chapter provide insight into ways to design future electrochemical studies of the Fe-protein of nitrogenase.

Introduction

Nitrogenase, the protein that converts inert dinitrogen to bioavailable ammonia, is composed of two different component proteins, the MoFe-protein and the Fe-protein (1-3). The MoFe-protein contains two different metal centers, including the FeMo-cofactor, the site of dinitrogen reduction. The Fe-protein is an ATPase that serves as the reductase for the MoFe-protein with ATP hydrolysis at the Fe-protein gating electron transfer to the active site in the MoFe-protein. This mechanism is currently unknown; however, the discovery of specific structural states that define how nitrogenase can exist during catalysis has aided in investigations of this mechanism (4-7). One way to expand on how these structures could be involved in nitrogen reduction is through the investigation of the thermodynamic properties of the nitrogenase component proteins in these forms.

The structure and thermodynamic properties of different states of the Fe-protein and the MoFe-protein have been determined, and are described in the introduction of this thesis (**Table 1.2**). Of particular interest for the studies described in this chapter is the observation that the Fe-protein can exist in three different oxidation states: 2+, 1+, and 0. A second important observation was that the Fe-protein can exist in a variety of conformations with different nucleotides bound, which could provide insight into different intermediates in the nitrogenase electron transfer mechanism. From these observations arise two questions: (1)

what is the contribution of the all ferrous state of the Fe-protein to the biological mechanism of nitrogenase? (2) What is the role of the recently identified mixed nucleotide conformation of the Fe-protein?

An answer to the first question would provide insight into the mechanism by which nitrogenase delivers eight electrons to facilitate nitrogen reduction. In this process, it is generally accepted that one electron is delivered from the $[4\text{Fe}-4\text{S}]^{1+}$ of the Fe-protein to the FeMo-cofactor of the MoFe-protein. This process is coupled to the hydrolysis of two molecules of ATP at the ATP binding sites of the Fe-protein. The Thorneley-Lowe model predicts that eight consecutive electron-transfer cycles that each involves a rate limiting protein-dissociation reaction provides a mechanism by which nitrogenase is able to transfer eight electrons to reduce dinitrogen (8). This mechanism relies on the prediction that the Fe-protein of nitrogenase cycles between the 1+ and 2+ oxidation states to deliver one electron at a time to the MoFe-protein. This process would consume sixteen ATP molecules per molecule of nitrogen reduced. However, the observation that the Fe-protein can reversibly cycle through three different oxidation states rather than two, suggests that this model may be incorrect (9,10). Specifically, if the Fe-protein accessed the all ferrous state during catalysis, two electrons could be donated per ATP hydrolysis cycle. Thus, only eight ATP molecules would be consumed for each molecule of dinitrogen that was reduced to ammonia during four separate cycles of protein association and dissociation.

Experimental results have suggested that this mechanism could be plausible since at relatively low potentials of -470 mV v. NHE, the number of ATP molecules hydrolyzed by the Fe-protein per two electrons transferred to the MoFe-protein (ATP/2e⁻ ratio) was significantly less than the ATP/2e⁻ ratio when nitrogenase activity was monitored at higher solution potentials. Thus, at low potentials, when the Fe-protein may be reduced to the all ferrous oxidation state, the enzyme catalyzed reaction was more energy efficient (11). However, despite these results, the observed midpoint potential for the 1+/0 redox couple of the Fe-protein has left the involvement of the all-ferrous form of the Fe-protein in the

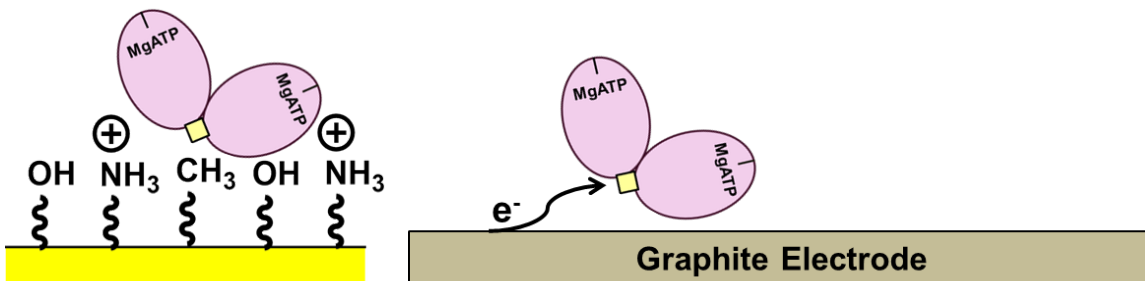


Figure 6.1. Methods for Studying the Redox Properties of Av2. (Left) Schematic depicting the use of SAM-modified single crystal gold electrodes for studying the redox properties of Av2. (Right) Schematic showing the use of edge-plane pyrolytic graphite electrodes to study the redox chemistry at the iron-sulfur cluster of Av2. The iron protein is shown in purple. The 4Fe-4S cluster is a yellow square.

nitrogenase mechanism controversial. Specifically, depending on the method used to measure this potential, it has been reported as ranging from -460 mV v. NHE to -790 mV v. NHE (12,13). The former potential would be physiologically relevant based on the potentials of known biological reductants whereas the potential of the latter would not be accessible in a biological setting. Thus, the exact midpoint potential of this redox process must be accurately determined to understand the physiological role of the all ferrous oxidation state of the Fe-protein.

The second question presented above relates to the thermodynamic properties of a recently discovered form of the Fe-protein that binds one ADP molecule, and one ATP hydrolysis mimic, MgAMP-PCP (5). The structure of this complex suggested that ATP hydrolysis occurs by a stepwise mechanism. Furthermore, it was observed that the orientation of the peptide bond between residues Asp129 and Val130, in the switch II region that connects nucleotide binding to the 4Fe-4S cluster, is different in this structure relative to other structures of the nitrogenase complex. This structural change suggested that there may be a shift in the redox potential of the iron-sulfur cluster when the Fe-protein is in that conformational state. The determination of the midpoint potential for this state could provide insight into the role of the mixed nucleotide form of the Fe-protein in the nitrogenase mechanism.

To answer the questions presented above, two direct electrochemical methods were developed to determine the midpoint potential of the 4Fe-4S cluster in the *Azotobacter vinelandii* nitrogenase Fe-protein (Av2) (**Figure 6.1**). The first method utilized edge-plane pyrolytic graphite electrodes. This method has been widely applied to study the redox cofactors in enzymes (20,21). These electrodes provide both a surface for proteins to adsorb to undergo interfacial electron transfer, as well as a relatively wide potential window over which to study the redox properties of proteins. These properties of edge plane graphite electrodes would make it feasible to measure the midpoint potential of the all ferrous form of the iron-sulfur cluster in Av2, as well as the midpoint potential of the mixed nucleotide state of Av2.

The second method applied to studying the redox properties of Av2 was single crystal gold electrodes modified with self-assembled monolayers (SAMs) of organosulfur compounds. This experimental strategy has provided a versatile tool for studies of electron transfer to redox active proteins (14). The stability of these densely packed ω -derivatized alkane-thiol SAMs on gold electrodes have been well characterized, and the specific chemical properties of these SAMs can be varied by changing the ω -functional group to encourage adsorption of different types of proteins. Furthermore, a variety of surface properties can be achieved by mixing alkane-thiols of different lengths or different ω -functionalization, which allows for the binding of a variety of proteins. Using this technique, well-defined voltammetric responses have been observed for a number of redox-active proteins, including azurin, the Cu_A domain, and cytochrome c (15-17). Despite the utility of this method, due to its limited potential window of electrode stability, it could not be used to study the redox properties of the all ferrous form of Av2. Thus, this method was only developed to study the nucleotide-bound states of Av2.

In summary, edge-plane pyrolytic graphite electrodes were used to examine the midpoint potential of the 0/1+ couple of the iron-sulfur cluster in Av2. Then, a combination of electrochemical studies with edge-plane pyrolytic graphite

electrodes and single crystal gold electrodes were used to study the midpoint potential of the 1+/2+ couple of the iron-sulfur cluster in Av2 in different nucleotide-bound forms. These studies provide a foundation to study the mechanism of ATP hydrolysis-coupled electron transfer from the Fe-protein to the MoFe-protein through the development of electrochemical methods to study Av2.

Methods

Nitrogenase Expression and Purification. The two nitrogenase component proteins were purified from *Azotobacter vinelandii* as described previously (6,18). This protocol is summarized below. The following buffers were prepared, were adjusted to the correct pH at room temperature, and were filtered with a glass fiber filter: ion exchange column wash buffer (50 mM tris-HCl, pH 7.5, 150 mM NaCl, 5mM sodium dithionite), ion exchange column elution buffer (50 mM tris-HCl, pH 7.5, 1 M NaCl, 5 mM sodium dithionite), size exclusion column buffer (50 mM tris-HCl, pH 7.5, 200 mM NaCl, 5 mM sodium dithionite), protein electrochemistry buffer (50 mM potassium phosphate, pH 7.5, 150 mM NaCl), and phosphate buffer (10 mM potassium phosphate, pH 7.5). Dioxygen was removed from all buffers by iterative cycles of vacuum followed by argon filling. All buffers were stored under argon pressure following removal of dioxygen. Sodium dithionite was added to all buffers the day of each purification. All purification steps were either performed in an anaerobic chamber (McCoy) containing an atmosphere of 95 % Ar / 5 % H₂ (< 0 ppm O₂) or by using Schlenk line techniques with argon.

Azotobacter vinelandii were grown in Burke's medium (pH 7.5) in a 100 % air atmosphere. A 1 mL 25 % glycerol stock of *Azotobacter vinelandii* was used to inoculate a 50 mL Burke's medium culture supplemented with 10 mM ammonium chloride. This culture was incubated at 30 °C with shaking for twenty-four hours. This culture was diluted 1/100 into a 500 mL Burke's medium culture supplemented with 10 mM ammonium chloride. This culture was incubated at 30 °C with shaking for twenty-four hours, and then diluted 1/120 into a 60 L

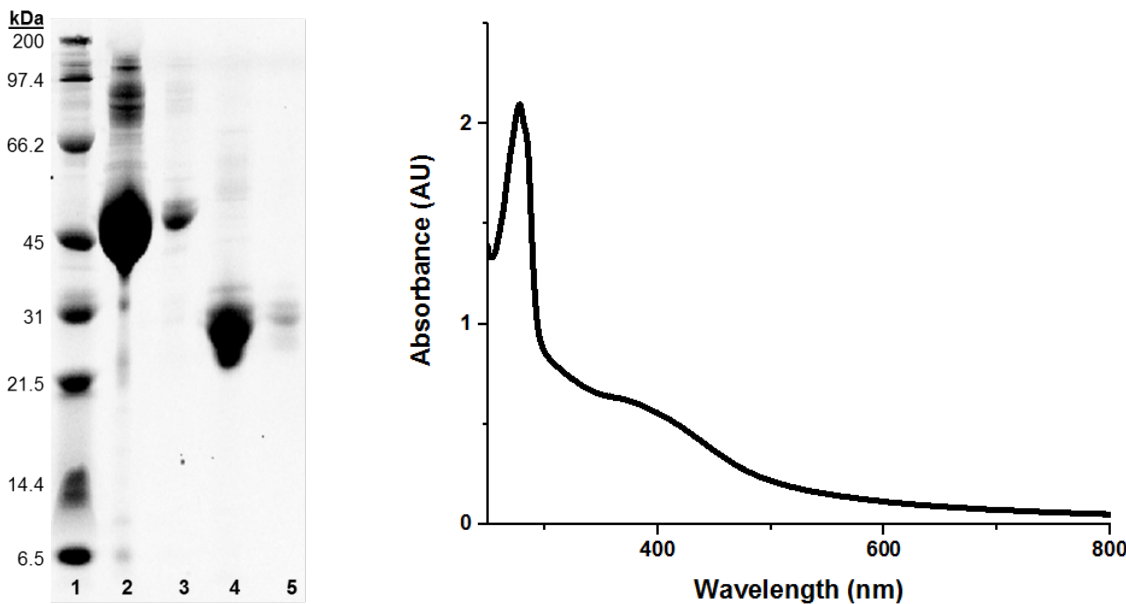


Figure 6.2. Analysis of Purified Nitrogenase Component Proteins. (Left) Coomassie-stained denaturing polyacrylamide gel of the nitrogenase component proteins after purification. Lane 1 = Protein Ladder, Lane 2 = stored Av1, Lane 3 = 1/10 dilution of stored Av1, Lane 4 = stored Av2, Lane 5 = 1/10 dilution of stored Av2. (Right) UV-visible absorption spectrum of Av2 following buffer exchange of the protein into protein electrochemistry buffer.

Burke's medium culture supplemented with 1.3 mM ammonium chloride. The nitrogenase genes were expressed under these conditions due to ammonium depletion in the media. Cells were grown with stirring at 30 °C, and were harvested at an optical density of 1.5-2.0. The cells were pelleted via centrifugation at 6238 x g for 20 minutes at 4 °C. The cell pellets were stored at -80 °C until purification.

The day of purification, *Azotobacter vinelandii* cell pellets were brought into the anaerobic chamber to thaw at room temperature. The cell pellets were re-suspended in ion exchange column wash buffer with 10 mM sodium dithionite in a glass homogenizer. Once re-suspended, the cells were lysed with an Avestin Emulsiflex C5 homogenizer under argon. The cell debris was pelleted by centrifugation in a floor centrifuge at 30,000 x g at 4 °C.

The clarified cell lysate was loaded to a 70 mL HiTrapQ HP anion exchange column (GE Healthcare). The column was attached to an Akta FPLC (GE

Healthcare). The column was washed with ion exchange column wash buffer until the absorbance at 410 nm trace was at baseline levels. Then, a gradient was performed that went from 0 to 100% ion exchange column elution buffer over fourteen column volumes. The MoFe-protein eluted in the first peak almost immediately after beginning the salt gradient. The Fe-protein eluted as the second major peak on the chromatogram. The protein was collected, and was concentrated in an Amicon ultrafiltration cell under an argon overpressure of 35 psi to a final volume of between 8-10 mL. The protein was flash frozen in liquid nitrogen, and was stored under liquid nitrogen until purification by size exclusion chromatography.

The protein purified through the HiTrapQ column was thawed at room temperature in an anaerobic chamber, and was loaded to the Superdex200 26/60 column (GE Healthcare) equilibrated in size exclusion column buffer (450 mL total column volume). The maximum volume of protein loaded to the column was 10 mL. The protein was run through the column with size exclusion column buffer, and the protein eluted from the column at the expected retention time based on the size of the protein. The MoFe-protein eluted at about 235mL following injection of the protein to the size exclusion column. The Fe-protein eluted at about 280 mL following injection of the protein to the size exclusion column. The protein was collected as it eluted from the column, and was concentrated in an Amicon ultrafiltration cell under an argon overpressure of 35 psi to a final concentration of 10-50 mg/mL. This protein was flash frozen in liquid nitrogen. The protein was stored under liquid nitrogen.

The concentration of both proteins was estimated based off of the absorption of the sample at 410 nm (7). The extinction coefficient of the MoFe-protein (Av1) at 410 nm is $76,000 \text{ M}^{-1} \text{ cm}^{-1}$. The extinction coefficient of the Fe-protein (Av2) at 410 nm is $9,400 \text{ M}^{-1} \text{ cm}^{-1}$. The purity of the purified protein was analyzed on a denaturing polyacrylamide gel stained with coomassie blue (**Figure 6.2**).

Acetylene Reduction Assay. The activity of all purified protein was confirmed by monitoring acetylene reduction to ethylene by nitrogenase. The following reaction components were assembled in a 9 mL vial: 50 mM tris-HCl, pH 7.5, 20 mM creatine phosphate, 5 mM ATP, 5 mM MgCl₂, 25 units/mL phosphocreatine kinase, and 25 mM sodium dithionite. The final volume of this reaction mixture was 1 mL. All dioxygen was removed from the reaction mixture by iterative cycles of vacuum followed by argon filling. The final solutions were kept under argon pressure, and all acetylene reduction assays were performed using anaerobic Schlenk line technique under an argon atmosphere. 1 mL of argon headspace was replaced by 1 mL acetylene, and the solution was incubated at 30 °C for five minutes with shaking. The nitrogenase component proteins were added to the reaction mixture along with extra size exclusion column buffer if necessary to keep the total volume of the reaction constant at 1.3 mL. The component protein for which the specific activity was being measured was added last to initiate the reaction. The reactions were incubated at 30 °C for ten minutes with shaking. The reactions were stopped by addition of 1 mL 3 M citric acid. The amount of ethylene produced during the course of the reaction was measured by gas chromatography (activated alumina 60/80 mesh column, flame ionization detector). The total amount of ethylene produced was estimated using an acetylene standard curve.

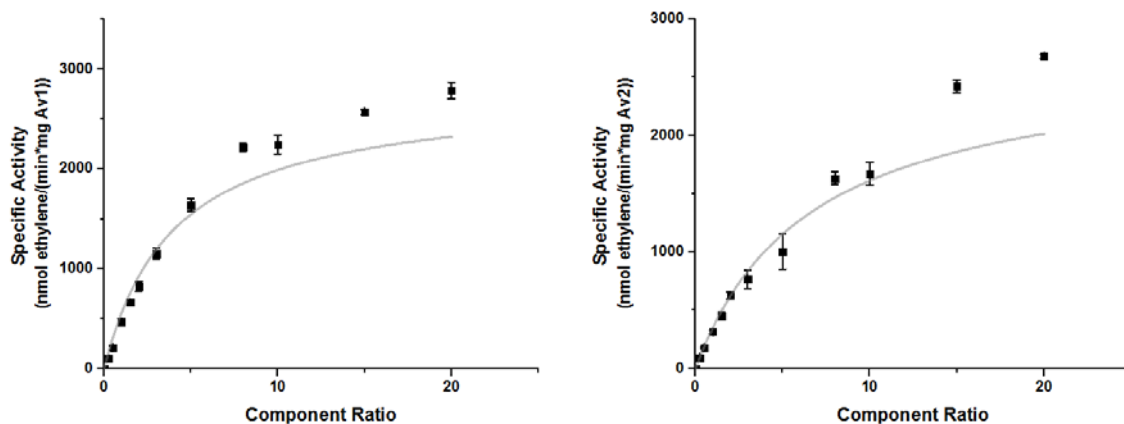


Figure 6.3. Acetylene Reduction Assay. Each point is the average of four assays. Error is reported as standard error. The gray curve indicates the best fit of the data with the Michaelis-Menten equation.

The specific activity of Av1 was 2785 (nmoles ethylene/(min*mg Av1)). The specific activity of Av2 was 2680 (nmoles ethylene/(min*mg Av1)) (**Figure 6.3**). The component ratio (CR) was defined as:

$$\text{CR} = (1.82[\text{Av2}])/[\text{Av1}], \text{ when the units of concentration are mg/mL.}$$

Preparation of Av2 for Electrochemistry Experiments. Prior to electrochemistry experiments, sodium dithionite was removed from all protein samples using a PD10 column (GE Healthcare). This procedure was performed in a McCoy anaerobic chamber with a 95 % / 5 % Ar / H₂ atmosphere with less than 0 ppm dioxygen. The column was first equilibrated in 5 column volumes of protein gold electrochemistry buffer (50 mM potassium phosphate, pH 7.5, 150 mM NaCl) with 10 mM sodium dithionite. Then, the column was equilibrated in 5 column volumes of protein gold electrochemistry buffer. All buffers were filtered with a 0.2 micron filter, and all dioxygen was removed from the buffer by iterative cycles of vacuum followed by filling with argon. The protein was exchanged into protein gold electrochemistry buffer using the PD10 column. UV-visible absorption spectroscopy was used to quantify protein concentration, and to determine the extent of protein oxidation during the course of sample preparation. Following this procedure, the protein was flash frozen in liquid nitrogen, and was brought to Occidental College under liquid nitrogen for experiments.

Av2 Direct Electrochemistry on Edge-Plane Pyrolytic Graphite Electrodes. Edge-plane pyrolytic graphite electrodes were polished with 0.3 micron alumina resin. An electrochemical cell was degassed with argon, and all work was performed using Schlenk line technique under argon. The electrode was submerged in a 400-800 μM Av2 solution in the electrochemical cell. The protein used in these experiments was stored in ion exchange column wash buffer without sodium dithionite (50 mM tris-HCl, pH 7.5, 150 mM NaCl). A platinum auxiliary electrode was also submerged in the protein solution. A Ag/AgCl electrode (made at Occidental College) was used as a reference electrode, and was connected to the chamber of

the electrochemical cell with the working and auxiliary electrodes via a luggin capillary. The Ag/AgCl reference electrode was calibrated with potassium ferricyanide. The electrochemical cell was sealed, and was kept under argon pressure for the entirety of the experiment. Cyclic voltammograms and square wave voltammograms were acquired using a CH instruments potentiostat. All data analysis was performed with the CH instruments software.

Preparation of Single Crystal Gold Electrodes Modified with ω -Functionalized Alkane-Thiols. The single crystal gold electrodes were prepared by Dr. Keiko Yokoyama as described previously (14-16).

Av2 Electrochemistry on Single Crystal Gold Electrodes Modified with ω -Functionalized Alkane-Thiols. The protein was brought into a glovebox along with the single crystal gold electrodes submerged in phosphate buffer. The atmosphere in the glovebox was N₂ with less than 0 ppm dioxygen. The electrodes were soaked in a 200 μ M Av2 solution for 16-20 hours. Then, the electrode was transferred to phosphate buffer for voltammetry studies. A platinum auxiliary electrode and a solid state Ag/AgCl reference electrode (Warner Instruments) were used for all experiments. The Ag/AgCl reference electrode was calibrated with potassium ferricyanide. The total amount of alkane-thiol coating the electrode surface was determined by cathodic stripping voltammetry in 0.5M KOH solution from -0.5 to -1.3V v. Ag/AgCl. Cyclic voltammograms and square wave voltammograms were acquired using a CH instruments potentiostat. All data analysis was performed with the CH instruments software.

Results

Preparation of Active Fe-Protein for Electrochemistry. Robust electrochemical methods require that no contaminating redox active species be present in solution that interfere with the redox process occurring at the electrode. Thus, the reductant sodium dithionite was removed from all preparations of the Fe-protein prior to electrochemical studies. Sodium dithionite was removed from the protein by buffer

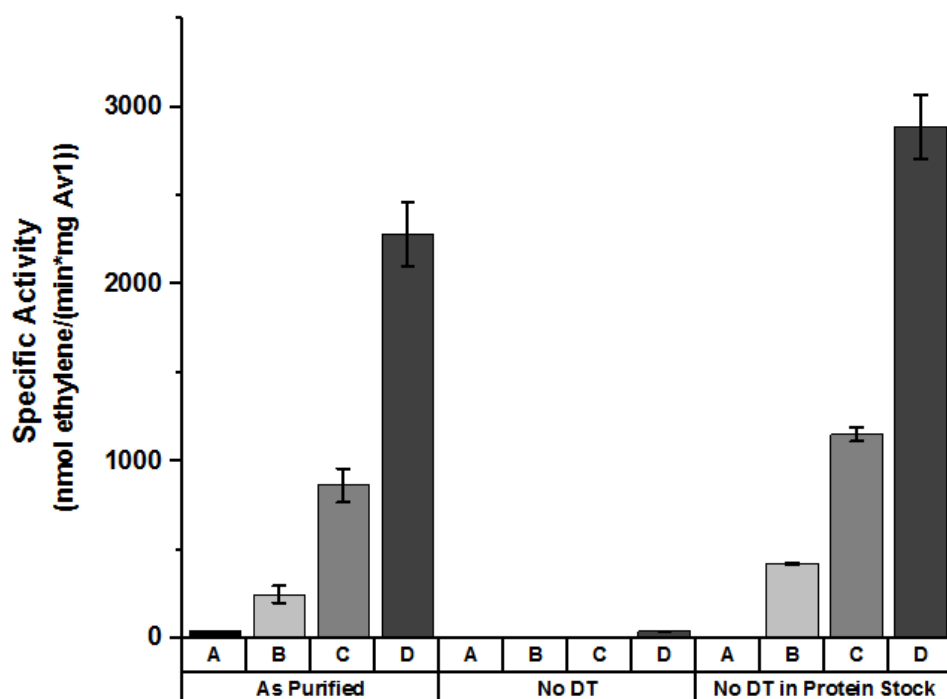


Figure 6.4. Nitrogenase Activity Following Preparation for Electrochemistry Experiments. Acetylene reduction assays were performed to monitor nitrogenase activity. The designation 'as purified' indicated that the protein was assayed following isolation from *Azotobacter vinelandii*. There was 25 mM sodium dithionite added to the acetylene reduction assays performed with this protein. The designation 'No DT' indicates that sodium dithionite was removed from the purified protein with a PD10 column, and there was 0 mM sodium dithionite added to the acetylene reduction assay reaction. The designation 'No DT in Protein Stock' indicated that the sodium dithionite had been removed from the protein, but the acetylene reduction assay was prepared with 25 mM sodium dithionite to determine whether the purification procedure affected protein activity. The letters A-D indicate the component ratio (CR) used for the assay: A = CR 0, B = CR 0.5, C = CR 2, and D = CR 10. Each point is the average of two assays. Error is reported as standard error.

exchange with a PD10 size exclusion column. The removal of sodium dithionite was confirmed by UV-visible absorption spectroscopy and by an acetylene reduction assay for nitrogenase activity (**Figure 6.2 and 6.4**). Sodium dithionite has a characteristic absorption band at about 310 nm, so the absence of sodium dithionite was confirmed by disappearance of this band (19). Furthermore, UV-visible absorption spectroscopy was used to determine that the protein was not oxidized during the course of the experiment by comparing the absorption spectrum of the desalted protein to both the absorption spectrum of the air-oxidized protein and the absorption spectrum of the protein isolated during purification.

Acetylene reduction assays to test nitrogenase activity performed with the protein for electrochemistry experiments revealed that this protein was as active as the protein purified in the presence of sodium dithionite, suggesting that the 4Fe-4S cluster in the protein was intact for electrochemistry experiments. Additionally, the lack of acetylene reduction in the absence of added sodium dithionite suggested that there was no contaminating sodium dithionite in the protein prepared for electrochemistry experiments.

Direct Electrochemistry of the Fe-Protein on Edge-Plane Pyrolytic Graphite Electrodes. The redox properties of Av2 were studied on edge-plane pyrolytic graphite electrodes to determine the midpoint potential of both the 1+/2+ couple and the 1+/0 couple of the iron-sulfur cluster. Edge-plane pyrolytic graphite electrodes were chosen for this study because they have been shown to be a good material for protein adsorption for electrochemical measurements (20,21). Additionally, the potential range accessible with this type of electrode would make it possible to measure the low midpoint potential of the all-ferrous form of the 4Fe-4S cluster in Av2.

The high charging current observed with these electrodes precluded the use of cyclic voltammetry for the study of the Fe-protein since the background was too large to observe the faradaic current associated with the iron cofactor in Av2.

Therefore, square wave voltammetry was used to study the electrochemical response of the Fe-protein on edge-plane pyrolytic graphite electrodes. There were two redox active species that were reproducibly observed only when the electrodes were soaked in Av2. The first species had an oxidation potential of 63 ± 38 mV v. NHE, and was hypothesized to be a degradation product of the 4Fe-4S cluster in Av2 (**Figure 6.5**). The second redox-active species had a midpoint potential of -270 ± 20 mV v. NHE, and this was assigned as the oxidation potential of the $[4\text{Fe}4\text{S}]^{1+/2+}$ couple. The $[4\text{Fe}-4\text{S}]^{1+/0}$ couple was not observed during the course of these experiments. Upon addition of MgADP or MgATP in five-fold molar excess over the concentration of Av2, the oxidation potential of the $[4\text{Fe}-4\text{S}]^{1+/2+}$ couple did not shift (**Figure 6.5**). This result is in disagreement with previous studies using chemical redox titrations, which suggested that the midpoint potential of the $[4\text{Fe}-4\text{S}]^{1+/2+}$ couple shifted -160 mV upon MgADP binding by Av2 or -120 mV upon MgATP binding by Av2 (22,23). Due to the absence of the expected potential shift upon nucleotide binding in the context of this experiment, this method was not used to study the proposed mixed nucleotide state of Av2.

Cyclic Voltammetry of the Fe-Protein on Single Crystal Gold Electrodes Modified with Alkane-Thiol SAMs. Single crystal gold electrodes modified with self-assembled monolayers of ω -functionalized alkane-thiols are a versatile method for studying the direct electrochemistry of a variety of redox active proteins, such as azurins (14-17). This electrode system was used to study the redox properties of the 4Fe-4S cluster of Av2. Notably, the potential window for this technique is limited since scanning to negative potentials less than about -0.45 V v. NHE would drive the reduction of the gold-sulfur bond attaching the alkane-thiols at the electrode surface. Thus, this technique was not used to determine the midpoint potential of the $1+/0$ couple of Av2. However, this technique could be used to study the proposed mixed nucleotide state of Av2.

In this study, eight different SAMs of ω -derivatized alkane thiols ($\omega\text{-C}_{10}\text{-SH}$) on single crystal gold electrodes were assayed to determine the best system to

monitor the redox chemistry of Av2. The redox chemistry of Av2 on these different monolayers is summarized in **Table 6.1**, and is described below.

Three types of alkane thiols were combined in different ratios to form SAMs on single crystal gold electrodes to make eight different types of electrodes in total. All SAMs were formed with an alkane thiol that consisted of a ten carbon linker that connected the thiol functional group that covalently linked this molecule to the electrode and the head group that formed a non-covalent interaction with Av2 to bind the protein to the electrode. The alkane-thiols only differed by the head group, which was either an alcohol, an amine, or a methyl functional group. The only self-assembled monolayers that did not have a redox-active species adsorbed were those formed with a ratio of 1:1 HS-C₁₀-OH: HS-C₁₀-CH₃ and 1:2:1 HS-C₁₀-NH₂ : HS-C₁₀-CH₃: HS-C₁₀-OH. Thus, it could be concluded that the amine functional group at the terminus of the alkane-thiol favored binding of Av2 to the electrodes. This observation is consistent with the overall negative charge on Av2.

On all single crystal gold electrodes, there was generally a reversible redox process observed with a midpoint potential between -36 and -119 mV v. NHE

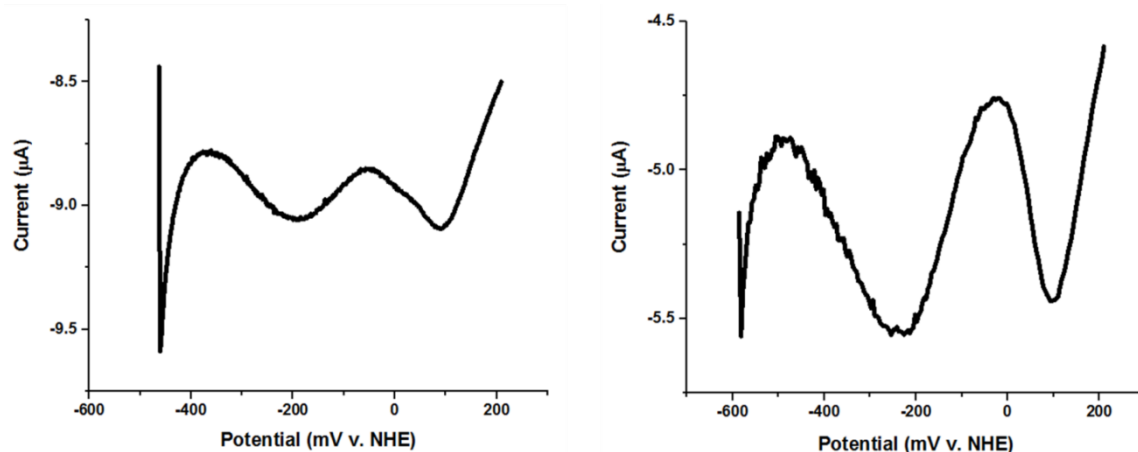


Figure 6.5. Av2 Direct Electrochemistry on Edge-Plane Pyrolytic Graphite Electrodes. (Left) Square wave voltammogram of 250 μ M Av2 in ion exchange column wash buffer with 10 mM MgCl₂. Potential Increment = 2 mV, Amplitude = 25 mV, Frequency = 2 Hz. (Right) Square wave voltammogram of 400 μ M Av2 in ion exchange column wash buffer with 10 mM MgCl₂ and 10 mM ADP. Potential Increment = 4 mV, Amplitude = 25 mV, Frequency = 2 Hz.

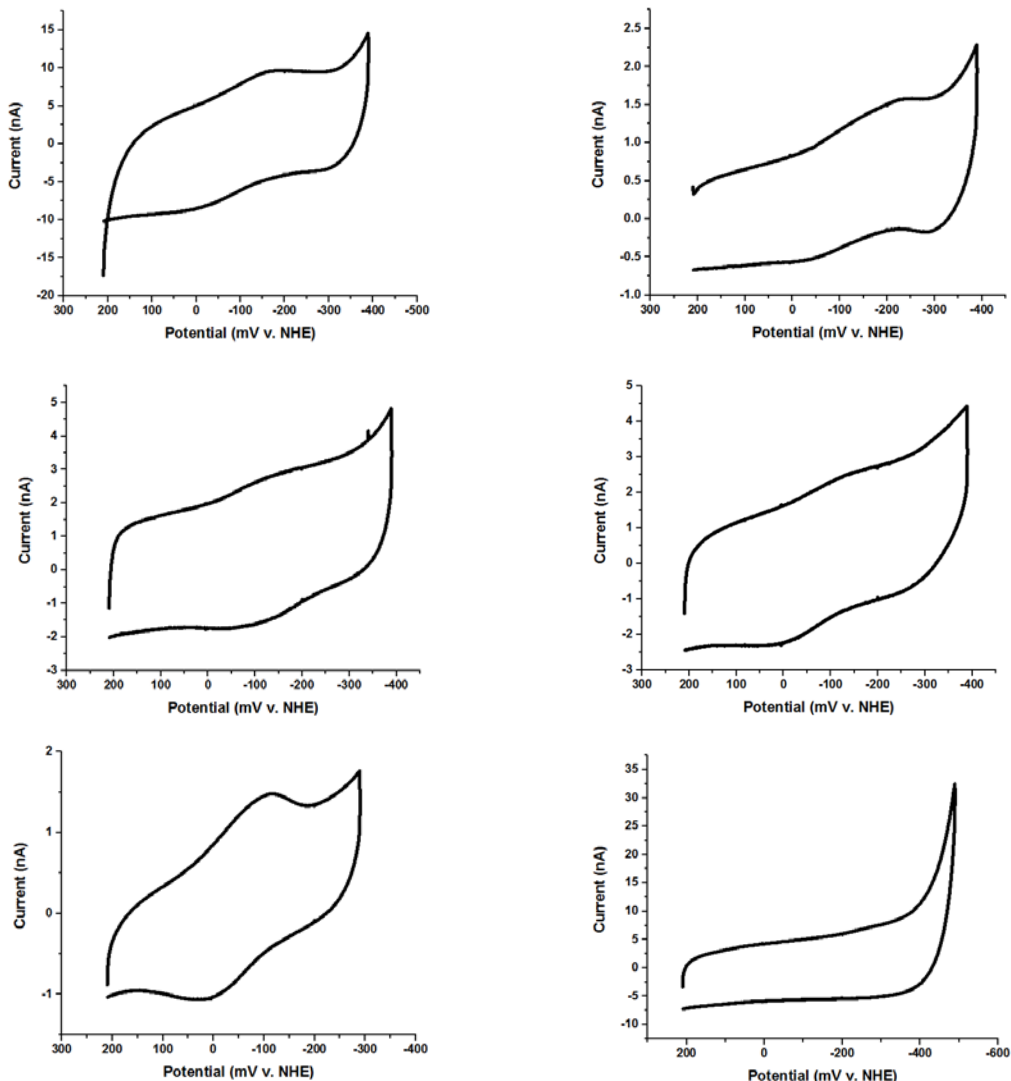


Figure 6.6. Cyclic Voltammograms of Av2 on Single Crystal Gold Electrodes.

Electrodes were modified with self-assembled monolayers of alkane thiols with different ω -functionalization. (Top Left) A self-assembled monolayer was formed with a ratio of 1:1 $\text{NH}_2\text{-C}_{10}\text{-SH} : \text{CH}_3\text{-C}_{10}\text{-SH}$. The cyclic voltammogram was acquired at a scan rate of 5 mV/s. (Top Right) A self-assembled monolayer formed with ratio of 1:1:1 $\text{NH}_2\text{-C}_{10}\text{-SH} : \text{CH}_3\text{-C}_{10}\text{-SH} : \text{OH-C}_{10}\text{-SH}$. The cyclic voltammogram was acquired at a scan rate of 1 mV/s. (Middle Left) A self-assembled monolayer formed with a ratio of 3:1 $\text{NH}_2\text{-C}_{10}\text{-SH} : \text{OH-C}_{10}\text{-SH}$. The cyclic voltammogram was acquired at a scan rate of 2 mV/s. (Middle Right) A self-assembled monolayer was formed with a ratio of 3:1 $\text{OH-C}_{10}\text{-SH} : \text{NH}_2\text{-C}_{10}\text{-SH}$. The cyclic voltammogram was acquired at a scan rate of 2 mV/s. (Bottom Left) A self-assembled monolayer was formed with a ratio of 2:1:1 $\text{NH}_2\text{-C}_{10}\text{-SH} : \text{OH-C}_{10}\text{-SH} : \text{CH}_3\text{-C}_{10}\text{-SH}$. The cyclic voltammogram was acquired at a scan rate of 0.5 mV/s. (Bottom Right) Cyclic voltammogram of an electrode soaked in protein electrochemistry buffer. The self-assembled monolayer was formed with a ratio of 1:1 $\text{OH-C}_{10}\text{-SH} : \text{NH}_2\text{-C}_{10}\text{-SH}$. The cyclic voltammogram was acquired at a scan rate of 5 mV/s.

Table 6.1. Midpoint Potential of Av2 on Gold Electrodes.

Self-Assembled Monolayer	Midpoint Potential (mV v. NHE)
1:1:1 CH ₃ -C ₁₀ -SH : NH ₂ -C ₁₀ -SH : OH-C ₁₀ -SH	-113
1:1:2 CH ₃ -C ₁₀ -SH : OH-C ₁₀ -SH : NH ₂ -C ₁₀ -SH	-42 ± 6
1 : 1 OH-C ₁₀ -SH : NH ₂ -C ₁₀ -SH	-111 ± 64
1 : 1 OH-C ₁₀ -SH : CH ₃ -C ₁₀ -SH	No Redox Process Observed
1 : 1 NH ₂ -C ₁₀ -SH : CH ₃ -C ₁₀ -SH	-76
2:1:1 CH ₃ -C ₁₀ -SH : OH-C ₁₀ -SH : NH ₂ -C ₁₀ -SH	No Redox Process Observed
1 : 3 OH-C ₁₀ -SH : NH ₂ -C ₁₀ -SH	-119
3 : 1 OH-C ₁₀ -SH : NH ₂ -C ₁₀ -SH	-61

depending on the electrode type (**Figure 6.6**). The difference in midpoint potential on different ω -derivatized alkane-thiol modified electrodes suggested that the protein has a different affinity depending on the electrode type (24,25). The kinetics of both of the redox processes observed for Av2 on single crystal gold electrodes was very slow, with reversibility only observed on cyclic voltammograms acquired at scan rates less than 5 mV/s. This observation was consistent with the finding that upon slow oxidation of the protein bound to the electrode by square wave voltammetry, the reductive peak potential shifted by about -60 mV v. NHE, and increased in size (**Figure 6.7**). This result was reversible, and suggested that there could be some sort of conformational change occurring upon oxidation of the iron-sulfur cluster in the Av2 that is the rate limiting step in the re-oxidation of this protein. In a biological context, the slow oxidation kinetics of Av2 could be rationalized since, under optimal conditions, protein oxidation should be regulated such that the Fe-protein is only oxidized when donating electrons to the MoFe-protein.

In addition to the general features outlined above describing Av2 redox chemistry on single crystal gold electrodes, there were also distinguishing features of the redox process observed on the different alkane-thiol modified gold electrodes. Specifically, under certain conditions the reductive redox process appeared to have two overlapping peaks as observed by cyclic voltammetry on gold electrodes modified with a ratio of 1:1:1 HS-C₁₀-CH₃ :HS-C₁₀-NH₂ :HS-C₁₀-OH and 2:1:1 HS-C₁₀-NH₂: HS-C₁₀-CH₃: HS-C₁₀-OH. Thus, on these monolayers, there may have been multiple orientations of Av2 that each had different midpoint potentials. This finding is consistent with the variation observed in redox potential between the different types of alkane-thiol modified electrodes. Since the cathodic peaks on these voltammograms could not be easily distinguished when determining the midpoint potential of the redox process, the potential of the combined cathodic peak was used to calculate this value. The monolayers composed of either a 1:1 HS-C₁₀-OH: HS-C₁₀-NH₂, 1:3 HS-C₁₀-OH: HS-C₁₀-NH₂, or 3:1 HS-C₁₀-OH: HS-C₁₀-NH₂ monolayer had very large anodic peaks at slow scan rates, suggesting that oxidation of Av2 on these monolayers was more facile

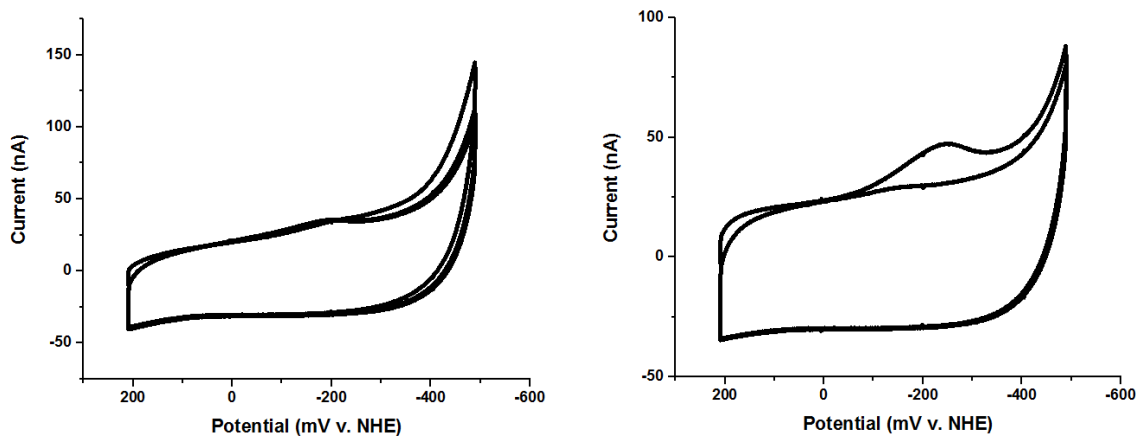


Figure 6.7. Oxidation of Av2 on Single Crystal Gold Electrodes. Comparison of cyclic voltammograms of Av2 (Left) and Av2 after slow oxidation with square wave voltammogram (Potential Increment = 2mV, amplitude = 25mV, Frequency = 2Hz) from -0.6V v. Ag/AgCl to 0 V v. Ag/AgCl. (Right). The cyclic voltammograms were acquired at 50 mV/s.

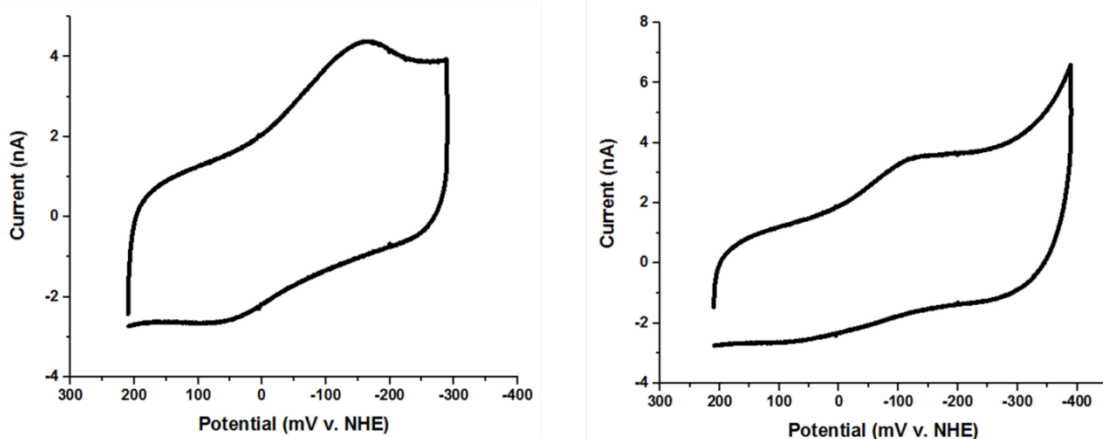


Figure 6.8. Redox Chemistry of Av2 Bound to MgATP on Single Crystal Gold Electrodes. Comparison of Cyclic Voltammograms of Av2 in phosphate buffer (Left) and Av2 bound to MgATP in phosphate buffer with 1 mM MgATP (Right). The cyclic voltammograms were acquired at 2 mV/s.

than on the other monolayers. Thus, the alkane-thiol monolayer formed on the gold electrode seemed to affect both the electron transfer kinetics and midpoint potential of the observed redox process, suggesting that the redox chemistry of Av2 can be affected by environmental factors.

To further study the redox process observed at the single crystal gold electrode, the midpoint potential of Av2 was determined under two different conditions in which Av2 was expected to bind MgATP. First, the protein was adsorbed to the electrode. Then, the electrode was soaked in a solution of phosphate buffer with 1 mM MgATP for cyclic voltammogram acquisition. Second, the electrode was soaked in a solution of the Fe-protein with 1 mM MgATP to adsorb the ATP-bound protein to the electrode. Under both of these conditions, the midpoint potential of the observed redox-active species did not shift as predicted by literature precedence (**Figure 6.8**) (24,25). Thus, it was concluded that the redox-active species being monitored on single crystal gold electrodes was not relevant to nitrogen fixation, and was more likely a degradation product of this iron cofactor.

Conclusion

The Fe-protein is the biological reductant of nitrogenase, and uses energy derived from ATP hydrolysis to drive electron transfer to the metal clusters of the MoFe-protein to catalyze substrate reduction (1-3). The redox properties of this protein have been extensively characterized by redox titration with chemical mediators (12,13,22,23). Although these methods have provided insight into the thermodynamic properties of the iron-sulfur cluster bound by the Fe-protein, these techniques were not able to conclusively determine the midpoint potential of the all ferrous form of the iron-sulfur cluster in the Fe-protein. This ambiguity in midpoint potential has left open the question of the biological relevance of the all ferrous form of the Fe-protein in nitrogenase catalysis. To gain additional insight into the midpoint potential in this electronic transition, as well as to better determine the shift in midpoint potential of the iron-sulfur cluster in the Fe-protein in different nucleotide bound states, two direct electrochemical methods were developed. The first method used edge-plane pyrolytic graphite electrodes to monitor redox chemistry occurring at the iron-sulfur cluster in Av2. This system was employed to study the all ferrous state of the iron-sulfur cluster of the Fe-protein, as well as to study the Fe-protein bound to different nucleotides. Single crystal gold electrodes were employed to study the redox chemistry of the Fe-protein in different nucleotide-bound forms.

Square wave voltammetry on edge-plane pyrolytic graphite electrodes revealed two redox active species on the electrode surface. Using this method, a redox species was observed at -270 ± 20 mV v. NHE that was consistent with the potential of the $[4\text{Fe}-4\text{S}]^{1+/2+}$ of the Fe-protein based on similarity to previous measurements of this redox couple using redox titrations with chemical mediators. However, unlike in previous solution studies, the midpoint potential of this couple did not shift when the electrode was submerged in a solution of Fe-protein with MgADP or MgATP. Thus, using this method, there was no potential shift observed for the Fe-protein upon binding of nucleotides. Therefore, the midpoint potential of the mixed nucleotide form of the Fe-protein was not measured with this technique.

The large background charging current most likely precluded observation of the 1+/0 couple in either the nucleotide-free or nucleotide-bound forms of the protein.

Cyclic voltammetry of Av2 on single crystal gold electrodes revealed a redox active species at -36 to -119 mV v. NHE. The positive potential of this species, as well as an absence in midpoint potential shift upon nucleotide binding suggested that it was most likely a degradation product of the iron-sulfur cluster. Thus, this method did not accurately measure the redox potential of the iron-sulfur cluster in Av2, and this method could not be used to determine the redox chemistry of Av2 in different nucleotide-bound forms. Although unsuccessful, these studies provide insight into direct electrochemical methods to study the redox chemistry of the Fe-protein.

References

1. Howard, J. B. and Rees, D. C. (2006) How Many Metals Does it Take to Fix N₂? A Mechanistic Overview of Biological Nitrogen Fixation. *Proc Natl Acad Sci USA*. 103, 17088-17093.
2. Burgess, B. K. and Lowe, D. J. (1996) Mechanism of Molybdenum Nitrogenase. *Chem Rev*. 96, 2983-3011.
3. Spatzal, T. (2015) The Center of Biological Nitrogen Fixation: FeMo Cofactor. *Z Anorg Allg Chem*. 1, 10-17.
4. Tezcan, F. A., Kaiser, J. T., Mustafi, D., Walton, M. Y., Howard, J. B., and Rees, D. C. (2005) Nitrogenase Complexes: Multiple Docking Sites for a Nucleotide Switch Protein. *Science*. 309, 1377-1380.
5. Tezcan, F. A., Kaiser, J. T., Howard, J. B., and Rees, D. C. (2015) Structural Evidence for Asymmetrical Nucleotide Interactions in Nitrogenase. *J Am Chem Soc*. 137, 146-149.
6. Spatzal, T., Perez, K. A., Einsle, O., Howard, J. B., and Rees, D. C. (2014) Ligand Binding to the FeMo-Cofactor: Structure of CO-Bound and Reactivated Nitrogenase. *Science*. 345, 1620-1623.
7. Spatzal, T., Perez, K. A., Howard, J. B., and Rees, D. C. (2015) Catalysis-Dependent Selenium Incorporation and Migration in the Nitrogenase Active Site Iron-Molybdenum Cofactor. *Elife*. E11620.
8. Thorneley, R. N. F.; Lowe, D. J. In Molybdenum Enzymes; Spiro, T. G., Ed.; Wiley-Interscience: New York, 1985; p 221.
9. Angrove, H. C., Yoo, S. J., Münck, E., and Burgess, B. K. (1998) An All-Ferrous State of the Fe Protein of Nitrogenase. Interaction with Nucleotides and Electron Transfer to the MoFe Protein. *J Biol Chem*. 273, 26330-26337.
10. Strop, P., Takahara, P. M., Chiu, H., Angove, H. C., Burgess, B. K., and Rees, D. C. (2001) Crystal Structure of the All-Ferrous [4Fe-4S]⁰ Form of the Nitrogenase Iron Protein from *Azotobacter vinelandii*. *Biochem*. 40, 651-656.

11. Hallenbeck, P. C. (1983) Nitrogenase Reduction by Electron Carriers: Influence of Redox Potential on Activity and the ATP/2e⁻ Ratio. *Archives of Biochem and Biophys.* 220, 657-660.
12. Watt, G. D. and Reddy, K. R. N. (1994) Formation of an All Ferrous Fe₄S₄ Cluster in the Iron Protein Component of *Azotobacter vinelandii* Nitrogenase. *J Inorg Biochem.* 53, 281-294.
13. Guo, M., Sulc, F., Ribbe, M. W., Farmer, P. J., and Burgess, B. K. (2002) Direct Assessment of the Reduction Potential of the [4Fe-4S]^{1+/0} Couple of the Fe Protein from *Azotobacter vinelandii*. *J Am Chem Soc.* 124, 12100-12101.
14. Yokoyama, K., Leigh, B. S., Sheng, Y., Niki, K., Nakamura, N., Ohno, H., Winkler, J. R., Gray, H. B., and Richards, J. H. (2008) Electron Tunneling through *Pseudomonas aeruginosa* Azurins on SAM Gold Electrodes. *Inorganica Chim Acta.* 361, 1095-1099.
15. Fujita, K., Nakamura, N., Ohno, H., Leigh, B. S., Niki, K., Gray, H. B., and Richards, J. H. (2004) Mimicking Protein-Protein Electron Transfer: Voltammetry of *Pseudomonas aeruginosa* Azurin and the *Thermus thermophilus* Cu_A Domain of ω -Derivatized Self-Assembled-Monolayer Gold Electrodes. *J Am Chem Soc.* 126, 13954-13961.
16. Katsumi, N., Hardy, W. R., Hill, M. G., Li, H., Sprinkle, J. R., Margoliash, E., Fujita, K., Tanimura, R., Nakamura, N., Ohno, H., Richards, J. H., and Gray, H. B. (2003) Coupling to Lysine-13 Promotes Electron Tunneling through Carboxylate-Terminated Alkanethiol Self-Assembled Monolayers to Cytochrome *c*. *J Phys Chem B.* 107, 9947-9949.
17. Gaigalas, A. K. and Niaura, G. (1997) Measurement of Electron Transfer Rates between Adsorbed Azurin and a Gold Electrode Modified with a Hexanethiol Layer. *J. Colloid Interface Sci.* 193, 60-70.
18. Spatzal, T., Aksoyoglu, M., Zhang, L., Andrade, S. L. A., Schleicher, E., Weber, S., Rees, D. D., and Einsle, O. (2011) Evidence for Interstitial Carbon in Nitrogenase FeMo Cofactor. *Science.* 334, 940.
19. Mayhew, S. G. and Massey, V. (1973) Studies on the Kinetics and Mechanism of Reduction of Flavodoxin from *Peptostreptococcus Elsdenii* by Sodium Dithionite. *Biochim et Biophys Acta.* 315, 181-190.

20. Armstrong, F. A., George, S. J., Cammack, R., Hatchikian, E. C., and Thomson, A. J. (1989) Electrochemical and Spectroscopic Characterization of the 7Fe Form of Ferredoxin III from *Desulfovibrio africanus*. *Biochem J.* 264, 265-273.
21. Maiocco, S. J., Grove, T. L., Booker, S. J., and Elliott, S. J. (2015) Electrochemical Resolution of the [4Fe-4S] Centers of the AdoMet Radical Enzyme BtrN: Evidence of Proton Coupling and an Unusual, Low-Potential Auxiliary Cluster. *J Am Chem Soc.* 137, 8664-8667.
22. Ryle, M. J. and Seefeldt, L. C. (1996) Elucidation of a MgATP Signal Transduction Pathway in the Nitrogenase Iron Protein: Formation of a Conformation Resembling the MgATP-Bound State by Protein Engineering. *Biochem.* 35, 4766-4775.
23. Ryle, M. J. and Seefeldt, L. C. (1996) The [4Fe-4S] Cluster Domain of the Nitrogenase Iron Protein Facilitates Conformational Changes Required for the Cooperative Binding of Two Nucleotides. *Biochem.* 35, 15654-15662.
24. Rivas, L., Soares, C. M., Baptista, A. M., Simaan, J., Di Paolo, R. E., Margida, D. H., and Hildebrandt, P. (2005) Electric-Field-Induced Redox Potential Shifts of Tetraheme Cytochromes c₃ Immobilized on Self-Assembled Monolayers: Surface-Enhanced Resonance Raman Spectroscopy and Simulation Studies. *Biophys J.* 88, 4188-4199.
25. Genereux, J. C., Boal, A. K., and Barton, J. K. (2010) DNA-Mediated Charge Transport in Redox Sensing and Signaling. *J Am Chem Soc.* 132, 891-905.

*Appendix 1***MATERIALS FOR *S. CEREVISIAE* DNA2 EXPRESSION IN
*E.COLI***

Table A1.1. Primers for Construction of the Wildtype and Mutant pQTEV-DNA2 Overexpression Plasmids

Primer	Sequence
yDna2-pQTEV Primer 1**	5'- CGATTACGACATCCCCACTACTGAGAATCTT ATTTTCAGGGATCCATGCCCGGAACGCCACAGAA G -3'
yDna2-pQTEV Primer 2	5'- CTCTTTGTAGTTGGCGAGATTTGCG -3'
yDna2-pQTEV Primer 3	5'- GACAAACCATTGTCGCAAAATCTGCCAACT ACAAAGAG -3'
yDna2-pQTEV Primer 4**	5'-GGAGTCCAAGCTCAGCTAATTAAAGCTTGGCT GCAGGTCGAGCGGCCGCTCAACTTCATACTCTT GTAGAATTCCTTATGATAGG -3'
pQTEV-yDna2 N-Met Del. Forward	5'- CTGAGAATCTTATTTCAAGGGATCCCCGG AACGCCACAG -3'
pQTEV-yDna2 N-Met Del. Reverse	5'- CCTCTTGTCTCTGTGGCGTCCGGGGAT CCCTGAAAATAAG -3'
pQTEV-Dna2 Check Primer 1	5'- TGAGCGGATAACAATTACACAG -3'
pQTEV-Dna2 Check Primer 2	5'- GGCAACCGAGCGTTCTGAAC -3'
pQTEV-Dna2 Check Primer 3	5'- CTTCAGACGAATTCAGACG -3'
pQTEV-Dna2 Check Primer 4	5'- GCAAAAACCTCGTTATTCCCGC -3'
pQTEV-Dna2 Check Primer 5	5'- GTTCGAAAAGTAACATGG -3'
pQTEV-Dna2 Check Primer 6	5'- ATCTCTAAACTAGGTGCTC -3'
pQTEV-yDna2 Check7	5'- GGACGGCCCCATGGAAGAAG -3'
pQTEV-yDna2 Check8	5'- CTTGATGTATTCGTACTTGTG -3'

**Purified via PAGE

^a Primer sequence adapted from 5.

Table A1.2. Primers for Site-Directed Mutagenesis of the Dna2 Overexpression Plasmid

Primer	Sequence
Dna2 E675A Forward	5'- GTTGAAAACAATAAAAAACACATCGTTCCTTAGCAGTGAAA ACTG -3'
Dna2 E675A Reverse	5'- CGCTTCTGGATTTCCAGTTTCACTGCTAAAGGAACGAT GTG -3'
Dna2 K1080E Forward	5'-CAGGGACTGGTGAGACTACTGTTATCGCAGAAATTATTAAA ATTCTCG -3'
Dna2 K1080E Reverse	5'- CTGCGATAACAGTAGTCTCACCAAGTCCCTGGCATTCCAA TATCAATG -3'
Dna2 P504S Forward	5'- CTGTTGGTGCTAAACTCTGATGTATTATTTCG -3'
Dna2 P504S Reverse	5'- CGAAAATAATACATCAGAGTTAGCACCAACAG -3'
Dna2 C771S Forward	5'- CATCTTGTGATTCATCTTCATCAAAGAACATC -3'
Dna2 C771S Reverse	5'- GATTCTTGATGAAAGATGAATCACAAGATG -3'
yDna2 C771A Forward ^a	5'- CATCTTGTGATTCAGCTTCATCAAAGAACATC -3'
yDna2 C771A Reverse ^a	5'- GATTCTTGATGAAAGCTGAATCACAAGATG -3'
Dna2 C519A Forward ^a	5'- GGAAGTTCAGTAGGTGCTTAAGACGTTCAATT -3'
Dna2 C519A Reverse ^a	5'- GAATTGAACGTCTAAAGCACCTACTGAACCTCC -3'
Dna2 C768A Forward ^a	5'- CTGCGCGATTCATCTGCTGATTCATGTTCATC -3'
Dna2 C768A Reverse ^a	5'- GATGAAACATGAATCAGCAGATGAATCGCGCAG -3'
Dna2 C777A Forward ^a	5'- GTTTCATCAAAGAACATGCCATGGTGTGAATAAGCTAC -3'
Dna2 C777A Reverse ^a	5'- GTAGCTTATTCAACACCAGGCTGATTCTTGATGAAAC -3'

^a Primer sequence from Pokharel, S. and Campbell, J. L. (2012) *Nucleic Acids Res.* 40, 7821-7830.

Table A1.3. Plasmids for Dna2 Overexpression

Plasmid	Description
pQTEV-Δ1-107 DNA2	Plasmid for Dna2 Δ1-107 Dna2 Overexpression in <i>E. coli</i>
pQTEV-DNA2 (with N-terminal Methionine)	Plasmid for Dna2 Overexpression in <i>E. coli</i> (with N-terminal Methionine)
pQTEV-DNA2*	Plasmid for Dna2 Overexpression in <i>E. coli</i> (without N-terminal Methionine)*
pQTEV-DNA2 E675A	Plasmid for Dna2 E675A Overexpression in <i>E. coli</i>
pQTEV-DNA2 K1080E	Plasmid for Dna2 K1080E Overexpression in <i>E. coli</i>
pQTEV-DNA2 P504S	Plasmid for Dna2 P504S Overexpression in <i>E. coli</i>
pQTEV-DNA2 C771S	Plasmid for Dna2 C771S Overexpression in <i>E. coli</i>
pQTEV-DNA2 C771A	Plasmid for Dna2 C771A Overexpression in <i>E. coli</i>
pQTEV-DNA2 C519A	Plasmid for Dna2 C519A Overexpression in <i>E. coli</i>
pQTEV-DNA2 C768A	Plasmid for Dna2 C768A Overexpression in <i>E. coli</i>
pQTEV-DNA2 C777A	Plasmid for Dna2 C777A Overexpression in <i>E. coli</i>

^a Construct used as template to make mutant Dna2 overexpression plasmids.

Table A1.4. *E. coli* Strains for Wildtype and Mutant Dna2 Overexpression

Strain	Genotype
Rosetta2 (DE3) pLysS pQTEV- Δ 1-107 DNA2	F^+ ompT hsdS _B (r _B m _B) gal dcm (DE3) pLysSRARE2 (Cam ^R) pQTEV- Δ 1-107 DNA2 (Amp ^R)
Rosetta2 (DE3) pLysS pQTEV-DNA2 (with N-terminal Methionine)	F^+ ompT hsdS _B (r _B m _B) gal dcm (DE3) pLysSRARE2 (Cam ^R) pQTEV-DNA2 (with N-terminal Methionine) (Amp ^R)
Rosetta2 (DE3) pLysS pQTEV-DNA2	F^+ ompT hsdS _B (r _B m _B) gal dcm (DE3) pLysSRARE2 (Cam ^R) pQTEV-DNA2 (Amp ^R)
Rosetta2 (DE3) pLysS pQTEV-DNA2 E675A	F^+ ompT hsdS _B (r _B m _B) gal dcm (DE3) pLysSRARE2 (Cam ^R) pQTEV-DNA2 E675A (Amp ^R)
Rosetta2 (DE3) pLysS pQTEV-DNA2 K1080E	F^+ ompT hsdS _B (r _B m _B) gal dcm (DE3) pLysSRARE2 (Cam ^R) pQTEV-DNA2 K1080E (Amp ^R)
Rosetta2 (DE3) pLysS pQTEV-DNA2 P504S	F^+ ompT hsdS _B (r _B m _B) gal dcm (DE3) pLysSRARE2 (Cam ^R) pQTEV-DNA2 P504S (Amp ^R)
Rosetta2 (DE3) pLysS pQTEV-DNA2 C771S	F^+ ompT hsdS _B (r _B m _B) gal dcm (DE3) pLysSRARE2 (Cam ^R) pQTEV-DNA2 C771S (Amp ^R)
Rosetta2 (DE3) pLysS pQTEV-DNA2 C771A	F^+ ompT hsdS _B (r _B m _B) gal dcm (DE3) pLysSRARE2 (Cam ^R) pQTEV-DNA2 C771A (Amp ^R)
Rosetta2 (DE3) pLysS pQTEV-DNA2 C519A	F^+ ompT hsdS _B (r _B m _B) gal dcm (DE3) pLysSRARE2 (Cam ^R) pQTEV-DNA2 C519A (Amp ^R)
Rosetta2 (DE3) pLysS pQTEV-DNA2 C768A	F^+ ompT hsdS _B (r _B m _B) gal dcm (DE3) pLysSRARE2 (Cam ^R) pQTEV-DNA2 C768A (Amp ^R)
Rosetta2 (DE3) pLysS pQTEV-DNA2 C777A	F^+ ompT hsdS _B (r _B m _B) gal dcm (DE3) pLysSRARE2 (Cam ^R) pQTEV-DNA2 C777A (Amp ^R)

Table A1.5. *E. coli* Strains for Storage of the Dna2 Overexpression Plasmids

Strain	Genotype
TOP10 pQTEV-Δ1-107 DNA2	F ⁻ <i>mcrA</i> Δ(<i>mrr-hsdRMS-mcrBC</i>) <i>Φ80lacZΔM15 ΔlacX74 recA1 araD139 Δ(ara-leu)7697 galU galK rpsL endA1 nupG pQTEV-Δ1-107 DNA2 (Amp^R)</i>
TOP10 pQTEV-DNA2 (with N-terminal Methionine)	F ⁻ <i>mcrA</i> Δ(<i>mrr-hsdRMS-mcrBC</i>) <i>Φ80lacZΔM15 ΔlacX74 recA1 araD139 Δ(ara-leu)7697 galU galK rpsL endA1 nupG pQTEV-DNA2 (with N-terminal Methionine) (Amp^R)</i>
TOP10 pQTEV-DNA2	F ⁻ <i>mcrA</i> Δ(<i>mrr-hsdRMS-mcrBC</i>) <i>Φ80lacZΔM15 ΔlacX74 recA1 araD139 Δ(ara-leu)7697 galU galK rpsL endA1 nupG pQTEV-DNA2 (Amp^R)</i>
TOP10 pQTEV	F ⁻ <i>mcrA</i> Δ(<i>mrr-hsdRMS-mcrBC</i>) <i>Φ80lacZΔM15 ΔlacX74 recA1 araD139 Δ(ara-leu)7697 galU galK rpsL endA1 nupG pQTEV (Amp^R)</i>
TOP10 pGal18-DNA2	F ⁻ <i>mcrA</i> Δ(<i>mrr-hsdRMS-mcrBC</i>) <i>Φ80lacZΔM15 ΔlacX74 recA1 araD139 Δ(ara-leu)7697 galU galK rpsL endA1 nupG pGal18-DNA2 (Amp^R)</i>
TOP10 pQTEV-DNA2 E675A	F ⁻ <i>mcrA</i> Δ(<i>mrr-hsdRMS-mcrBC</i>) <i>Φ80lacZΔM15 ΔlacX74 recA1 araD139 Δ(ara-leu)7697 galU galK rpsL endA1 nupG pQTEV-DNA2 E675A (Amp^R)</i>
TOP10 pQTEV-DNA2 K1080E	F ⁻ <i>mcrA</i> Δ(<i>mrr-hsdRMS-mcrBC</i>) <i>Φ80lacZΔM15 ΔlacX74 recA1 araD139 Δ(ara-leu)7697 galU galK rpsL endA1 nupG pQTEV-DNA2 K1080E (Amp^R)</i>
TOP10 pQTEV-DNA2 P504S	F ⁻ <i>mcrA</i> Δ(<i>mrr-hsdRMS-mcrBC</i>) <i>Φ80lacZΔM15 ΔlacX74 recA1 araD139 Δ(ara-leu)7697 galU galK rpsL endA1 nupG pQTEV-DNA2 P504S (Amp^R)</i>
TOP10 pQTEV-DNA2 C771S	F ⁻ <i>mcrA</i> Δ(<i>mrr-hsdRMS-mcrBC</i>) <i>Φ80lacZΔM15 ΔlacX74 recA1 araD139 Δ(ara-leu)7697 galU galK rpsL endA1 nupG pQTEV-DNA2 C771S (Amp^R)</i>
TOP10 pQTEV-DNA2 C771A	F ⁻ <i>mcrA</i> Δ(<i>mrr-hsdRMS-mcrBC</i>) <i>Φ80lacZΔM15 ΔlacX74 recA1 araD139 Δ(ara-leu)7697 galU galK rpsL endA1 nupG pQTEV-DNA2 C771A (Amp^R)</i>
TOP10 pQTEV-DNA2 C519A	F ⁻ <i>mcrA</i> Δ(<i>mrr-hsdRMS-mcrBC</i>) <i>Φ80lacZΔM15 ΔlacX74 recA1 araD139 Δ(ara-leu)7697 galU galK rpsL endA1 nupG pQTEV-DNA2 C519A (Amp^R)</i>

*Appendix 2***DNA2 ELECTROCHEMICAL NUCLEASE ASSAY
SUPPORTING FIGURES AND TABLES**

Figure A2.1. Comparison of Wildtype Dna2 and Dna2 E675A Nuclease Activity with Methylene Blue DNA. A) Radiolabeling method for methylene blue modified DNA. **B)** Phosphoradiogram of the 12% sequencing gel to analyze the nuclease activity assay reaction products. (Lane 1 = No Dna2, Lanes 2 = 20 μ M Dna2, Lane 3 = 5nM Dna2, Lane 4 = 0.5nM Dna2, Lanes 5 = 0.05nM Dna2, Lanes 6 = 5nM Dna2 E675A, Lanes 7 = 0.5nM Dna2 E675A, Lanes 8 = 0.05nM Dna2 E675A)

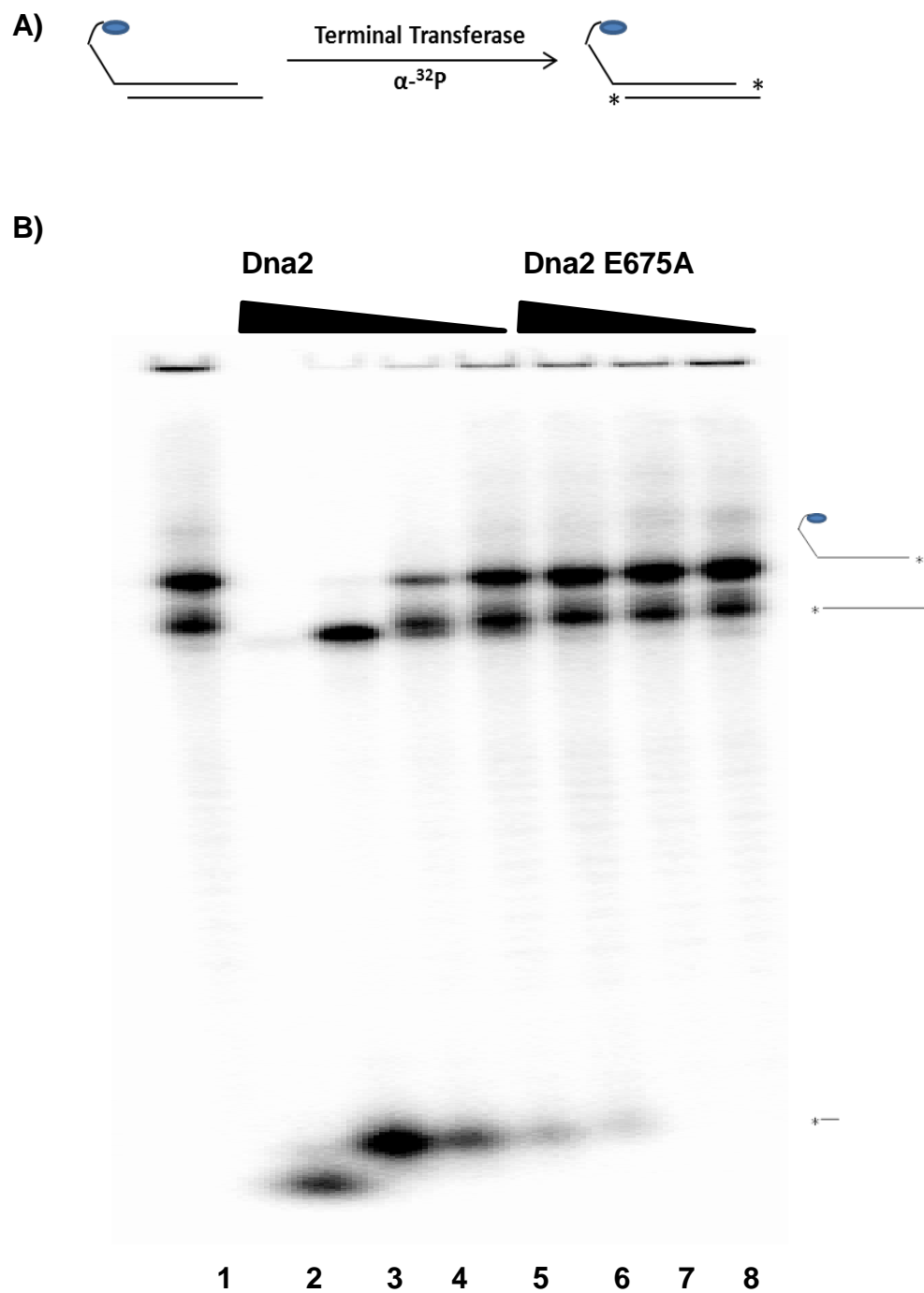


Figure A2.2. Electrochemical Nuclease Assay on the Duplex DNA Substrate.
Cyclic voltammograms of a gold working electrodes modified with duplex DNA following a nuclease activity assay with different concentrations of Dna2.

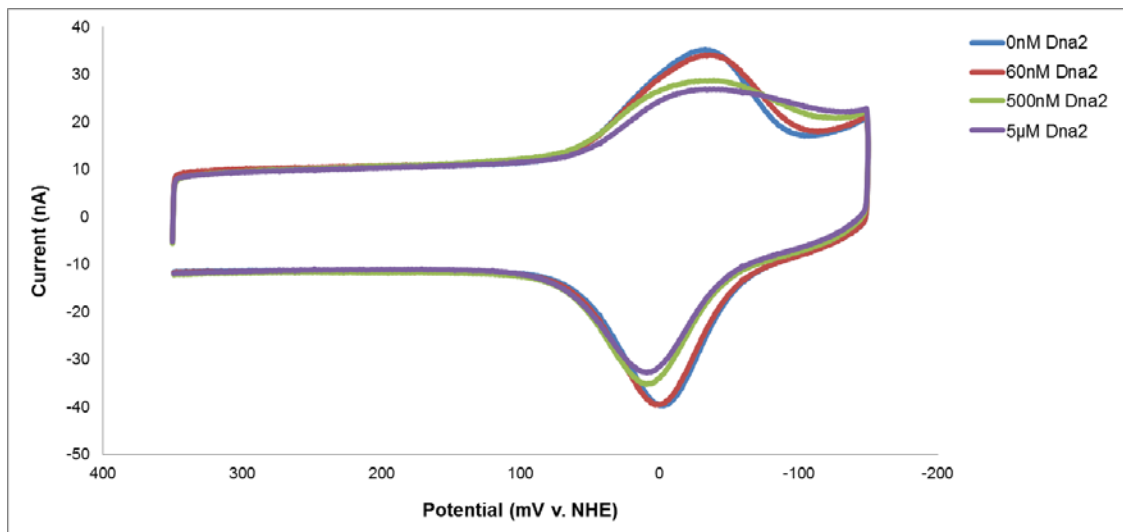


Figure A2.3. Electrochemical Nuclease Assay on the 5'-Tail with a Two Nucleotide Overhang DNA Substrate. Cyclic voltammograms of gold working electrodes modified with the 5'-tail with a two nucleotide overhang DNA substrate following a nuclease activity assay with different concentrations of Dna2.

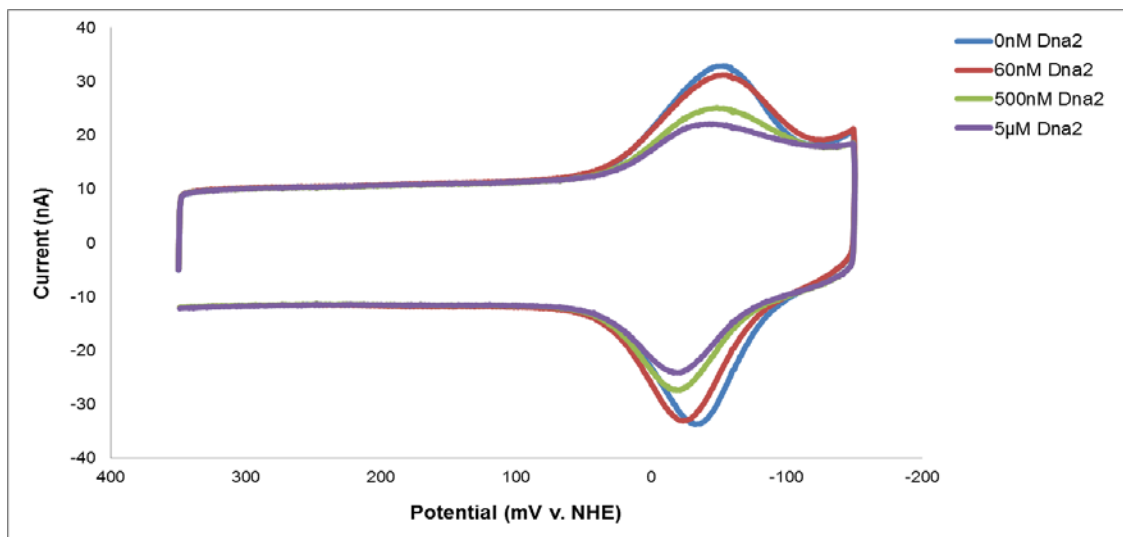


Figure A2.4. Electrochemical Nuclease Assay on the 5'-Tail with a Twenty Nucleotide Overhang. Cyclic voltammograms of gold working electrodes modified with the 5'-tail with a twenty nucleotide overhang following a nuclease activity assay with different concentrations of Dna2.

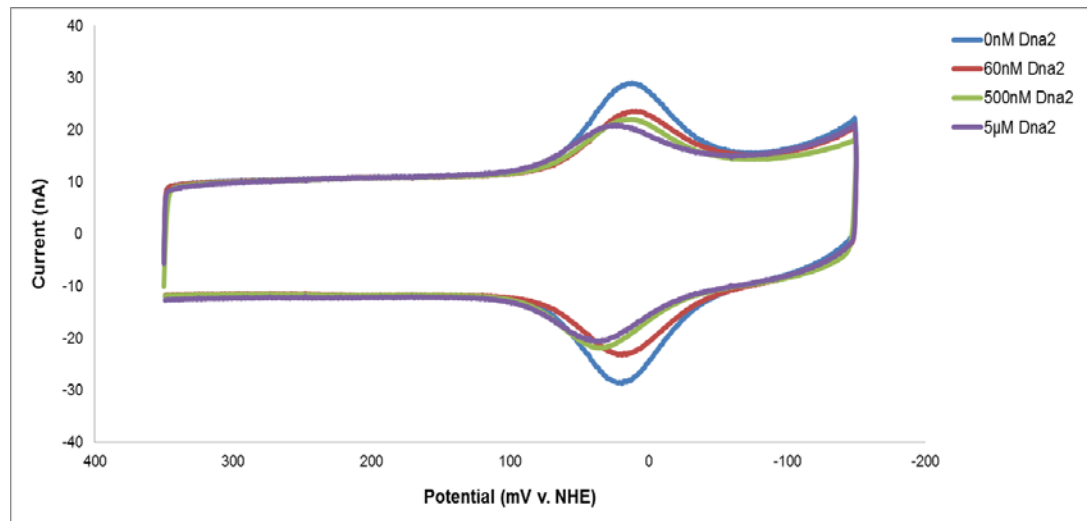


Figure A2.5. Quantification of DNA on the Working Electrode. To confirm that the same concentration of DNA was present on the electrodes modified with the different DNA substrates, the amount of DNA deposited on the surface in each experiment was calculated with the following equation:

$$\Gamma = Q/nF$$

where Γ =surface coverage in moles of adsorbate, Q =charge, n =number of electrons, F =Faraday's constant. All values for the amount of DNA on the electrode surface were an average of the amount of DNA calculated from cyclic voltammograms acquired at different scan rates. The error was the standard deviation of the amount of DNA calculated for the same electrode surface based on cyclic voltammograms acquired at different scan rates.

A) DNA quantification based off of integration of the total charge under the cathodic peak.
B) DNA quantification based off of integration of the total charge under the anodic peak.

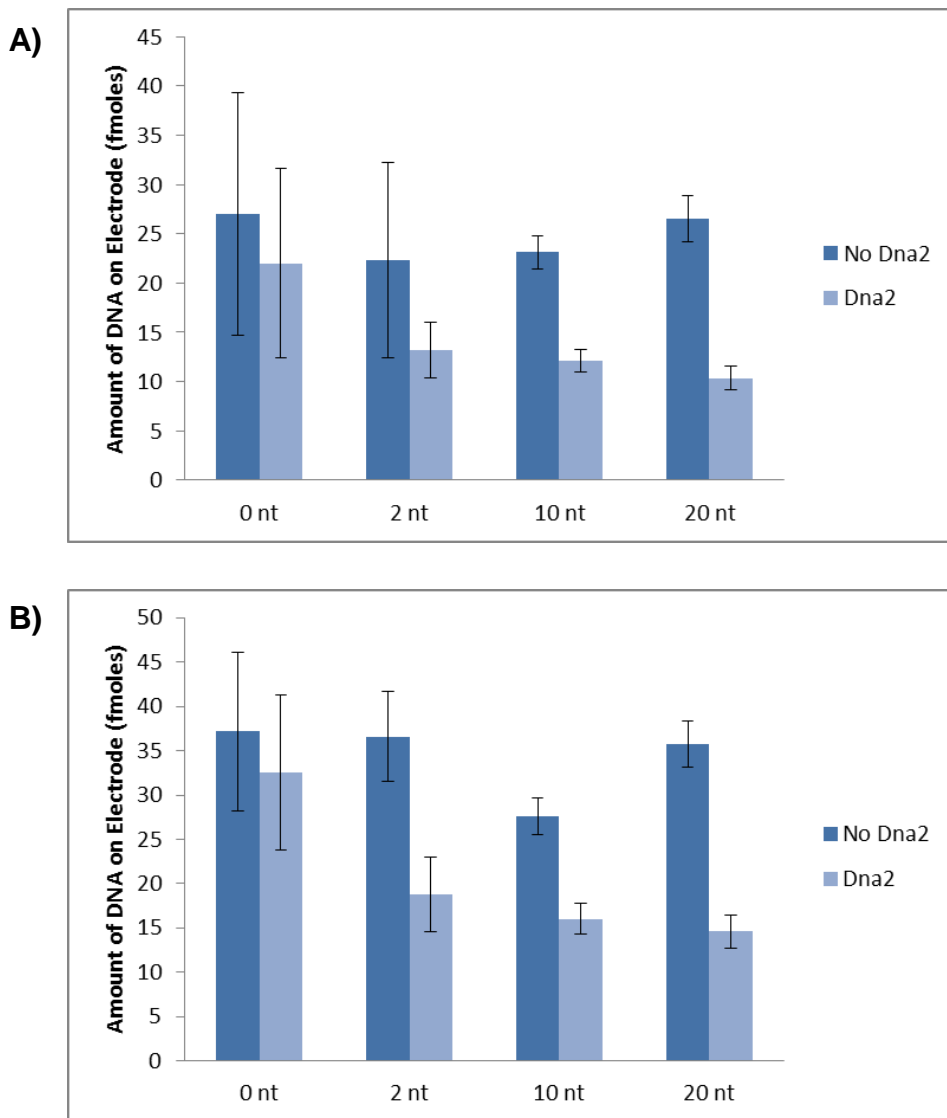


Figure A2.6. Scan Rate Analysis 1. Scan rate analysis of a gold working electrode modified with the duplex DNA Substrate. Each data point on the graph is the average of data collected from two DNA-modified electrodes. (Top Left) Plot of scan rate versus cathodic peak intensity. (Top Right) Plot of scan rate versus anodic peak intensity. (Bottom Left) Plot of scan rate^{1/2} versus cathodic peak intensity. (Bottom Right) Plot of scan rate^{1/2} versus anodic peak intensity.

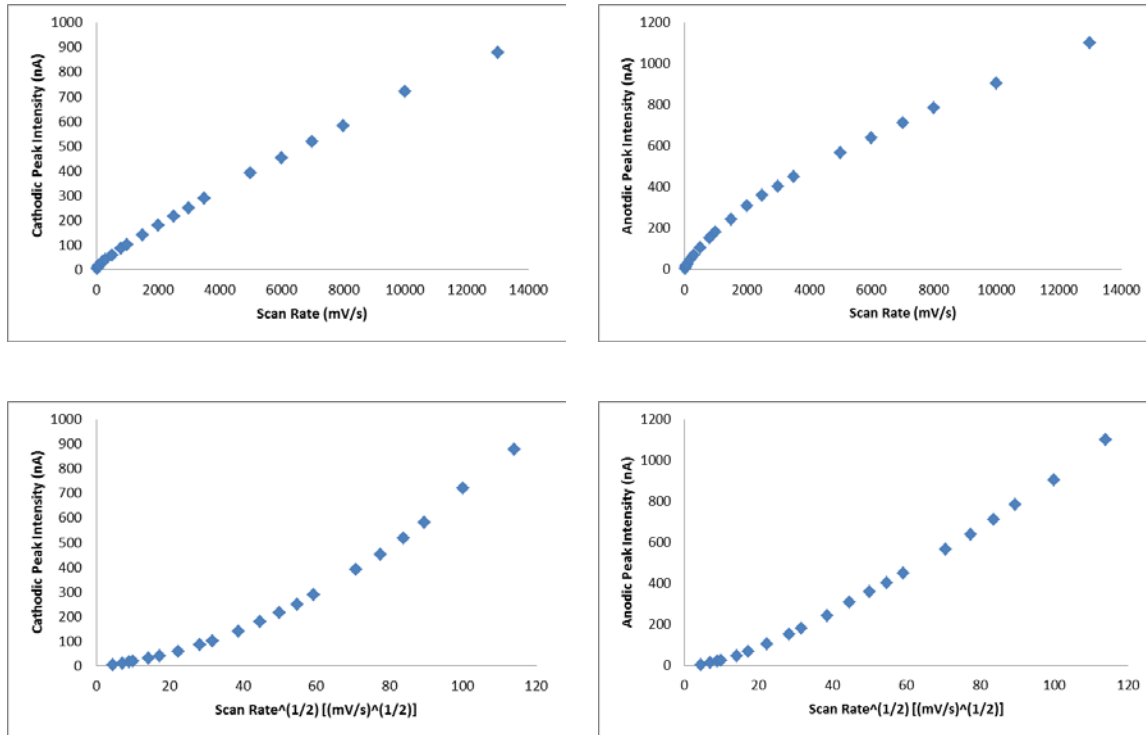


Figure A2.7. Scan Rate Analysis 2. Scan rate analysis of a gold working electrode modified with the 5'-tail DNA Substrate with a two nucleotide overhang. Each data point on the graph is the average of data collected from two DNA-modified electrodes. (*Top Left*) Plot of scan rate versus cathodic peak intensity. (*Top Right*) Plot of scan rate versus anodic peak intensity. (*Bottom Left*) Plot of scan rate^{1/2} versus cathodic peak intensity. (*Bottom Right*) Plot of scan rate^{1/2} versus anodic peak intensity.

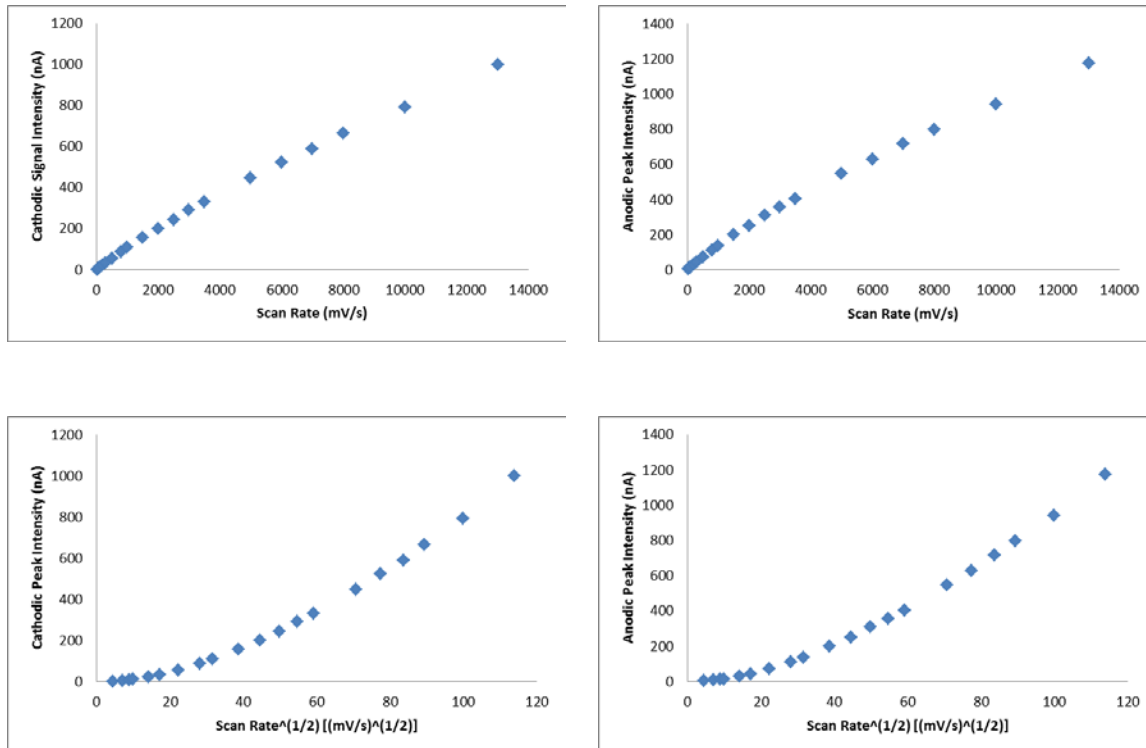


Figure A2.8. Scan Rate Analysis 3. Scan rate analysis of a gold working electrode modified with the 5'-tail DNA substrate with a ten nucleotide overhang. Each data point on the graph is the data collected from one DNA-modified electrode. (*Top Left*) Plot of scan rate versus cathodic peak intensity. (*Top Right*) Plot of scan rate versus anodic peak intensity. (*Bottom Left*) Plot of scan rate^{1/2} versus cathodic peak intensity. (*Bottom Right*) Plot of scan rate^{1/2} versus anodic peak intensity.

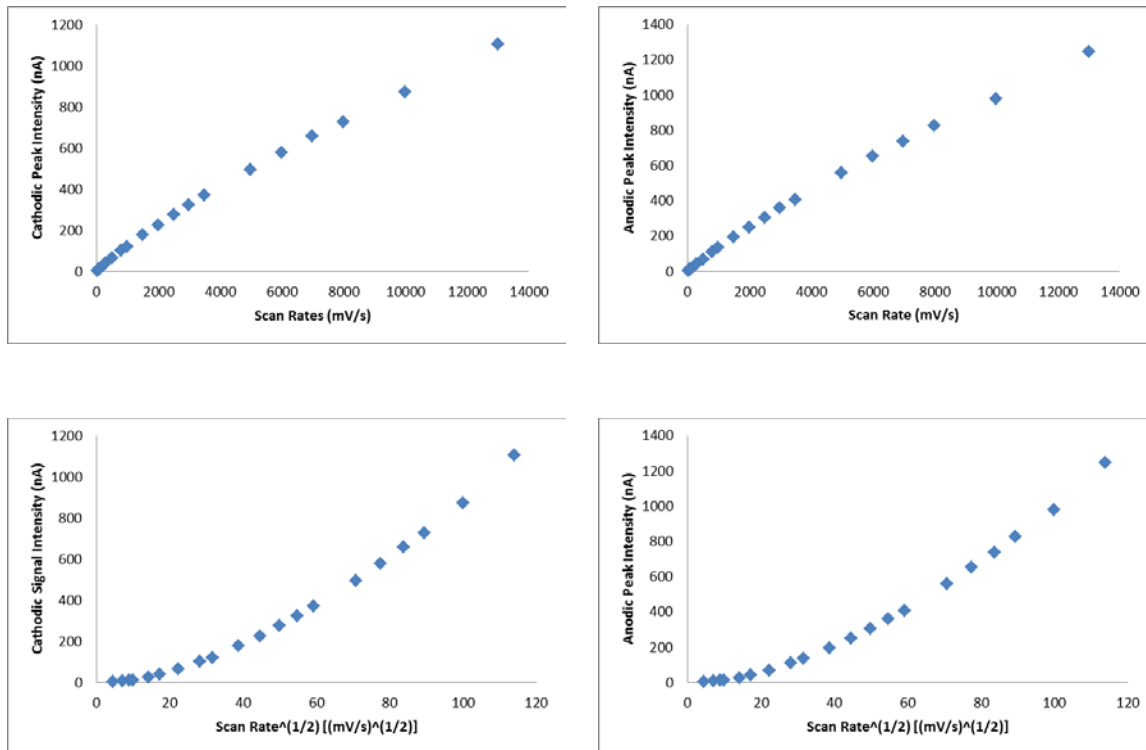


Figure A2.9. Scan Rate Analysis 4. Scan rate analysis of a Gold Working Electrode Modified with the 5'-Tail DNA Substrate with a Twenty Nucleotide Overhang Modified with Methylene Blue. Each data point on the graph is the average of data collected from two DNA-modified electrodes. (*Top Left*) Plot of scan rate versus cathodic peak intensity. (*Top Right*) Plot of scan rate versus anodic peak intensity. (*Bottom Left*) Plot of scan rate^{1/2} versus cathodic peak intensity. (*Bottom Right*) Plot of scan rate^{1/2} versus anodic peak intensity.

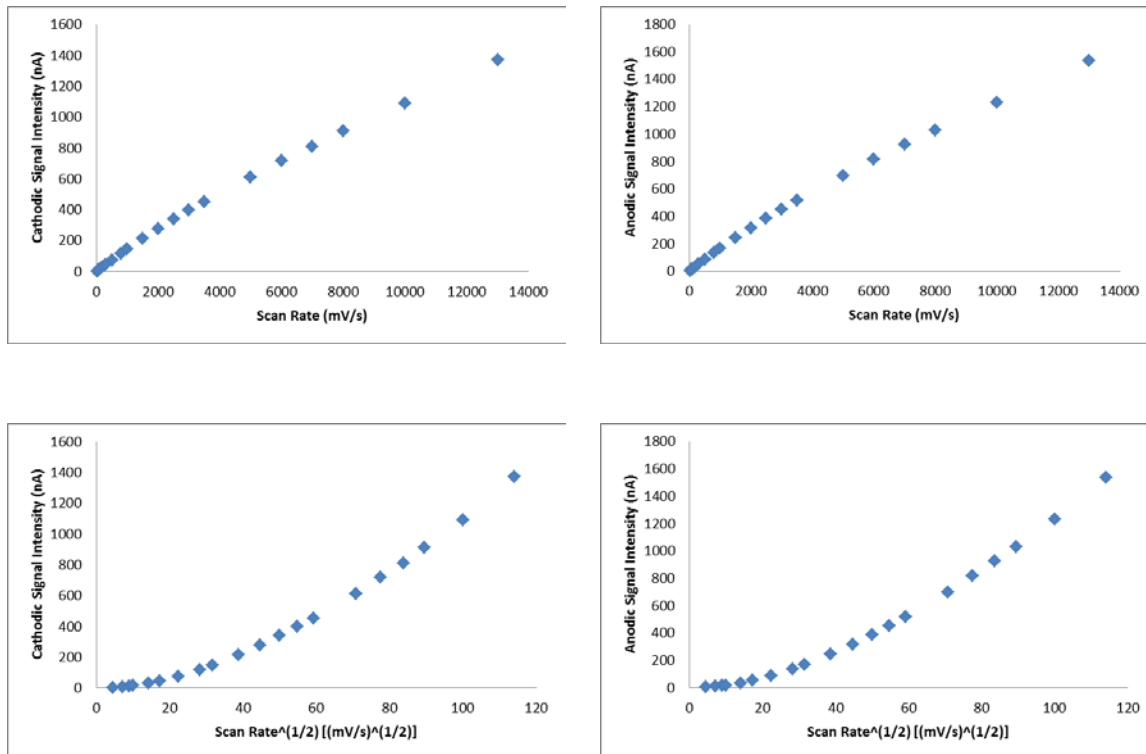


Figure A2.10. Scan Rate Analysis 5. Scan rate analysis of a gold working electrode modified with the duplex DNA Substrate following the electrochemical nuclelease assay. Each data point on the graph is the average of data collected from two DNA-modified electrodes. (Top Left) Plot of scan rate versus cathodic peak intensity. (Top Right) Plot of scan rate versus anodic peak intensity. (Bottom Left) Plot of scan rate^{1/2} versus cathodic peak intensity. (Bottom Right) Plot of scan rate^{1/2} versus anodic peak intensity.

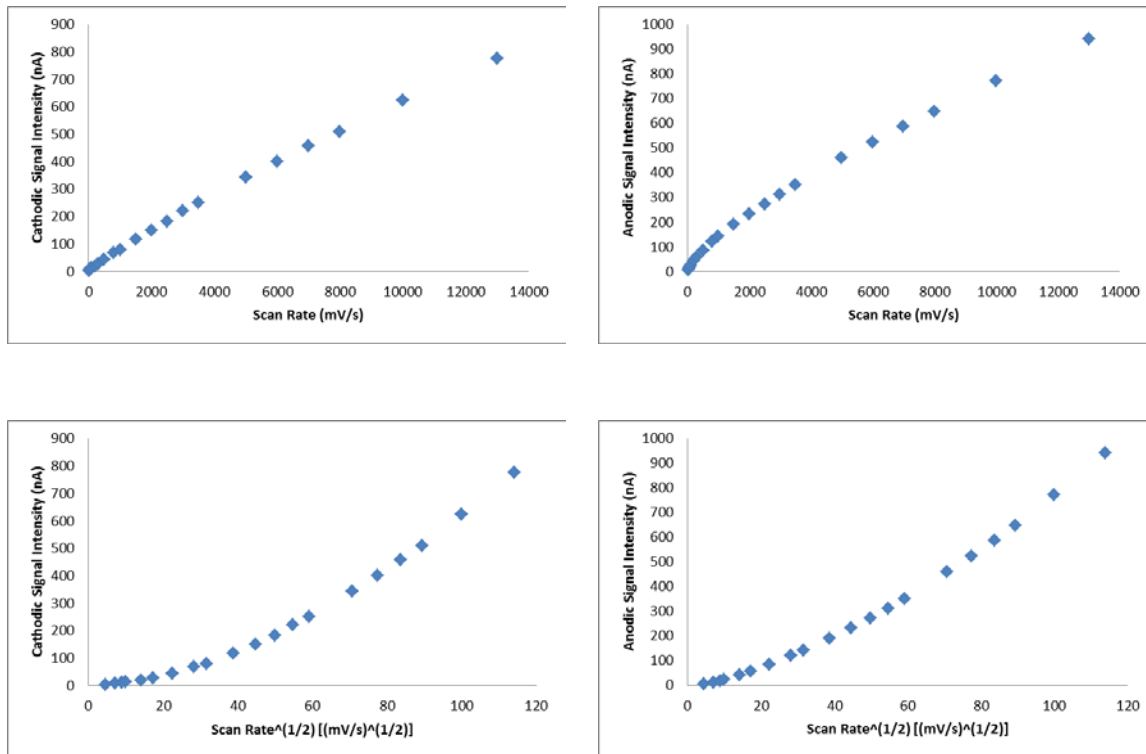


Figure A2.11. Scan Rate Analysis 6. Scan rate analysis of a gold working electrode modified with the 5'-tail DNA substrate with a two nucleotide overhang following the electrochemical nuclease assay. Each data point on the graph is the data collected from one DNA-modified electrode. (Top Left) Plot of scan rate versus cathodic peak intensity. (Top Right) Plot of scan rate versus anodic peak intensity. (Bottom Left) Plot of scan rate^{1/2} versus cathodic peak intensity. (Bottom Right) Plot of scan rate^{1/2} versus anodic peak intensity.

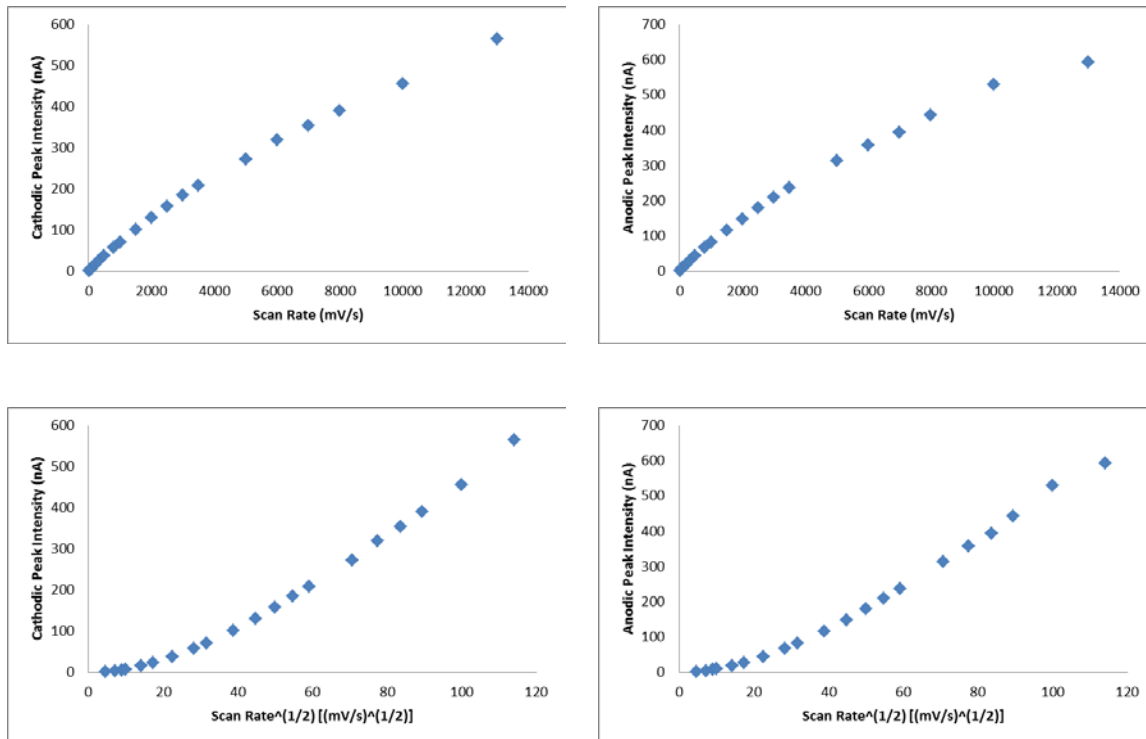


Figure A2.12. Scan Rate Analysis 7. Scan rate analysis of a gold working electrode modified with the 5'-tail DNA substrate with a ten nucleotide overhang following the electrochemical nuclease assay. Each data point on the graph is the average of data collected from two DNA-modified electrodes. (*Top Left*) Plot of scan rate versus cathodic peak intensity. (*Top Right*) Plot of scan rate versus anodic peak intensity. (*Bottom Left*) Plot of scan rate^{1/2} versus cathodic peak intensity. (*Bottom Right*) Plot of scan rate^{1/2} versus anodic peak intensity.

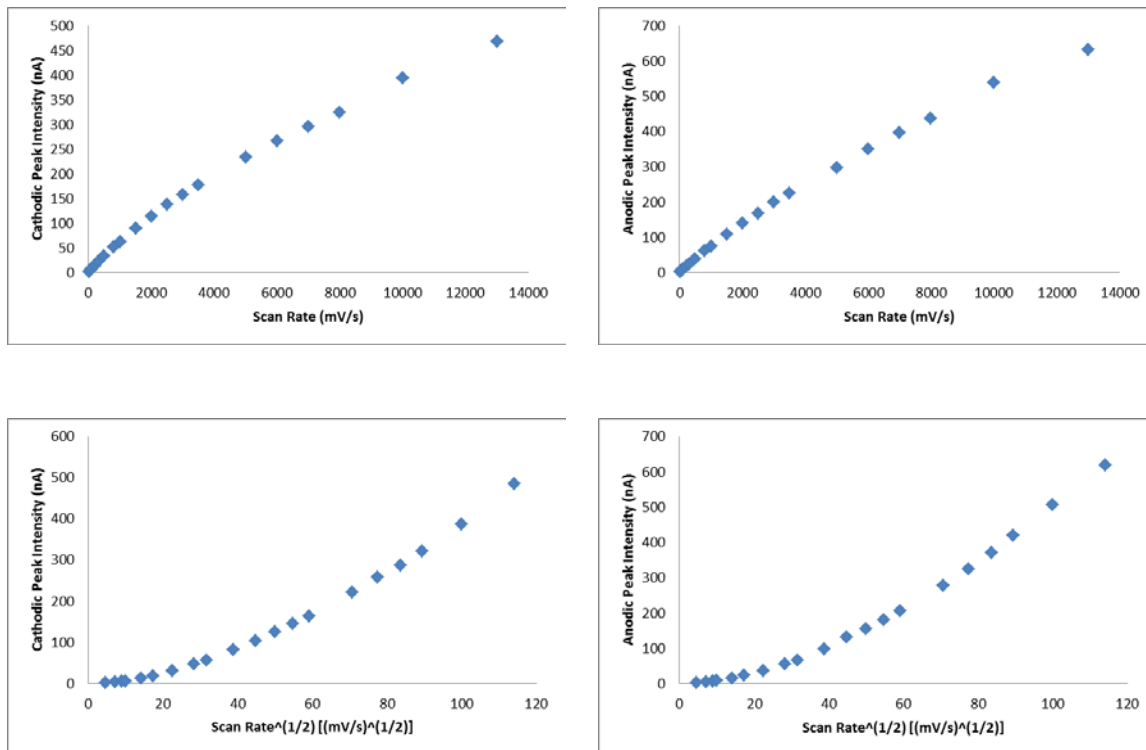


Figure A2.13. Scan Rate Analysis 8. Scan rate analysis of a gold working electrode modified with the 5'-tail DNA substrate with a twenty nucleotide overhang following the electrochemical nuclease assay. Each data point on the graph is the average of data collected from two DNA-modified electrodes. (*Top Left*) Plot of scan rate versus cathodic peak intensity. (*Top Right*) Plot of scan rate versus anodic peak intensity. (*Bottom Left*) Plot of scan rate^{1/2} versus cathodic peak intensity. (*Bottom Right*) Plot of scan rate^{1/2} versus anodic peak intensity.

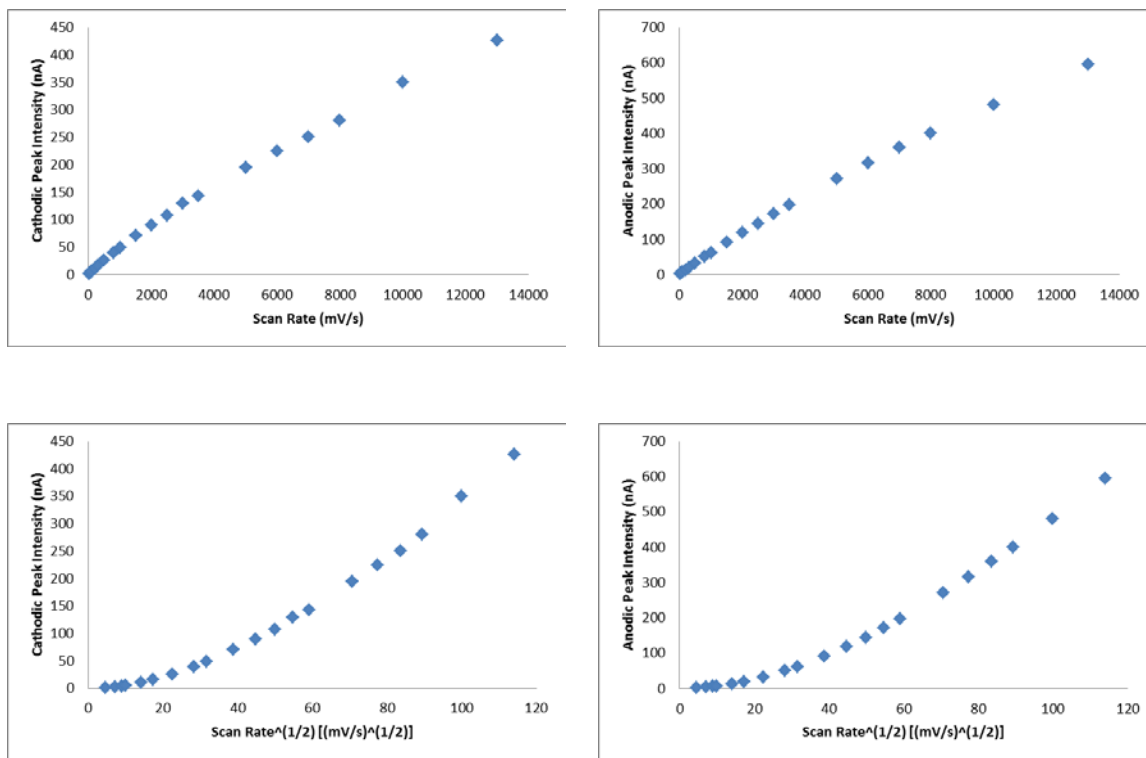


Table A2.1. Oligonucleotides for the Electrochemical Nuclease Assay

Name	Sequence (5'-3')	Extinction Coefficient at 260nm (M ⁻¹ cm ⁻¹)	
5'-Tail 2mer	5'-Amino Overhang Complement	/5AmMC6T/TGTAGGGTTCGCGACATGATGCA TCGTTAGGCAC	336,000
5'-Tail 2mer	5'-Methylene Blue Overhang Complement	/5MBC6T/TGTAGGGTTCGCGACATGATGCAT CGTTAGGCAC	346,300
5'-Tail 10mer	5'-Amino Overhang Complement	/5AmMC6T/ACTGTGGCTGTAGGGTCGCGAC ATGATGCATCGTTAGGCAC	409,300
5'-Tail 10mer	5'-Methylene Blue Overhang Complement	/5MBC6T/ACTGTGGCTGTAGGGTCGCGACA TGATGCATCGTTAGGCAC	419,600
5'-Tail 20mer	5'-Amino Overhang Complement	/5AmMC6T/TACTTATTCACTGTGGCTGTAGG GTTCGCGACATGATGCATCGTTAGGCAC	498,700
5'-Tail 20mer	5'-Methylene Blue Overhang Complement	/5MBC6T/TACTTATTCACTGTGGCTGTAGGG TTCGCGACATGATGCATCGTTAGGCAC	509,000
5'-Tail Disulfide 33		/5ThioMC6-D/GTGCCTAACGATGCATCATGT CGCGAACCTAC	309,700
5'-Tail Thiol 33		HS – GTGCCTAACGATGCATCATGTCGCG AACCTAC	309,700
5'-Tail Disulfide 35		/5ThioMC6-D/GTGCCTAACGATGCATCATGTC GCGAACCTACAA	335,500
5'-Tail Thiol 35		HS – GTGCCTAACGATGCATCATGTCGCGA ACCCTACAA	335,500
5'-Tail Comp for TT labeling		TGTGCCTAACGATGCATCATGTCGCGAACCC TAC	317,200

*/5AmMC6T/ = Amino Modifier dT C6 on the IDT DNA website

**/5MBC6T/ = Methylene Blue dT C6

***/5ThioMC6-D/ = 5' Thiol Modifier C6 S-S (Disulfide)

****HS = Thiol

Table A2.2. DNA Substrates for the Electrochemical Nuclease Assay

5'-Tail DNA Substrate	Complement DNA	Thiol DNA
duplex	5'-Tail 5'-Methylene Blue 2mer Overhang Complement	5'-Tail Thiol 35
5'-tail with a two nucleotide overhang	5'-Tail 5'-Methylene Blue 2mer Overhang Complement	5'-Tail Thiol 33
5'-tail with a ten nucleotide overhang	5'-Tail 5'-Methylene Blue 10mer Overhang Complement	5'-Tail Thiol 33
5'-tail with a twenty nucleotide overhang	5'-Tail 5'-Methylene Blue 20mer Overhang Complement	5'-Tail Thiol 33

Appendix 3

ELECTROCHEMICAL AND STRUCTURAL CHARACTERIZATION
OF *AZOTOBACTER VINELANDII* FLAVODOXIN II
SUPPORTING FIGURES AND TABLES

Figure A3.1. Cyclic Voltammogram of Flavodoxin II on Unmodified Basal Plane Graphite Electrodes. The basal plane graphite electrode (BPGE) was placed in a 200 μ M solution of flavodoxin II in 50 mM potassium phosphate, pH 7.5, 150 mM NaCl, and a cyclic voltammogram was acquired at a scan rate of 50 mV/s (gray). A basal plane graphite electrode was modified with 10 mM DDAB. This electrode was placed in a 200 μ M solution of flavodoxin II in 50 mM potassium phosphate, pH 7.5, 150 mM NaCl, and a cyclic voltammogram was acquired at a scan rate of 50 mV/s (black).

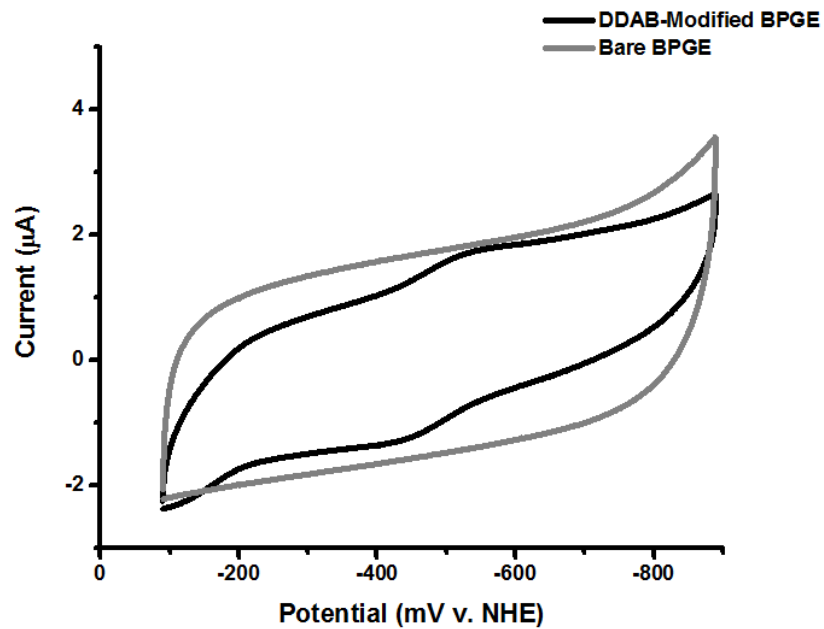


Figure A3.2. Cyclic Voltammogram of Flavodoxin II Purified from *E. coli*.

The DDAB-modified basal plane graphite electrode was soaked in a 200 μ M solution of flavodoxin II purified from *E. coli* for twenty minutes. The electrode was transferred to phosphate buffer, and a cyclic voltammogram was acquired at a scan rate of 50 mV/s. The low potential peak was at -427 ± 3 mV v. NHE. The high potential peak was at -151 ± 3 mV v. NHE.

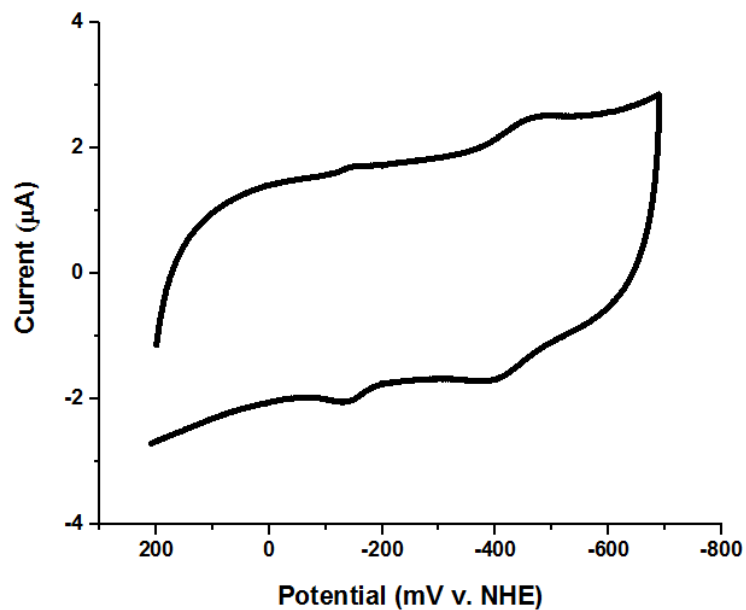


Figure A3.3. Cyclic Voltammogram of FMN. The basal plane graphite electrode was placed in a 200 μ M solution of FMN in 50 mM potassium phosphate, pH 7.5, 150 mM NaCl, and a cyclic voltammogram was acquired at a scan rate of 20 mV/s. The high potential peak on the voltammogram had a midpoint potential of -138 ± 3 . The low potential peak on the voltammogram had a midpoint potential of -303 ± 1 . The scan rate dependence of the signal intensity for free FMN in solution indicated that this molecule diffused in the DDAB films at a diffusion rate of $5.7 \times 10^{-7} \pm 1.4 \times 10^{-7}$ cm^2/s . This calculation assumed that the concentration of FMN was the same in solution as it was in the surfactant film, and that the redox process observed was a two electron process.

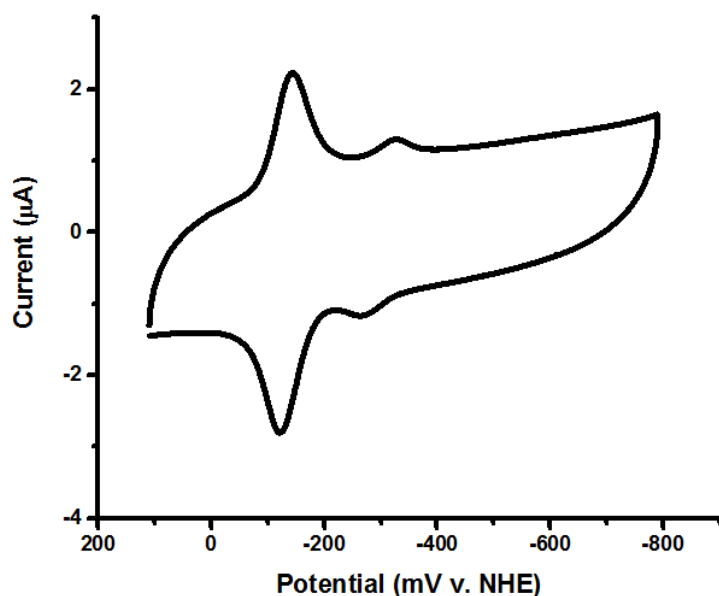


Figure A3.4. Cyclic Voltammogram of Flavodoxin II with the High and Low Potential Species. The electrode was soaked in 200 μ M flavodoxin II in 50 mM potassium phosphate, pH 7.5, 150 mM NaCl for 20 minutes. The electrode was transferred to 10 mM phosphate buffer, pH 7, and a cyclic voltammogram was acquired at a scan rate of 20 mV/s.

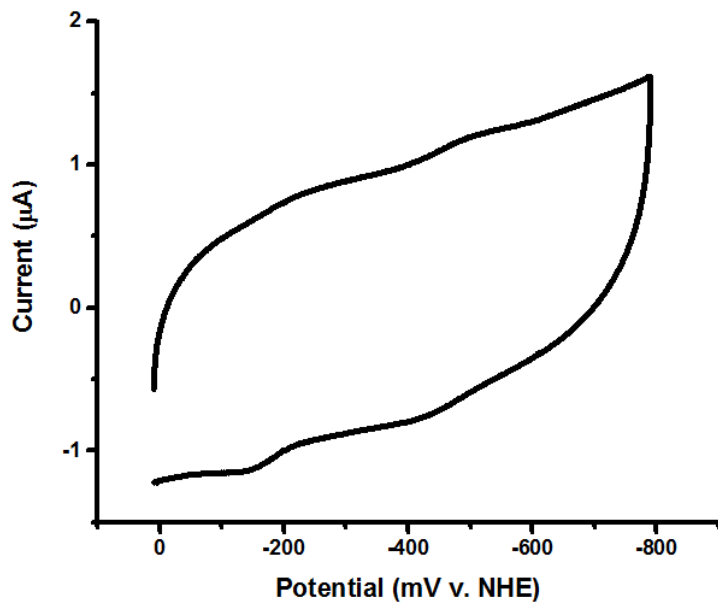


Figure A3.5. Flavodoxin II Scan Rate Analysis (Top) Dependence of the signal intensity on the scan rate of the low potential peak of flavodoxin II on DDAB-modified basal plane graphite electrodes. The cyclic voltammogram was acquired in a 200 μ M flavodoxin II solution in 50 mM tris-HCl, pH 7.5, 200 mM NaCl. (Bottom) Dependence of the signal intensity on the scan rate of the low potential peak of the cyclic voltammogram of flavodoxin II on DDAB-modified basal plane graphite electrodes. The electrode was initially soaked in 200 μ M flavodoxin II in 50 mM tris-HCl, pH 7.5, 200 mM NaCl. The electrode was moved to phosphate buffer for cyclic voltammetry.

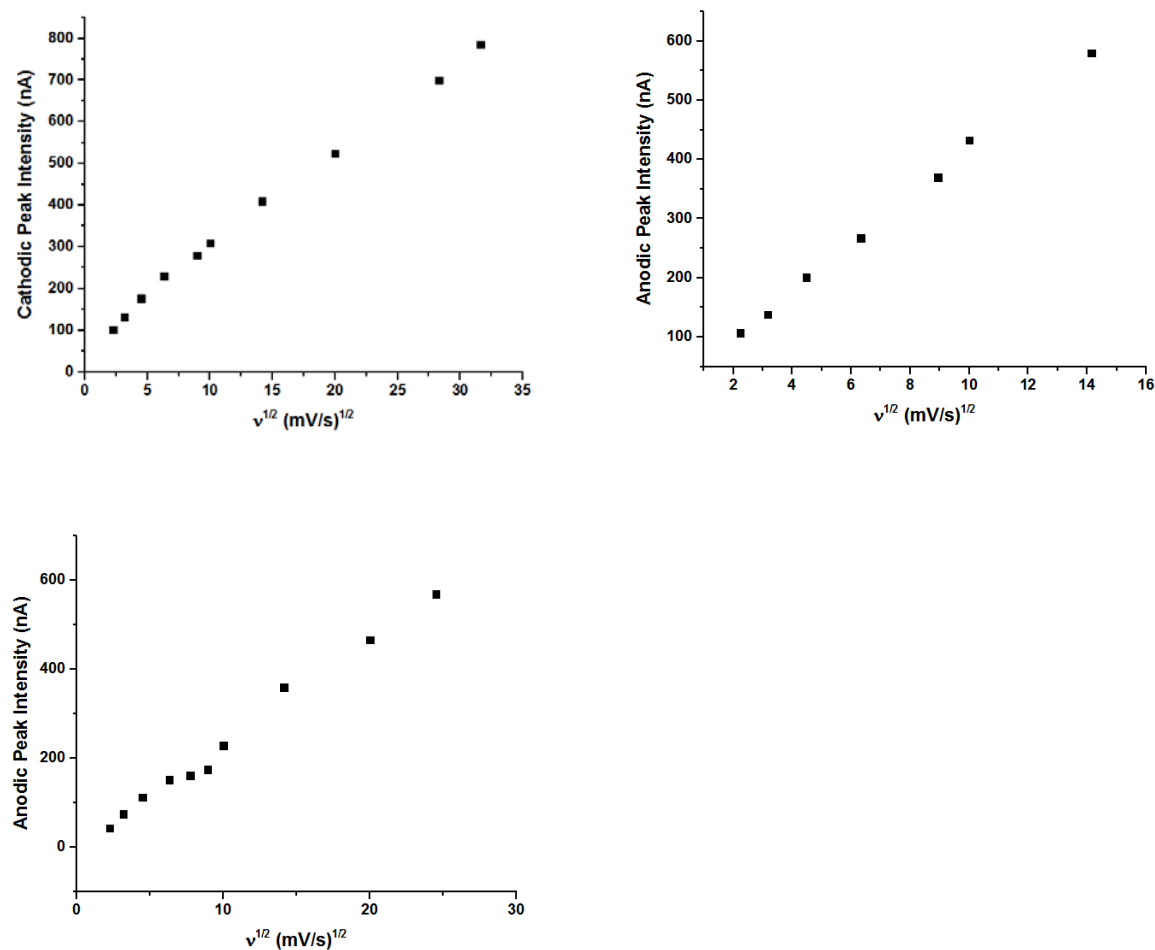


Figure A3.6. FMN Scan Rate Analysis. Dependence of the signal intensity on the scan rate of the high potential peak of FMN on DDAB-modified basal plane graphite electrodes. The electrode was initially soaked in 200 μ M FMN in 50 mM tris-HCl, pH 7.5, 200 mM NaCl for twenty minutes. The electrode was transferred to phosphate buffer where the voltammograms were acquired.

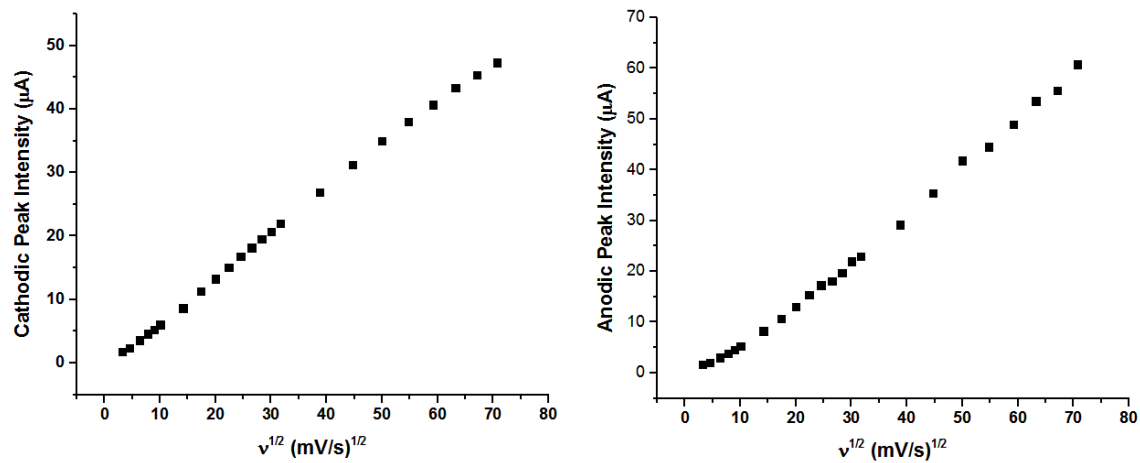


Figure A3.7. Potential Reduction Mechanisms of FMN Bound by Flavodoxin II.
(Top) Scheme describing a sequential electron transfer mechanism occurring at FMN. The pH dependence of the midpoint potential of the semiquinone/quinone couple occurs by a proton-coupled electron transfer mechanism that converts between FMN and HFMN[·].
(Bottom) Scheme depicting a concerted electron transfer reaction that does not involve a stable semiquinone intermediate state. This type of mechanism is observed for FMN free in solution.

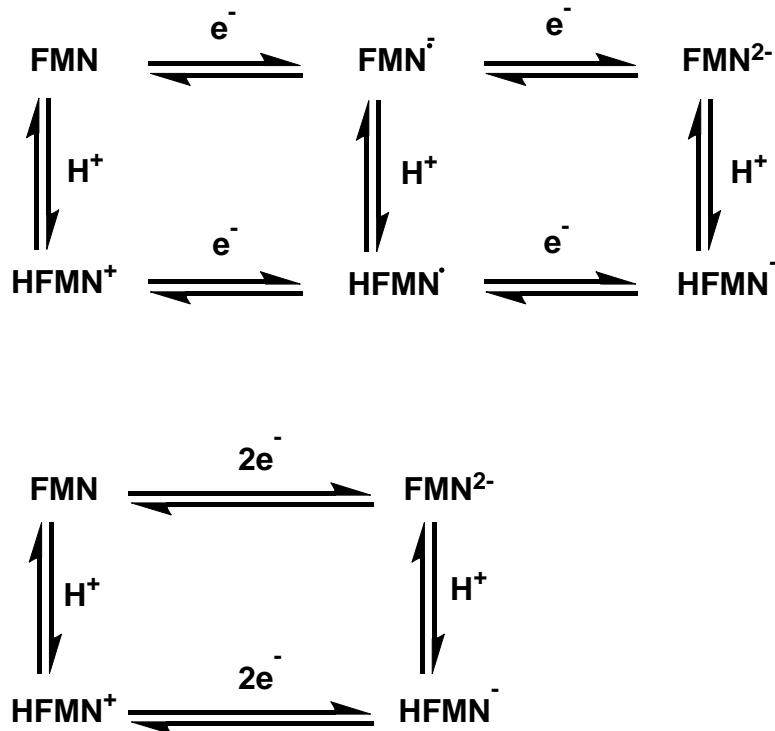


Table A3.1. Midpoint Potentials of *Azotobacter vinelandii* Flavodoxin II

E_2 (mV v. NHE) (pH)	E_1 (mV v. NHE) (pH)	Electrochemical Method (Detection Method)	Reference
-224 (pH 8)	-458 (pH 8)	Redox titration with chemical mediators (UV-visible absorption spectroscopy)	23
-245 (pH 8)	-515 (pH 8)	Microcoulometry at Controlled Potentials (UV-visible absorption spectroscopy)	18
-270 (pH 7.7)	-464 (pH 7.7)	Redox titration with chemical mediators (UV-visible absorption spectroscopy)	24
+50 (pH 8.2)	-495 (pH 8.2)	Redox titration with chemical mediators (UV-visible absorption spectroscopy)	25
--	-500 \pm 10 (pH 7)*	Redox titration with chemical mediators (UV-visible absorption spectroscopy)	12
--	-449 (pH 6) -488 (pH 8.5)	Direct electrochemistry on glassy carbon modified with neomycin (Cyclic voltammetry)	26
-74 \pm 10 (pH 6) -183 \pm 10 (pH 8.5)	-446 \pm 10 (pH 6) -468 \pm 10 (pH 8.5)	Redox titration with chemical mediators (EPR spectroscopy)	26

*Measurement not accurate due to mediator system chosen

Table A3.2. Data Collection and Refinement Statistics for *A. vinelandii* Flavodoxin II (*nifF*). Values in brackets represent the highest resolution shell.

Data collection statistics		Oxidized (Quinone)	Reduced (Hydroquinone)
Wavelength (Å)		0.99987	0.99987
Resolution range (Å)		35.73 – 1.17 (1.24 – 1.17)	35.62 – 1.38 (1.46 – 1.38)
Unique reflections		56,103 (7,613)	34,606 (4,689)
Completeness (%)		99.2 (95.0)	99.1 (94.2)
Multiplicity		18.4 (15.3)	18.1 (14.7)
Space group		P3 ₁ 2 ₁ 1	P3 ₁ 2 ₁ 1
Unit cell parameters			
a, b, c		39.87, 39.87, 178.66	39.82, 39.82, 178.09
α, β, γ		90.0, 90.0, 120.0	90.0, 90.0, 120.0
R _{merge}		0.069 (0.686)	0.077 (0.782)
R _{p.i.m.}		0.016 (0.177)	0.018 (0.205)
CC _{1/2}		0.999 (0.885)	1.000 (0.843)
Mn (I / σ(I))		24.8 (4.4)	22.1 (4.1)
Refinement statistics			
R _{cryst} (%)		13.22	17.42
R _{free} (%)		16.56	20.10
r.m.s.d. bond lengths (Å)		0.029	0.014
r.m.s.d. bond angles (°)		2.431	1.280
Average B-factor (Å ²)		9.33	18.00
Ramachandran: allowed (outliers) (%)		99.4 (0.6)	99.4 (0.6)

Table A3.3. Predicted Amino Acid Residue Interactions Between Flavodoxin II and the Iron Protein*

Fe-Protein	Flavodoxin II
R140	S66
C97	E59
R100	D154
D69	R15

*Analysis was done with the model presented in Figure 5.5.

Appendix 4

A METHOD FOR MONITORING DNA CHARGE TRANSPORT SIGNALING BETWEEN DNA REPAIR PROTEINS

Adapted from: Grodick, M. A., Segal, H.M., Zwang, T. J., and Barton, J. K. (2014) DNA-Mediated Signaling by Proteins with 4Fe-4S Clusters is Necessary for Genomic Integrity. *J Am Chem Soc.* 136, 6570-6478. doi: 10.1021/ja501973c.

Abstract

An assay was developed to study DNA Charge Transport (DNA CT) signaling between DinG, Endonuclease III (EndoIII), and MutY, three DNA repair proteins with 4Fe-4S clusters. It was observed that inactivation of DinG within the *E. coli* genome led to an increase in the number of GC to TA transversion mutations. These mutations occur when MutY does not excise 8-oxoguanine from the *E. coli* genome, so it was hypothesized that DinG helped target MutY to 8-oxoguanine. Furthermore, it was shown that expression of EndoIII D138A, a catalytically inactive form of EndoIII that could participate in DNA CT signaling can partially rescue the mutagenic phenotype of the DinG knockout strain. It was also shown that expression of EndoIII Y82A, a form of EndoIII that is catalytically active, but DNA CT deficient, showed no significant difference in the levels of mutagenesis relative to both the DinG knockout strain and the DinG knockout strain with EndoIII D138A. Thus, DNA CT could be used by the DNA repair proteins in *E. coli* to coordinate the repair of 8-oxoguanine.

Introduction

A variety of *in vitro* experiments have suggested that DNA CT has an important biological role; however, finding evidence for DNA CT *in vivo* still remains a major challenge. Toward this end, an *E. coli* *lac*⁺ forward reversion assay has been developed to probe whether EndoIII, MutY, and DinG use a redox-active 4Fe-4S clusters bound by these enzymes to signal via long range DNA CT as a first step in DNA damage detection (1,2). This assay will herein be referred to as the Helper Function Assay.

The Helper Function Assay is adapted from an experiment designed to identify *E. coli* proteins involved in the repair of 8-oxoguanine (8-OxoG) (3,4). For these experiments, an *E. coli* strain was constructed that contains a version of *lacZ* with an internal AT to CG point mutation (*LacZ*) in the codon that corresponds to amino acid residue 461, an essential catalytic residue in β -galactosidase (**Figure**

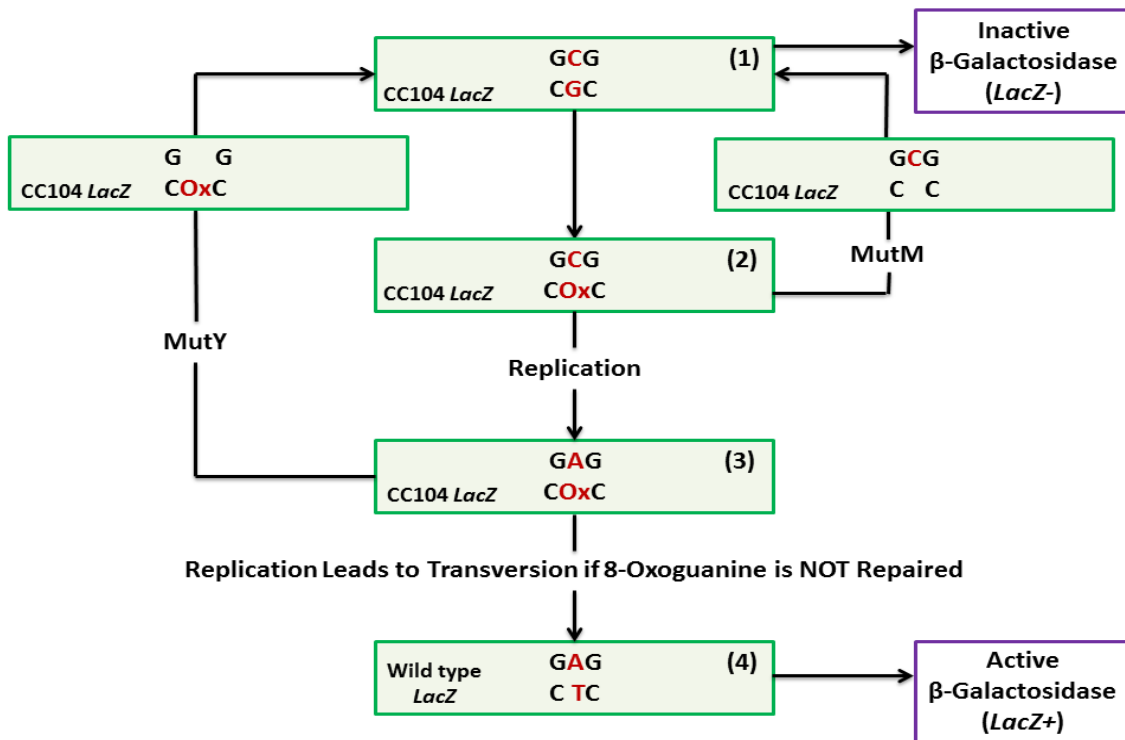


Figure A4.1. Helper Function Assay. The CC104 strain does not have a genomic copy of *lacZ*; however, this strain does contain an episome with a version of *lacZ* (*LacZ*) that codes for an inactive form of β -Galactosidase due to a point mutation at amino acid residue 461 (1). When the guanine in the codon for residue 461 is oxidized to 8-OxoG (2), there can be two possible outcomes. Either *MutM*, another DNA glycosylase will excise 8-OxoG, or this residue will not be repaired, and DNA polymerase may mispair adenine opposite 8-OxoG (3). 8-OxoG:A can be repaired by *MutY* to restore the original version of *LacZ*. If this lesion is not repaired by *MutY*, thymine will be added opposite adenine during replication (4) to generate a transversion mutation that restores the gene for wild type *lacZ* (*lacZ⁺*).

A4. 1). Thus, prior to any mutagenesis, inactive β -galactosidase is expressed by the CC104 strain. However, when the guanine of this point mutation is oxidized to 8-OxoG, it can mispair with adenine during replication. A GC to TA transversion mutation occurs if repair of 8-OxoG mispaired with adenine (8-OxoG:A) is impaired. This transversion mutation restores the wildtype amino acid residue at position 461, resulting in expression of active β -galactosidase. Notably, the main function of *MutY* is to excise adenine paired opposite 8-OxoG. Therefore, *MutY* repair activity can be indirectly assayed by measuring changes in β -

galactosidase activity. In the Helper Function Assay, this was done by assessing *E. coli* growth on a medium where lactose was the only carbon source. Specifically, an increase in the number of colonies observed on lactose minimal medium agar plates indicated that there was an increase in the number of GC to TA transversion mutations when the gene for *mutY* was removed from the genome.

Previous work in the Barton lab using the CC104 strain demonstrated that there was an increase in β -galactosidase activity upon deletion of *nth*, the gene for EndolII. This result suggested that there was a decrease in the ability of MutY to find and repair 8-OxoG in the absence of EndolII (1). Consistent with this hypothesis, expression of wildtype EndolII within a CC104 $\Delta nth::cat$ strain decreased the number of GC to TA transversion mutations to the level observed for the wildtype strain. If a charge transport deficient mutant of EndolII, the Y82A mutant, was expressed in the same CC104 strain, the number of transversion mutations did not change relative to CC104 $\Delta nth::cat$ strain. Therefore, the Y82A mutation effectively eliminated the ability of EndolII to help MutY find and repair 8-OxoG:A (1). Additionally, Endo III D138A, a mutant form of EndolII that is glycolytically inactive, but retains the DNA charge transport ability of the wildtype enzyme was used as a control for this experiment to test whether the glycosylase activity of EndolII was required to prevent mutagenesis (1). When this form of EndolII was expressed in the CC104 $\Delta nth::cat$ strain, *lac*⁺ revertant counts were restored to the levels observed for the CC104 wildtype strain (1). Thus, the ability of EndolII to participate in DNA CT, rather than its enzymatic activity, was causing the observed increase in the frequency of GC to TA transversion mutations when *nth* was removed from the *E. coli* genome.

In this section, the Helper Function Assay was adapted to study DNA CT signaling between *E. coli* DNA repair proteins. The assay was extended to examine how DinG, a helicase with a 4Fe-4S cluster signals MutY and EndolII via DNA CT to help direct these DNA repair proteins to damaged regions of the genome (2).

Materials and Methods

Materials. All restriction enzymes and QuikLigase were purchased from New England BioLabs. DNA polymerase and dNTPs were purchased from Roche. All primers were purchased from IDT DNA. All chemicals were purchased from Sigma Aldrich. Luria Bertani (LB) broth was used as the rich growth medium (5). NCE supplemented with MgSO₄ (100 µM) and glucose (11 mM) was used as the minimal growth medium (7). NCE agar plates supplemented with MgSO₄ (100 µM) and glucose (11 mM), as well as NCE agar plates supplemented with MgSO₄ (100 µM) and lactose (6 mM) were used to evaluate the number of Lac⁺ revertants (6).

Construction of the CC104 ΔdinG::cat (CC104 dinG⁻) Strain. The gene for DinG was inactivated in the CC104 strain. The method used to inactivate *dinG* was adapted from a previously published procedure (**Figure A4.2**) (7). The CC104 *E. coli* strain was a gift from Professor Jeffrey H. Miller (UCLA). pKD3 and pKD46 were obtained from Professor Dianne Newman (Caltech). The sequences for all DNA primers used to construct the strain are shown in Table 1. All *dinG* knockout colonies were screened by PCR, and all PCR check products were sent to Laragen to confirm by sequencing that there was no unexpected mutagenesis within 500 base pairs of *dinG*.

EndoIII D138A and EndoIII Y82A Recovery Plasmids. The EndoIII recovery plasmid was made by Amie Boal. This plasmid consisted of *nth* cloned into the pBBR1MCS-4 vector (8). The EndoIII D138A and EndoIII Y82A plasmids were generated by site-directed mutagenesis with the primers outlined in Table 1 and an Agilent QuikChange II Site-Directed Mutagenesis Kit. The plasmid DNA was isolated with a miniprep kit (Qiagen), and was sent to Laragen for sequencing with primer pBBR1MCS-4 forward check and primer pBBR1MCS-4 reverse check (**Table A4.1**).

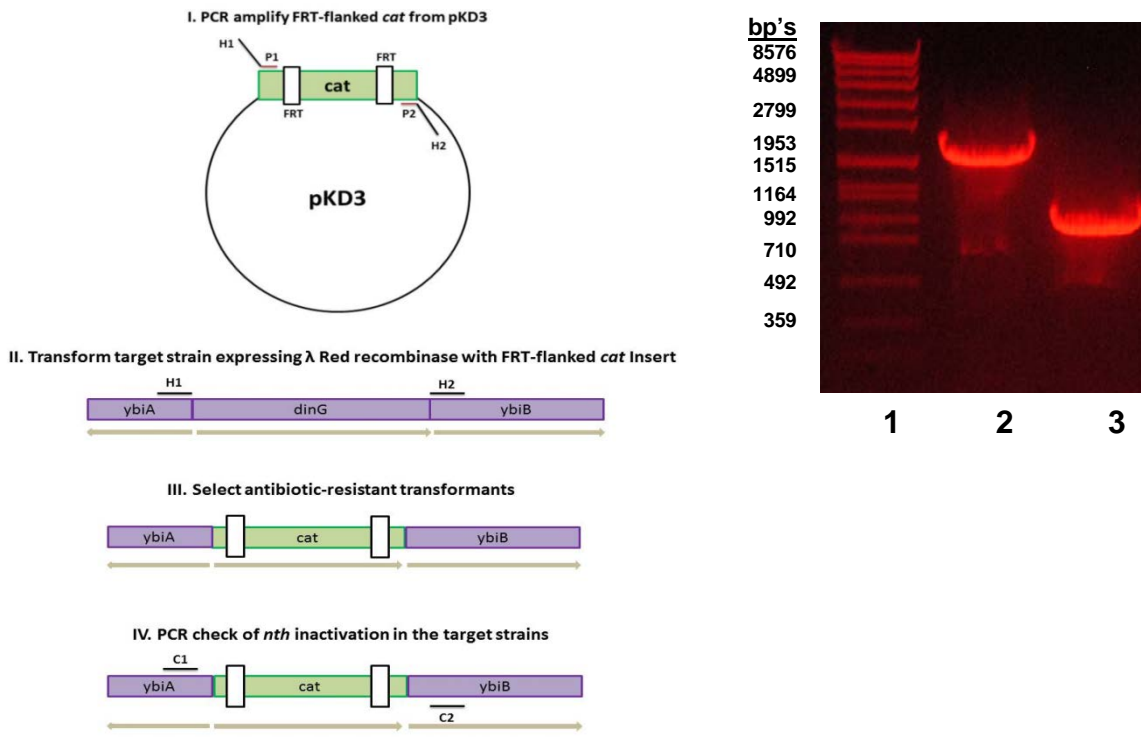


Figure A4.2. In-frame Inactivation of *dinG* via the Wanner Method. (Left) Strategy for the in-frame inactivation of *dinG* in the CC104 strain. First, primers were constructed that had a 50 base pair region of homology to the region surrounding *dinG* in the *E. coli* genome (H1 and H2) and a 20 base pair region of homology to the pKD3 plasmid (P1 and P2). These primers were used to PCR amplify the chloramphenicol resistance gene from the pKD3 plasmid such that there were FRT sites flanking the chloramphenicol resistance gene. These sites allow for the removal of the antibiotic resistance gene. Second, the CC104 gene was transformed with the pKD46 plasmid, which contains the genes for the bacteriophage λ Red recombinase machinery under control of an arabinose promoter. The cells were also transformed with the PCR product, which was subsequently integrated into the genome via homologous recombination. If successful, the PCR product following *dinG* inactivation should be smaller than the wild type gene, and this can be verified on an agarose gel (Right – Lane1=Roche Marker VII, Lane2=PCR Product of CC104 wild type, Lane 3=PCR Product of CC104 Δ dinG::cat). The PCR products were the expected size of about 800 base pairs for both strains. The integration event was verified via PCR that were made such that they flanked the outside of the region of the genome that was manipulated. The PCR products were also sequenced to ensure that there was no unexpected mutagenesis during the course of *dinG* inactivation.

DinG Recovery Plasmid. Mike Grodick isolated and restriction enzyme digested the pBBR1MCS-4 cloning vector (8) with XbaI and SacI. Mike Grodick also prepared and restriction enzyme (XbaI and SacI) digested the *dinG* insert generated by colony PCR in *E. coli* K12 MG1655. The *dinG* insert was ligated into pBBR1MCS-4, and was transformed into TOP10 electrocompetent cells (Invitrogen). The plasmid DNA was isolated from the transformed cells with a Qiagen miniprep kit. All plasmids were sent to Laragen for sequencing with the sequencing primers: primer pBBR1MS-4 forward check, primer pBBR1MCS-4 reverse check, primer *dinG* internal forward check, and primer *dinG* internal reverse check (**Table A4.1**).

Lac⁺ Reversion Assay (without plasmid transformation). Strains were streaked to LB agar plates with the appropriate antibiotic:

Strain	Antibiotic Resistance (Concentration in media)
CC104	None
CC104 Δ <i>dinG</i> ::cat	Chloramphenicol (25 μ g/mL)

The plates were incubated at 37 °C for 12 hours. Then, one colony was suspended in 1 mL LB, and incubated with shaking at 37 °C for 16 hours. 250 μ L of this culture was spread to NCE lactose (0.2% w/v) ampicillin (40 μ g/mL) agar plates, and incubated at 37 °C. The number of *lac*⁺ revertants was counted after 48 hours and 72 hours.

Lac⁺ Reversion Assay (with plasmid transformation). Strains were streaked to LB agar plates with the appropriate antibiotic:

Strain	Antibiotic Resistance (Concentration in media)
CC104	None
CC104 Δ <i>dinG</i> ::cat	Chloramphenicol (25 μ g/mL)

The plates were incubated at 37 °C for 12 hours. Then, one colony was suspended in 1 mL LB, and incubated with shaking at 37 °C for 12 hours. The next day the cells were transformed with the appropriate plasmid. First, 50 µL of the starter culture was used to inoculate a 10 mL LB culture, and these cultures were incubated at 37 °C with shaking until the OD₆₀₀ was between 0.6 and 0.8. Then, the cells were pelleted via centrifugation, and were washed with 10 % glycerol five times to make them electrocompetent. The cells were re-suspended in 300 µL 10 % glycerol. Then, 75 µL of these cells were transformed with 25 ng of the desired plasmid via electroporation (1.8 kV). Following electroporation, the cells were recovered in 1 mL LB for 2 hours, then the cells were spread onto LB ampicillin agar (100 µg/mL) plates to select for successful transformants. These plates were incubated for 16 hours. The cells were re-streaked onto fresh LB ampicillin (100 µg/mL) agar plates. These plates were incubated at 37 °C for 12 hours. One colony from each plate was suspended in a 1 mL LB ampicillin (100 µg/mL) culture. These cultures were incubated with shaking at 37 °C for 16 hours. 250 µL of each culture was spread onto NCE lactose (0.2% w/v) ampicillin (40 µg/mL) agar plates, and the plates were incubated at 37 °C. The number of *lac*⁺ revertants was counted after 48 hours and 72 hours.

Cell growth between strains was monitored by evaluating the total number of colony forming units on NCE glucose (0.2% w/v) ampicillin (40 µg/mL) agar plate. The agar plates were incubated at 37 °C for 24 hours. Three replicates were performed for each sample. One sample was chosen from each strain to assay for cell growth.

Growth Curves. The CC104 and CC104 *dinG*⁻ strains were transformed with plasmid according to the procedure outlined above in '*Lac*⁺ Reversion Assay for *DinG* (with Plasmid Transformation)'. The transformed strains were streaked to fresh LB ampicillin (100 µg/mL) agar plates, and then these plates were incubated at 37 °C for 12 hours. Three separate colonies from each plate were suspended in

an LB ampicillin (100 μ g/mL). These cultures were incubated at 37 °C with shaking (200 RPM) for about 13 hours.

The next day, 20 μ L of each overnight culture was used to inoculate a fresh 10 mL LB ampicillin (100 μ g/mL) culture. These cultures were incubated at 37 °C with shaking (200 RPM, Multitron Shaking Incubator (Model #AJ150 from ATR Biotech)). At different time points, a sample was removed from each culture, and was placed in a plastic cuvette. The OD₆₀₀ of each culture was obtained on a UV-Visible absorption spectrometer (Beckman-Coulter). 500 μ L total volume was assayed for each time reading. 500 μ L of LB was used to blank the instrument. The amount of culture used was diluted appropriately such that all OD₆₀₀ measurements were between 0.2 and 1.0 absorbance units (AU).

Table A4.1. Primers for Construction of the DinG Helper Function Assay Plasmids and *E. coli* Strains

Primer	Sequence
DinG Wanner Inactivation Forward	5'- CCGAAAAATGCCACAATATTGGCTGTTA TACAGTATTCAGGTTCTCGTAGGCTGG AGCTGCTTC -3'
DinG Wanner Inactivation Reverse	5'- TTAATGATTTGCGATAGTCCATTTACGA CTCCTTACCTGACTCACATCACATATGAATAT CCTCCTTAG -3'
DinG Knockout Forward Check	5'- GATGGTGTCTTGCATGACGTG -3'
DinG Knockout Reverse Check	5'- TCAATACGCCGCCAACTCA -3'
Primer <i>nth</i> Y82A Forward	5'-GCTTGCTGTTA GCA AGCCCAATCGTTT GATATAGGTTTCACCCC -3'
Primer <i>nth</i> Y82A Reverse	5'- CGATTGGGCT TGCT AACAGCAAAGCAGA AAATATCATCAAAACCTGC -3'
Primer <i>nth</i> D138A Forward	5'- CTATTCGTGTC GCC ACGCACATTTCCGC GTTTGTAAATC -3'
Primer <i>nth</i> D138A Reverse	5'- CGGAAAATGTGCGT GGC GACAGCAATAG TCGGCCAGC -3'
Primer pBBR1MCS-4 Forward Check	5'- GGTGCTGATGCCGCTGGCGATTCAAG -3'
Primer pBBR1MCS-4 Reverse Check	5'- TGTGCTGCAAGGCGATTAAGTTGG -3'
Primer <i>dinG</i> Internal Forward Check	5'- GCATGCCATTGCCCGCGAAG -3'
Primer <i>dinG</i> Internal Reverse Check	5'- CCTGTTCGCAGTGGTTAAAGG -3'

Results and Discussion

The CC104 $\Delta dinG::cat$ (CC104 *dinG*) strain was assayed to determine if the absence of *dinG* in the *E. coli* genome led to an increase in the frequency of GC to TA transversion mutations relative to the wild type CC104 strain. This result would suggest that DinG helps MutY find 8-OxoG:A. Initial results showed that the absence of *dinG* did result in an increase in the frequency of GC to TA transversion mutations (**Figure A4.3**). However, this result could not distinguish between a general increase in mutagenesis as a result of deletion of DinG, a DNA repair protein, or whether deletion of DinG led to an increase in the amount of unrepaired 8-OxoG.

Furthermore, the observation that knocking out *dinG* has an effect on the frequency of GC to TA transversion mutations does not allow for definitive conclusions to be drawn regarding whether DinG uses DNA-mediated CT to help MutY find its target lesion within the genome of *E. coli*. To more directly investigate this process, the *dinG* knockout strain was transformed with a plasmid that allowed for constitutive expression of a mutant form of EndoIII, EndoIII D138A. EndoIII D138A retains its CT properties, but is enzymatically inactive. It was hypothesized that this mutant form of EndoIII could substitute for the missing CT-signaling

strain	plasmid ^a	no. of <i>lac</i> ⁺ revertants ^b	relative to CC104 ^c
CC104	p(empty)	4.6 \pm 0.4	1
CC104 $\Delta dinG$	p(empty)	7.5 \pm 0.7	1.6 ^d
CC104	p(EndoIII D138A)	8.5 \pm 1.1	1
CC104 $\Delta dinG$	p(EndoIII D138A)	6.7 \pm 0.6	0.8 ^d
CC104	p(EndoIII Y82A)	3.4 \pm 0.3	1
CC104 $\Delta dinG$	p(EndoIII Y82A)	5.8 \pm 0.8	1.7 ^d

Figure A4.3. Results of the Helper Function Assay for MutY Activity. Table 1 from Reference 2. CC104 $\Delta dinG$ is synonymous with CC104 *dinG*. ^b Values for *lac*⁺ revertants per 10^9 cells are reported for at least twenty independent trials \pm standard error. ^c Relative to CC104 is defined as the ratio of *lac*⁺ revertants for the CC104 *dinG* knockout strain to the number of *lac*⁺ revertants for the wild type CC104 strain containing the sample plasmid as the *dinG* knockout strain. ^d $p < 0.01$ as calculated with a two-tailed Student's t-test.

capacity of DinG. This experiment suggested that the presence of this plasmid did in fact decrease the number of *lac*⁺ revertants observed for the CC104 *dinG* strain (Figure 4). However, when the CT-deficient mutant of EndoIII, EndoIII Y82A, was introduced into the strain there was not a statistically significant change in the number of *lac*⁺ revertants, suggesting that the decrease in GC to TA transversion mutations upon introduction of the pBBR1MCS-4 *nth* D138A plasmid was not due to the CT proficiency of the version of EndoIII that was introduced into the CC104 strain.

The wild type CC104 strain was also transformed with the plasmids that contained the gene for Endonuclease III Y82A and Endonuclease III D138A. Based on previous results, it was expected that all of the strains should have the same number of *lac*⁺ revertants (1). In contrast to this expectation, the number of *lac*⁺ revertants was slightly different for the wild type CC104 strain transformed with the different types of plasmid DNA. Thus, when the CC104 wild type strain that was transformed with a specific plasmid was compared with the CC104 *dinG* strain transformed with that same plasmid, the trends predicted by the redistribution model were observed. Specifically, EndoIII D138A rescued the mutagenic phenotype of the CC104 *dinG* strain while EndoIII Y82A could not rescue this phenotype.

To confirm that disruption of *dinG* was responsible for the mutagenic phenotype of the strain, the gene for this DNA helicase was introduced into the CC104 *dinG* strain on a plasmid with the pBBR1MCS-4 backbone (*dinG* recovery plasmid). This recovery plasmid contained both *dinG*, and the region upstream of *dinG* in the *E. coli* genome that contained transcriptional regulatory elements. Introduction of DinG on this medium copy number plasmid led to a decrease in overall cell viability as measured by the total number of colony forming units on NCE glucose agar plates. This result is consistent with previous observations that, expression of DinG at levels above those natural for the cell is toxic. Growth curves were also performed to confirm this growth deficiency (**Figure A4.4**). Due to the differences in cell viability between the CC104 *dinG* strain and the CC104

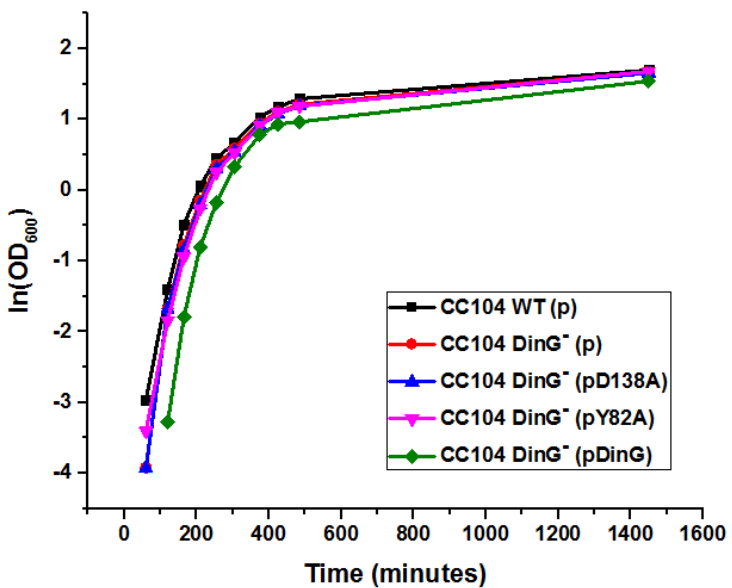


Figure A4.4. Growth Curves for the CC104 *E. coli* Strains. Each data point is an average of the data from three separate trials. The word in parenthesis indicates the type of plasmid with which the indicated strains were transformed: (p) = pBBR1MCS-4, (pD138A) = pBBR1MCS-4 with *nth* D13A, (pY82A) = pBBR1MCS-4 with *nth* Y82A, (pDinG) = pBBR1MCS-4 with *dinG*.

dinG⁻ strain that contained the DinG recovery plasmid, it was not possible to conclusively determine whether the recovery plasmid fully rescued the CC104 *dinG*⁻ mutagenic phenotype. Future work should be done to determine a better plasmid backbone for the recovery plasmid to both confirm the phenotype and test potential CT-deficient mutants of DinG in the context of the Helper Function Assay.

Conclusions

The Helper Function Assay was optimized to determine whether DinG, a helicase from *E. coli* that contains a 4Fe-4S cluster, signals MutY via DNA CT to find and repair mutagenic 8-OxoG:A lesions in the cell. A CC104 *dinG*⁻ strain was created by replacing *dinG* with the gene for chloramphenicol acetyltransferase within the *E. coli* genome. This strain had an increase in the frequency of GC to TA transversion mutations relative to the wildtype strain, suggesting that DinG may

signal MutY via DNA CT to help MutY more effectively find and repair sites of damage in the genome. To investigate this process further a plasmid was introduced into the DinG knockout strain that contained the gene for an EndolII mutant, EndolII D138A, that was catalytically inactive, but CT proficient. It was shown that this strain led to a decrease in the total number of GC to TA transversion mutations relative to the DinG knockout strain transformed with an empty plasmid. When a CT deficient form of EndolII was introduced into the DinG knockout strain the rate of mutagenesis was the same as that observed for CC104 *dinG*⁻. These results suggest that DinG, MutY, and EndolII all participate in DNA CT signaling as a first step in DNA damage detection and repair.

References

1. Boal, A. K., *et al.* (2009) Redox Signaling Between DNA Repair Proteins for Efficient Lesion Detection. *Proc Natl Ac Sci USA.* 106, 15237-15242.
2. Grodick, M. A., Segal, H. M., Zwang, T. J., and Barton, J. K. (2014) DNA-Mediated Signaling by Proteins with 4Fe-4S Clusters Is Necessary for Genomic Integrity. *J Am Chem Soc.* 136, 6470-6478.
3. Cupples, C. G. and Miller, J. H. (1989) A Set of *lacZ* Mutations in *Escherichia coli* that Allow Rapid Detection of Each of the Six Base Substitutions. *Proc Natl Acad Sci USA.* 86, 5345-5349.
4. Michaelis, M. L., Cruz, C., Grollman, A. P., and Miller, J. H. (1992) Evidence that MutY and MutM Combine to Prevent Mutations by an Oxidatively Damaged Form of Guanine in DNA. *Proc Natl Ac Sci USA.* 89, 7022-7025.
5. Davis, R.W.; Botstein, D.; Roth, J.R. (1980) *Advanced Bacterial Genetics. A Manual for Genetic Engineering* Cold Spring Harbor Laboratory.
6. Miller, J. H. (1992) *A Short Course in Bacterial Genetics: A Laboratory Manual and Handbook for Escherichia coli and Related Bacteria.* Cold Spring Harbor Laboratory.
7. Datsenko, K. A. and Wanner, B. L. (2000) One-Step Inactivation of Chromosomal Genes in *Escherichia coli* K-12 using PCR Products. *Proc. Natl. Ac. Sci. USA.* 97, 6640-6645.
8. Kovach, M. E., Elzer, P. H., Hill, D. S., Robertson, G. T., Farris, M. A., Roop II, R. M., and Peterson, K. M. (1995) Four New Derivatives of the Broad-Host-Range Cloning Vector pBBR1MCS, Carrying Different Antibiotic-Resistance Cassettes. *Gene.* 166, 175-176.